

**The Host Galaxies and Progenitors of  
Core-Collapse Gamma-Ray Bursts**

by

**Ashley Aston Chrimes**

**Thesis**

Submitted to the University of Warwick

for the degree of

**Doctor of Philosophy**

**Department of Physics**

March 2020

# Contents

<b>List of Tables</b>	<b>vi</b>
<b>List of Figures</b>	<b>vii</b>
<b>Acknowledgments</b>	<b>xi</b>
<b>Declarations</b>	<b>xii</b>
<b>Abstract</b>	<b>xiii</b>
<b>Chapter 1 Introduction</b>	<b>1</b>
1.1 The Discovery of Gamma-Ray Bursts . . . . .	1
1.2 GRB Light Curves and Spectra . . . . .	4
1.2.1 Prompt Emission . . . . .	4
1.2.2 Afterglow . . . . .	5
1.2.3 The Neil Gehrels Swift Observatory . . . . .	9
1.2.4 Non-Standard Phenomena . . . . .	10
1.2.5 GRB-Supernovae . . . . .	12
1.3 The Evolution of Massive Stars . . . . .	12
1.3.1 Star Formation . . . . .	14
1.3.2 The Main Sequence . . . . .	15
1.3.3 Post-Main Sequence Evolution . . . . .	17
1.3.4 Supernovae . . . . .	19
1.4 $\Lambda$ CDM Cosmology, Reionisation and Galaxy Evolution . . . . .	23
1.5 The Host Galaxies of Core-Collapse GRBs . . . . .	32
1.6 Core-Collapse GRB Mechanisms and Progenitors . . . . .	38
1.7 Multi-Messenger Astronomy and other Extragalactic Transients . . . . .	42
1.7.1 Short duration GRBs, Kilonovae and Gravitational Waves . . . . .	42
1.7.2 Very High Energy photons and Neutrinos . . . . .	44

1.7.3	Superluminous Supernovae . . . . .	45
1.7.4	Tidal Disruption Events . . . . .	45
1.7.5	Fast Radio Bursts . . . . .	45
1.8	Overview and Scientific Aims of this Thesis . . . . .	47

**Chapter 2 Investigating a population of infrared-bright gamma-ray burst host galaxies** **50**

2.1	Introduction . . . . .	50
2.2	Sample Selection . . . . .	52
2.2.1	Rationale . . . . .	52
2.2.2	Initial Cross-Matching and Cuts . . . . .	52
2.2.3	Consideration of Burst Error Radii and Local Background Densities . . . . .	54
2.2.4	Sample summary so far . . . . .	59
2.3	Observations . . . . .	59
2.3.1	WHT Imaging . . . . .	59
2.3.2	WHT Spectroscopy . . . . .	61
2.3.3	VLT Spectroscopy . . . . .	61
2.3.4	ATCA Radio Observations . . . . .	65
2.4	Archival and Survey Data . . . . .	67
2.5	Previously Reported GRB Hosts and Observations . . . . .	72
2.5.1	Optical Survey Detections . . . . .	72
2.5.2	Optical Survey Non-Detections . . . . .	74
2.5.3	Lacking Coverage . . . . .	75
2.6	SED Fitting . . . . .	75
2.6.1	Multiple Candidate Hosts . . . . .	75
2.6.2	Galaxy SED fitting with MAGPHYS . . . . .	76
2.6.3	Galaxy SED fitting Summary . . . . .	79
2.6.4	Stellar Fitting . . . . .	80
2.7	Results and Discussion . . . . .	81
2.7.1	SED Fitting Results . . . . .	81
2.7.2	Short GRBs . . . . .	81
2.7.3	Redshift Distribution . . . . .	83
2.7.4	Masses, Dust Extinction and SFR . . . . .	85
2.7.5	Host Luminosity . . . . .	87
2.7.6	Burst Luminosity . . . . .	90
2.8	Interpretation . . . . .	92

2.8.1	IR Sources with an Optical Counterpart . . . . .	92
2.8.2	IR Sources without an Optical Counterpart . . . . .	92
2.8.3	Host Galaxy Properties . . . . .	94
2.8.4	The Nature of the IR-bright population . . . . .	94
2.8.5	The Utility of IR-bright GRB host selection . . . . .	96
2.9	Conclusions . . . . .	96
2.10	Subsequent Developments . . . . .	97

**Chapter 3 Chandra and Hubble Space Telescope Imaging of dark gamma-ray bursts and their host galaxies 99**

3.1	Introduction . . . . .	100
3.2	Observations and Data Reduction . . . . .	102
3.2.1	Target Catalogue . . . . .	102
3.2.2	<i>Hubble Space Telescope</i> . . . . .	104
3.2.3	<i>Chandra</i> . . . . .	105
3.3	Methodology . . . . .	105
3.3.1	Astrometric Alignment . . . . .	105
3.3.2	Host Measurement with SEXTRACTOR . . . . .	109
3.3.3	Concentration and Asymmetry . . . . .	109
3.3.4	Morphological Uncertainties . . . . .	112
3.4	Results . . . . .	113
3.4.1	Host Colours and Luminosities . . . . .	114
3.4.2	Host Morphologies . . . . .	116
3.4.3	Burst Offsets . . . . .	118
3.5	Discussion . . . . .	121
3.5.1	Host Colours and Magnitudes . . . . .	121
3.5.2	Host Galaxy Morphologies . . . . .	121
3.5.3	Host Galaxy – GRB Offsets . . . . .	122
3.6	Conclusions . . . . .	124
3.7	Subsequent Developments . . . . .	125

**Chapter 4 The case for a high-redshift origin of GRB100205A 126**

4.1	Introduction . . . . .	126
4.2	Observations, Data Reduction and Results . . . . .	127
4.2.1	Gemini . . . . .	128
4.2.2	<i>Hubble Space Telescope</i> . . . . .	128
4.3	Interpretation . . . . .	131
4.3.1	X-ray based SED construction . . . . .	132

4.3.2	NIR based SED construction . . . . .	136
4.3.3	High energy properties . . . . .	138
4.3.4	Non-detection of the host . . . . .	139
4.4	Conclusions . . . . .	141
4.5	Subsequent Developments . . . . .	141

**Chapter 5 The progenitors and event rates of long-duration gamma-ray bursts with BPASS 142**

5.1	Introduction . . . . .	142
5.2	Classification of Core-Collapse Progenitor Models . . . . .	144
5.3	Introducing Complex Tidal Interactions to BPASS . . . . .	151
5.3.1	Tidal forces . . . . .	152
5.3.2	Convective damping of the equilibrium tide . . . . .	154
5.3.3	Radiative damping of the dynamical tide . . . . .	154
5.3.4	Implementation of tides . . . . .	155
5.3.5	The effect of tides on high-mass stars . . . . .	157
5.4	Calculation of long GRB volumetric event rates and inference of progenitor properties . . . . .	162
5.4.1	Transient population synthesis . . . . .	162
5.4.2	Bayesian parameter estimation . . . . .	165
5.5	Predicted long gamma-ray burst rates and progenitors . . . . .	167
5.5.1	MCMC results . . . . .	167
5.5.2	Metallicity distribution . . . . .	170
5.5.3	Delay-time distribution . . . . .	171
5.5.4	Progenitor systems . . . . .	172
5.5.5	Core angular momentum . . . . .	173
5.6	Discussion . . . . .	176
5.6.1	The production of GRBs . . . . .	176
5.6.2	The metallicity dependence of GRBs . . . . .	179
5.6.3	Uncertainties in the stellar modelling . . . . .	182
5.6.4	Magnetars as GRB central engines . . . . .	184
5.6.5	Future possibilities . . . . .	185
5.7	Conclusions . . . . .	187
5.8	Subsequent Developments . . . . .	187

**Chapter 6 Conclusions and future prospects 189**

6.1	Summary of results . . . . .	190
6.1.1	The nature of infrared-bright gamma-ray burst host galaxies . . . . .	190

6.1.2	Dark gamma-ray bursts and their host galaxies . . . . .	190
6.1.3	Core-collapse gamma-ray burst progenitors via binary evolution pathways . . . . .	191
6.2	Future prospects . . . . .	192
6.2.1	Core-collapse GRB synthesis: additions and improvements . .	192
6.2.2	Core-collapse GRB synthesis: other observables . . . . .	193
6.2.3	Population synthesis of other transients . . . . .	194
6.2.4	Opportunities from next-generation facilities . . . . .	194
6.3	Final conclusions . . . . .	198
<b>Appendix A IR-bright GRB hosts: additional information</b>		<b>203</b>
<b>Appendix B CXO and HST Dark GRBs: additional information</b>		<b>209</b>
<b>Appendix C Data and funding acknowledgements</b>		<b>214</b>

# List of Tables

2.1	GRBs with a <i>WISE</i> source coincident with the X-ray afterglow . . .	56
2.2	GRB- <i>WISE</i> matches rejected due to false alarm probability cuts or <i>WISE</i> data quality flags . . . . .	57
2.3	WHT/ACAM imaging of IR-bright GRB host candidates . . . . .	60
2.4	VLT/X-shooter and WHT/ACAM spectroscopy of IR-bright GRB host candidates . . . . .	61
2.5	Emission line measurements from the host of GRB 141212A . . . . .	66
2.6	Observations of the radio emission from 14 ATCA targets . . . . .	66
2.7	Photometric star-galaxy classification of candidate hosts . . . . .	71
2.8	Galaxy SED fitting results . . . . .	82
2.9	IR-bright GRB hosts properties compared to literature samples . . .	86
3.1	$\beta_{\text{OX}}$ limits for the dark burst sample . . . . .	103
3.2	Details of the dark burst host galaxy <i>HST</i> observations . . . . .	106
3.3	Details of the dark burst <i>CXO</i> observations . . . . .	107
3.4	Host properties for the dark burst sample . . . . .	112
3.5	Dark GRB host properties for which a redshift is required . . . . .	113
3.6	Limits on dark GRB host properties where a redshift is unavailable .	114
3.7	Statistical comparisons of the dark GRB offset distribution . . . . .	119
4.1	Gemini observations of the GRB 100205A afterglow . . . . .	129
4.2	GRB 100205A afterglow spectral and temporal fit parameters . . . .	136
5.1	BPASS metallicity scalings . . . . .	150
5.2	MCMC posterior distribution properties . . . . .	168
5.3	Properties of tidally-spun GRB progenitors . . . . .	174
A.1	Archival photometry for 30 GRB locations with reliable <i>WISE</i> de- tected counterparts . . . . .	204

# List of Figures

1.1	The distribution of GRBs across the sky from the first BATSE catalogue	2
1.2	The distribution of GRB $T_{90}$ durations from the first BATSE catalogue	3
1.3	Illustration of the GRB fireball model . . . . .	7
1.4	Example model spectra for the afterglows of GRBs . . . . .	8
1.5	$T_{90}$ duration versus spectral hardness for all <i>Swift</i> GRBs up to 2016	10
1.6	A theoretical Hertzsprung-Russell diagram with observational data overlaid . . . . .	13
1.7	Imaging of the afterglow of GRB 090423 . . . . .	25
1.8	The star formation rate density history of the Universe . . . . .	29
1.9	The steps required to produce a synthetic galaxy SED . . . . .	30
1.10	The host galaxy of GRB 980425 / SN 1998bw . . . . .	35
1.11	The comoving rate density of GRBs over cosmic time . . . . .	36
1.12	The sky localisation of GW 170817 (GRB 170817A) in gravitational waves and high energy photons, and the kilonova discovery image . .	44
2.1	The surface density of sources in the <i>WISE</i> W1 band as a function of Galactic latitude and apparent magnitude . . . . .	55
2.2	The evolution of apparent angular extent with redshift . . . . .	57
2.3	Slit positions for VLT/X-shooter and WHT/ACAM spectroscopic observations of IR-bright GRB host candidates . . . . .	62
2.4	The WHT/ACAM spectrum of the object associated with GRB 111222A	63
2.5	The VLT/X-shooter spectrum of the object associated with GRB 091102	63
2.6	The VLT/X-shooter spectrum of the object associated with GRB 120612A	64
2.7	Emission lines from the host galaxy of GRB 141212A . . . . .	64
2.8	Star-galaxy separation for IR-bright sources which have an <i>i</i> -band PSF and Kron magnitude . . . . .	68
2.9	Star-galaxy separation for sources which have a W1 and <i>J</i> -band magnitude . . . . .	68

2.10	Source selection flowchart . . . . .	73
2.11	SEDs for objects best-fit or otherwise confirmed as galaxies . . . . .	77
2.12	SDSS stellar templates for sources which were best-fit or otherwise confirmed as stars . . . . .	78
2.13	The redshift cumulative distribution of the IR-bright long GRB host sample . . . . .	83
2.14	The cumulative distribution of stellar masses in the IR-bright host population . . . . .	86
2.15	The cumulative distribution of $A_V$ in the IR-bright host population . . . . .	88
2.16	The cumulative distribution of SFR in the IR-bright host population . . . . .	88
2.17	Rest-frame absolute magnitude versus redshift for the IR selected hosts . . . . .	89
2.18	Placement of GRBs occurring in IR-bright galaxies on the Amati relation . . . . .	91
2.19	Comparison of IR-bright GRB hosts to other samples across galaxy parameter space . . . . .	93
3.1	A comparison between the redshift distribution of the dark GRB sample, other similar studies and the GOODS-MUSIC galaxy survey . . . . .	104
3.2	GRB positions on their host galaxies after astrometric alignment . . . . .	110
3.3	Host and X-ray afterglow of GRB 090113 . . . . .	111
3.4	Dark GRB host redshifts versus absolute magnitude . . . . .	115
3.5	The F160W apparent magnitude of dark GRB hosts versus their observed F606W-F160W colour . . . . .	117
3.6	Dark GRB host galaxies in $CA$ parameter space . . . . .	118
3.7	The cumulative distribution of $R_{50}$ normalised host offset for dark GRBs and comparison data sets . . . . .	120
4.1	Gemini image cutouts around the afterglow of GRB 100205A . . . . .	129
4.2	<i>HST</i> image stamps at the location of GRB 100205A . . . . .	130
4.3	The gamma-ray, X-ray and NIR/optical light curve of GRB 100205A . . . . .	131
4.4	Fitting a broken power law to the $J$ , $H$ , $K$ and X-ray observations of GRB 100205A . . . . .	133
4.5	Constraining the extinction and redshift of the host of GRB 100205A assuming the X-ray afterglow decay rate . . . . .	135
4.6	Constraining the extinction and redshift of the host of GRB 100205A assuming the NIR afterglow decay rate . . . . .	137
4.7	The isotropic equivalent energy of GRB 100205A compared with the SHOALS sample . . . . .	139

4.8	GRB host galaxy apparent magnitudes versus redshift . . . . .	140
5.1	Matching synthesised type II, Ib and Ic SN relative fractions to observations . . . . .	146
5.2	The ratio of stripped envelope (SE) to hydrogen-rich (type II) supernovae as a function of metallicity . . . . .	147
5.3	Pre-core collapse HR diagram with BPASS predictions and observed progenitors . . . . .	148
5.4	A schematic diagram demonstrating the operation of the equilibrium tide . . . . .	152
5.5	An example of the tidal algorithm implementation . . . . .	158
5.6	The change in the number of Ic SNe and black holes produced per $10^6 M_{\odot}$ of star formation due to the inclusion of tidal interactions . . . . .	159
5.7	The number of high-mass progenitor core-collapse events arising from each BPASS model type - without tides . . . . .	160
5.8	The number of high-mass progenitor core-collapse events arising from each BPASS model type - with tides . . . . .	161
5.9	The effect of tides on the specific angular momentum of stars at core-collapse . . . . .	162
5.10	The effect of tides on the delay time distribution . . . . .	163
5.11	The cosmic star formation rate history employed, decomposed into 12 constituent metallicities . . . . .	164
5.12	Covariances between the four fitted parameters in the two-pathway GRB model, and the marginalised posterior probability density distributions for each . . . . .	168
5.13	The distribution of observed and fitted GRB rates, as a function of redshift . . . . .	169
5.14	BPASS predictions for the intrinsic volumetric rate of GRBs arising from QHE and tidal pathways . . . . .	169
5.15	BPASS and KK04 metallicity scaling . . . . .	171
5.16	Cumulative metallicity distributions of the predicted GRB progenitors . . . . .	172
5.17	Delay time distributions for QHE and tidal GRB progenitors . . . . .	173
5.18	The relative occurrence of the predicted non-QHE GRB progenitors across binary parameter space . . . . .	175
5.19	The enclosed mass as a function of radius in pre-collapse stars . . . . .	176
5.20	The minimum specific angular momenta required for a GRB in the selected BPASS models . . . . .	177

5.21	BPASS models which produce a GRB via the tidal pathway, placed on the HR diagram . . . . .	179
5.22	The efficiency of GRB progenitor production across metallicity . . .	180
5.23	The intrinsic GRB rate if only magnetar central engines are allowed	185
5.24	The synthesised host metallicity distribution if GRBs are limited to magnetar central engines only . . . . .	186
6.1	Artist’s impression of a gamma-ray burst in a binary star system. . .	202
A.1	Archival imaging of IR-bright GRB host candidates in the W1, <i>J</i> and <i>r</i> bands . . . . .	205
B.1	Re-sampling distributions for asymmetry and enclosed flux radii in the F606W band . . . . .	210
B.2	Re-sampling distributions for asymmetry and enclosed flux radii in the F160W band . . . . .	211

# Acknowledgments

First of all I have to thank my supervisor Elizabeth Stanway, whose vast knowledge, insight and support have made this thesis not only possible, but dare I say it, as long as it is! Thanks to Andrew Levan, whose support both at Warwick and from across the North Sea has been greatly appreciated, and also to the many collaborators around the world who provided comments and feedback along the way. Thanks to the academic staff at Warwick for giving me the chance to do a PhD in the first place - I honestly never thought I would and still can't quite get my head around it! Thanks to Danny, for the chance to 'go to GOTO'. Thanks to Boris and Mark for the coffee, and Ares for the cakes. No thanks are given to Genkai or Heath, but Purcari and Katsuura were OK. Thanks to Klaas, Ben, Joe, Henry, Matt Batt, Tim, Elena and Ry for being the best office mates, and shout out to Greg, Emma, Matt and Ares for their sterling work running the planetarium over the last four years! Thank you for the memes (particularly the spicy ones), thanks to my STFC cohort James and Ry for going on this journey together all the way from Hull, and thanks to everyone else at Warwick who I haven't mentioned, but who made my time here the best.

For Lilac - everyone should have a cat to help them through a PhD. And finally, for Mum, who doesn't have the first clue what any of this astro lark is about, but insists on being proud of me anyway.

# Declarations

This is a declaration of the extent of the original work within this thesis and of the work that has been published. This thesis has not been submitted in part or full to any other institution for any other qualification.

Chapter 2 is based on a paper published in *Monthly Notices of the Royal Astronomical Society* (MNRAS) under the title ‘Investigating a Population of Infrared Bright Gamma-ray Burst Host Galaxies’ (Chrimes et al., 2018). The ATCA, WHT and VLT data presented in this Chapter were obtained by Elizabeth Stanway, Luke Davies, Charlotte Angus and Stephanie Greis. Section 2.3.4 on ATCA radio observations was written by, and the analysis therein performed by, Elizabeth Stanway. All other analyses were completed by the author.

Chapter 3 is based on a MNRAS publication titled ‘Chandra and Hubble Space Telescope observations of dark gamma-ray bursts and their host galaxies’ (Chrimes et al., 2019a). The *HST* and *CXO* data presented here was obtained through programmes led by Andrew Levan (and in one case Chryssa Kouveliotou). Key collaborators on this Chapter were Andrew Levan, Elizabeth Stanway and Joseph Lyman. All analyses were completed by the author.

Chapter 4 is based on work published in MNRAS as ‘The case for a high-redshift origin of GRB 100205A’ (Chrimes et al., 2019b). The Gemini datasets presented in this Chapter were obtained by Neil Tanvir and Derek Fox. All analyses were completed by the author, with the exception of the Gemini data reduction described in section 4.2.1, which was performed in collaboration with Klaas Wiersema. The other primary collaborators on this Chapter were Andrew Levan and Elizabeth Stanway.

Chapter 5 is based on ‘Binary population synthesis models for core-collapse gamma-ray burst progenitors’, previously published in MNRAS (Chrimes et al., 2020). Elizabeth Stanway and JJ Eldridge were collaborators. Elizabeth Stanway performed the model re-weightings described in this Chapter. All other analyses were completed by the author.

For complete lists of co-authors and their contributions, as well as data and funding acknowledgements, please see Appendix C.

# Abstract

Ever since their discovery over 50 years ago, gamma-ray bursts (GRBs) have been the subject of intense interest in transient astronomy. Despite being extremely luminous, their distance and transient nature have made studies challenging. By investigating their galactic environments, lightcurves and spectra, a consensus has arisen that long-duration ( $> 2$ s) GRBs are highly beamed relativistic explosions, arising from the collapse of massive, fast-spinning, stripped-envelope stars. However, the exact nature of their central engines and progenitor systems remain mysterious, not least due to the variety of environments they inhabit. The challenge is to explain all of the observed properties of long GRBs and their host galaxies simultaneously. In this thesis, I present multi-wavelength observational studies of unusual GRB host galaxies, the hosts of unusual GRBs, and a theoretical investigation into the progenitor systems of long GRBs using binary population synthesis techniques.

I begin by characterising a population of GRB hosts which are detected in the *WISE* infrared all-sky survey. It is pertinent to ask whether such a sub-population of galaxies have physically distinct properties. Making use of specifically obtained data, in addition to a wealth of archival imaging, I show that  $\sim 50\%$  of the *WISE*-GRB associations are chance alignments, and that the genuine galaxy matches are in the dusty and nearby tails of the established GRB host distributions.

I then describe an investigation into dark GRB host galaxies. Dark GRBs lack the optical emission expected from the spectral extrapolation of their X-ray afterglows. In this work, I use data from the *Hubble Space Telescope* and *Chandra X-ray Observatory* to measure how dark GRBs trace their host galaxy light. The findings indicate that dark bursts are not tracing light in a significantly different way to optically bright GRBs, and that at most  $\sim 20\%$  of dark GRBs occur at redshift  $> 5$ . It also suggests that the dust within lower redshift dark GRB hosts is uneven on sub-galactic scales, due to the absence of a morphological difference between the hosts of optically-dark and optically-bright GRBs. A follow-up study on GRB 100205A, whose host is undetected in both the observed NIR and optical *HST* bands, is performed. This burst's afterglow indicates that it lies at redshift  $> 4.5$ , consistent with the host non-detections. This adds GRB 100205A to the small sample of GRBs known at these redshifts. The fact that this burst had not already been characterised demonstrates the important of rapid, multi-wavelength follow-up for unambiguous high-redshift GRB identifications.

Finally, I use BPASS (Binary Population and Spectral Synthesis) to model the occurrence rates of long GRBs from rapidly-spinning, stripped envelope progenitors. I introduce tidal interactions to the BPASS model outputs, and track stellar spins across a grid of models in binary and metallicity parameter space. A dual pathway model (of accretion and tidally driven spin) can reproduce the observed rates, the host galaxy metallicities, and theoretical GRB requirements for the angular momenta of accretion discs around newly formed black holes. Next-generation facilities, combined with new observational tests of these and other proposed models, will help to narrow the gap between GRB observation and theory over the next decade.

# Chapter 1

## Introduction

*“All you really need to know for the moment is that the Universe is a lot more complicated than you might think, even if you start from a position of thinking it’s pretty damn complicated in the first place.”— Douglas Adams, The Hitchhikers Guide to the Galaxy*

### 1.1 The Discovery of Gamma-Ray Bursts

For millennia, human beings have looked at the night sky and have tried to make sense of it. Stars appear fixed on the celestial sphere, moving across the sky with the rotation of the Earth, seemingly unchanging in appearance across our lifetimes. Other celestial bodies, like planets and comets, appear to move with respect to the background stars, continuously changing in their apparent brightness. And then there are transient events. These are stationary, but temporary, brightening and fading, never to be seen again. Astrophysical transients have been documented for as long as astronomy has existed. The earliest recorded example was likely the violent death of massive star, a supernova, noted by Chinese astronomers in AD 185 as being a ‘guest star’ (Xi, 1955). Over the centuries, many bright transients have been observed, with exponentially more being seen in recent years as telescope and imaging technology evolves and improves. Culminating in the multi-wavelength, ground and space-based facilities of today, our increasing ability to study astrophysical transients has brought about some understanding of their origin, but also more questions. This thesis will focus on one class of astrophysical transient, charting their discovery and subsequent ongoing efforts to understand their origin. The work carried out during my PhD is then presented as the latest contribution to our understanding of one of the most extreme of all astrophysical phenomena - core-collapse gamma-ray bursts.



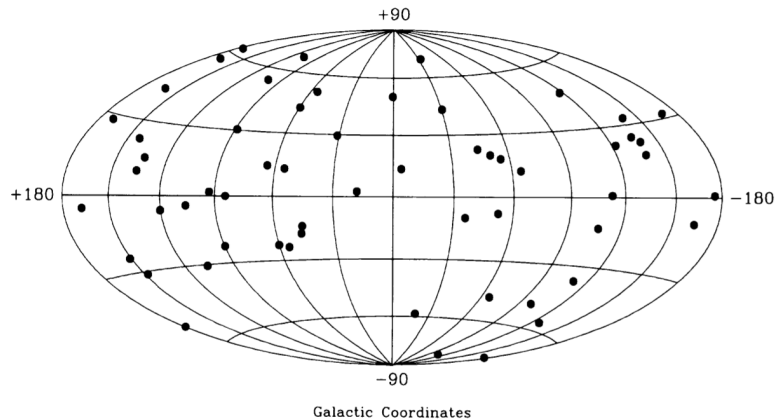


Figure 1.1: The distribution of 58 short duration GRBs across the sky from the first BATSE catalogue (figure from Kouveliotou et al., 1993). The bursts were statistically consistent with being isotropic, favouring a cosmological origin (Briggs, 1993).

The gamma-ray burst (GRB) story begins in 1967. The American Vela satellites, gamma-ray observatories designed to monitor nuclear testing in the Soviet Union, began detecting bursts of radiation with temporal profiles inconsistent with such tests. Even more intriguingly, detections by several satellites and the measured time delays between them allowed the bursts to be triangulated, ruling out the Earth or Sun as an origin. An initial sixteen events were published by Klebesadel et al. (1973). The authors noted no spatial or temporal coincidence with bright novae or supernovae. However, they calculated that the fluence of these bursts would make them consistent with supernova energetics if placed at an extragalactic distance of 1 Mpc, the approximate distance of the Andromeda galaxy.

The race to understand this newly discovered phenomenon had begun. The first aim was to discover more GRBs, and to study this high-energy emission in greater detail. However, it wasn't until the launch of NASA's Compton Gamma-Ray Observatory in 1991 that a significant population of GRBs began to be observed. The on-board instrument BATSE (Burst and Transient Source Experiment) was specifically designed to characterise GRBs (Fishman et al., 1993), and was a great success, detecting GRBs at a rate of approximately one per day. Several major discoveries were made: that the bursts were isotropic across the sky (Briggs, 1993), all but confirming a cosmological origin, and that they had a range of durations and spectral shapes. A key result was confirmation that the bursts produced a bimodal distribution in  $T_{90}$  duration, the time taken for 90 per cent of the gamma-ray fluence to arrive. Fluence is defined as the total energy received per unit area, typically

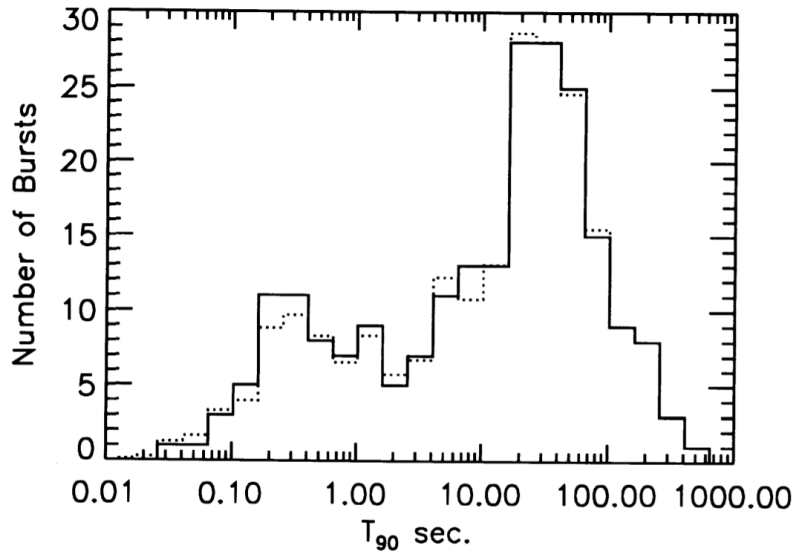


Figure 1.2: The distribution of GRB  $T_{90}$  durations from the first BATSE catalogue (figure from Kouveliotou et al., 1993). The distribution is clearly bimodal with peaks at  $\sim 0.5$ s and  $\sim 30$ s - the solid line is from the raw data, the dashed line arises from consideration of the uncertainties on these data. A dividing line at 2s was established, based on these observations, to distinguish short and long duration events.

measured in units of  $\text{erg cm}^{-2}$  in high energy astronomy. Flux, on the other hand, is the energy received per unit area per unit time. Fluence is therefore the integral of flux over time. When count rates are low, it is often more convenient to work in terms of photon flux, which is the number of photons arriving per area per time. The GRB  $T_{90}$  distribution is split into short ( $< 2$ s with hard spectra) and long ( $> 2$ s with soft spectra) duration events (Mazets et al., 1981, 1982; Kouveliotou et al., 1993). The BATSE isotropic sky distribution and durations are shown in figures 1.1 and 1.2.

By the mid nineties, theories abounded on the nature of GRBs (e.g. Nemiroff, 1994; Harding, 1994). Earth based, Solar and Milky Way sources were ruled out or disfavoured due to the sky distribution, although Galactic halo events remained a possibility. Remaining ideas were influenced by the short timescale ( $< 1$ s) variability in the BATSE light curves, which correspond to emitting regions less than  $10^5$  m across. This implied that objects large in extent, such as supermassive black holes (found in the centres of galaxies, sometimes as active galactic nuclei), could not be responsible. The merger of two neutron stars, or a neutron star and black hole, was suggested as a possible pathway (Paczynski, 1986; Narayan et al., 1992). Other ideas

included the rapid spin-down of millisecond period, highly magnetised neutron star (a magnetar, Duncan and Thompson, 1996; Wheeler et al., 2000), or the formation of a black hole accretion disc in the collapsing core of a exploding star (Woosley, 1993). In all these scenarios, a relativistic outflow would be powered by a nascent compact object. However, no burst had yet been well localised, so the galactic environments producing them were unknown, and observations were limited to gamma-rays and X-rays, with poor spectral resolution. At this time, a succinct summary would be that GRBs were thought to be highly energetic, possibly cataclysmic events, isotropically distributed across the sky - but beyond this little was known.

The remainder of the introduction continues this story from the 1990s to the present day, by focusing separately on three areas of research. These include discoveries made through (i) improved observations of GRB light curves and spectra, across the electromagnetic spectrum, (ii) advances in stellar evolution theory and GRB theoretical modelling, and (iii) the improved localisation of bursts and subsequent host galaxy studies. Throughout, I focus on the long-duration class of bursts, which as we shall see are now understood to arise from a subset of collapsing massive stars. Wherever I refer simply to ‘GRBs’, this means the long-duration, core-collapse variety. I end the introduction with a summary of other extreme extragalactic transients, followed by the scientific aims of this thesis.

## 1.2 GRB Light Curves and Spectra

### 1.2.1 Prompt Emission

The first information gleaned about GRBs was from their light curves and spectra, initially from space-based observations of their prompt gamma-ray and X-ray emission (typically lasting seconds to minutes). The Earth’s atmosphere acts as a barrier to most of the gamma-rays and X-rays arriving from astrophysical sources, due to photoelectric absorption. This means that the study of gamma and X-ray emitters requires space-based instrumentation. The difficulty and cost of designing, launching and operating satellites with respect to ground-based observatories was a barrier to the progress of GRB studies throughout the 1970s and 80s. However, in the 1990s several high-energy observatories were launched, including the aforementioned Compton Gamma-Ray Observatory. The first models of GRB spectra were based on high-energy Compton/BATSE data. Band et al. (1993) developed an empirical model to describe BATSE GRB spectra, which has subsequently become known as the ‘Band function’. This is given by a broken power-law with an exponential cut-off,

$$\begin{aligned}
N(E) &\propto E^\alpha \exp(-E/E_0), E < E_0 \\
N(E) &\propto E^\beta, E > E_0
\end{aligned}
\tag{1.1}$$

where  $N(E)$  is the number of photons with energy  $E$ ,  $E_0$  is the break energy, and  $\alpha, \beta$  are the low and high energy indexes respectively. Band et al. (1993) noted that although this model could fit the majority of GRB spectra over the BATSE energy range of 20 keV to 8 MeV, there was a large amount of scatter (covering several orders of magnitude) in the parameters  $E_0$ ,  $\alpha$  and  $\beta$ .

Efforts were also being made to explain the spectra theoretically. The rapid, millisecond timescale variability in the prompt light curves, and photons above the pair-production limit (Cavallo and Rees, 1978), suggested that the events were highly relativistic. Combined with the power-law nature of the spectra being measured, this led to synchrotron radiation from shocks being put forward as a possible emission mechanism (Rees and Meszaros, 1992; Sari et al., 1996). Upon the discovery of GRB afterglows, synchrotron radiation was established as the likely source of that multi-wavelength emission, but there is still debate to this day whether it is the dominant process in the prompt phase (e.g. Zhang et al., 2016).

### 1.2.2 Afterglow

In 1997, BeppoSAX (Boella et al., 1997) detected X-ray emission in the direction of GRB 970228 (Costa et al., 1997). The coded mask on BeppoSAX allowed for spatial resolutions as good as one arcminute, which was sufficient to identify a host galaxy for the burst, and make optical follow-up searches feasible. A fading optical source - an afterglow - was detected within a  $\sim 3$  arcminute X-ray error region 21 hours post-burst (van Paradijs et al., 1997). The source was coincident with a galaxy, presumed to be the host. Spectra of the candidate host galaxy suggested a redshift for the first time ( $z = 0.695$ ), and the multi-wavelength data made it possible to estimate an isotropic-equivalent energy,  $E_{\text{iso}}$ , of around  $10^{52}$  erg (Waxman, 1997a). This was an extremely high value, comparable to the total output of supernovae, although in supernovae the majority of the energy released is in the form of neutrinos (Hartmann, 1999). This implied that some degree of outflow beaming was required in GRBs.

The second burst to have a afterglow detection was GRB 970508. Also caught by BeppoSAX, and followed up in the optical, GRB 970508 was the first GRB to have an afterglow detection in the radio (Frail et al., 1997). This added even more

weight to the synchrotron afterglow theory. Significantly, absorption lines were detected in the optical afterglow spectrum, making this burst the first to have a secure redshift estimate (Metzger et al., 1997). At  $z \sim 1$ , their cosmological origin was now confirmed beyond doubt.

The consequence of these afterglow detections was two fold: first, host and afterglow spectra led to a definitive extragalactic identification for GRBs, thus making them intrinsically extremely luminous if the emission was assumed to be isotropic. Second, they provided a wealth of temporal and spectral data, providing insights into the emission mechanisms and geometry. The nature of the post-burst emission, fading and becoming spectrally softer with time (typically optical afterglows are visible for days to months, and months to years in the radio, e.g. Fruchter et al., 1999b; Lyman et al., 2016), narrowed down the list of plausible theories substantially. The ‘fireball’ model emerged as the favoured hypothesis (Meszaros and Rees, 1992; Rees and Meszaros, 1994; Wijers et al., 1997; Waxman, 1997b; Tavani, 1997), in which a relativistic outflow interacts with the circumburst medium, forming shock fronts, and producing synchrotron emission (Paczynski and Rhoads, 1993; Band et al., 1993; Meszaros et al., 1994; Sari et al., 1998; Piran, 2005). An illustration of the fireball model is shown in Figure 1.3. Although the event or central engine driving the outflow was still unknown, the resultant fireball would not necessarily be dependent on the details of its progenitor. In this model, afterglow light curve variety and variability arises primarily from differences in the circumburst medium density profiles (e.g. Gompertz et al., 2018).

Sari et al. (1998) provide prescriptions for the light curves and spectra expected from synchrotron-emitting, expanding relativistic shells. Synchrotron radiation arises because electric charges (e.g. electrons), travelling relativistically through a magnetic field, will gyrate around the field lines, and accelerating charges emit electromagnetic radiation. Electrons dominate this process in plasmas because the emission depends solely on the acceleration of charge, and given their lower mass, electrons undergo far more acceleration than baryons with the same magnitude charge (i.e. protons). The spectrum from a single electron is a curve, but given a distribution of Lorentz factors  $\gamma$  and pitch angles, the emission from all electrons sums to produce a power law (Duric, 2004). The  $N(E)$  distribution assumed for the electrons (which depends on the number of electrons being injected versus removed per unit time at each energy) determines the index of this power law, where electrons have energy  $E = \gamma m_e c^2$ . Sari et al. (1998) improve on this model by describing two regimes - ‘fast cooling’ and ‘slow cooling’. In each case there are three break frequencies in the synchrotron spectrum, and their positions relative to each other

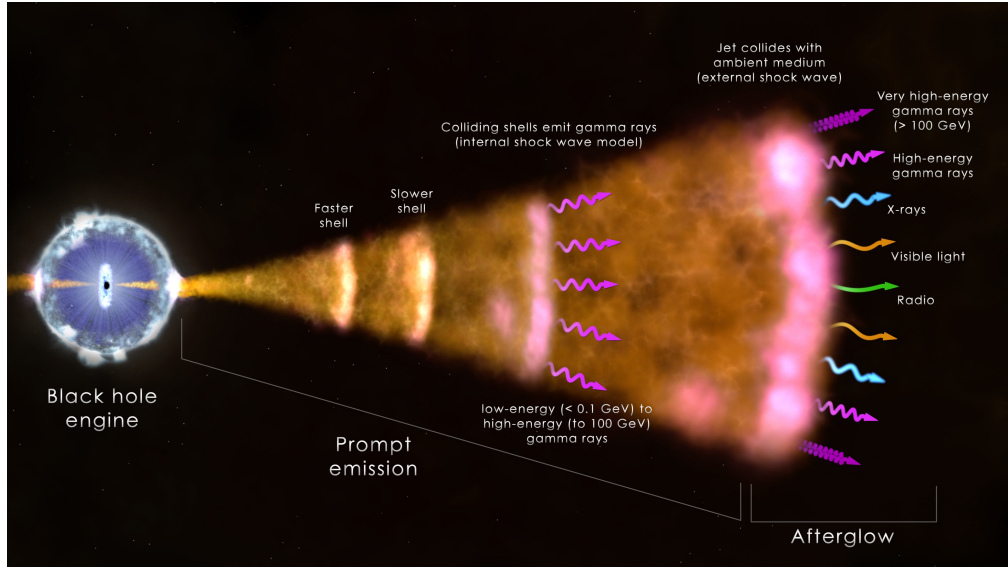


Figure 1.3: An illustration of GRB emission mechanisms in the fireball model. The prompt emission (gamma-rays) originates from internal shocks in the jet immediately after launch, and the afterglow arises from external shocks in the circumburst medium. *Figure credit: NASA/Goddard Space Flight Center/ICRAR.*

define the cooling regime. The break frequencies are as follows,

- $\nu_m$  - the frequency of peak emission from electrons which have the lowest Lorentz factor in the distribution,
- $\nu_c$  - the cooling break (critical) frequency, below which electrons have not yet had time to radiate most of their energy. Above the cooling break, the electron population is rapidly cooling, because they are radiating their energy faster than new electrons at these energies can be produced in the shocks,
- $\nu_a$  - the self-absorption frequency, below which photons are re-absorbed by electrons.

If  $\nu_m > \nu_c$ , then *all* electrons in the distribution will be gyrating above the critical frequency and will therefore be cooling rapidly - this is defined as ‘fast-cooling’. If  $\nu_m < \nu_c$ , then only those electrons above  $\nu_c$  will cool rapidly - hence the term ‘slow-cooling’. The positions of these breaks move towards lower frequencies with time, but  $\nu_m$  falls faster than  $\nu_c$ , leading to a transition from fast to slow cooling.

Although the synchrotron fireball model for afterglows is now well established, if data is limited or over a restricted wavelength range, a good approximation is to use a simple broken power law in frequency (and power law in time for the

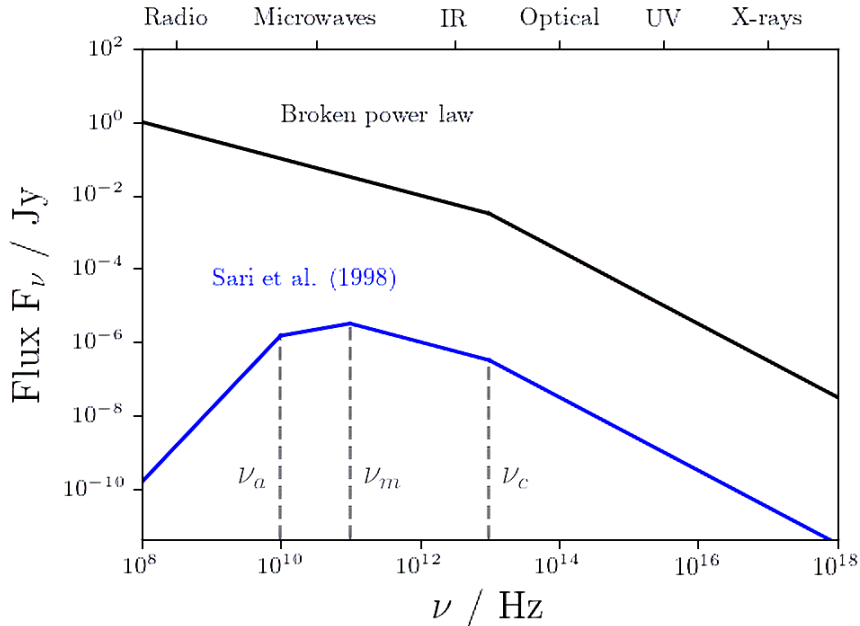


Figure 1.4: Two example model spectra for the afterglows of GRBs. The  $y$ -axis flux scaling is arbitrary. The single break in the simplified model is aligned here with the cooling break from the Sari et al. (1998) slow-cooling model. The frequencies are in the burst-frame (i.e. neglecting redshift) but are purely representative, and the break frequencies can lie over a wide range. For example, the cooling break  $\nu_c$  typically occurs between the optical and X-rays (Greiner et al., 2011). The spectrum will move down and to the left with time, as the afterglow fades and the peak emission moves towards lower photon energies. This figure is based on plots presented in Sari et al. (1998).

temporal decay). This is often expressed in terms of the photon index  $\Gamma$ , equal to  $\beta + 1$ , where  $\beta$  is the spectral index. The difference between  $\Gamma$  and  $\beta$  arises from the conversion of  $N(E)$  to flux density,  $F_\nu$ . A broken power law afterglow spectrum can therefore be modelled as,

$$\begin{aligned}
 F_\nu(t) &\propto t^\alpha \nu^{-\Gamma+1}, \nu > \nu_c \\
 F_\nu(t) &\propto t^\alpha \nu^{-\Gamma+1+\Delta\beta}, \nu < \nu_c
 \end{aligned}
 \tag{1.2}$$

where  $\Delta\beta$  accounts for the shallowing gradient of the spectrum below the cooling break. Typical values for  $\Gamma$  are around  $\sim 2$  (Evans et al., 2009), and  $\Delta\beta \sim 0.5$  (Greiner et al., 2011). The form of this function, along with the slow-cooling model of Sari et al. (1998), is shown in Figure 1.4. I use the Band function and broken power law approximations to model prompt emission and afterglows later in this thesis.

The light curves of GRB afterglows also provide insights into the burst mechanisms. Aside from energetics arguments, strong evidence that GRBs are highly beamed events with collimated outflows comes from ‘jet breaks’ observed in their light curves (Rhoads, 1999). Initially, when the bulk Lorentz factor  $\gamma_{\text{bulk}}$  of the outflow is very large, emission is relativistically beamed along the direction of travel. This is a special relativistic effect whereby radiation is emitted preferentially in the direction of travel, for velocities approaching the speed of light. Initially isotropic emission is beamed into an angle  $\phi \sim \gamma^{-1}$ . The observer therefore only sees a small portion of the entire emitting region. When the collimated outflow interacts with the circumburst medium, it sweeps up mass and begins to slow. As  $\gamma_{\text{bulk}}$  drops, the effects of relativistic beaming reduce, and so the flux received from any individual part of the outflow reduces. The outflow itself begins to widen after light has had time to travel from the jet edge to the centre, so that we see emission from a larger area of the outflow, and the two effects initially counteract. A stage is reached when further spreading can no longer compensate for the decreasing  $\gamma_{\text{bulk}}$ , and the observed flux begins to rapidly decrease. This transition manifests in afterglow light curves as a jet break, and occurs when  $\gamma_{\text{bulk}} < \theta_j^{-1}$ , where  $\theta_j$  is the jet opening angle. Given some assumptions about the expansion and deceleration of the blast wave, it is therefore possible to infer the jet opening angle from the timing of the jet break (Sari et al., 1999; Frail et al., 2001; Ghirlanda et al., 2004), which can occur as long as months post-burst. Because the afterglow fades with time, a jet break is not observable in every GRB.

### 1.2.3 The Neil Gehrels Swift Observatory

The panchromatic nature of GRB afterglows prompted the development of observatories with multi-wavelength capabilities such as the High Energy Transient Explorers (HETE 1 and 2, Lamb et al., 2004), and notably, the *Neil Gehrels Swift Observatory* (Gehrels et al., 2004). *Swift* has been instrumental in GRB science since its launch in 2004, having detected  $\sim 1300$  bursts at the time of the writing<sup>1</sup>. As the name suggests, *Swift* is capable of rapidly slewing to point at a burst. The initial detections are made with the wide-field ( $\sim 10$  per cent of the sky) Burst Alert Telescope (BAT), which is sensitive to X-ray/gamma-ray photons in the range 15-150 keV (Barthelmy et al., 2005). A  $T_{90}$  - spectral hardness plot from the third *Swift* BAT GRB catalogue is shown in Figure 1.5 (Lien et al., 2016). Once a burst is detected by BAT, the telescope slews within seconds to observe with its X-ray telescope (XRT), which has a 0.2-10 keV energy range. Thanks to a grazing incidence

<sup>1</sup>[https://www.swift.ac.uk/xrt\\_products/index.php](https://www.swift.ac.uk/xrt_products/index.php)

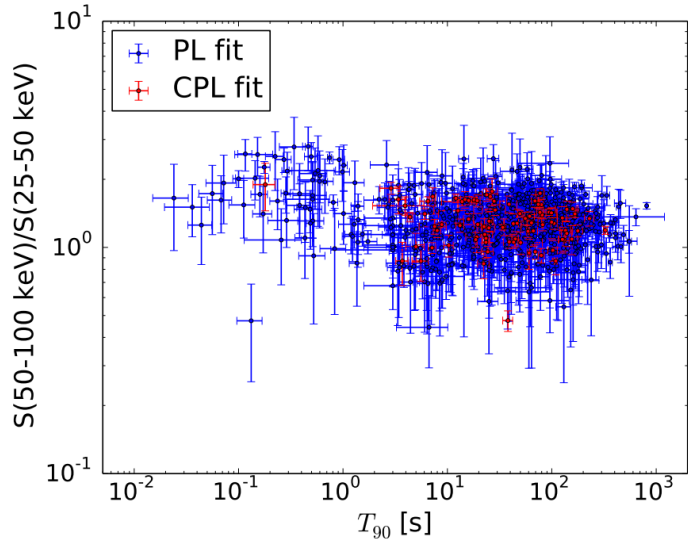


Figure 1.5: The  $T_{90}$  duration versus spectral hardness (ratio of the fluence in 50-100 keV and 25-50 keV energy ranges) for all *Swift* GRBs up to 2016 (figure reproduced from Lien et al., 2016). Bimodality is seen in both duration and spectral hardness. The blue data are best fit by a power-law to their prompt spectra, the red are best fit by a broken (cut-off) power law.

mirror design, XRT can localise X-ray emission to within a few arc seconds (Burrows et al., 2004). The on-board UV-optical telescope (UVOT) can simultaneously observe, performing photometry and spectroscopy over the 1600-8000 Å wavelength range and providing sub-arcsecond spatial resolution (Roming et al., 2005). *Swift* has discovered the majority of GRBs since 2004, measuring their gamma-ray/X-ray/UV/optical light curves and spectra, but also leading to the identification of hundreds of candidate host galaxies and several extremely distant events (discussed later in the introduction, and throughout this thesis).

#### 1.2.4 Non-Standard Phenomena

The description of GRB light curves and spectra so far is complicated by the presence of other sources of emission, in addition to the outwards moving synchrotron-emitting blast wave. For example, when the Compton Gamma-ray Observatory detected GRB 990123, rapid follow-up in the optical led to the observation of a prompt optical flash. This was attributed to a reverse shock, where material catches up with the external shock and bounces back into the ejecta (Sari and Piran, 1999). Subsequently, other prompt optical flashes have been observed, including in the ‘naked eye’ GRB 080319B (Bloom et al., 2008; Racusin et al., 2008; Woźniak et al.,

2009). In many cases, non-synchrotron emission cannot be ruled out (e.g. Starling et al., 2012; Nappo et al., 2017), and X-ray flares are common in both prompt and afterglow light curves, as are plateaus and bursts with extended X-ray emission (sometimes giving rise to anomalously steep or shallow decay rates, Nousek et al., 2006; Norris and Bonnell, 2006; Zhang et al., 2006; Chincarini et al., 2007; Yu et al., 2015). A class of burst was identified almost as soon afterglows were discovered, in which the optical emission is significantly below that expected from synchrotron afterglow theory, given a measured X-ray flux (Groot et al., 1998a; Jakobsson et al., 2004). We will return to these ‘dark GRBs’ later in the introduction, and in detail in Chapters 3 and 4, suffice to say their existence has implications for the environments capable of producing GRB progenitors, and therefore the nature of the progenitors themselves.

In addition to afterglow-focused missions like HETE and *Swift*, further satellites capable of studying the high energy prompt radiation were launched (e.g. INTEGRAL and *Fermi*, Winkler et al., 2003; Atwood et al., 2009). Over a decade of observations with these facilities has produced a wide variety of burst light curves and spectra. This includes low-luminosity GRBs, events seen at low redshift with an inferred  $E_{\text{iso}}$  one or two orders of magnitude less than the bulk of the population (Galama et al., 1998; Stanway et al., 2015a; Schady, 2017). It is unclear whether they are intrinsically fainter, or if we are seeing them off-axis (Dereli et al., 2017; Zhang et al., 2018; Anchordoqui et al., 2019). A population of intermediate duration GRBs was claimed (de Ugarte Postigo et al., 2010), although subsequent studies have suggested that the distribution is only bimodal (Tunnicliffe and Levan, 2012; Narayana Bhat et al., 2016). It should be noted that the bimodality initially seen by Compton/BATSE is less clear in subsequent data sets, and that the strength of this effect depends on the energy range of the gamma-ray detector used (see for example the difference between *Swift* and *Fermi*, Zhang and Choi, 2008; Tarnopolski, 2015).

A better established class are the ultra-long duration events ( $t \gtrsim 1000\text{s}$ , Gendre et al., 2013; Levan et al., 2014), and their origin remains unclear. Finally, some bursts have been observed to have a much lower gamma-ray flux, whilst still showing X-rays and the accompanying afterglow. These are known as X-ray flashes (XRFs) and are thought either to be GRBs in which the relativistic outflow is baryon-heavy, and therefore less accelerated, or GRBs seen slightly off-axis (Rhoads, 1997; Dermer et al., 1999; Rhoads, 2003).



### 1.2.5 GRB-Supernovae

Perhaps the most significant observable property of long GRBs is their frequent association with supernovae (SNe). In 1998, BeppoSAX detected the long-duration GRB 980425, and one day later, supernova SN 1998bw was discovered at the same location (SNe tend to rise on a timescale of days and last for weeks to months, Galama et al., 1998; Nakamura et al., 2001; Nomoto et al., 2004b). Subsequent BeppoSAX narrow-field observations detected a new X-ray source, emerging after the afterglow, at a position consistent with the supernova and GRB, implying that the two events were related. This was the first hint that long GRBs can be triggered by core-collapse supernovae (Iwamoto et al., 1998). SN 1998bw was of type Ic, meaning that it showed no hydrogen or helium lines in its spectra (see Section 1.3.4). This suggested that the GRB had a massive, stripped envelope progenitor star. The ‘collapsar’ model subsequently became the favoured mechanism for long-duration bursts (Woosley, 1993).

GRB 980425 did not definitively link long GRBs with SNe due to the lack of a spectral identification, and its unusual nature as a relatively nearby ( $z = 0.0085$ ) and low-luminosity burst (Galama et al., 1998). Five years later, the detection of GRB 030329 and identification of a supernova imprinted on the smooth afterglow spectrum provided solid evidence of the long GRB-SN connection (Hjorth et al., 2003). Since then, the connection has been well established (e.g., Cano et al., 2017, and references therein), confirming that the long-duration bursts arise from the collapse of massive stars as first proposed by Woosley (1993). To understand the conditions leading up to such an event, a discussion of high mass stellar evolution is now needed.

## 1.3 The Evolution of Massive Stars

In this section, I will outline the formation and subsequent evolution of stars, with emphasis on high mass stars (initial mass  $> 8_{\odot}$ ) that will go on to produce either a neutron star or a black hole. The evolution will be followed across the Hertzsprung-Russell (HR) diagram, a representative example of which is given in Figure 1.6. These diagrams plot temperature versus luminosity for stars in a stellar population. Observationally, this is usually in terms of colour and magnitude (Russell, 1914). How stars move across the HR diagram, and the physical processes occurring at each stage, will now be discussed.

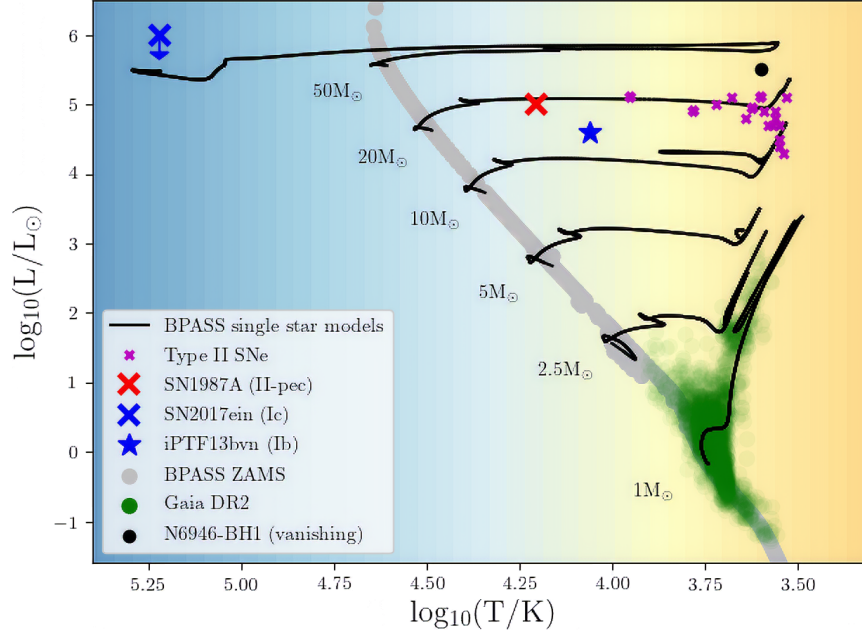


Figure 1.6: A theoretical Hertzsprung-Russell diagram, at Solar metallicity, with observational data overlaid. The grey band extending from hot and bright stars to cool and faint is the main sequence, shown here by plotting the zero-age main sequence (ZAMS) temperature and luminosity of stellar models in the BPASS code (Binary Population and Spectral Synthesis v2.2.1, Eldridge et al., 2017; Stanway and Eldridge, 2018). The evolution of single star models across  $T - L$  parameter space, starting at the indicated ZAMS masses, is shown by black lines. A random sample of  $\sim 2000$  stars which have  $T$  and  $L$  fits, from the second *Gaia* data release (Gaia Collaboration et al., 2018), is shown in green (shading indicates the density of stars in this parameter space). White dwarfs are not shown, but lie blue-wards and faint-wards of the main sequence. The other data show the pre-collapse properties of all candidate core-collapse progenitors observed to date. These are the vanishing star N6946-BH1 (marked by a black circle, Adams et al., 2017), SN 1987A (marked by a red cross, Walborn et al., 1987), several type II SN progenitors from Smartt (2015), Smartt (2015) and Aldering et al. (1994) (all magenta crosses), the progenitor of SNIPTF13bvn (type Ib, Eldridge and Maund, 2016, a blue star) and SN 2017ein (Ic, Van Dyk et al., 2018, a blue cross). The latter luminosity is an upper limit, assuming a single star progenitor (Kilpatrick et al., 2018). Single star evolution at Solar metallicity cannot explain the position of many of these progenitors on the HR diagram. This is just one aspect of the justification for modelling binary stellar evolution across a range of metallicities.

### 1.3.1 Star Formation

Stars are born from the collapse of clouds of gas and dust under gravity. In-falling gas, predominantly hydrogen ( $\sim 75$  per cent) and helium ( $\sim 25$  per cent), heats up as gravitational potential energy is converted into kinetic energy and atomic collisions increase. The temperature, pressure and density at the centre of the gas cloud increases. To undergo further collapse, efficient cooling processes are needed. At local Universe metal abundances, atomic transitions in metals (elements heavier than hydrogen or helium) and molecules provide a way for thermal energy to be radiated and the gas to cool. At very low metallicity (the fraction of mass that is composed of elements heavier than hydrogen or helium), cooling through these means is less efficient, meaning that greater masses are required before gravity can overcome the gas pressure (at the Jeans mass, Schaerer, 2002). This results in higher mass stars at lower metallicity.

Eventually, the gas temperature and density in the plasma becomes such that hydrogen nuclei are separated by a characteristic length scale across which quantum tunnelling can readily take place. At this point, protons can overcome the Coulomb barrier, and the (attractive) strong nuclear force dominates instead. Nuclear fusion reactions therefore begin, releasing energy in the form of gamma-ray photons, neutrinos, energetic positrons and heavier particles, depending on the reaction chain (Hoyle, 1946). The dense environment means that these photons have a high interaction probability, and much of the energy of the outwards photon flux is transferred into thermal energy, supporting the star against further collapse. The new star stabilises once an equilibrium has been reached between radiation pressure and gravity.

Observationally, stars form with a range of masses according to a distribution that can be described by an initial mass function (IMF), where high mass stars are rarer than low mass. Although no single IMF appears to be Universally applicable (e.g., Salpeter, 1955; Kroupa, 2001; Chabrier, 2003), they are typically of the form,

$$N(M < M_{\max}) \propto \int_{M_{\min}}^{M_{\text{break}}} \left(\frac{M}{M_{\odot}}\right)^{-a} dM + \int_{M_{\text{break}}}^{M_{\max}} \left(\frac{M}{M_{\odot}}\right)^{-b} dM \quad (1.3)$$

where  $M_{\min}$  is the lowest mass considered,  $M_{\text{break}}$  is the position of a break in the IMF (between  $0.5$ - $1M_{\odot}$ ), and  $M_{\max}$  is the maximum mass considered. The indices  $a$  and  $b$  typically take values of  $\sim 1$  and  $\sim 2 - 3$  respectively (Stanway and Eldridge, 2018). The first attempt to quantify an IMF that included stars more massive than the Sun was performed by Salpeter (1955), with a slope  $\alpha = 2.35$  (across all masses). The maximum initial mass a star can have,  $M_{\max}$ , is uncertain. Theoretically, a

maximum should exist (and be metallicity dependent), as the stellar luminosity scales faster with mass than the surface gravity: at some point, the Eddington luminosity is exceeded and the outer layers are ejected, producing a cap on the zero-age main sequence mass. There is observational evidence for stars  $\gtrsim 200 M_{\odot}$  in the  $\sim 0.5 Z_{\odot}$  Large Magellenic Cloud (Hainich et al., 2014; Ramírez-Agudelo et al., 2017); the current record-holder has an estimated mass of  $315 M_{\odot}$  (Crowther et al., 2016).

Aside from mass, other variation in initial conditions comes from the metallicity and the initial stellar rotation. Metallicity is determined by the previous chemical enrichment of the gas cloud producing new stars, this will be discussed further in Section 1.4. Initial rotation velocities depend on the efficiency of angular momentum transfer between the protostar and its progenitor cloud. A final and crucial aspect to consider is multiplicity. Whether or not a star is born isolated or as part of binary system (or indeed as one of  $> 2$  stars) can greatly affect the subsequent stellar evolution. Observations of stars in the Local Group indicate that binaries are common, particularly in high-mass systems where the majority of stars are in binaries (Sana et al., 2012). Low mass ratios (large differences in mass) are rare, whereas twin-systems are relatively more common (Moe and Di Stefano, 2017).

### 1.3.2 The Main Sequence

Once stars have formed and are burning hydrogen to helium in their core, they settle into a band on the HR diagram called the ‘main sequence’. The initial masses of stars are referred to as ZAMS masses (Zero Age Main Sequence). This main sequence runs from the cool and faint bottom right to the hot and bright top left. Stars spend the majority of their lives here, because (i) hydrogen dominates their composition and (ii) hydrogen fusion is relatively slow. It is slow because hydrogen fusion reactions release a relatively large amount of energy per nucleon, meaning that relatively few are required per unit time to provide the required radiation pressure to balance gravity. The hydrogen fusion processes are the proton-proton chain (primarily two protons into deuterium, then deuterium plus hydrogen into helium) and the CNO cycle in higher mass, hotter stars (various reactions in which carbon, oxygen and nitrogen act as catalysts for hydrogen to helium fusion, Eggleton, 2006).

On the main sequence, stellar luminosity  $L$  is proportional to  $M^n$  (Kuiper, 1938), where  $n \sim 3.5$ . The value of  $n$  varies by a factor of a few across the range of stellar masses (Duric, 2004), but 3.5 is a typical and widely adopted value. The dependence arises because more massive stars must burn their fuel faster to produce the necessary outwards radiation pressure to balance gravity. Massive stars are



therefore hotter, appearing blue in colour, and exhibit emission lines in their spectra. The time on the main sequence  $\tau_{\text{ms}}$  is proportional to the fuel supply available, divided by the rate it is used, so that  $\tau_{\text{ms}} \propto M/L \propto M^{-2.5}$ . Hence, high mass stars live shorter lives (however, this dependence plateaus for very high mass stars and the stellar lifetime does not get shorter than 1-2 Myr, independent of mass). If the fusion reaction rate were to drop, the star would contract, heating up and increasing the burning rate. Main sequence stars are therefore in hydrostatic equilibrium (Eddington, 1916), with an approximately constant radius (barring mass loss and chemical enrichment effects). Assuming hydrostatic equilibrium, the structure of stars on the main sequence can be described by the following set of equations,

$$\frac{dP}{dr} = \frac{-GM\rho}{r^2} \quad (1.4)$$

$$\frac{dm}{dr} = 4\pi r^2 \rho \quad (1.5)$$

$$\frac{dL}{dr} = 4\pi r^2 \rho (\epsilon - \epsilon_\nu) \quad (1.6)$$

where  $P$  is the pressure,  $r$  is the radius,  $M(r)$  is the mass enclosed within radius  $r$ ,  $\rho(r)$  is the local density,  $L$  is the luminosity,  $\epsilon$  is the total energy released per unit time per unit mass, and  $\epsilon_\nu$  is the luminosity per unit mass radiated away in the form of (essentially non-interacting) neutrinos. We then have two different equations for the temperature profile, depending on whether energy transport is primarily radiative or convective. Low mass stars  $< 2M_\odot$  have convective cores and radiative envelopes, and vice versa for high mass stars. This behaviour arises because convection occurs where temperature gradients and opacities are high. In the most massive stars, the entire bulk can be convective. Temperature profiles in each regime are given by:

$$\left(\frac{dT}{dr}\right)_{\text{radiative}} = \frac{-3\kappa\rho(r)L}{64\pi r^2\sigma T^3} \quad (1.7)$$

$$\left(\frac{dT}{dr}\right)_{\text{convective}} = \left(1 - \frac{1}{\gamma}\right) \frac{T}{P} \frac{dP}{dr} \quad (1.8)$$

where  $\kappa$  is the opacity (from atomic electron transitions, ionisation, free-free scattering),  $\sigma$  is the Stefan-Boltzmann constant, and  $\gamma$  is the adiabatic index. Given a set of boundary conditions, the equations above can be solved as a set of coupled differential equations, typically numerically (Eggleton, 2006).

Stars on the main sequence lose mass through winds. This process is metallicity dependent as metals, predominantly iron, have many more possible electron

energy level transitions than simpler atoms and are therefore more likely to interact with photons. Therefore, the higher the metal content in a stellar atmosphere, the higher the opacity and the more effective the radiation flux is at driving atoms from the surface of the star (Vink et al., 2001, 2011b). An important result of this mass and angular momentum loss is that stars, in the absence of other factors such as binary interactions, spin down over their lifetimes. Stellar rotation is discussed further, including the effects of tidal interactions and radial structure, in Chapter 5.

### 1.3.3 Post-Main Sequence Evolution

Once hydrogen runs out in the core, the star moves off the main sequence. In high mass stars, because the core is convective, fuel is well mixed. When it runs out, it runs out rapidly across a wide area. The sudden reduction in radiation pressure allows the core to collapse under gravity. In doing so, it heats up, heating the hydrogen envelope and triggering hydrogen burning in this layer. This causes the star to expand, and cool, but hydrogen burning continues at the base of the envelope. The star is now a red supergiant - cool but extremely luminous, with a radius  $\sim 100 - 1000$  times greater than on the main sequence. The transition from main sequence to red giant is an extremely rapid process, with the region in-between on the HR diagram called the ‘Hertzsprung Gap’ (stars are rarely seen here). The outer layers of the star are now cooler, with a greater opacity, so the envelope becomes convective. Helium ash falls down and adds mass to the already contracting core. Envelope convection can penetrate into the core in a first ‘dredge up’ phase.

Eventually, the increasing temperature and pressure in the contracting core is sufficient to trigger helium fusion to carbon and oxygen. Ignition is gentle for massive stars, but occurs as a ‘helium flash’ for low mass stars. Further core collapse is halted by the core helium burning, while shell hydrogen burning continues. The star moves back towards the main sequence on the HR diagram along a ‘blue loop’. The first part of this loop, where the luminosity is approximately constant but the star heats up, produces the horizontal branch. This is most prominent in the  $10M_{\odot}$  model marked on Figure 1.6.

When core helium runs out, the core again contracts, heating the envelope, it again expands and cools, and the star turns redder once more. This is the return part of the first blue loop. Higher temperatures are required to start carbon-oxygen fusion (the Coloumbic repulsion between nuclei is stronger, and because they are larger, they must get closer before the strong force can dominate). The star now has three layers of burning - core carbon-oxygen, shell helium and shell hydrogen.



The star moves up the asymptotic giant branch (AGB), which is visible as a branch off the main sequence in the *Gaia* data plotted on Figure 1.6. Multiple layers of shell burning causes instabilities in which the star contracts and expands repeatedly (thermal pulsing), ejecting mass in the process. These pulses can cause further dredge-up stages. In low mass stars, this instability fully ejects the envelope as a planetary nebula, leaving behind an inert carbon-oxygen core held up by electron degeneracy pressure - a white dwarf (Hurley et al., 2000; Eggleton, 2006). These occupy the lower left of the HR diagram. The maximum mass of a white dwarf is determined by the maximum degeneracy pressure that relativistic electrons can exert, and is around  $1.4M_{\odot}$  (Chandrasekhar, 1931; Duric, 2004).

The evolution of stars in the latter part of their life depends on their metallicity (initial metal content, and metal content in the envelope), and binary effects. High mass stars can lose their outer envelopes entirely, leaving behind a predominantly helium - oxygen - carbon star. These ‘Wolf-Rayet’ stars are extremely hot; observationally they are characterised by Doppler-broadened emission lines from ionised helium, carbon and oxygen (Crowther, 2007). These stars have metallicity sensitive mass loss rates, with  $\dot{M} \propto Z$  (Vink and de Koter, 2005; Hainich et al., 2015). Wolf-Rayet-like stars, if spinning fast, may be candidates for core-collapse gamma-ray bursts progenitors, as will be discussed in Section 1.6 and Chapter 5.

Binary evolution processes can also strip a star of its outer envelope, producing a helium star even when wind-driven mass loss rates are low. When a star expands post main sequence, it can fill its Roche lobe. Tracing the equipotential surface around each star inside which material is gravitationally bound, taking into consideration centrifugal forces, defines the Roche lobe. Where the two Roche lobes meet, the acceleration towards each star is equal. This is called the L1 Lagrange point. Once a Roche lobe is filled, mass transfer can take place through this Lagrange point. This process also transfers angular momentum to the secondary star, spinning it up (Eggleton, 2006; Eldridge and Tout, 2019).

Stars that are spun up enough (or are born spinning rapidly enough) can become rotationally mixed, so that envelope hydrogen, helium, and later metals, are mixed into the hot core and more efficiently burned. This process is called chemically homogeneous evolution (Maeder, 1987), and also might be relevant for GRB progenitors (refer to Section 1.6 and Chapter 5). Fully chemically homogeneous stars do not have a stratified structure, and move blue-wards off the main sequence as they advance through the stages of nuclear burning. A more realistic scenario is quasi-homogeneous evolution (QHE), where mixing occurs, but to a lesser extent. These stars, once formed, are expected to spin down rapidly at higher metallicities,

halting QHE. They should therefore be rare in the local Universe. A small number of candidates have been proposed in the literature using two methods (Mokiem et al., 2006; Bestenlehner et al., 2011; Martins et al., 2013; Almeida et al., 2015). First, QHE can be inferred from temperatures that are higher than predicted for the dynamically calculated masses in a binary. Alternatively, their existence can be deduced from a class of stars that lie blue-wards of the main sequence on the Hertzsprung-Russel diagram, but which are still rich in hydrogen. Furthermore, their existence may be required to explain the UV output from stellar populations (Eldridge and Stanway, 2012; Szécsi et al., 2015; Stanway et al., 2016), and they are also invoked to explain the observed black hole mass distribution (Mandel and de Mink, 2016; de Mink and Mandel, 2016).

Alternatively, if the binary is sufficiently tight and/or the primary expansion sufficiently large, a common envelope phase can occur. In this case, the secondary star is fully engulfed by the diffuse atmosphere of the primary. How common envelope evolution proceeds is still uncertain, but the process is important as it influences the final stellar separations and the degree of mass loss from the system. Some fraction of the orbital energy is transferred to the envelope, ejecting it, typically parameterised as  $\alpha_{\text{CE}}$  (Izzard et al., 2012; Eldridge et al., 2017). It should also be noted that tidal interactions, being strongly radius dependent, get stronger in post-main sequence evolution, but I leave a discussion of this to Chapter 5.

If the core is massive enough, it can reach temperatures sufficient to ignite carbon and oxygen burning. Once this burning stage is complete, the core contracts again, reaching temperatures high enough to ignite neon. Fusion processes continue with heavier nuclei at each stage (Hoyle, 1954), all the way to iron. Fusion proceeds via the alpha and triple-alpha processes. Slow neutron capture reactions (s-process, where  $\beta$  decay occurs faster than neutrons are captured) also occur (Burbidge et al., 1957). The rapid capture r-process, where nuclei capture neutrons faster than they decay, is also possible but is only thought to be significant in supernova, kilonovae (from neutron star mergers, Abbott et al., 2017b, see Section 1.7) and collapsar GRBs (Nomoto et al., 2004a; Siegel et al., 2019).

### 1.3.4 Supernovae

At each burning phase in the late life of a massive star, less energy is released per reaction, so more must occur per unit time in order to provide the radiation pressure required to support the core. Furthermore, not all the material from each phase will be converted. The duration of each step is therefore shorter than the last, for example silicon burning may only last for a matter of days, compared to

Myrs for hydrogen (Woosley and Janka, 2005). The process ends with iron fusion, which is an endothermic process. Thermal energy is sapped from the core and it begins to rapidly contract. As it heats up, the photons become so energetic that iron atoms undergo photo disintegration. The density becomes sufficiently high that the available electron quantum states become saturated, and the  $\beta$ -decay back-reaction of  $e^- + p \rightarrow n + \nu_e$  becomes favoured. This removes another source of pressure (electron degeneracy) and so collapse continues. If the core mass at this stage is  $\lesssim 3M_\odot$ , then neutron degeneracy pressure eventually halts the collapse. The in-falling envelope rebounds off the solid core surface, and explodes outwards in a supernova. A neutron star remnant is left behind. If the core mass is instead  $\gtrsim 3M_\odot$ , then no known quantum effects can stop the gravitational collapse. The radius of the star falls below the Schwarzschild radius, and the escape velocity exceeds the speed of light - producing a black hole (Hurley et al., 2000; Eggleton, 2006). At very high masses, gamma-ray photons in the core can undergo pair production, transforming into electron-positron pairs. The reduction in radiation pressure leads to a rapid collapse and runaway fusion rate increase, exploding the star and leaving no remnant - such an event is called a ‘pair instability’ supernova (Heger and Woosley, 2002). These might be hard to distinguish from regular supernovae, but there are a handful of candidates (e.g., Gal-Yam et al., 2009).

It is an open question whether supernovae can occur in black hole forming events. It may be that a short lived neutron star is required to provide a solid surface for the inner envelope layers to rebound off - the neutron star could initially be supported against collapse by rotation (Margalit and Metzger, 2017) or it may collapse after it has gained mass from fallback accretion. The mechanism driving the initial supernova explosion is not fully understood (Janka, 2012), but is likely aided by the core neutrino flux (neutrinos were directly observed in coincidence with SN 1987A, Hirata et al., 1987), and in some cases rotational energy injection (Woosley and Janka, 2005). It is now generally accepted that in some high-mass stars, black hole production prevents any supernova and the star will instead ‘vanish’ (Smartt, 2015; Adams et al., 2017). Determining the pre-collapse stellar properties that lead to this outcome, versus a successful supernova, is an area of active research (Sukhbold et al., 2016; Sukhbold and Adams, 2019; Ertl et al., 2019).

Even without a full theoretical understanding of the initial supernova mechanism, we can still draw some conclusions about supernovae and their progenitors from their observed properties (Filippenko, 1997; Crowther and Smartt, 2007; Smartt, 2009). Once the ejecta has been launched, the longer lived supernova emission (lasting days to weeks) arises from the radioactive decay of heavy elements,

particularly  $^{56}\text{Ni}$  and  $^{56}\text{Co}$ , synthesised in the hot, dense, neutron rich environment of the exploding progenitor (Matz et al., 1988). Variety in supernova light curves and spectra then arises from differences in the initial deposited energy, the ejected masses, the circumstellar medium density profile, and the ejecta composition (Eldridge et al., 2018, 2019b).

Supernovae are classified according to features in their spectra, and the morphology of their light curves (Filippenko, 1997). Type I supernovae show no signatures of hydrogen in their spectra, whereas type II do. I now summarise the observational properties of the main supernova sub-types in turn;

- **Type IIL:** Hydrogen-rich supernova with a rapidly declining light curve post-peak.
- **Type IIP:** Like IIL SNe, but with more hydrogen in the pre-explosion envelope. The hydrogen is ionised by the initial supernova shock, and produces a longer lived plateau phase due to the recombination of the ejecta hydrogen.
- **Type IIIn:** Narrow hydrogen emission lines are present. Their width implies a low velocity, ruling out the ejecta itself as an origin, and suggesting that the ejecta is interacting with a much slower-moving circumstellar medium.
- **Type IIb:** Hydrogen lines are initially visible, but they quickly fade. The progenitors are thought to have a trace amount of hydrogen in their envelopes. As the hydrogen shell expands, heavier elements in the following ejecta shine through and dominate the spectrum.
- **Type Ia:** No hydrogen lines, but prominent silicon lines are present. The rest-frame luminosities at peak show little variation. Type Ia SNe arise from the detonation of a white dwarf, typically by accreting material until it approaches the Chandrasekhar mass. Before it is reached, carbon burning is triggered in the core, causing a runaway deflagration.
- **Type Ib:** A core-collapse event producing no hydrogen lines in the spectrum, but helium is present.
- **Type Ic:** A core-collapse supernova with no hydrogen or helium present in the spectrum.
- **Type Ic-BL:** A type Ic supernova with doppler broadened lines implying relativistic ejecta velocities. These SNe are associated with some long-duration GRBs.



It should be noted that a lack of visible lines in the spectrum of a supernova does not mean that the progenitor was entirely lacking in that element, as it is possible for emission to be absorbed before it can escape the ejecta (if the level of nickel mixing in the ejecta is low, e.g., Fremling et al., 2018).

The progenitors of each supernova type cluster in different areas of the HR diagram as shown in Figure 1.6. For example, massive stars can fully strip their envelopes through winds, resulting in helium stars (or Wolf-Rayets) which produce type I supernovae. Lower mass stars tend to retain proportionally more of their envelope - and explode as a less luminous red supergiant, producing a type II event. Stars can also explode as blue supergiants, as evidenced by the nearest supernova in recent times, SN 1987A (which exploded in the Large Magellanic Cloud, Walborn et al., 1987). This simple picture is complicated by metallicity dependencies of nuclear reaction and mass loss rates, and particularly binary interactions, which can strip stars of their envelopes, or add mass by accretion. Modelling supernovae using initial progenitor systems which span a range of metallicities and binary parameters can produce a plethora of variety (e.g., Ertl et al., 2019; Eldridge et al., 2018, 2019b).

As previously noted, a fraction of long-duration, spectrally soft GRBs are associated with type Ic-BL supernovae (correcting for beaming and selection effects, this fraction is around 10%, Fryer et al., 2007). The presence of a supernova can be disentangled from the GRB afterglow because (i) the radioactive decay of  $^{56}\text{Ni}$  and  $^{56}\text{Co}$  produces a distinct rise and fall light curve that does not match afterglow trends and (ii) elements in the ejecta produce absorption lines in the otherwise smooth afterglow spectrum. However, the supernova must be bright enough, with respect to the afterglow, to be detected. Indeed, at  $z > 1$ , the associated supernovae are too faint and only the afterglows are measurable (Cano et al., 2017). This is despite the fact that GRB-SNe are more energetic than typical supernovae, by up to a few orders of magnitude. These highly energetic supernovae are often dubbed ‘hypernovae’ (Woosley, 1993). They are generally more asymmetric than other supernovae (Wang et al., 2003; Nomoto et al., 2005), but although a link between asymmetry and internal jet production has been suggested, it has not yet been firmly established (Stevance et al., 2017).

In this section, I have summarised the current understanding and open questions surrounding high mass stellar evolution and death. Long-duration GRBs are associated with type Ic supernova, but not all Ic SNe produce GRBs - other criteria must be satisfied in order to produce a collapsar event. What can be inferred from the GRB association with Ic-BL SNe, is that the progenitor stars must be stripped of their envelope prior to core-collapse. This can be achieved either through single-

star mass loss processes, or stripping by a companion. If we are unable to study the pre-GRB progenitors star directly, further insights can be gained from the study of GRB galactic environments. The evolution of galaxies across cosmic history, and the investigation of GRB host galaxies, will therefore be the subject of the next two sections.

## 1.4 $\Lambda$ CDM Cosmology, Reionisation and Galaxy Evolution

Galaxies are collections of stars (typically hundreds to thousands of millions), gas and dust, bound by the gravity of these components and dark matter (Navarro et al., 1997). After the first galaxies formed in the early Universe, they evolved through the ageing of their stellar populations, feedback processes (supernova winds and active galactic nuclei, Heckman et al., 1990; Croton et al., 2006), galaxy and intracluster medium interactions (Baldry et al., 2006; Peng et al., 2010), hierarchical merging (Kauffmann et al., 1993) and new star formation, to produce the variety of galaxies we see both locally and across cosmic history. In this section, I will briefly outline the history of galaxy evolution across cosmic time, and how we can infer the content of galaxies through observations and modelling, with a focus on the details most pertinent to GRB studies.

A key factor in our ability to study galaxies is a determination of their distance. Due to the expansion of the Universe, galaxies further away are receding faster (the Hubble–Lemaître law, Hubble, 1929). Measuring the wavelength  $\lambda$  of atomic transition lines in their spectra, and comparing to laboratory rest-frame values, yields a redshift measurement, defined as  $1 + z = \lambda_{\text{observed}}/\lambda_{\text{emitted}}$ . Up to  $\sim 100$  Mpc, redshift is proportional to distance. Beyond this, the accelerating expansion of the Universe becomes apparent (implying the existence of dark energy, Riess et al., 1998; Perlmutter et al., 1999) - which combined with evidence from the cosmic microwave background (CMB, Peebles, 1968; Planck Collaboration et al., 2018) and galaxy dynamics, informs the currently accepted  $\Lambda$ CDM cosmology (dark energy plus cold dark matter). At the time of writing, there is tension between the constant of proportionality in the Hubble-Lemaître law, the Hubble constant, as determined by ‘standard candle’ type Ia supernova observations, versus the CMB (Riess et al., 2016; Planck Collaboration et al., 2018; Freedman et al., 2019). The cosmological parameters for the contributions of matter ( $\Omega_m$ ) and dark energy ( $\Omega_\Lambda$ ) to the overall energy density of the Universe are therefore uncertain. Throughout this thesis, I use 0.3 and 0.7 as rounded approximations for these values respectively,



and  $H_0 = 70 \text{ kms}^{-1} \text{ Mpc}^{-1}$  for the Hubble constant. The radiation contribution is negligible ( $\Omega_r \sim 0$ ), and the Universe appears to be spatially flat ( $\Omega_k = 0$ , with  $\Omega_k + \Omega_r + \Omega_m + \Omega_\Lambda = 1$ ). Because of the expansion, inferred distances depend on the assumed cosmology. For example, the angular extent of an object on the sky decreases with increasing redshift up to  $z \sim 1.5$ , before increasing again (because the Universe was smaller at the time the light was emitted - this effect dominates over the object being more distant from around  $z \sim 1.5$ ). The angular diameter distance can be defined as,

$$D_A(z) = \frac{c}{(1+z)H_0} \int_0^z \frac{dz'}{\sqrt{\Omega_m(1+z')^3 + \Omega_\Lambda}} \quad (1.9)$$

where  $c$  is the speed of light. If instead we have an observed flux  $F$  and wish to know the luminosity  $L$ , we can use  $F = L/4\pi D_L^2$ , where  $D_L$  is the luminosity distance, defined as,

$$D_L(z) = \frac{c(1+z)}{H_0} \int_0^z \frac{dz'}{\sqrt{\Omega_m(1+z')^3 + \Omega_\Lambda}} \quad (1.10)$$

which is equivalent to  $D_A \times (1+z)^2$ . Finally, it can be useful to work in terms of lookback time, given by,

$$t_{\text{lookback}}(z) = \frac{1}{H_0} \int_0^z \frac{dz'}{(1+z')\sqrt{\Omega_m(1+z')^3 + \Omega_\Lambda}} \quad (1.11)$$

which is the time light has taken to reach us since emission at a given redshift. Another important concept is that of the comoving volume. Because the Universe is expanding, it is naturally less densely packed with galaxies today than in the past. However, if we want to measure for example how the star formation rate density has varied over cosmic time, we need to account for this effect. The proper distance  $d_p(t)$  depends on the scale factor  $a(t)$  (defined as 1 today) and the comoving distance  $r$ , according to  $d_p(t) = a(t) \times r$ . Comoving volumes are therefore corrected for expansion by dividing by the scale factor cubed, and do not change as the Universe evolves (Ryden, 2003).

Once the first stars and galaxies started to form, the next significant phase in the history of the Universe was the epoch of reionisation. Most of the hydrogen gas in the Universe today is ionised. Evidence for the presence of a neutral hydrogen intergalactic medium in the distant Universe (defined throughout this thesis as  $z > 5$ ) comes from redshift dependent breaks and troughs in the spectra of distant galaxies, quasars and GRB afterglows (as well as CMB measurements). The transition from neutral to ionised gas is now believed to have completed around  $z \sim 4 - 8$

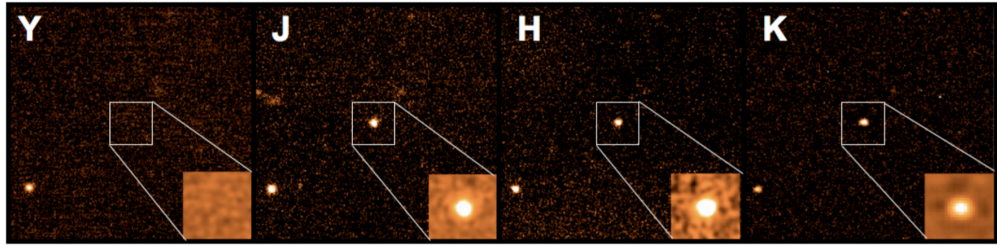


Figure 1.7: The afterglow of GRB 090423 is shown (from Tanvir et al., 2009), with a clear flux deficit in the  $Y$ -band ( $\lambda \sim 1 \mu\text{m}$ ) compared to the longer wavelength  $J$ ,  $H$  and  $K$  bands (Rodrigo et al., 2012, 2013). Accompanying spectroscopy confirmed that this is due to the Lyman break, placing GRB 090423 at  $z = 8.2$ , making it the most distant spectroscopically confirmed GRB and second most distant with a photometric redshift (Cucchiara et al., 2011).

(see Robertson et al., 2010, for a review).

The breaks in the spectra of high-redshift sources are due to the Lyman-break in the rest frame. UV photons with wavelengths less than  $912 \text{ \AA}$  (the Lyman limit) can ionise hydrogen, and are therefore efficiently absorbed by neutral gas. At wavelengths shorter than this break, the observed flux drops abruptly. Photon wavelengths between  $912\text{-}1216 \text{ \AA}$  correspond to Lyman-series electron transitions in hydrogen (transitions from excited states to the  $n = 1$  ground state). Therefore, absorption also occurs in this range, but to a lesser degree. Over the expansion of the Universe, photon wavelengths are stretched by a factor  $(1 + z)$ , so that the position of the Lyman break is *observed* at  $912(1 + z) \text{ \AA}$ . The break can be measured spectroscopically, or inferred with a photometric drop-out method using wide band filters, as shown in Figure 1.7. Because the fraction of flux reaching us at rest-frame wavelengths between  $912\text{-}1216 \text{ \AA}$  decreases rapidly above  $z \sim 5$ , this is evidence for neutral hydrogen fraction increasing at these redshifts and above (Madau, 1995).

A transition line of key importance in the Lyman series is Lyman- $\alpha$  (from the  $n = 2$  to  $n = 1$  energy level), which occurs at  $1216 \text{ \AA}$ . It is important in both emission and absorption. In emission, Lyman- $\alpha$  is produced by recombining hydrogen, and can therefore be seen strongly in galaxies undergoing bursts of star formation. Because it lies at the red end of the Lyman continuum, and is only reddened further by cosmological expansion, it can be seen across the Universe provided it is not absorbed in the vicinity of its emission. Lyman- $\alpha$  emitters are therefore useful windows to the sources producing ionising radiation in the early Universe, but an extrapolation from the observed line flux to the total emitted radiation requires knowledge of the Lyman- $\alpha$  escape fraction: is the gas arranged



in a thin screen, uniformly spread, or is it arranged in dense clumps? Efforts are ongoing to determine the escape fraction, and therefore the contribution of regular, star forming galaxies to reionisation.

GRB afterglows play an important role in these efforts (Tanvir et al., 2019), and more widely in high-redshift astronomy. If localised to high enough precision, they pin-point the position of high-redshift galaxies up to and beyond  $z = 9$  which cannot be identified in any other way (McGuire et al., 2016; Tanvir et al., 2012). Furthermore, the hosts of GRBs at high redshift are low-mass and faint, representing the population which likely dominates reionisation. GRBs also act as cosmic lighthouses, providing a bright background source which allows the imprint of host galaxy ISM absorption lines to be measured. This enables chemical composition measurements of these galaxies, which are otherwise not possible with current facilities (Kawai et al., 2006; Chornock et al., 2014c; Sparre et al., 2014; Hartoog et al., 2015).

Once the UV radiation has escaped, intervening neutral hydrogen clouds resonantly scatter photons at  $1216(1+z)\text{\AA}$  (as observed) out of the line of sight. If the background source is emitting photons below this, and beyond the Lyman limit, then we see a spectrum with absorption features at wavelengths corresponding to the redshifts of the intervening absorbers. For objects in the distant Universe, these absorption features can be numerous, and are referred to as the Lyman- $\alpha$  forest. Around  $z\sim 6$ , they overlap, becoming the Gunn-Petersen trough (Gunn and Peterson, 1965). In the case of GRBs, if the host galaxy itself has a large reservoir of neutral hydrogen and lies at high-redshift, in addition to an absorption feature at  $1216(1+z)\text{\AA}$ , the afterglow emission short-wards of  $912(1+z)\text{\AA}$  (and to a lesser degree in the Lyman-series) will be absorbed before it can escape the host ISM and circumgalactic medium. This produces a spectral break at  $912(1+z)\text{\AA}$  as discussed above and shown in Figure 1.7. At lower redshifts where the IGM is ionised, only the Lyman- $\alpha$  absorption feature (at the host redshift) is prominent. I refer the reader to Selsing et al. (2019b) and Tanvir et al. (2019) for examples of GRB spectra containing these features.

The greater the column density of a gas cloud, whether it be in the GRB host or in an intervening galaxy, the stronger the Lyman- $\alpha$  scattering. If we know the opacity of the cloud (from the fraction of flux missing) and the Lyman- $\alpha$  absorption cross-section, we can infer the column density of neutral hydrogen through the cloud,  $N_{HI}$  (Duric, 2004). If  $N_{HI} > 2 \times 10^{20} \text{ atoms cm}^{-2}$ , the cloud is defined as a damped Lyman- $\alpha$  (DLA) system. If the density is the range  $10^{17} < N_{HI} < 2 \times 10^{20} \text{ atoms cm}^{-2}$ , it is a Lyman limit system. Anything less than this is simply

produces a Lyman- $\alpha$  line (Prochaska, 1999; Péroux et al., 2003). DLAs are physically distinct because they contain predominantly neutral hydrogen - and hence have far greater column densities.

The source of the UV photons required to power reionisation has been the topic of much debate for decades. One idea is that quasars, a particularly luminous form of AGN, were the dominant source (Madau and Haardt, 2015; Adams et al., 2019). Alternatively, stellar populations with many young, massive, population III stars (the first generation to form) might also be able to start reionisation, followed by later generations of stars, with the UV luminosity dominated by low mass galaxies (Bouwens et al., 2012). This is the current theory preferred in the literature. These conclusions are drawn from both local observations of high-redshift galaxy analogues (Greis et al., 2016, 2017) and modelling of young, metal poor stellar populations (Schaerer, 2003). It is thought that the faint-end of the UV galaxy luminosity function is very steep at high redshift (Bouwens et al., 2012) - meaning that low mass galaxies, currently beyond the reach of telescopes - are capable of powering reionisation. Next generation facilities, particularly the *James Webb Space Telescope*, will be able to detect galaxies further down the luminosity function (Vogelsberger et al., 2019), helping to answer these questions.

Post-reionisation, galaxy evolution is characterised by ongoing star formation, population ageing, feedback, galaxy interactions and mergers. Early galaxies at high-redshift were low-mass and irregular in structure; through IGM hydrogen accretion and mergers, the build up of mass proceeded to produce more massive, star-forming galaxies. The cosmic star formation rate density (CSFRD) reached a peak at  $z \sim 2-3$  ('cosmic noon', Madau and Dickinson, 2014; Taylor and Kobayashi, 2015). Over this period, we observe a change from mostly young, blue, star forming galaxies which are irregular or spiral in structure, to a mixed population which includes red, quiescent elliptical galaxies. These are typically more massive than spiral galaxies and are found preferentially in dense environments, such as the cores of galaxy clusters (Dressler, 1980; Kennicutt, 1998) - these are the result of galaxy mergers. Mergers, which occur more often in dense environments, perform three tasks: (i) they disrupt spiral structure, causing the change to elliptical morphologies, (ii) they result in higher mass galaxies, and (iii) they induce bursts of star formation and trigger AGN activity, using up galactic reserves of hydrogen gas and resulting in supernova and AGN winds which clear the remaining gas away, quenching star formation (Heckman et al., 1990). Tidal interactions between galaxies can have similar effects. Galaxies can also become quiescent simply by exhausting their reserves of hydrogen gas, after which no more stars can form. This can occur in



under-dense or hot cluster environments where there is a limited supply of cool gas from the intergalactic medium (Fraser-McKelvie et al., 2016).

The supermassive black holes powering AGN also play a key role. These black holes have masses proportional to their host galaxy mass (Ferrarese and Merritt, 2000), and so at around  $z \sim 1 - 2$  their influence peaked, due to the balanced effects of increasing galaxy masses and black hole growth, versus the AGN-powered clearing of gas in these systems. The CSFRD began to decline, with the remaining star formation occurring in lower mass galaxies (a trend referred to as cosmic downsizing). The relative impact of internal versus external effects (nature versus nurture) is debated (Sobral et al., 2016), but the overall result of this complexity is a characteristic shape in the CSFRD as a function of redshift (see Figure 1.8). This evolutionary history leads to the observed trend in long GRB host galaxy masses over cosmic time, shown later in Figure 1.11. Long GRBs trace low-mass hosts at  $z > 5$  (which are low-metallicity and comprise the bulk of star formation), higher mass galaxies at intermediate redshifts (where the peak of star formation has moved to), and lower mass galaxies again in the local Universe (these are the only strongly star-forming and low- $Z$  sites remaining).

The CSFRD can be measured in various ways. Because massive stars have short lives of order Myrs, they are only seen in currently star forming galaxies. They are bright, and blue, with significant output at UV wavelengths. Therefore, the UV luminosity of a galaxy can be calibrated as a proxy for the star formation rate. Measuring the rest-frame UV luminosity of galaxies, and their number density, as a function of redshift, yields an estimate for the CSFRD. However, UV light is particularly susceptible to absorption and scattering by dust, and therefore pure UV indicators underestimate the true rate. These indicators are also typically corrected for an inferred dust extinction, introducing uncertainty. An alternative method is to measure far-IR emission. This is the region of the spectrum in which dust, warmed by the absorption of UV light from young stellar populations, emits. Therefore, a joint approach using UV and far-IR light provides the best estimate. Madau and Dickinson (2014) used these methods to produce the cosmic star formation rate history (CSFRH) shown in Figure 1.8, which is now widely used in the literature.

Another significant change since reionisation is the chemical enrichment of galaxies. The early Universe was comprised nearly entirely of hydrogen (75%) and helium (25%) (with trace amounts of other elements, Peebles, 1966). Successive generations of stars, which burn hydrogen and helium in their cores as described in Section 1.3, ejected these products into the interstellar medium. Supernovae were particularly important in this process, spreading their ejecta further, and contribut-

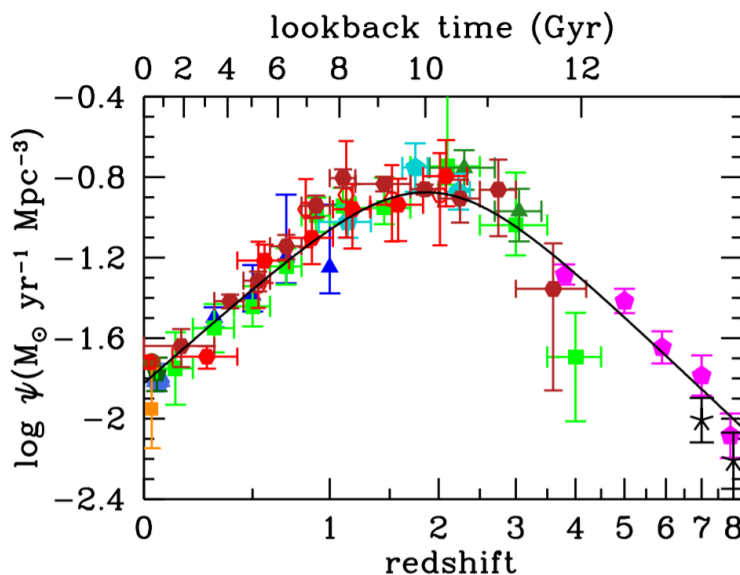
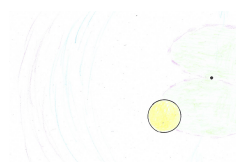


Figure 1.8: The current best estimate for the star formation rate density (SFRD,  $\psi$ ) history of the Universe (figure reproduced from Madau and Dickinson, 2014). The blue, green and magenta measurements are based on (rest-frame) UV data, whereas the red data points are calibrated from far-IR emission.

ing heavier elements. The products were then mixed into the ISM and incorporated in subsequent generations of star formation (e.g. Songaila, 2001). The result is that galaxies, on average, have become increasing metal-rich over cosmic time. Metal signatures are visible via absorption lines in stellar and galaxy spectra, and from IGM absorption in galaxies. Older galaxies that have previously experienced star formation episodes tend to have higher metallicities ( $Z$ ). Metallicity also correlates with mass (Tremonti et al., 2004). This is partly due to the star formation history of massive galaxies, but also due to their greater potential wells, which stops metal-rich supernova outflows from escaping. A consequence of increasing galactic metallicities is greater dust production. Astrophysical dust is comprised of predominantly of carbon and silicate grains, which can be produced either by mass loss from the cool envelopes of evolved stars (e.g. AGB stars), or in supernovae (Morgan and Edmunds, 2003; Dunne et al., 2003; Ferrarotti and Gail, 2006). Metallicity also influences the evolution of stellar systems, affecting mass loss rates, the size of stellar envelopes and the rate of stellar evolution. These factors all contribute to the observed spectral energy distribution (SED) of galaxies.

Given observations of the integrated, unresolved light from a galaxy, either spectroscopic or photometric, we would often like to infer the contents (in terms of stellar population age, star formation rate, mass, gas and dust content). There are



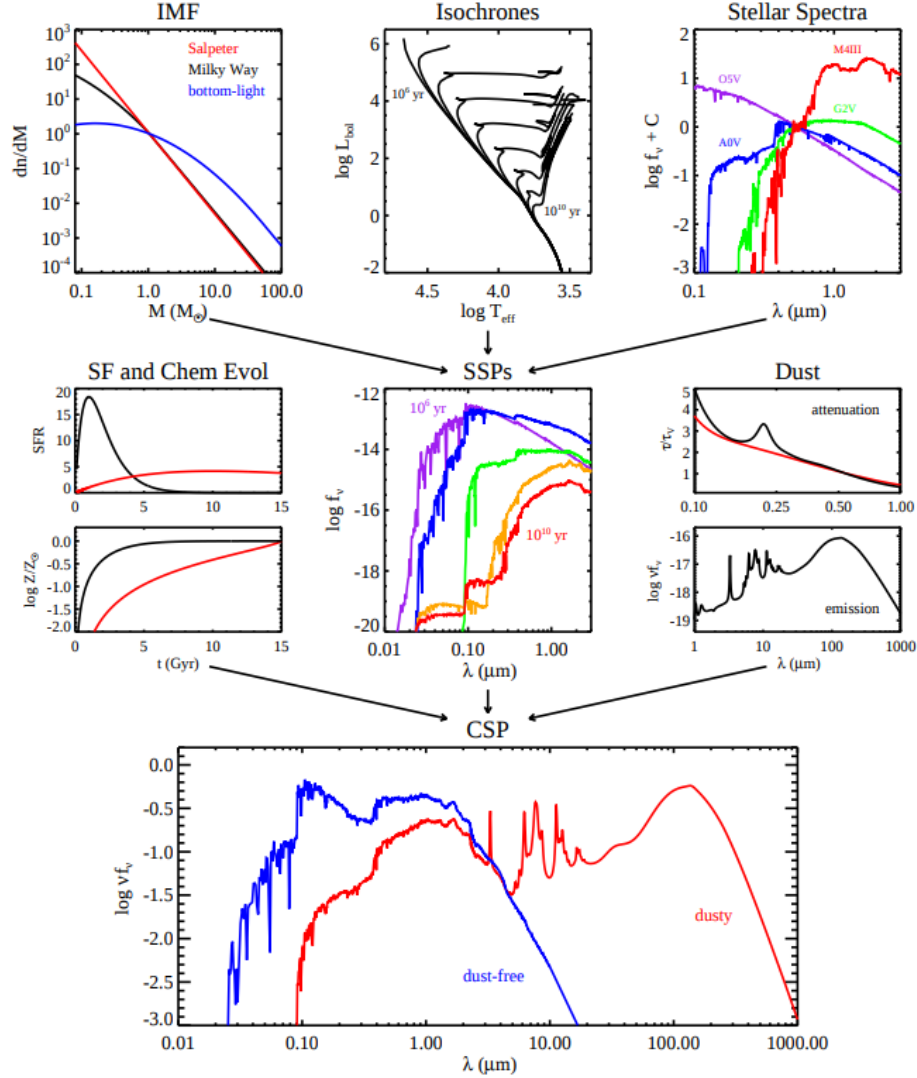
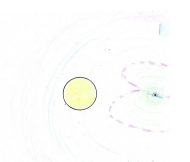


Figure 1.9: A representation of the steps required to produce a synthetic galaxy SED (figure from Conroy, 2013). An IMF determines how many stars there should be at each ZAMS mass. Isochrones, or evolutionary tracks, define the temperature and luminosity of the stars at a given age. Stellar spectra are then summed, in proportion to the stars present and their respective luminosities, to produce a simple SED. More complex (and realistic) SEDs can be constructed by summing the contributions from populations at different ages and metallicities, and considering the effect of dust on the absorption and re-emission of light.

various methods for doing this, but all fall under the umbrella of SED fitting. The basic principle of SED fitting is the comparison of observational data to either observed galaxy templates, synthetic templates, or models which are generated based on input conditions from the user. A ‘simple stellar population’ SED is built up from (i) a population of stars of a single age, given an IMF and initial mass of gas, (ii) the contribution of each star to the SED, determined by each stars luminosity and temperature at the considered age and (iii) the stellar atmospheres, and resultant spectra. The sum of the spectrum from each star, weighted by their luminosity, produces a simple stellar population SED. ‘Complex stellar population’ SEDs go further, taking into account bursts or ongoing star formation, metal enrichment and reddening by dust. These ideas are demonstrated in Figure 1.9. The ‘fitting’ part of SED fitting is then performed by finding the resultant synthetic SED that best matches the data, given observational uncertainties. This can be done with a simple  $\chi^2$  minimisation, or more complex Bayesian techniques which take into account our prior knowledge about the likelihood distributions of the parameters being fit. SED fitting can be used to infer several properties of a galaxy at once; but if more parameters are desired, more data points are required. Alternatively, it can be used to estimate just one parameter, such as redshift, by identifying strong features in the data such as a Balmer break (due to absorption by metals in cool stars below  $\sim 4000 \text{ \AA}$ ) or the Lyman break.

There is a wide range of SED fitting codes available, using different methods and tailored for different purposes. Commonly used codes include Le Phare and HYPERZ (for photometric redshifts, Bolzonella et al., 2000; Arnouts et al., 1999; Ilbert et al., 2006), CIGALE, FAST and BEAGLE (which employ Bayesian inference to ascertain galaxy properties, Noll et al., 2009; Serra et al., 2011; Kriek et al., 2018; Chevillard and Charlot, 2016). Some stellar models often used by SED fitting codes include those of Bruzual and Charlot (2003), Maraston (2005), Pegase (Kewley et al., 2001) and MAGPHYS (da Cunha et al., 2008, 2015). MAGPHYS is also a fitting code, which self consistently accounts for the absorption of UV radiation by dust and re-emission in the far-IR. I use MAGPHYS for SED fitting of IR-bright galaxies in Chapter 2.3. In Chapter 5, I use the stellar evolution models of BPASS (Binary Population and Spectral Synthesis Eldridge et al., 2017; Stanway and Eldridge, 2018). BPASS constructs stellar populations and SEDs according to the methodology shown in Figure 1.9, but explicitly accounts for the effects of binary interactions on stellar evolution. The impacts of this are wide ranging, but for example include bluer populations at a given age due to the stripping of massive star envelopes and mass transfer. BPASS can produce consistent estimates



for gravitational wave and electromagnetic transients (Eldridge et al., 2019a), whilst simultaneously producing synthetic spectra for their host galaxy stellar populations. This is thanks to its star-by-star, bottom up approach, and is a feat that other population synthesis codes struggle to achieve.

In this Section I have reviewed the assumed cosmology, the history of galaxy and stellar population evolution since the epoch of reionisation, and how we can infer the properties of galaxies with SED fitting. Next, I will discuss observations of GRB host galaxies, and how this informs our current understanding of GRBs, but also leaves several questions open.

## 1.5 The Host Galaxies of Core-Collapse GRBs

Much of our current understanding of core-collapse gamma-ray bursts, and indeed many of the questions we still have today, arose from the study of their host galaxies. GRB galactic environments can inform our understanding in two ways: by post-burst observations, followed by analysis such as SED fitting, or by direct observation of the burst and its afterglow while it is occurring in the galaxy (Schady, 2017). This allows us to pinpoint the position of the burst within its host, and, if spectroscopy is performed, probe the circumstellar, interstellar and intergalactic medium with absorption line measurements. In this section, I provide a brief review of the history of core-collapse GRB host studies and their findings.

In the late 1990s, the first host galaxy identifications were made. The key to more discoveries was better burst localisation in the gamma-ray and X-ray regimes. The first two hosts (of GRBs 970228 and 970508, Bloom et al., 1998, 2001) were found thanks to the  $\sim$ arcminute spatial resolution of BeppoSAX, making deep targeted searches for a longer wavelength afterglow possible. If the X-ray localisation is poor, then the afterglow can fade beyond detection limits before it is found. The launch of *Swift* was a game changer in this regard. Within minutes, *Swift* can provide X-ray positional uncertainties of only a few arcseconds, enhanced by astrometric matching of sources detection by UVOT (Goad et al., 2007; Evans et al., 2009). With better localisations from *Swift* came more positive host identifications. Almost immediately, breakthroughs were made, such as the first identifications of short GRB host galaxies (Gehrels et al., 2005; Prochaska et al., 2006). It became clear that short and long duration bursts favoured different environments: short GRBs were seen in a variety of galaxies, including massive ellipticals with old stellar populations, while long GRBs were almost exclusively found in low mass, star forming hosts (Bloom et al., 1998; Fruchter et al., 1999a; Sokolov et al., 2001; Vreeswijk et al., 2001; Le

Floc'h et al., 2003; Christensen et al., 2004). Short GRBs, now thought to arise from compact object mergers, are discussed further in Section 1.7.1. GRB localisation was also aided by (and is to this day) the IPN (Interplanetary Network). The IPN coordinates observations from several space-based observatories (including AGILE, *Konus/Wind*, FERMI, INTEGRAL and *Swift*), determining approximate burst locations based on the arrival times of high energy photons at each telescope in the network.

Increasing numbers of host detections led to the emergence of a GRB redshift distribution. Redshifts are measured with absorption lines in GRB afterglows, absorption and emissions lines in the host spectrum, or with photometric redshift estimates. The initial consequence was that isotropic equivalent energies could be calculated for the first time - these were too high to feasibly be the total energies, and so the evidence mounted that GRBs must be highly beamed events (supported by their light curve behaviour, see Section 1.2). Correcting  $E_{\text{iso}}$  for beaming made them consistent with the most energetic supernovae (Panaitescu and Kumar, 2001; Frail et al., 2001), but also had implications for the *intrinsic* volumetric GRB rate. Redshift information also led to the discovery of relations in the prompt data, such as the Amati relation (Amati, 2006) -  $E_{\text{iso}} \propto E_p$ , where  $E_p$  is the energy of the photons emitted at the peak of the spectrum, and the Ghirlanda relation (Ghirlanda et al., 2004, which corrects burst energies for beaming.). The low redshift and observed flux of some bursts implies that they are underluminous - these low-luminosity bursts are up to  $\sim 100$  times fainter than their cosmological counterparts (Galama et al., 1998; Stanway et al., 2015a; Schady, 2017).

Even before *Swift*, greater precision X-ray observations (e.g. from BeppoSAX), and therefore more afterglow detections in the optical and IR, made it possible to measure where GRBs occur *within* their host galaxies, and how they traced their host light. Bloom et al. (2002) pioneered the measurement of burst positions with respect to their host galaxies. Using a variety of long GRB afterglow data from the optical to radio regimes, and rest-frame UV *Hubble Space Telescope* (*HST*) imaging, they demonstrated that the median offset from their host centres was approximately equivalent to the half-light radius. This is the radius enclosing 50% of the galaxy light - only representative of the true light distribution in spherical or face-on spiral geometries. The implications were twofold: (i) long GRBs cannot be originating from compact object mergers, which were expected to undergo kicks upon their formation, placing them further from their point of origin, and (ii) long GRBs were strongly concentrated on the UV light of their hosts, associated with the most massive stars. Along with the GRB-SN connection first established by



SN 1998bw (Bloom et al., 1999; Galama et al., 2000; Hjorth et al., 2003; Levan et al., 2005), the case for a massive star long GRB progenitor was growing. Fruchter et al. (2006) built on these ideas, measuring not only the position of long GRBs within their hosts, but ranking them based on the brightness of the pixel they fell on. This fractional light, or  $F_{\text{light}}$ , technique defines all pixels above a background level as being associated with the host, and then ranks the pixels in order of brightness. An  $F_{\text{light}}$  of 1 means that the burst occurred on the brightest pixel in the galaxy. This method was motivated by the fact that the galaxy barycentre may not be the brightest pixel (i.e., where the most star formation is occurring), particularly in irregular galaxies, and we are interested in the burst offset from the most intensely star forming regions. The GRB results from this work were compared with the  $F_{\text{light}}$  distributions of core-collapse supernovae. There were two key findings. First, long GRBs are more strongly correlated with the brightest regions of their hosts than the general core-collapse supernova population, which traces their host UV light. This implied GRBs require higher mass progenitor stars. Subsequent studies using larger samples, deeper host imaging and better burst localisations have backed up these findings (Kelly et al., 2008; Svensson et al., 2010; Blanchard et al., 2016; Lyman et al., 2017). The second key result of Fruchter et al. (2006), from the *HST* imaging, is that long GRBs in the local ( $z < 2$ ) Universe strongly prefer lower mass galaxies with irregular morphologies. The well established mass-metallicity relation therefore implied that they have an aversion to high metallicity environments.

Studies of GRB hosts have consistently shown them to be systematically lower in mass and metal content than both the wider star forming galaxy population, (Stanek et al., 2006; Le Flocc’h et al., 2006; Savaglio et al., 2009; Levesque et al., 2010b,c; Svensson et al., 2010; Graham and Fruchter, 2013; Vergani et al., 2015), and even the hosts of type Ic-BL supernovae *without* GRBs specifically (Modjaz et al., 2008). An example core-collapse GRB host is shown in Figure 1.10. However, many of the pre-*Swift* studies of GRB host populations suffered from a bias - only the brightest optical afterglows were detected before precise X-ray localisations were available (Le Flocc’h et al., 2003). There is a subset of GRBs, ‘dark GRBs’, which show suppressed optical emission below that expected from extrapolation of the X-ray spectral slope (Groot et al., 1998a; Fynbo et al., 2001; Jakobsson et al., 2004; van der Horst et al., 2009, more detail on this class of bursts is given in Chapters 3 and 4). These make up a significant proportion of the total long GRB populations, with estimates around 25-40% (Fynbo et al., 2009; Greiner et al., 2011; Perley et al., 2016a). A small proportion of dark GRBs are optically faint due to their high redshift placing the observed optical bands short-wards of the Lyman break (Kawai

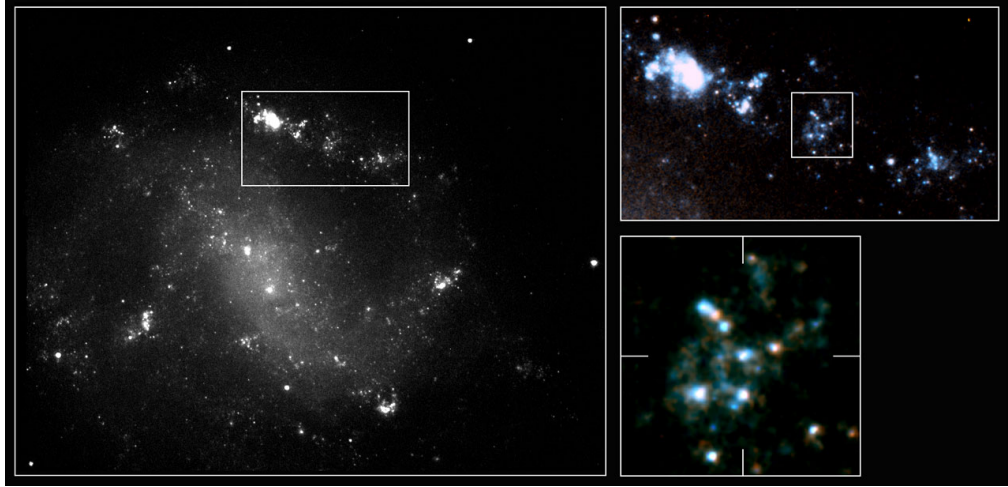


Figure 1.10: An example of a GRB host galaxy. This is the host of GRB 980425 / SN 1998bw, imaged 778 days post-explosion with *HST* (Fynbo et al., 2000). This is one of the nearest GRBs to date, at a redshift  $z = 0.0085$ . The burst occurred at the centre of the box in the lower right panel. Each panel progressively zooms in to the explosion site (figure from Hjorth and Bloom, 2012). Although the burst was significantly offset from host centre, it did occur in a strongly star forming region, although not the nearby Wolf-Rayet region to the left.

et al., 2006; Cenko et al., 2006; Grazian et al., 2006a; Jakobsson et al., 2006; Ruiz-Velasco et al., 2007; Salvaterra et al., 2009; Greiner et al., 2009; Tanvir et al., 2009; Cucchiara et al., 2011; Afonso et al., 2011; Castro-Tirado et al., 2013; Laskar et al., 2014; Jeong et al., 2014a; Chornock et al., 2014b; Tanvir et al., 2018). However, the majority are dark due to dust absorption within their host galaxies (e.g. Castro-Tirado et al., 2007; Rol et al., 2007a; Perley et al., 2009; Fynbo et al., 2009; Higgins et al., 2019). Accounting for the hosts of dark GRBs (by pinpointing them with precise X-ray observations and deep NIR imaging) weakened the metallicity aversion somewhat (Krühler et al., 2012b; Michałowski et al., 2012; Perley et al., 2013), allowing for bursts up to  $\sim$  Solar metallicity, but they still show an overall preference for low mass, low metallicity hosts (Perley et al., 2016a,b; Graham and Fruchter, 2017; Japelj et al., 2016; Palmerio et al., 2019). GRBs become less biased tracers of star formation as redshift increases, as expected given a metallicity aversion and the chemical enrichment of galaxies over cosmic time (Kocevski et al., 2009; Jakobsson et al., 2012; Schulze et al., 2015; Krühler et al., 2015). This is demonstrated in Figure 1.11. However, the qualitative observation that GRBs prefer lower metallicity environments (which can be inferred from the  $M - Z$  relation) is harder to measure in a quantitative sense, and efforts are ongoing (Graham et al., 2019; Gatkine



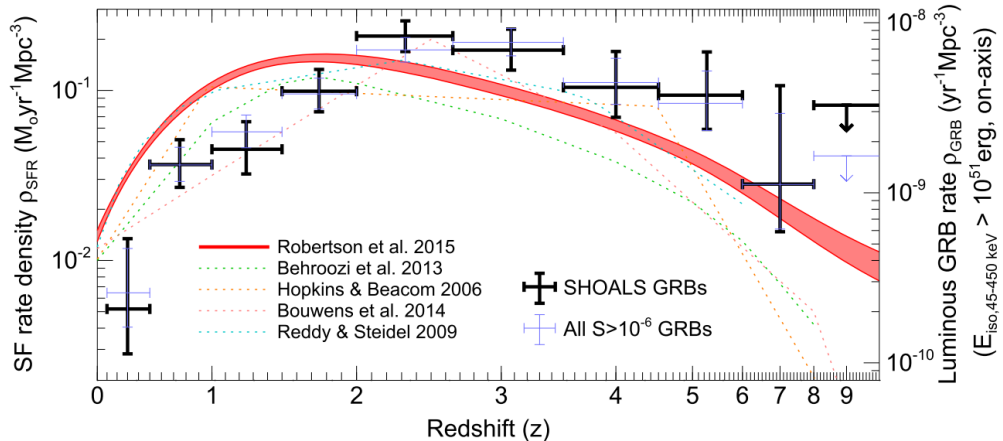


Figure 1.11: The comoving rate density of GRBs over cosmic time (not corrected for beaming effects), compared with the star formation rate density equivalent from Robertson et al. (2015) (Madau and Dickinson, 2014), Behroozi et al. (2013), Hopkins and Beacom (2006), Bouwens et al. (2014) and Reddy and Steidel (2009). Two GRB samples are shown: the SHOALS sample has been carefully selected to avoid biases in the host galaxies followed up (i.e., includes dark bursts in proportion), whereas the other is all *Swift* long GRBs with a fluence  $S > 10^6 \text{ erg cm}^{-2}$ . It is clear that the GRB rate is suppressed with respect to star formation at redshifts  $\lesssim 2$ . This figure is adapted from Perley et al. (2016a).

et al., 2019). Integral field unit spectroscopy can be used to examine the burst site specifically of the nearest hosts (Christensen et al., 2008; Krühler et al., 2017; Izzo et al., 2017). Of note are the differences in the environments of type Ic, Ic-BL and GRB-SNe, providing clues as to the conditions for jet production. Modjaz et al. (2016), Japelj et al. (2018) and Modjaz et al. (2019) show that the metallicities of Ic-BL and GRB-SN hosts are systematically lower than those of regular Ic SNe.

Because GRBs appear to less biased star formation tracers at high redshift, they are a useful probe of stellar populations in the epoch of reionisation. Furthermore, their afterglows are imprinted with signatures of the interstellar and intergalactic medium in the distant Universe - while quasars can perform a similar function, GRBs are uniquely capable of providing this information for *low-mass* galaxies (e.g. Cucchiara et al., 2015). For example, redshift measurements or limits from afterglow spectroscopy or photometry, combined with measurements or deep limits on host magnitudes, provides information on the luminosity of galaxies producing GRBs in this epoch (Tanvir et al., 2012; McGuire et al., 2016). The rate of events can be used infer the star formation rate, but this requires an understanding of GRB production biases (Kistler et al., 2009; Trenti et al., 2012; Robertson

and Ellis, 2012; Tanvir et al., 2019). Direct measurement of the Lyman- $\alpha$  line in emission is possible for some GRB hosts at  $z \gtrsim 2$  (Milvang-Jensen et al., 2012).

Given that GRBs tend to occur in a subset of blue, low mass, star forming galaxies, another question arises: are they typical low-mass star forming galaxies? And what is the nature of the high-mass end of the GRB host distribution? One way to investigate these questions is through galaxy morphologies. Several studies have compared the structure of GRB hosts with supernova hosts and other star forming galaxies (McGuire et al., 2016; Lyman et al., 2017). Although difficult to establish Hubble-sequence morphologies with such distant galaxies, these studies have shown that long GRB hosts are not distinct from the star forming population in terms of their structure, comprising spiral and irregular morphologies. There is some evidence that massive, dustier GRB hosts typically have more disturbed morphologies (e.g. Svensson et al., 2012; Arabsalmani et al., 2019), perhaps indicating that galaxy interactions or mergers are taking place. I return to this question in Chapter 3.

Another point of interest is the molecular gas content of GRB hosts. The neutral hydrogen column density in GRB hosts can be obtained from their X-ray afterglows. These are inferred from the X-ray spectra, after they have been corrected for Galactic absorption (Evans et al., 2009). Molecular gas can also be observed in GRB hosts through their afterglows (Prochaska et al., 2009). Alternatively, the hosts can be directly observed. The hydrogen 21 cm emission line traces atomic gas, and has been found to be more prominent than expected in GRB hosts (Michałowski et al., 2015, 2016), given the standard relations between SFR and gas density (e.g. the Schmidt-Kennicutt Law, Schmidt, 1959). The implication is that stars are forming from atomic gas, rather than molecular gas, something that has been shown to be theoretically possible (Glover and Clark, 2012). However, molecular species have more energy level transitions, facilitating efficient cooling, and therefore star formation. Molecular hydrogen,  $\text{H}_2$ , forms readily in the presence of dust grains, and is shielded from dissociating photons by them. Therefore, a  $\text{H}_2$  deficit for a given SFR implies that (i) dust grains have yet to form and (ii) the gas is cooling faster than it can be converted into  $\text{H}_2$ . If the star formation episode is brief, as is thought to be the case in many GRB hosts (see e.g. Perley et al., 2015; Stanway et al., 2015b), then the stars might be forming from fresh, low metallicity atomic gas in-falling from the IGM. However, the significance of the  $\text{H}_2$  deficit result is unclear, with at least some GRB host galaxies that contradict the trend (Perley et al., 2017; Arabsalmani et al., 2018; Michałowski et al., 2018a; Wiersema et al., 2018; Heintz et al., 2019b; Bolmer et al., 2019).

The molecular gas content in galaxies is correlated with the dust mass. For



example, the optical darkness of a GRB (i.e., the extinction  $A_V$  which increases with dustier sight-lines) is greater in bursts with high X-ray HI absorption (Zafar et al., 2011; Selsing et al., 2019b). Other work has shown that molecular gas content is correlated with specific dust absorption features in GRB afterglows, such as the 2175 Å bump (Zafar et al., 2012, 2018a; Heintz et al., 2019c). This is a poorly understood feature in galaxy extinction curves, but it may be due to ordered carbon dust grains (Draine, 2003). Such grains might be easily destroyed in the intense UV radiation field of a starburst galaxy. Similarly, dust in the vicinity of GRBs might be destroyed (therefore suggesting that dark bursts are optically extinguished by dust further from the explosion site, Fruchter et al., 2001). Because  $H_2$  formation is aided by dust, this might explain earlier claims of atomic gas excess in GRB hosts (Heintz et al., 2019a).

Alongside their afterglows, the host galaxies of long GRBs have been a rich source of clues as to their origin. Thanks to these studies over the last  $\sim 20$  years, we know that long GRB progenitors are massive stars, with a strong *preference* (but not an absolute requirement) for low metallicity environments. I discuss our current best understanding of long GRB progenitors, the mechanisms powering GRBs, and outstanding questions, in the next section.

## 1.6 Core-Collapse GRB Mechanisms and Progenitors

Having been through the observational properties of gamma-ray bursts, high mass stellar evolution, supernovae, galaxy evolution and the host galaxies of GRBs, I now turn to a key question that will permeate this thesis: what do these observations tell us about core-collapse GRB mechanisms and their progenitors? For comprehensive reviews of this topic, I refer the reader to Kumar and Zhang (2015), Levan et al. (2016) and Fryer et al. (2019).

The energies observed in GRBs, and the timescale of variability in their prompt light curves, points towards a compact object central engine. Characteristic breaks in these light curves, again combined with energetics arguments, is evidence that the central engine launches relativistic jets (see Section 1.2), the emission from which can be observed as a GRB if Earth is oriented along the jet axis. Although the association of GRBs with supernovae and star forming regions is strong evidence for a massive star progenitor, there is no direct evidence yet for the nature of the central engines that are produced. There are two main competing theories, although it may be the case that both occur in nature: these are (i) jets are powered by accretion onto a nascent black hole (Narayan et al., 1992) and (ii) jet launch by a newly formed

magnetar (Duncan and Thompson, 1996; Metzger et al., 2011; Mazzali et al., 2014). In the former scenario, the energy required to launch jets is likely extracted from either the rotation of the black hole (the Penrose mechanism and Blandford-Znajek process, Penrose and Floyd, 1971; Williams, 1995; Blandford and Znajek, 1977), or from the accretion flow through neutrino - anti-neutrino annihilation (which also produces  $e^-e^+$  pairs) near the poles (Zalamea and Beloborodov, 2011). The  $\nu_e$  and  $\bar{\nu}_e$  neutrinos are produced by  $e^- + p \rightarrow n + \nu_e$  and  $e^+ + n \rightarrow p + \bar{\nu}_e$  reactions - the weak interaction probabilities of these are enhanced at the extreme temperatures involved (Leng and Giannios, 2014). It is also possible that general relativistic, *and* neutrino annihilation processes, play a role (Lei et al., 2017). A popular framework is the collapsar model (Woosley, 1993), in which an accretion disc forms at the innermost stable orbit around a newly formed black hole. Energy is extracted from the angular momentum of this disk, powering bipolar jets.

Magnetars, on the other hand, are rapidly rotating, highly magnetised neutron stars (with field strengths of order  $10^{10}\text{T}$ ). Evidence for millisecond-period magnetars as central engines comes from the presence of extended X-ray plateaus in some GRB light curves (e.g. Zhang and Mészáros, 2001; Gompertz et al., 2013), particularly in short GRBs. In order to slow the light curve decline, the argument is that there must be an internal source of energy injection in the  $\sim 100\text{s}$  following the initial jet launch. The spin-down of a highly magnetised neutron star within the expanding ejecta shell is theoretically capable of providing this energy.

Although short bursts are now known to arise from compact object mergers (see Section 1.7), rather than the collapse of massive stars, the initial conditions of the newly formed central engine are probably similar (hence the production of relativistic jets in both cases). The recent advent of gravitational wave astronomy has opened the possibility that the mass of the newly formed object in such mergers could be constrained, although GW signal-to-noise ratios are currently insufficient. If black holes are unambiguously produced in the immediate aftermath of these mergers, that would be strong evidence that long GRBs can also be powered by the black hole collapsar mechanism (Margalit and Metzger, 2017; Abbott et al., 2018a). It has also been suggested that magnetars may be the engine powering long GRBs that are associated with superluminous supernovae (Metzger et al., 2015; Wang et al., 2017a) and ultra-long duration bursts (Greiner et al., 2015a; Gompertz and Fruchter, 2017; Kann et al., 2018).

Even though it is still unclear which central engines play a role in long GRB production, all suggestions have two key features in common: they require a compact object, and high angular momentum at core-collapse. Combined with the observa-



tional constraint of type Ic SN associations, the need for rapidly-spinning, high mass, stripped envelope progenitor emerges. The stripped envelope requirement can be understood in terms of jet escape. If the environment the jet immediately faces is dense, relativistic velocities would be hard to achieve (the baryon loading problem, Lei et al., 2013). The jet could even be choked entirely. Perhaps the clearest way to remove a stellar envelope is through winds, which is a Wolf-Rayet formation channel. However, stellar winds, by virtue of carrying away mass, also reduce the angular momentum of the star (Vanbeveren et al., 1997). Mass loss increases with increasing metallicity due to line driven winds, dominated by iron (Vink et al., 2001; Vink and de Koter, 2005). Indeed, this effect helps to explain the dearth of GRBs at high metallicity. There is even a trend for metallicity to increase across type Ic supernova sub-types: GRB-SNe have the lowest metallicity environments, on average, followed by Ic-BL SNe and finally ‘regular’ Ic events (Modjaz et al., 2016; Japelj et al., 2018; Modjaz et al., 2019). This can be explained by the jet *strength*, specifically the energy released and the degree of beaming, decreasing as metallicity increases and the progenitor star spins slower. In Ic SNe, it may be that no jet is produced or it is completely choked, in Ic-BL SNe a jet is launched, but is impeded by what remains of the envelope, and in GRB-SNe a jet is launched and successfully tunnels out of the envelope (Izzo et al., 2019; Piran et al., 2019). In this framework, low-luminosity GRBs might result from the shock break out of jets which were impeded by the envelope (Mazzali et al., 2008; Piran et al., 2013; Schulze et al., 2014; Piran et al., 2019). It is also possible that many Ic-BL SNe are successfully launching GRBs, but we are observing them off-axis (Woosley and Bloom, 2006)

Because mass loss through wind struggles to produce stripped envelope progenitors that are rapidly rotating, other pathways must be considered (Hirschi et al., 2005; Trenti et al., 2015). A plausible route is through (quasi) chemically homogeneous evolution. In this binary star scenario, the secondary is spun-up by accretion from the primary, to such a degree that rotational mixing occurs (Maeder and Meynet, 1987; Brott et al., 2011). If hydrogen and helium are mixed efficiently into the core, the resulting star can become deficient in these elements (and therefore a type Ic-SN progenitor). Provided the rapid rotation continues once accretion has stopped, the star is a good core-collapse GRB candidate (Yoon and Langer, 2005; Cantiello et al., 2007; Eldridge et al., 2011). This requires low metallicity, otherwise the secondary will spin down due to winds as soon as accretion ends. The QHE pathway was explored by Eldridge et al. (2017) and Eldridge et al. (2019a), by assuming that too much spin down occurs for GRB production to occur above

a metallicity mass fraction of  $Z = 0.04$ . Alternatively, a star could be spun up to QHE velocities through tidal interactions (Mandel and de Mink, 2016). It is still possible, however, that some single Wolf-Rayet type stars are rotating fast enough at core-collapse to produce GRBs (Gräfener et al., 2012; Vink and Harries, 2017)

Although QHE and single star pathways are possible, they both face issues, namely restriction to very low metallicities and scarcity respectively. Furthermore, although rare, long GRBs do occur in  $\sim$  Solar metallicity environments (see for example, Castro-Tirado et al., 2007; Graham et al., 2009; Prochaska et al., 2009; Levesque et al., 2010a; Hunt et al., 2011; Krühler et al., 2012a; Savaglio et al., 2012; Elliott et al., 2013; Hashimoto et al., 2015; Schady et al., 2015; Stanway et al., 2015a; Wang et al., 2018; Michałowski et al., 2018b). The task, therefore, is to find GRB pathways which have a preference for low metallicity but not an absolute requirement. One method is to strip the envelope from a primary star (Podsiadlowski et al., 2004; Izzard et al., 2004; Petrovic et al., 2005; Detmers et al., 2008; Podsiadlowski et al., 2010; Trenti et al., 2015), although tidal interactions may be required to maintain rotation in this scenario (see Chapter 5). Other ideas involve systems that are intrinsically rarer, but nonetheless may occur, such as neutron star collapse induced by accretion of supernova ejecta from a companion (a ‘binary driven hypernova’, Rueda et al., 2019). A small number of unambiguously long-duration GRBs appear to be lacking an associated supernova to deep limits, presenting a challenge to the collapsar or magnetar engine theories (e.g. GRBs 060605, 060614 and 111005A, Gal-Yam et al., 2006; Thöne et al., 2008; Michałowski et al., 2018b; Tanga et al., 2018). These might be a subset of the compact object merger population typically associated with short GRBs. Their longer duration could be indicative of greater mass asymmetry than NS-NS mergers, such as a WD-BH (Fryer et al., 1999), NS-BH (Paczynski, 1991), or BH-helium star merger (Fryer and Woosley, 1998). GRB 060605 occurred in a young, star forming galaxy, typically associated with core-collapse GRBs, making the lack of a supernova particularly puzzling. In this case, the host SED suggests a quantity of dust that is (a) insufficient to hide a supernova and (b) consistent with the *Swift* X-ray afterglow - suggesting that the burst did take place in the galaxy, rather than ‘behind it’ at higher redshift. The merger ideas for long GRBs are still somewhat speculative, but multi-messenger gravitational wave observations might provide answers in the coming years (Wang et al., 2017b).

In this section, I have summarised the state of the community’s knowledge about the progenitors of long duration GRBs, and the physical mechanisms producing them. The evidence points towards core-collapse progenitors, but there are

still significant uncertainties, and the exact nature of these systems is unknown. To build an understanding of which stars produce GRBs and why, we must also consider other transients that can occur at the end of stellar evolution. This is the topic of the next section.

## 1.7 Multi-Messenger Astronomy and other Extragalactic Transients

Long-duration, core-collapse GRBs are not the only extragalactic transients driven by central engines. An understanding of how they fit into the zoo of transient phenomena, including supernovae as described in section 1.3.4, not only helps to identify them observationally, but also advances our understanding of the stellar populations which give rise to the diverse range of transients observed. It is a particularly exciting time for transient astronomy, as the era of multi-messenger astrophysics is now underway. In this section, I give an overview of multi-messenger astronomy in the context of GRBs, and discuss other engine-driven extragalactic transients.

### 1.7.1 Short duration GRBs, Kilonovae and Gravitational Waves

Short-duration, spectrally hard GRBs (sGRBs) have long been suspected to arise from the merger of compact objects, due to their mixed to older host populations and lack of associated supernovae. Studies of the host-burst offsets for sGRBs provided strong evidence that the progenitors were experiencing kicks, giving them high velocities, sometimes sufficient to escape their host galaxies altogether. The offsets were also indicative of long delay times between the kick and point of explosion, given the large host offsets observed. This implied a binary progenitor, with momentum kicks imparted upon supernova of each of the components (Berger, 2010, 2014; Tunnicliffe et al., 2014).

The merger of two neutron stars - the favoured channel for producing sGRBs - was expected to be a strong gravitational wave source (Abadie et al., 2010), according to Einstein's general relativity (GR, Dirac, 1996). The existence of gravitational waves was experimentally confirmed with observations of a pulsar in a pulsar-neutron star binary, whose orbital decay corroborated GR's predictions of gravitational waves (Hulse and Taylor, 1975; Taylor et al., 1979).

In 2015, the commissioning of two upgraded Michelson-Morley style interferometers in Louisiana and Washington State began (LIGO, Laser Interferometer

Gravitational Wave Observatory). This was followed by Virgo, Italy, in 2017. These interferometers are sensitive to the changing relative path lengths that their perpendicular laser beams must travel before interfering at the detector - the changes being induced solely by the passage of gravitational waves, if the detectors are isolated from terrestrial vibrations. Eight binary black hole mergers were detected up to August 2017 (Abbott et al., 2019), marking the first *direct* experimental verification of the gravitational wave prediction of GR (Abbott et al., 2016).

On the 17<sup>th</sup> August 2017, the three facilities detected the signal from the inspiral and merger of two neutron stars - GW 170817 (Abbott et al., 2017a). The detection of a sGRB by *Fermi*  $\sim 2$ s after the GW signal (Goldstein et al., 2017), and the subsequent localisation of the burst thanks to *Fermi*, INTEGRAL and the IPN, was combined with the relatively good localisation from LIGO/VIRGO ( $31 \text{ deg}^2$ ) to provide a manageable area of sky to search for a counterpart at other wavelengths (Abbott et al., 2017b). At  $\sim 11$  hours post-burst, an optical transient was discovered in the galaxy NGC 4993 (see Figure 1.12). An extensive follow-up campaign showed that the transient was a long predicted kilonova, produced by the radioactive decay of heavily neutron enriched material synthesised via the r-process (Li and Paczyński, 1998). The evidence was overwhelming: GW 170817 was the merger of two neutron stars, observed in both gravitational waves and electromagnetic radiation. Other kilonovae had been claimed previously, and the confirmation of the short GRB-kilonova connection with GW 170817A made these previous claims substantially more convincing (Tanvir et al., 2013b; Berger et al., 2013; Gompertz et al., 2018).

Despite demonstrating that compact object mergers are the cause of sGRBs, and that such mergers produce kilonova explosions, many questions were raised or left unanswered. GRB 170817A is the nearest GRB seen to date, at  $z = 0.009783$ , or 42.5 Mpc (Levan et al., 2017). Not being a particularly bright burst, it was therefore under-luminous - was this because we observed the event off-axis, or was it intrinsically faint (D'Avanzo et al., 2018)? What type of jet was launched - was it top hat-like, structured, or a cocoon (Lyman et al., 2018; Troja et al., 2019)? What type of remnant was formed? And can other combinations of compact objects, such as a NS-BH merger, also produce a GRB (MacFadyen and Woosley, 1999)? NS-BH mergers have now been detected by LIGO/VIRGO (of particular note is S190814bv which was extremely well localised, Gomez et al., 2019), along with further NS-NS mergers, but at the time of writing GW 170817 remains the only confirmed multi-messenger GW event.

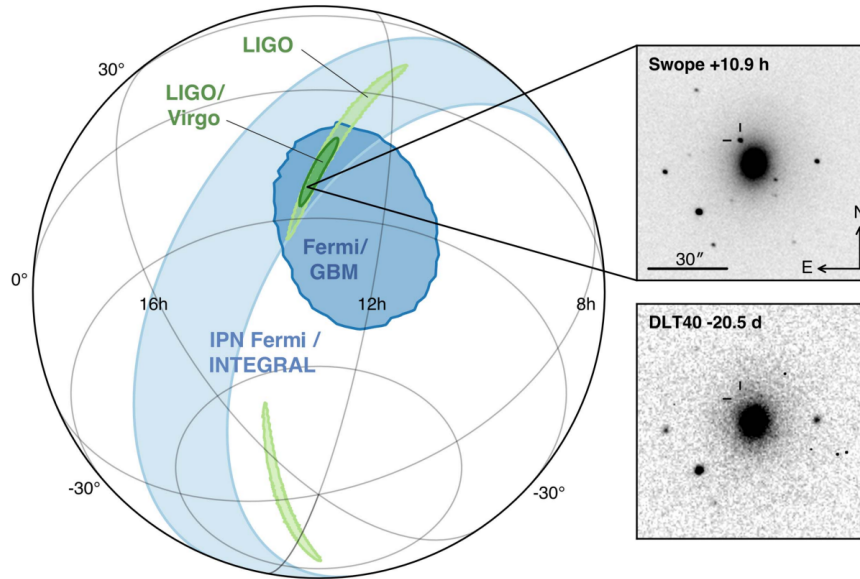


Figure 1.12: The sky localisation of GW170817 (GRB170817A) in gravitational waves (green) and high energy photons (blue) (figure from Abbott et al., 2017b). Also shown is the kilonova discovery image, at  $\sim 11$  hours post merger, and the host galaxy NGC 4993 as seen 20.5 days before.

### 1.7.2 Very High Energy photons and Neutrinos

Very High Energy (VHE) photons ( $\gtrsim 10$  GeV) are detected from ground using Cherenkov telescopes such as MAGIC and H.E.S.S. Photons of these energies create particle showers upon interacting with atoms in the atmosphere; these particles are travelling faster than the speed of light in air at the point of creation, thus producing flashes of Cherenkov radiation, detectable by telescopes. To date, 3 GRBs (all long-duration) have been seen at VHE. These are GRBs 180720B (Fraija et al., 2019), 190114C (Mirzoyan, 2019) and 190829A (de Naurois, 2019). The next generation VHE observatory will be the Cherenkov Telescope Array, due to commence operations in the next few years (Actis et al., 2011; Nandra et al., 2013).

Beyond the electromagnetic spectrum, many extreme astrophysical environments are expected to produce neutrinos (Guépin and Kotera, 2017). In supernovae, the majority of the energy is released in this form (Janka, 2017). Major neutrino observatories, which rely on detecting optical flashes when neutrinos undergo extremely rare interactions with electrons, include KM3NeT, IceCube, Super-Kamiokande and the upcoming DUNE. Although many extreme transients produce neutrinos, they have only been detected so far from a single supernova (SN1987A, Hirata et al., 1987) and quasar (blazar 0506+056, IceCube Collaboration et al., 2018).

### 1.7.3 Superluminous Supernovae

Another rare class of transient, thought to be powered by central engine, are superluminous supernovae. These are  $\sim 100$  times more luminous than other core-collapse supernovae (Gal-Yam, 2012). They occur in two varieties, type I and type II, which again correspond to being hydrogen poor versus hydrogen rich. While type II SLSNe can be explained by shock break out into a dense circumstellar environment (Ofek et al., 2014), type I SLSNe remain the subject of much investigation. Intriguingly, the host galaxies of type I SLSNe are similar to those of GRBs (Lunnan et al., 2014, 2015; Leloudas et al., 2015; Angus et al., 2016; Lyman et al., 2017). The additional energy released in type I SLSNe, compared to standard SNe, cannot be explained by additional  $^{56}\text{Ni}$  or other ejecta products. A popular idea in the literature is that the spin down of a newly formed magnetar powers the explosion, although how this mechanism operates, and what distinguishes these events from magnetar driven GRBs, is not well understood (Woosley, 2010; Inserra et al., 2013; Nicholl et al., 2017a; Margalit et al., 2018b,a; Dessart, 2019; Angus et al., 2019).

### 1.7.4 Tidal Disruption Events

Gamma-ray bursts are not the only way to produce transient relativistic jets. Jets which are at least superficially similar can be launched when a star is tidally disrupted as it passes close to a supermassive black hole, forming a short lived accretion disc. These are called relativistic tidal disruption events (or flares) and appear similar to GRBs in the X-ray and gamma-ray bands. However, their rates are much lower than GRBs, they are centrally located on their hosts, and they have durations a factor of  $\sim 10$  longer than even ultra-long GRBs (Levan et al., 2016). The three events observed so far are *Swift* J1644+57 (Levan et al., 2011), J2058+05 (Cenko et al., 2012) and J1112–8238 (Brown et al., 2017).

### 1.7.5 Fast Radio Bursts

First detected by Lorimer et al. (2007), Fast radio bursts (FRBs) are transient, millisecond-duration pulses of radio waves (Petroff et al., 2019; Cordes and Chatterjee, 2019). Of the  $\sim 100$  bursts detected over the last 13 years (Petroff et al., 2016)<sup>2</sup>, 20 sources have been observed to repeat (Spitler et al., 2016; CHIME/FRB Collaboration et al., 2018, 2019; Kumar et al., 2019; Fonseca et al., 2020). Various cm-wavelength facilities including CHIME, Parkes, UTMOST and ASKAP are together detecting  $\gtrsim 10$  FRBs per year (based on published events so far). Only

---

<sup>2</sup><http://www.frbcat.org>



recently has the number of detected bursts exceeded the number of origin theories (Platts et al., 2019)<sup>3</sup>. The upcoming square kilometre array (SKA) is expected to discover 10-100 day<sup>-1</sup> (SKA1-MID Macquart et al., 2015), based on an all-sky rate of  $\sim 10^3$  sky<sup>-1</sup> day<sup>-1</sup> (Thornton et al., 2013; Champion et al., 2016). The FRB sky distribution, and their dispersion measures, suggest cosmological distances. This has recently been confirmed by the localisation of five bursts to distant galaxies (Chatterjee et al., 2017; Ravi et al., 2019; Bannister et al., 2019; Prochaska et al., 2019; Marcote et al., 2020). The first host, that of the repeating FRB 121102, is similar to the hosts of GRBs and SLSNe (Tendulkar et al., 2017; Metzger et al., 2017; Nicholl et al., 2017b). Two single burst hosts are more akin to the hosts of sGRBs. Two more tentative associations have also been suggested (Mahony et al., 2018; Lee, 2019). No emission at other wavelengths has yet been observed, despite real-time and post-burst searches (e.g., Hardy et al., 2017; Bhandari et al., 2018). Timescale and energetics arguments suggest that stellar-scale engines such as black holes or neutron stars play a role, although no firm evidence has yet arisen, and FRBs remain unexplained. With increasing numbers of FRB detections, and host galaxy identifications just beginning, the next few years promise to be a period of discovery in FRB astronomy.

The primary science question for FRBs is simple: what is their origin? Specifically, we would like to know, (i) are there two populations of FRB (repeating vs non-repeating, James et al., 2019), or do all bursts repeat, with a distribution of periods, (ii) do all FRBs have the same origin, or are there multiple ways to produce them, (iii) what galactic environments do they inhabit, and how often do they occur across cosmic time, and (iv) do we expect emission at other wavelengths, or multi-messenger signals such as gravitational waves? These are all open questions at the present time. Ideas for the origin of FRBs include magnetar flares (e.g., Margalit and Metzger, 2018), compact object mergers (e.g., Mingarelli et al., 2015; Kundu and Ferrario, 2019), and mechanisms invoking exotic physics. Testing of the magnetar hypothesis has begun, by observing the positions of known GRBs and supernovae, in the expectation that a recently formed magnetar might be actively producing FRBs. See for example Men et al. (2019), who observed the positions of six GRBs which showed an extended X-ray plateau, with the Arecibo and Green Bank radio telescopes. Despite 20 hours on-target, no FRBs were seen. Other studies have focused on the sites of short GRBs (Madison et al., 2019) and type-I superluminous supernovae (Law et al., 2019), again with null results. Efforts to determine the intrinsic FRB rate, and therefore determine the plausibility of different

---

<sup>3</sup><https://frbtheorycat.org>

pathways based on their rates, are underway (Gardenier et al., 2019).

## 1.8 Overview and Scientific Aims of this Thesis

Since the first GRB afterglow and host galaxy detection, over 20 years worth of research has shown that long duration GRBs arise from the core-collapse of massive, rapidly spinning, stripped envelope stars, with a bias to low metallicity environments. Beyond this, however, the nature of their progenitor systems and the reasons for their observed environmental preferences have proven difficult to establish. This thesis aims to further our understanding of the core-collapse GRB phenomena through two complimentary approaches. First is the study of unusual host galaxies which give rise to GRBs. This places limits on the conditions, for example in terms of population age and metallicity, which can give rise to the progenitor systems. Secondly, modelling of the stellar systems and the populations they arise from can inform us about the likelihood of different progenitor models. The dominant theme running through this work is the reconciliation of long GRB host observations with theoretical models of their origins. A full understanding of core-collapse GRBs will require observation and theory to meet in the middle - the aim of this thesis is to help bridge that gap.

The thesis is comprised of four science chapters. The first three are observational, dealing with GRB host galaxies and afterglows. The fourth is a theoretical chapter, which attempts to synthesise the observed long GRB rate using our current best knowledge about the conditions capable of producing GRBs and the physical mechanisms that generate them. I now summarise each science chapter below:

**Chapter 2** identifies and explores the properties of an infrared-bright gamma-ray burst (GRB) host population. Comparing the IR-bright population properties including redshift  $z$ , stellar mass  $M_*$ , star formation rate SFR, and V-band attenuation  $A_V$  to GRB host catalogues in the literature, I show that the infrared-bright population is biased towards low redshift, high stellar mass, and high dust content. This naturally arises from their initial selection - nearby and dusty galaxies are more likely to have the required IR flux to be detected in WISE. I conclude that while IR-bright GRB hosts are not a physically distinct class of GRB host, they are useful for constraining existing GRB host populations, particularly for long GRBs.

**Chapter 3** presents a study of 21 dark gamma-ray burst (GRB) host galaxies, predominantly using X-ray afterglows obtained with the *Chandra X-Ray Observatory* (*CXO*) to precisely locate the burst in deep *HST* imaging of the burst region. I measure magnitudes and perform a morphological analysis of each galaxy.



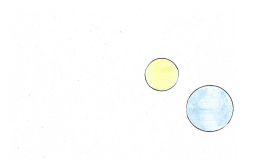
The asymmetry, concentration, and ellipticity of the dark burst hosts are compared against the host galaxies of optically bright GRBs. The distribution of projected spatial offsets for dark GRBs from their host galaxy centroids is comparable to that of optically bright bursts. The dark GRB hosts are physically larger, more massive and redder, but are morphologically similar to the hosts of bright GRBs in terms of concentration and asymmetry. The analysis constrains the fraction of high redshift GRBs in the sample to 14%, implying an upper limit for the whole long-GRB population of  $\lesssim 4\%$ . If dust is the primary cause of afterglow darkening amongst dark GRBs, the measured extinction may require a clumpy dust component in order to explain the observed offset and ellipticity distributions.

**Chapter 4** puts forward the case for GRB 100205A being a largely overlooked high-redshift event. While initially noted as a high- $z$  candidate, GRB 100205A and its host galaxy have not been explored in detail. By combining optical and near-infrared Gemini afterglow imaging (at  $t < 1.3$  d since burst) with deep late-time limits on host emission from the Hubble Space Telescope, I show that the most likely scenario is that GRB 100205A arose in the range  $4 < z < 8$ . GRB 100205A is an example of a burst whose afterglow, even at 1h post burst, could only be identified by 8-m class IR observations, suggesting that such observations of all optically dark bursts may be necessary to significantly enhance the number of high-redshift GRBs known.

**Chapter 5** uses BPASS stellar evolution models to investigate the possibility that some massive stars in binaries can maintain the angular momentum required for jet production, while still losing their outer envelope through winds or binary interactions. Tidal interactions in binaries are accounted for by applying a tidal algorithm to post-process the stellar evolution models output by BPASS. I show that the observed volumetric gamma-ray burst rate evolution can be recreated using two distinct pathways and plausible distributions for burst parameters. In the first pathway, stars are spun up by mass accretion into a quasi-homogeneous state. In the second, tides maintain rotation where otherwise the star would spin down. Both lead to type Ic supernova progenitors, and their combined metallicity distribution is consistent with the GRB host galaxy population. The inferred core angular momentum threshold for jet production is consistent with theoretical requirements for collapsars, given the assumptions made in our model. Several aspects of core collapse supernova/GRB observation and theory are therefore simultaneously reproduced. I discuss the predicted observable properties of GRB progenitors and their surviving companions.

Finally, in **Chapter 6** I conclude the thesis with a summary of the work car-

ried out and its findings, and a discussion of future research possibilities. Throughout this thesis, where required, a standard  $\Lambda$ CDM cosmology is used, with  $h = 0.7$ ,  $\Omega_M = 0.3$  and  $\Omega_\Lambda = 0.7$ . Magnitudes are quoted in the AB system (Oke and Gunn, 1983) unless stated otherwise.



## Chapter 2

# Investigating a population of infrared-bright gamma-ray burst host galaxies

*“The way I see it, every PhD is a pile of good things and bad things. The good things dont always soften the bad things, but vice versa, the bad things dont always spoil the good things and make them unimportant”*— The Doctor, *Vincent and the Doctor*, Doctor Who (adapted by the Author)

In this Chapter, I explore the properties of a population of IR-bright GRB host galaxies, detected in *WISE*. The hosts are localised in X-rays and are selected from all bursts detected between 2005-2016 inclusive. Such galaxies may be nearby, or extremely luminous and dusty. The sample is selected by spatially cross-matching GRBs with IR sources in *WISE*. Observations of a sub-sample of these candidate hosts, including VLT/X-shooter and WHT imaging and spectroscopy, in addition to archival survey data, are used to fit their SEDs. The inferred galaxy properties are then used to ascertain the nature of the IR-bright GRB host population. Throughout this Chapter, short and long bursts are denoted as SGRBs and LGRBs respectively.

### 2.1 Introduction

All-sky infrared surveys, such as the Wide-field Infrared Survey Explorer (*WISE*, Wright et al., 2010), can be used for the purpose of GRB host galaxy identification. Such surveys are shallow, favouring the identification of nearby (Kovács and

Szapudi, 2015) or luminous and dusty galaxies (unusual properties for long GRB hosts). A small number of LGRB hosts have been confirmed at  $z < 0.1$ , which I define as local in this Chapter. These include LGRBs 051109B, 060218, 100316D and 111005A (Perley et al., 2006; Liang et al., 2007; Starling et al., 2011; Michałowski et al., 2018b), while the host of LGRB 080517 was studied by Stanway et al. (2015a) following initial selection through coincidence with a notably bright source in the *WISE* bands. Subsequent follow-up resulted in characterisation of the stellar population and star formation rate in this galaxy through a number of indicators, including radio emission. It also secured the detection of molecular gas for only the third time in a GRB host, constraining the gas consumption timescale (Stanway et al., 2015b).

In general, the benefits of identifying local GRB hosts are threefold. Firstly, proximity makes observation at radio, submillimetre and infrared wavelengths more feasible (e.g., Michałowski et al., 2015). This is exemplified by the recent identification of infrared molecular hydrogen emission lines in low-redshift GRB host galaxies (Wiersema et al., 2018). Secondly, local galaxies will tend to have greater angular extent and thus be easier to spatially resolve for GRB environment studies, which increasingly use Integral Field Unit (IFU) spectrographs (e.g. Christensen et al., 2008; Starling et al., 2011). Finally, a rare class of low-luminosity long GRB (LLGRB) has emerged thanks to their low redshift identification (e.g. Galama et al., 1998; Stanway et al., 2015a). Because the supernovae associated with LLGRBs appear typical of GRB-SNe across the full range of LGRB energies, it seems unlikely that the progenitors of LLGRBs are different to ‘regular’ LGRBs (Schady, 2017). The question then is, what factors can produce the wide range of inferred LGRB isotropic energies, while influencing the range of SN energies much less? Suggestions have included the effect of viewing angle, differences between central engine activity duration versus the shock breakout time, and progenitor metallicity having an impact on burst efficiency (Hjorth, 2013; Fruchter et al., 2006; Schady, 2017). Studies of a large sample of low redshift LGRB hosts will be invaluable in determining the conditions capable of producing LGRBs, including low-luminosity bursts, as well as for studying the evolution of LGRB hosts over cosmic time.

In this Chapter, I aim to determine the nature of the IR-bright GRB host population - are they predominantly nearby or dusty? And are their properties consistent with the established host parameter distributions, or do they appear to be a distinct population? The remainder of the Chapter is structured as follows. Section 2.2 describes the sample and selection criteria used. Section 2.3 details observations of a sub-sample of these candidate hosts, including VLT/X-shooter and WHT imaging and spectroscopy, in addition to ATCA radio observations. Archival and



survey data is compiled in Section 2.4. In Section 2.5, previously studied hosts are identified. SED fitting is performed in Section 2.6. Section 5.5 presents results and discussions, with the broader implications considered in Section 2.8. Conclusions follow in Section 2.9.

## 2.2 Sample Selection

### 2.2.1 Rationale

The *Neil Gehrels Swift observatory* (Gehrels et al., 2004), which has detected the bulk of GRBs since 2005, is mounted with an X-ray telescope (XRT, Burrows et al., 2004), a Gamma-ray Burst Alert Telescope (BAT, Barthelmy et al., 2005) and an Ultraviolet and Optical Telescope (UVOT, Roming et al., 2005), as on-board instruments. UVOT provides the best localisations, however only one third of bursts with an X-ray detection have a UVOT determined position. At the other extreme, all detected GRBs have a BAT detection by definition, however the localisation is no better than a few arcminutes. The best balance between the number of detections and the ability to locate a host is therefore provided by X-rays, for which  $\sim 98$  per cent of bursts have a localisation. I have identified a sample of IR-bright GRB host galaxies by cross-matching X-ray afterglow coordinates with the ALLWISE IR all-sky catalogue from *WISE* (the *Widefield Infrared Survey Explorer*, Wright et al., 2010). This provides aperture matched photometry in four wavebands,  $W1 - 4$ , at 3.4, 4.6, 12 and 22  $\mu m$ . Any cross match procedure between these catalogues will identify both genuine matches and spurious matches to unassociated sources. Because the *WISE* dataset is relatively shallow, nearby or very luminous extragalactic sources are expected, in addition to Galactic stellar contaminants.

### 2.2.2 Initial Cross-Matching and Cuts

Data for GRBs (detected by *Swift*, *INTEGRAL*, *Konus-Wind* and the IPN) in the years 2005-2016 inclusive were downloaded from NASA's GRB catalogue<sup>1</sup>. *Swift* positions were checked against the *Swift* XRT-GRB catalogue<sup>2</sup>. The data include positions in the gamma-ray, X-ray and UV/optical bands, with their associated 90 per cent confidence error radii, in addition to the  $T_{90}$  durations. I do not, at this stage, differentiate between long and short bursts. The total sample contains 1001 bursts, which are used for the following analysis. TOPCAT<sup>3</sup> (Taylor, 2005) was

---

<sup>1</sup>[https://swift.gsfc.nasa.gov/archive/grb\\_table/](https://swift.gsfc.nasa.gov/archive/grb_table/)

<sup>2</sup>[http://www.swift.ac.uk/xrt\\_live\\_cat/](http://www.swift.ac.uk/xrt_live_cat/)

<sup>3</sup><http://www.star.bris.ac.uk/mbt/topcat/>

used to cross-match the X-ray locations with sources in the ALLWISE catalogue. Matching is primarily to the W1 band, i.e. every matched source has at least a W1 detection. No significance cut in W1 was made at this stage, since the quality of the sources are determined through flags and visual inspection, as described later.

An initial cross-matching analysis with a fixed radius is performed for all bursts. In order to determine the expected contamination fraction, I also match to a catalogue of positions created by shifting the 1001 GRB positions by  $\pm 1$  and 2 deg in each of Right Ascension (RA) and Declination (Dec). Because the search radii used are of the order arcseconds, and the X-ray positional uncertainties are also on this scale, shifting by 1 or 2 deg removes all physical correlations and creates a random sample of coordinates. Crucially however, the broad distribution of points in Galactic latitude and hence surface density is preserved. Various trial radii from 1 to 10 arcsec, in steps of 0.5 up to 3 and 1 above, were tested. The difference between the number of matches to actual GRB coordinates ( $N_A$ ), and to the 8008 new pseudo-random coordinates ( $N_R$ , divided by 8 for a fair comparison), is used to estimate a significance through the Poisson cumulative distribution,

$$P(\geq N_A | N_R) = \sum_{i=N_A}^{\infty} e^{-N_R} \times \frac{N_R^i}{i!}, \quad (2.1)$$

where the smallest  $P(\geq N_A | N_R)$  corresponds to the best matching radius (i.e., the greatest relative excess of actual matches). It was found that  $r = 2.5$  arcsec minimises  $P(\geq N_A | N_R)$ . The significance is further improved by employing cuts. This includes the removal of sources contaminated by diffraction spikes, optical ghosts and similar data artefacts, using the ALLWISE contamination and confusion flag (CCF). If one of the W1 or W2 bands is dominated by contaminating flux, the match is rejected, or if both of these bands are contaminated (but not dominated), the match is rejected. Matched sources which do not satisfy these criteria cannot be considered robust or reliable. The random matches include both brighter and fainter objects than the actual matches, therefore the random matches were limited to the same range in apparent magnitude to evaluate the probability of selecting the same population by chance. The cuts effectively act as a signal-to-noise filter, with the lowest W1 SNR after cuts of  $\sim 4.8$ . This gives a maximum centroiding error of  $\sim 0.5$  arcsec (given  $\sigma_{\text{centroid}} = \text{FWHM}/2.35 * \text{SNR}$ ). The X-ray positional uncertainties therefore dominate the cross-matching. A final cut was made by removing objects whose cross-matched counterparts were ambiguous or blended in W1 on visual inspection, but which otherwise satisfied the confusion flag cut. These are SGRB 060801 and LGRB 061007. Image cutouts of these (and all other) burst



locations in the W1 band are given in Appendix A. Given that visual inspection is both time consuming and subjective, this last cut was not applied to the randoms and as such all numerical comparisons between actual and random samples were made before this stage.

With these cuts, and with a 2.5 arcsec matching radius,  $N_A = 45$  matches to actual GRB positions were found, and  $N_R = 23$  to random coordinates. The corresponding Poisson cumulative probability  $P(\geq N_A | N_R)$  is  $\sim 10^{-5}$  (indicating a  $10^{-5}$  probability of counting  $N_A$  matches when  $N_R$  is expected). Using this methodology, I estimate a contaminant fraction  $f_c$  of 0.51, with a Poisson 95 per cent confidence interval covering the region  $0.36 \leq f_c \leq 0.67$ .

### 2.2.3 Consideration of Burst Error Radii and Local Background Densities

In the previous section, I used the same matching radius for all bursts to give an estimate of the contamination fraction. However, this fails to consider two important factors. First, while 2.5 arcsec is the best matching radius when averaging over the GRB sample, individual burst error radii vary and can be larger than this, so genuine matches which lie further out will be missed. Second, because GRBs occur in galaxies, and galaxies tend to exist as members of groups and clusters, the previous analysis considering only the effect of Galactic latitude on chance alignment probability is incomplete. The true chance of random alignment may be greater than suggested by averaging over degree-scales because GRBs should preferentially occur in over-densities (galaxy clusters), which have angular scales much smaller than this. Although there is not yet any direct evidence for GRBs occurring in clusters (Pinter et al., 2019), a methodology using the local source density will still, by definition, provide a more accurate estimate of the false alarm probability than one which averages over large scales.

To address the first issue concerning the tailoring of cross-matching radius to each GRB, I use a radius of  $1.5 \times R_{90}$ .  $R_{90}$  is the radius containing 90% of the spatial probability density, as described by Evans et al. (2009).  $1.5 \times R_{90}$  is approximately the 99 per cent error radius, assuming a Gaussian profile for the X-ray positional probability function. From 1001 GRBs, this yields 60 GRBs with one IR match and 4 with two or more, for a total of 64. Some *WISE* sources are included in this count, and not in the 45 discussed previously, because their associated GRB has  $1.5R_{90} > 2.5$  arcsec and a match at  $r > 2.5$  arcsec. Others are *not* included because the matched radius from the previous analysis is greater than  $1.5R_{90}$ . These are GRBs 050716, 060428B, 070208, 120119A, 120612A and 161108A. I add these 6

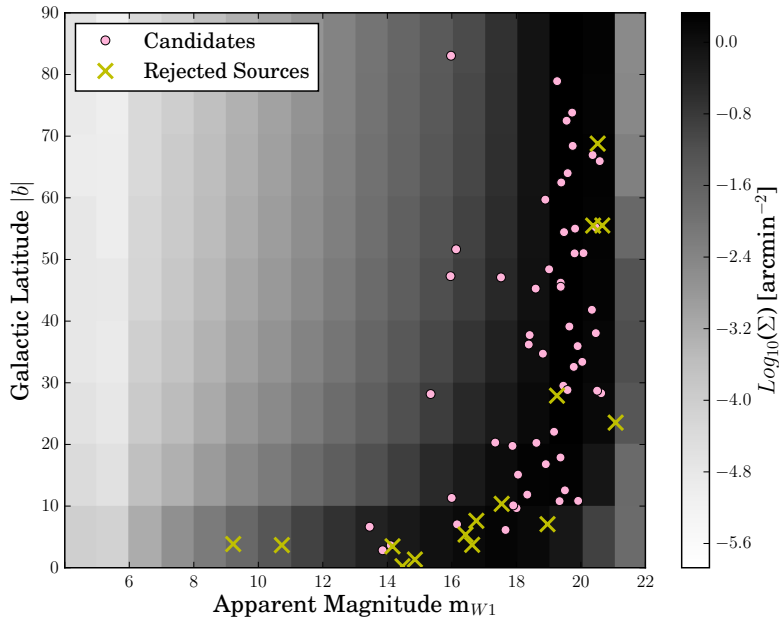


Figure 2.1: The projected surface density  $\Sigma$  of sources in the W1 band as a function of Galactic latitude  $|b|$  and  $m_{W1}$ . The latitudes and magnitudes of the 55 final candidates described in Section 2.2.4 are indicated by dots, and the rejected sources by crosses.

bursts back into the sample for a grand total, before quality cuts, of 70 - a *small* X-ray uncertainty is not used at this stage to reject an otherwise good match, because the source of the IR flux could plausibly be extended.

In order to estimate the chance that each association is genuine, I perform a false alarm probability (FAP) analysis. The surface density of sources in the entire ALLWISE catalogue is visualised in Figure 2.1, as a function of Galactic latitude and W1 magnitude. The matched bursts are indicated. Clearly the apparent magnitude and Galactic latitude both affect the probability that a match is spurious. However, sky object density also varies on small scales, in addition to the broad Galactic latitude trend. To sample the local surface density  $\Sigma$  around each burst, I cross-match the X-ray coordinates for each burst against ALLWISE with a 3 arcmin radius. Given that galaxy clusters have typical sizes of  $\sim 10$  Mpc, a 6 arcmin diameter is a small enough angular scale to sample density variation due to clustering and cosmic variance. This is demonstrated in Figure 2.2, which relates redshift to angular extent  $\theta$  for physical scales  $d$  of 2, 6 and 10 Mpc, through  $\theta = \frac{d}{D_A}$ , where  $D_A$  is the angular diameter distance.

For the region around each burst, the local density of sources of magnitude



Table 2.1: The 55 GRB X-ray positions for which a catalogued *WISE* source is identified within  $1.5R_{90}$  of the X-ray error circle centroid, and is not rejected based on FAP, CCF or blend cuts. Candidate classification is given in the final column, and is discussed throughout this Chapter in the appropriate sections. SGRB 050724 is a disguised short burst, despite the long  $T_{90}$ .

GRB	$T_{90}$ [s]	Short/ Long	X-ray Ra [deg]	X-ray Dec [deg]	$R_{90}$ [arcsec]	<i>WISE</i> Ra [deg]	<i>WISE</i> Dec [deg]	Sep [arcsec]	FAP	Type
050219A	23.7	L	166.4124	-40.6842	1.9	166.4128	-40.6847	2.13	0.013183	NC/LG
050318	32	L	49.7129	-46.3961	1.4	49.7129	-46.3961	0.02	0.000002	NC
050522	10.8	L	200.1458	24.7883	6	200.1440	24.7869	8.06	0.002003	s
050716	69.1	L	338.5866	38.6843	1.4	338.5866	38.6850	2.42	0.014346	ND/s
050721	98.4	L	253.4356	-28.3811	1.7	253.4352	-28.3814	1.90	0.018820	s
050724	96	S	246.1847	-27.5409	1.5	246.1849	-27.5407	0.89	0.002065	G
060428B	57.9	L	235.3570	62.0248	1.4	235.3583	62.0249	2.26	0.002668	CA
061002	17.6	L	220.3480	48.7414	2.6	220.3478	48.7413	0.65	0.000302	PG
070208	47.7	L	197.8859	61.9651	1.5	197.8866	61.9656	2.37	0.011924	PG/CA
070309	~40	L	263.6658	-37.9307	4.4	263.6647	-37.9306	3.33	0.026938	NC
070429B	0.47	S	328.0159	-38.8283	2.4	328.0156	-38.8286	1.40	0.011835	NC/LG
070724A	0.4	S	27.8085	-18.5944	1.7	27.8088	-18.5944	1.02	0.001910	G
071117	6.6	L	335.0439	-63.4433	1.5	335.0444	-63.4428	2.09	0.008035	NC
080207	340	L	207.5122	7.5022	1.4	207.5124	7.5018	1.55	0.008959	ND/LG
080307	125.9	L	136.6287	35.1388	1.4	136.6290	35.1392	1.98	0.011835	ND/CA
080405	40	L	162.5996	-4.2888	2.5	162.5988	-4.2888	2.71	0.001357	s
080517	64.6	L	102.2420	50.7352	1.6	102.2415	50.7353	1.06	0.000455	G
080605	20	L	262.1252	4.0157	1.5	262.1254	4.0156	0.60	0.000889	ND/LG
080623	15.2	L	237.6610	-62.0491	1.4	237.6616	-62.0487	1.56	0.012242	NC
090904B	47	L	264.1855	-25.2132	1.4	264.1854	-25.2129	1.11	0.005129	s
091102	6.6	L	72.6155	-72.5197	2	72.6149	-72.5199	1.01	0.003337	NC
100206A	0.12	S	47.1626	13.1570	3.3	47.1631	13.1581	4.15	0.010560	G
100316D $\geq$ 1300		L	107.6276	-56.2555	3.7	107.6255	-56.2562	4.96	0.030711	NC/LG
100816A	2.9	L?	351.7399	26.5784	1.4	351.7395	26.5780	1.97	0.009327	ND/LG
110206A	~20	L	92.3343	-58.8069	1.9	92.3331	-58.8067	2.24	0.024210	NC
110305A	12	L	260.8806	-15.8025	1.7	260.8810	-15.8030	2.22	0.006510	Ps
110918A	~22	L	32.5387	-27.1061	1.5	32.5386	-27.1057	1.24	0.003484	ND/LG
111222A	~1	S	179.2197	69.0709	2.9	179.2208	69.0704	2.40	0.000177	s
120119A	253.8	L	120.0288	-9.0817	1.4	120.0291	-9.0824	2.49	0.021870	Ps
120224A	8.13	L	40.9422	-17.7613	1.4	40.9424	-17.7617	1.76	0.003069	ND/g
120612A	90	L	126.7217	-17.5748	1.5	126.7212	-17.5743	2.41	0.009252	s
120819A	71	L	235.9075	-7.3091	1.7	235.9076	-7.3093	0.92	0.002322	ND
130515A	0.29	S	283.4401	-54.2791	2.4	283.4385	-54.2792	3.44	0.040879	NC/s
130527A	44	L	309.2763	-24.7250	1.4	309.2761	-24.7247	1.31	0.005843	ND/g
130528A	59.4	L	139.5051	87.3012	1.9	139.4988	87.3015	1.48	0.008832	ND/LG/CA
130603B	0.18	S	172.2006	17.0714	1.4	172.2012	17.0714	1.85	0.006614	G
130725A	101.8	L	230.0324	0.6276	1.8	230.0318	0.6276	2.09	0.007389	ND
130907A	>360	L	215.8922	45.6073	1.4	215.8921	45.6070	0.78	0.000969	PG
131018B	~38	L	304.5369	23.1876	4.9	304.5361	23.1876	2.84	0.009425	Ps
131122A	~70	L	152.5422	57.7277	4.8	152.5440	57.7292	6.50	0.044608	PG
140331A	209	L	134.8644	2.7173	1.7	134.8650	2.7175	2.05	0.007334	G
140927A	6.26	L	291.7916	-65.3936	1.8	291.7922	-65.3932	1.64	0.000745	Ps
141212A	0.3	S	39.1248	18.1470	2.6	39.1254	18.1468	2.23	0.018170	G
150101B	0.018	S	188.0205	-10.9336	1.8	188.0207	-10.9335	0.67	0.000070	G
150120A	1.2	S	10.3189	33.9949	1.8	10.3193	33.9952	1.49	0.003069	PG
150323C	159.4	L	192.6169	50.1912	1.6	192.6162	50.1909	1.93	0.010869	ND/g
150626A	144	L	111.3368	-37.7808	1.8	111.3370	-37.7813	1.97	0.005876	NC
151111A	76.93	L	56.8448	-44.1615	1.5	56.8447	-44.1619	1.53	0.004170	NC
160703A	44.4	L	287.4168	36.9175	3.9	287.4164	36.9174	1.16	0.005082	Ps
161001A	2.6	L?	71.9200	-57.2608	1.4	71.9195	-57.2604	1.69	0.007076	NC
161007A	201.7	L	103.4090	23.3068	1.5	103.4087	23.3064	1.65	0.011553	ND/g
161010A	~30	L	275.2143	-28.7852	2.9	275.2144	-28.7862	3.68	0.017848	s
161104A	0.1	S	77.8937	-51.4601	3	77.8941	-51.4613	4.47	0.024994	NC
161108A	105.1	L	180.7879	24.8682	1.5	180.7885	24.8678	2.44	0.006978	PG
161214B	24.8	L	3.8512	7.3524	1.5	3.8510	7.3524	0.73	0.000854	s

s - star. Ps - photometric star. G - galaxy. PG - photometric galaxy. NC - no coverage. ND - optical non-detection. LG - identified as an IR-bright host galaxy by comparison to the published literature. CA - rejected due to possible or confirmed chance alignment.

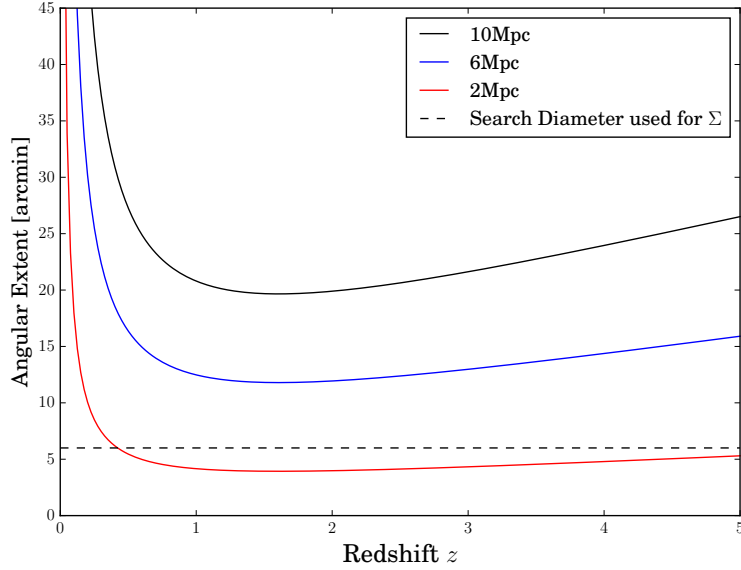
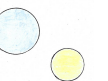


Figure 2.2: The apparent angular extent of physical scales as a function of redshift, using the angular diameter distance. The chosen scale for calculating surface densities is sufficient to capture local variations, for all but the smallest cluster sizes at moderate redshift.

Table 2.2: The 15 GRB X-ray positions which match to at least one *WISE* source within  $1.5R_{90}$ , but which have these matches rejected due to FAP, CCF or *WISE* blending cuts.

GRB	$T_{90}$ [s]	Short/ Long	X-ray Ra [deg]	X-ray Dec [deg]	$R_{90}$ [arcsec]	<i>WISE</i> Ra [deg]	<i>WISE</i> Dec [deg]	Sep [arcsec]	FAP	Type
050117	166.6	L	358.4708	65.9389	15	358.4747	65.9404	7.78	0.787461	FR
050306	158.3	L	282.3088	-9.1531	6	282.3101	-9.1545	6.87	0.004357	CC
060223B	10.3	L	254.2450	-30.8128	10	254.2454	-30.8141	4.94	0.197244	FR
060502B0.131		S	278.9385	52.6315	15	278.9413	52.6328	7.70	0.275397	FR
060801	0.49	S	213.0055	16.9818	1.5	213.0059	16.9818	1.40	0.007557	WB
061007	75.3	L	46.3317	-50.5007	1.4	46.3318	-50.5007	0.23	0.000191	WB
071001	58.5	L	149.7336	-59.7818	6	149.7353	-59.7822	3.44	0.004577	CC
071109	~30	L	289.9746	2.0465	9	289.9747	2.0463	0.96	0.022986	CC
080212	123	L	231.1474	-22.7417	1.4	231.1469	-22.7415	1.68	0.007351	CC
100909A	~70	L	73.9473	54.6594	5.4	73.9510	54.6594	7.75	0.161417	CC
120419A	~20	L	187.3876	-63.0079	4.5	187.3876	-63.0095	5.62	0.075810	CC
120811A	166	L	257.1654	-22.7106	2.8	257.1658	-22.7114	3.31	0.047855	WB
140103A	17.3	L	232.0875	37.7592	3.6	232.0876	37.7577	5.31	0.127637	FR
150301A	0.48	S	244.3047	-48.7131	5	244.3019	-48.7136	6.81	0.188791	FR
151004A128.4		L	213.6322	-64.9391	7	213.6343	-64.9369	8.58	0.091087	FR

CC - flagged as confused in *WISE*. WB - flagged as a blend in W1 band. FR - Rejected due to  $FAP > 0.05$



equal to the *WISE* match or brighter is given by,

$$\Sigma(m \leq m_g) = \frac{N(m \leq m_g)}{\pi r_3^2}, \quad (2.2)$$

where  $N(N_{m \leq m_g})$  is the number of sources within 3 arcmin of the burst of W1 magnitude  $m_g$  or brighter, and  $r_3 = 3$  arcmin. The probability of a match at angular distance  $r$  being genuine and not a false alarm can be written as,

$$P_{\text{chance}} = e^{-\Sigma(m \leq m_g)\pi r^2}, \quad (2.3)$$

which tends to 1 as  $r$  tends to 0, and tends to 0 as  $r$  tends to  $\infty$ , as required. Using this method, the false alarm probability (FAP) is given by  $1 - P_{\text{chance}}$  (Bloom et al., 2002). The CCF flag cuts from Section 2.2.2 are again used. After these are made, a cut of  $\text{FAP} < 0.05$  is chosen. This cut, when applied to the matching of random positions to ALLWISE, yields a theoretical maximum of 50 matches by chance. However, the distribution continues well below 0.05. The average FAP is therefore is much lower, and the number of false matches will also be lower. This is backed up by the addition of only 7 matches when going from a FAP cut of 0.025 to 0.05. Included in these 7 is LGRB 100316D, which has a previously noted  $z=0.059$  host galaxy. Using a FAP cut of 0.05 allows us to catch hosts which have larger projected sizes, such as that of LGRB 100316D. In addition, it allows us to identify the hosts of bursts with large X-ray uncertainties, provided the field is not crowded and the *WISE* source is sufficiently bright.

As in Section 2.2.2, SGRB 060801 and LGRB 061007 are removed due to possible blending in *WISE*, in addition to LGRB 120811A. Three GRBs with more than one IR match (GRBs 060223B, 071007 and 071109) had all of their candidates rejected due to CCF or FAP cuts. The fourth example with more than one match, LGRB 050117, lies in the galactic plane ( $|b| = 3$ ) and has two matches almost equidistant at  $\sim 7$  arcsec, with similar false alarm probabilities. The IR source most likely to be associated could not be distinguished, and the line of sight extinction meant there was no optical afterglow reported for this burst, precluding a improved localisation. Therefore, LGRB 050117 was rejected. This leaves a final sample of 55 bursts, each with one matched *WISE* source. This differs from the sample derived in Section 2.2.2, in that ten extra bursts are included: LGRB 050522, LGRB 070309, LGRB 080405, SGRB 100206A, LGRB 100316D, LGRB 130118B, SGRB 130515A, LGRB 131122A, LGRB 161010A and SGRB 161104A.

## 2.2.4 Sample summary so far

The final sample includes candidate host galaxies for 55 GRBs. These are listed in Table 2.1, with the candidates rejected for CCF flags, *WISE* blending and high false alarm probabilities given in Table 2.2. The tables give the X-Ray coordinates, *WISE* coordinates,  $T_{90}$  estimates, the 90 per cent confidence interval on the X-ray position, the X-ray-*WISE* separation and a false alarm probability for association with the *WISE* source. Given the analysis in Section 2.2.2, it is likely that around a third to two-thirds of the associations are spurious. However, some will be Galactic stars, and others may be galaxies with properties inconsistent with being a GRB host. These contaminants can be identified as such through their photometric and spectroscopic properties, as well as through better burst localisation. Observations and archival searches for these observations are thus the next objective of this analysis.

## 2.3 Observations

In order to investigate the true hosts and determine which matches are spurious, subsets of the sample were observed with WHT/ACAM (programme WHT/2015A/34, PI: Stanway - these data were obtained by Elizabeth Stanway, Charlotte Angus and Stephanie Greis), VLT/X-shooter (programme 096.D-0260(A), PI: Stanway) and ATCA (programme C3002, PI: Stanway). None of these data were obtained by the Author, and all observations were made in 2015. 7 targets were observed with ACAM/WHT, 5 with VLT/X-shooter and 14 with ATCA.

### 2.3.1 WHT Imaging

Observations of 7 candidate hosts were taken over two nights (2015 January 19 and 20) with the auxiliary-port camera (ACAM) on the William Herschel Telescope (WHT). These were associated with programme WHT/2015A/34 (PI: Stanway). Both nights were severely affected by poor observing conditions. The object associated with SGRB 111222A was observed on 2015 January 19, however observations were hampered by clouds and wind gusts in excess of  $70 \text{ km h}^{-1}$ . The objects associated with LGRB 100816A, SGRB 141212A, LGRB 140331A, LGRB 070208, LGRB 061002 and LGRB 080307 were observed on 2015 January 20. Conditions were clearer but still windy, with poor seeing ( $\sim 2$  arcsec). Sloan  $g$ ,  $r$ ,  $i$  and  $z$  filters were used. The images were reduced with standard IRAF procedures and aperture photometry performed on the candidate hosts. Aperture sizes were chosen to be 2 times the seeing FWHM, as measured in the band the band with the largest FWHM.



Table 2.3: WHT/ACAM observations, taken on 2015 Jan 19/20. If a magnitude uncertainty is not given, the value corresponds to the  $2\sigma$  limit at the position of the *WISE* source.

Target	Filter	Int. [s]	Mag(AB)	$2\sigma$ depth	Seeing [arcsec]
061002	g	573	$22.27 \pm 0.06$	24.6	1.86
	r	573	$21.84 \pm 0.05$	23.9	1.82
	i	572	$21.09 \pm 0.05$	23.8	1.88
	z	573	$20.45 \pm 0.07$	22.0	1.88
070208	g	573	$19.81 \pm 0.01$	24.9	1.80
	r	730	$19.46 \pm 0.01$	24.1	2.25
	i	573	$19.25 \pm 0.02$	22.8	1.75
	z	573	$19.13 \pm 0.03$	20.8	1.66
080307	g	897	$24.1 \pm 0.2$	24.6	1.78
	r	1653	$23.0 \pm 0.1$	24.3	1.90
	i	213	$> 22.8$	23.4	1.78
	z	731	$> 23.9$	22.4	2.32
100816A	g	573	$> 24.1$	24.0	2.52
	r	693	$22.6 \pm 0.1$	23.6	1.67
	i	514	$> 21.3$	21.8	1.49
111222A	g	261	$19.11 \pm 0.02$	22.5	2.46
	r	81	$18.14 \pm 0.03$	20.8	1.65
	i	81	$16.64 \pm 0.01$	20.5	1.73
	z	180	$15.89 \pm 0.02$	22.2	1.79
140331A	g	491	$> 25.0$	24.6	2.74
	r	933	$22.59 \pm 0.09$	23.9	2.38
	i	573	$> 20.0$	21.1	2.67
	z	371	$20.80 \pm 0.06$	22.4	2.31
141212A	r	573	$22.8 \pm 0.1$	23.3	2.08
	i	573	$22.7 \pm 0.2$	23.0	2.38
	z	573	$> 21.9$	22.4	1.46

Table 2.4: Details of the VLT/X-shooter and WHT/ACAM spectroscopic observations.

Target	Obsv.	Date	Int.UV [s]	Int.Vis [s]	Int.IR [s]	Seeing [arcsec]
111222A	WHT	2015 Jan 19	1260	1260	-	1.91
140331A	WHT	2015 Jan 20	1255	1255	-	2.53
091102	VLT	2015 Dec 07	1800	2220	2160	< 0.8
091102	VLT	2015 Dec 07	1800	2220	2160	< 0.8
120224A	VLT	2015 Dec 13	1800	2220	2160	< 0.8
120224A	VLT	2015 Dec 14	1800	2220	2160	< 0.8
120612A	VLT	2015 Dec 13	1800	2220	2160	< 0.8
120612A	VLT	2015 Dec 14	1800	2220	2160	< 0.8
140331A	VLT	2015 Dec 14	1788	2190	2664	< 0.8
140331A	VLT	2016 Jan 07	1788	2190	2664	< 0.8
141212A	VLT	2015 Dec 08	1788	2190	2664	< 0.8
141212A	VLT	2015 Dec 15	1788	2190	2664	< 0.8

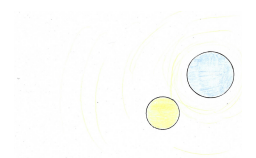
This size aperture was then used for all bands for a given object, if the target was a point source. Otherwise 2 times the FWHM of the object of interest (again in the largest band) was used. Details of the observations and measured quantities are listed in Table 2.3, along with  $2\sigma$  depths and the seeing. The quoted magnitudes are in broad agreement with archival data where available.

### 2.3.2 WHT Spectroscopy

Also as part of programme WHT/2015A/34, the candidate hosts of SGRB 111222A and LGRB 140331A were observed on 2015 January 19 and 20 respectively, using the V400 grism and a 1.5 arcsec slit on ACAM. The position of the slit with respect to the 90 per cent XRT error circle and *WISE* source are shown in Figure 2.3, overlaid on *r*-band images. Given the poor seeing, slit losses were significant. The observations are listed in Table 2.4. The LGRB 140331A candidate counterpart was not detected. The SGRB 111222A IR counterpart is identified as an M dwarf, as shown in Figure 2.4.

### 2.3.3 VLT Spectroscopy

Five GRB host candidates were observed using the echelle spectrograph on VLT/X-shooter (Vernet et al., 2011). Observations were associated with programme 096.D-0260(A) (PI: Stanway) and are detailed in Table 2.4. Images in the *r*-band and the position of the slit with respect to the XRT and *WISE* positions are also shown



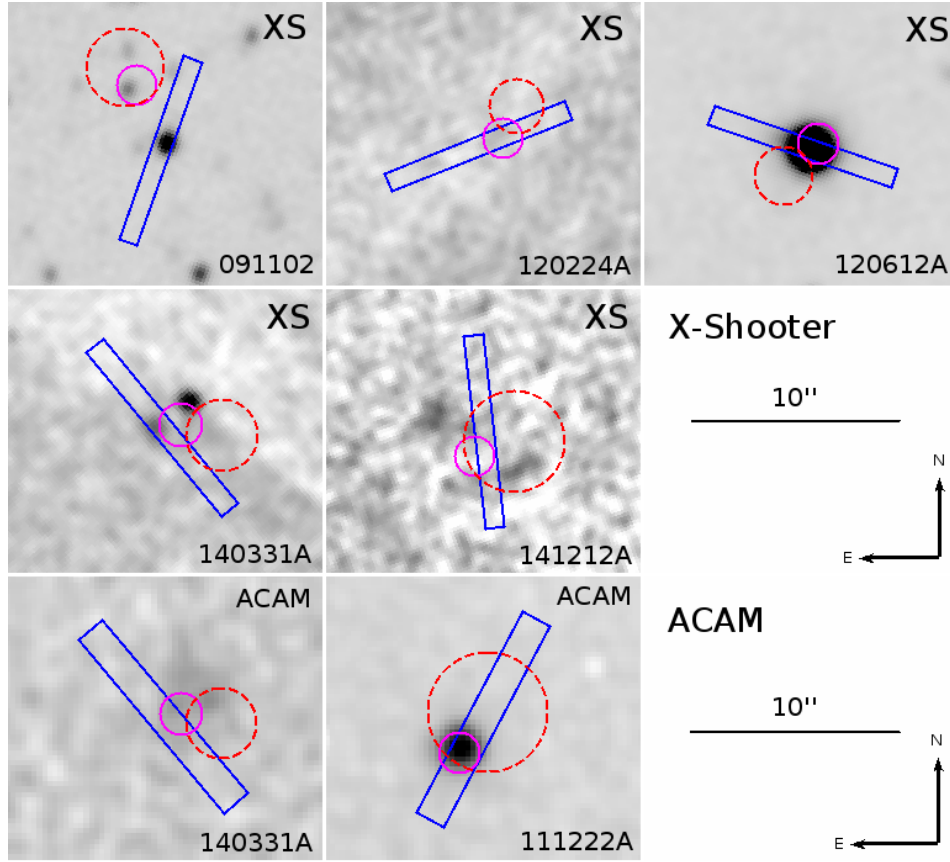


Figure 2.3: Slit positions for the VLT/X-shooter and WHT/ACAM spectroscopic observations, with the enhanced 90 per cent X-ray error radii overlaid in red. Blue rectangles represent the slit positions. Solid magenta circles indicate the centroid of the *WISE* sources. All images are in the *r*-band, and are stretched and smoothed with a Gaussian kernel of radius 3 pixels.

in Figure 2.3. The XS images are used primarily for visualising the slit placement. The  $2\sigma$  depths of the XS images corresponding to GRBs 091102, 120224A, 120612A, 140331A and 141212A are 23.5, 22.6, 24.1, 22.9 and 21.7 respectively. In each case, the slit placement was chosen to overlap with the *WISE* source.

The images and spectra were reduced using the standard ESO pipeline in GASGANO. Of the five targets, two were marginally detected (LGRBs 120224A and 140331A), one was detected with prominent emission lines (SGRB 141212A), and two were found to be foreground stars (LGRBs 091102 and 120612A). The two stellar spectra are shown in figures 2.5 and 2.6 respectively. Note that the service-mode observations of the counterpart of LGRB 091102 were misaligned, likely due to the misidentification of a selected offset and alignment star. Thus the spectroscopic

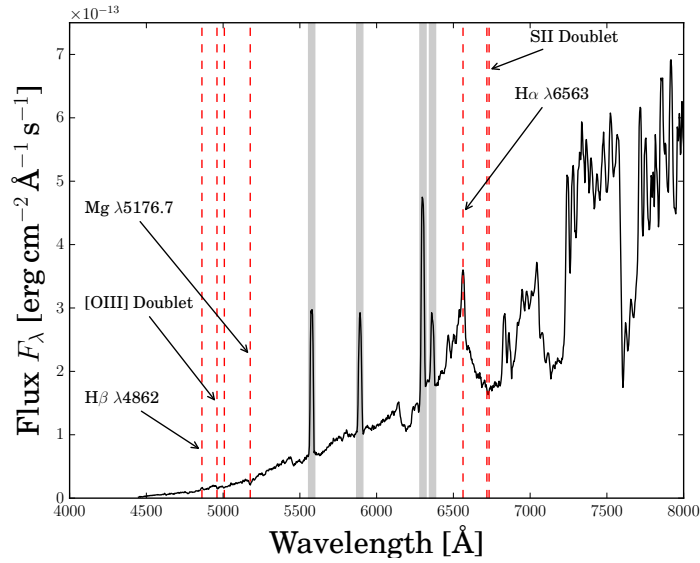


Figure 2.4: The WHT optical spectrum of the object associated with SGRB 111222A. The spectral shape and presence of absorption and emission lines at redshift  $\sim 0$  indicate that this is an M-star. OI, O<sub>2</sub> and NaD sky features are masked out.

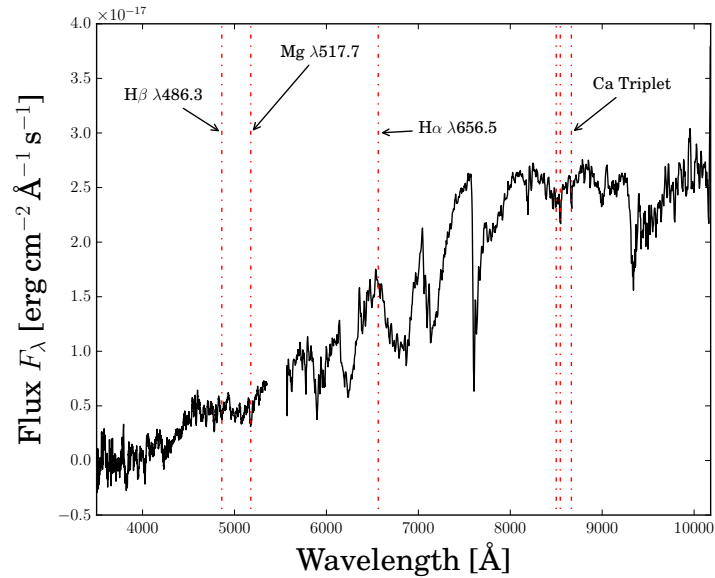
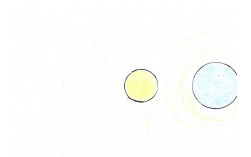


Figure 2.5: The VLT/X-shooter spectrum of the object associated with LGRB 091102 target. H $\beta$ , Mg, H $\alpha$  and Ca absorption lines at negligible redshift confirm that this is an M-star. However, the slit was misaligned with the IR source, so I do not consider this identification any further.



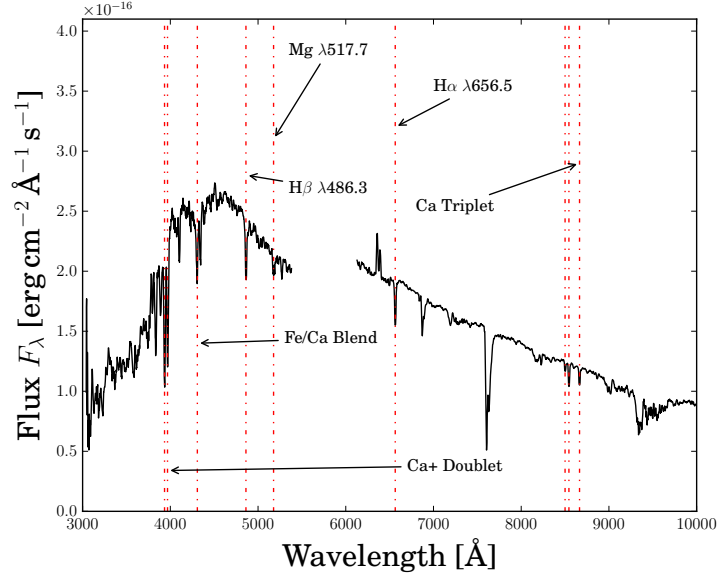


Figure 2.6: The VLT/X-shooter optical spectrum of the LGRB 120612A target.  $H\beta$ ,  $H\alpha$  and various metal absorption lines at  $z \approx 0$  indicate that this is a foreground K-star.

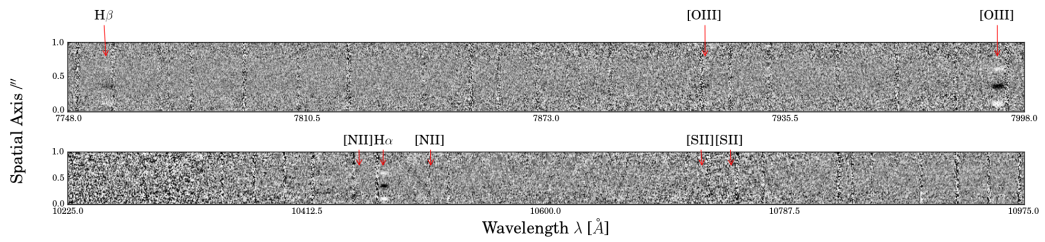


Figure 2.7: Emission lines from the host galaxy of SGRB 141212A. The upper nodded spectrum is from X-shooter's VIS arm, the lower from the NIR arm. The marked wavelengths correspond to, in order of increasing wavelength,  $H\beta$  and  $[OIII]$  on the VIS arm and  $[NII]$ ,  $H\alpha$ ,  $[NII]$  and the  $[SII]$  doublet in the NIR. The observed lines indicate a redshift of  $0.596 \pm 0.001$ .

identification of this as a star is irrelevant to the GRB and is presented here to avoid confusion in future studies of archival data for these observations. This is the only case where I am required to attempt photometry on the XS imaging, measuring an  $r$ -band magnitude of the faint *WISE* aligned source of  $\sim 21.4$  (anchored to the APOP magnitude for the nearby bright star, Qi et al., 2015). However, it is not detected in the other bands available,  $u$  and  $z$ . Combined with GALEX and 2MASS non-detections, there is insufficient data for fitting the SED of this object. It is classified as having no coverage in Table 2.1.

The spectra of the LGRB 120224A and 140331A targets are featureless, with only marginally detected continuum flux and no readily identifiable absorption or emission lines. LGRB 120224A’s candidate host has also been observed with X-shooter in a different programme, with similar results (Wiersema et al., 2012). If these are indeed the LGRB host galaxies, this requires them either to be mature stellar systems without nebular emission, or else heavily dust enshrouded. It should be noted that the WCS of the X-shooter images are misaligned with ALLWISE and the X-ray positions, leading to small offsets from their true positions. For example, the slit for LGRB 140331A has been deliberately placed over the fainter object south-east of the error circle, because the centroid of the IR flux aligns with it, suggesting that it corresponds to the source of the IR emission. While the other, brighter object *might* be the true host, it is likely not IR-bright, and would therefore be out of place in the sample.

The potential host of SGRB 141212A has a weak continuum with  $H\alpha$ ,  $H\beta$  and  $O\text{ III}$  emission lines. The wavelength of these correspond to a redshift of  $0.596 \pm 0.001$ . This is in agreement with Chornock et al. (2014a), who observed an object within the enhanced XRT error circle one day post burst with the Gemini-N spectrograph. They found that, out of two objects near the error circle, the likely host has a redshift  $z=0.596$ . Portions of the 2D spectrum covering key emission lines are shown in Figure 2.7. Emission line measurements are listed in Table 2.5. Owing to the low signal-to-noise ratio, meaningful constraints on the  $H\alpha/H\beta$  ratio are not possible. Note however that the presence of these lines is in qualitative agreement with the star-forming best-fitting SED as discussed later in Section 2.6.

### 2.3.4 ATCA Radio Observations

The radio observations and data reductions discussed here were performed by Elizabeth Stanway. Radio observations of 14 candidate hosts were made at central frequencies of 5.5 GHz and 9.0 GHz and a bandwidth of 2 GHz per frequency, with the Australia Telescope Compact Array (ATCA). Science targets and secondary

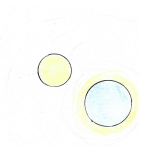


Table 2.5: Emission line measurements from the galaxy associated with SGRB 141212A.

Line	$\lambda$ [Å]	Flux [ $10^{-14}$ ergs cm $^{-2}$ s $^{-1}$ ]
H $\beta$	7759 $\pm$ 4	0.53 $\pm$ 0.47
[OIII]	7991 $\pm$ 3	1.8 $\pm$ 0.8
H $\alpha$	10474 $\pm$ 5	2.0 $\pm$ 0.9

Table 2.6: Observations and upper limits on the radio emission of the 14 ATCA targets.

GRB	z	Beam FWHM [arcsec]	Image RMS [ $\mu$ Jy]	$3\sigma$ SFR Limit [ $M_{\odot}$ yr $^{-1}$ ]
050219A	0.212	9.7 $\times$ 1.5	10.5	<10
050318	1.44	5.2 $\times$ 1.9	10.2	<990
070429B	0.902	8.9 $\times$ 1.9	9.6	<290
070724A	0.457	13 $\times$ 1.8	10.7	<62
071117	1.33	6.4 $\times$ 1.5	12.9	<1020
080623	–	5.5 $\times$ 1.8	13.3	-
080702B	2.09	51 $\times$ 1.6	17.2	<4100
091102	–	4.0 $\times$ 1.8	10.3	-
110206A	–	3.4 $\times$ 2.1	11.5	-
110918A	0.984	12 $\times$ 1.9	12.9	<480
120119A	1.73	34 $\times$ 1.8	10.0	<1500
120224A	–	17 $\times$ 1.8	9.0	-
120612A	–	18 $\times$ 1.7	11.1	-
120819A	–	42 $\times$ 1.7	10.8	-

phase calibrators were observed during programme C3002 (PI: Stanway). Observations were taken on 2015 January 31 and 2015 February 1 and 2. The array was in its most extended, 6A, configuration with a maximum baseline of 6km and six antennae in use. Short observations were taken across a range of hour angles to secure reasonable  $uv$ -plane coverage. The data were reduced with the standard data reduction software MIRIAD. Absolute flux calibration was performed using observations of PKS 1934-638.

None of the targets were detected. The observations are listed in Table 2.6. The synthesised beam size, which varied significantly from source to source given their wide range of declinations, and the final image RMS noise level, are also listed. Where a redshift for the source is known, the 1.4 GHz flux to star formation rate (SFR) calibration of Kennicutt and Evans (2012) is used to estimate a  $3\sigma$  upper limit on the star formation rate (assuming a radio spectral slope of -1).

## 2.4 Archival and Survey Data

Additional information for the candidate GRB host counterparts was gathered from archival surveys and the literature. The main source of optical photometry is the Pan-STARRS survey (DR1, Cucchiara et al., 2011), which covers the whole sky north of  $-30^\circ$  declination down to  $3\sigma$  depths of  $g, r, i, z, y < 23.3, 23.2, 23.1, 22.3, 21.3$ . Cross-matching between the Pan-STARRS 1 science archive and the 55 *WISE* counterparts was performed with a 2.5 arcsec matching radius, producing 27 matches. Of these, a small subset have more than one possible optical counterpart, and these are carefully considered in Section 2.6.1. The candidate hosts for SGRB 141212A are visible in Pan-STARRS but below the cataloguing threshold, so I measured the magnitudes from image cutouts, complementing the WHT photometry presented in Section 2.3.1. The Sloan Digital Sky Survey (SDSS, Alam et al., 2015, DR12 is used), VST/ATLAS (Shanks et al., 2015) and APASS (Henden and Munari, 2014) were also searched by matching to within 2.5 arcsec of the *WISE* source. All of these surveys extend south of  $-30^\circ$  declination. Two GRB locations have matches in VST/ATLAS, SGRBs 070724A and 150101B, which are also covered by Pan-STARRS, and only one in APASS (LGRB 140927A). There are 12 matches in SDSS, which provides the only optical photometry for LGRB 161108A. In the remaining 11 matched cases, Pan-STARRS data also exists, and I use the best available combination of photometry. At the very least,  $u$  band limits are used from the SDSS matches. There are a total of 29 optical survey detections.

The remaining 26 positions may fail to obtain a match because the source



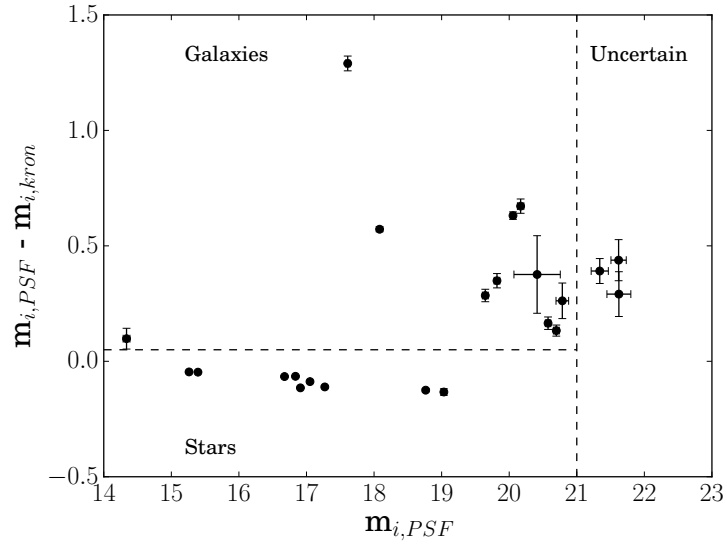


Figure 2.8: Star-galaxy separation for sources which have an  $i$ -band PSF and Kron magnitude. Faint sources cannot be reliably separated.

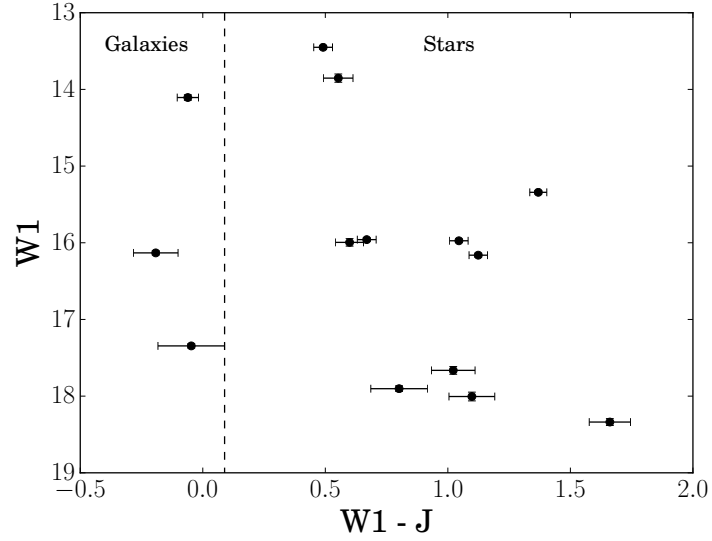


Figure 2.9: Star-galaxy separation for sources which have a W1 and  $J$ -band magnitude. The  $J$  magnitudes dominate the uncertainty here.

lies outside the Pan-STARRS survey region (14 objects), or because the galaxy is optically faint (12 instances). Where a GRB falls in a field covered by one of the surveys used, but no object is detected at that position,  $2\sigma$  upper limits are used. Four host candidates lacking coverage have been studied in the literature (GRBs 050219A, 070429B, 100316D and 130515A), so 10 are classified ‘NC’ (no coverage) in Table 2.1.

A total of 6 of the 12 optically undetected sources have been well studied in the literature. In these cases I use the results of those works. The total number of *WISE* sources for which survey coverage is available, but information on an optical counterpart is lacking, is therefore 6. The 12 undetected sources are discussed further in sections 2.5 and 2.7.

The *GALEX* All Sky Imaging Survey (AIS, Martin and *GALEX* Science Team, 2005) provides UV photometry or limits for all objects at near-constant depth (Martin et al., 2003). *GALEX* has two photometric bands, the Far and Near UV (FUV and NUV), with effective wavelengths of 1528Å and 2271Å respectively. Ten of the sample have a NUV source within 5.3 arcsec, the NUV PSF FWHM. Expanding the search radius to 10 arcsec yields only one more match (at 9 arcsec), suggesting that those matches identified are genuine. Of these, four (LGRB 080405, LGRB 080517, LGRB 100316D and SGRB 150101B) also have a FUV detection. Where there is no detection, I use the AIS mean  $2\sigma$  upper limits,  $m_{\text{FUV}} = 20.89$  and  $m_{\text{NUV}} = 21.79$ .

The 2 Micron All Sky Survey (2MASS) was used to provide NIR data or limits for the sample (Skrutskie et al., 2006). A catalogued 2MASS source was identified for 14 of the 55 *WISE* matches. Image cutouts for all the GRB positions were also inspected, and I measure *JHK*  $2\sigma$  upper limits for the remainder of the sample. I searched the FIRST (Becker et al., 1994) and NRAO VLA Sky Survey (NVSS, Condon et al., 1998) radio surveys, cross-matching to the *WISE* coordinates, finding only one match. The host of SGRB 150101B is detected in NVSS at 1.4 GHz. The full Table of FUV to W4 photometry derived from this compilation of observations and archival data is given in Table A.1 of Appendix A.

Initial checks were performed with the available data to discern the physical nature of the sources. The first method employed uses the difference between PSF and Kron magnitudes (Farrow et al., 2014, and references therein), which is a recommended technique for star-galaxy separation in Pan-STARRS. Because the Kron radii vary with the light distribution of the object in question, and the PSF does not, extended sources such as galaxies (or saturated stars) show discrepancies between the two magnitudes. A plot showing star-galaxy separations using this



method is given in Figure 2.8. Beyond an  $i$ -band apparent magnitude of  $\sim 21$ , the separation becomes unreliable. Additionally, PSF-Kron positions towards the lower right of the galaxy region might be contaminants, and I do not use positioning in this region as grounds for galaxy classification. For all sources, a visual check for extension was also made. It should be noted that while the PSF-Kron method can confirm an object as a galaxy, it cannot definitively classify stars. In particular, compact, dwarf or distant galaxies may be unresolved at Pan-STARRS resolution and appear star-like by this classifier. Where the only information available is an insecure galaxy or star classification using PSF-Kron, and the object is not obviously extended by eye, I use SED fitting to distinguish the possibilities (see Section 2.6).

An alternative method, proposed by Kovács and Szapudi (2015), separates stars and galaxies with the aid of the  $J$ -band. This is demonstrated in Figure 2.9. At fixed W1 magnitude, objects that are bluer in W1- $J$  are more likely to be galaxies. Kovács and Szapudi (2015) found that a cut at  $W1-J = 0.09$  (AB magnitudes) is an effective star-galaxy separator, with a stellar contamination on the galaxy side of only  $\sim 1.8$  per cent. However, this technique was applied to brighter sources than are dealt with here, with the galaxies lying at a median redshift of 0.14, much lower than this sample. Because it is unknown how the W1- $J$  colours vary for lower mass, star forming galaxies across a range of redshift, the use of the cut here is a suggestive, but not decisive, diagnostic.

I also checked for proper motion in *WISE*, classifying those with notable proper motion (a total proper motion of at least  $2\sigma$  significance is required) as stars. The HSOY catalogue (Altmann et al., 2017) is also searched. This is a precursor to the full Gaia Astrometric Survey second data release (see Section 2.10). Several optical sources are identified, all within 1 arcsec of their respective *WISE* match, which have proper motions identifying them as stars. A small number of sources have notable proper motion in HSOY but not *WISE*. These might be chance alignments between a foreground star and a background IR source. However, due to large uncertainties on the *WISE* proper motions, it is not possible to tell. When this scenario arises, I assume that the optical counterparts are associated with the IR sources, ruling them out as IR-bright galaxies. Table 2.7 gives the results for those sources that have data available for at least one of the star-galaxy checks discussed.

Table 2.7: Initial star galaxy separation results using archival photometry and catalogued data products, for those sources that had sufficient data for at least one of the separation tests. Note that sources with PSF-Kron positions towards the lower right of the galaxy region may actually be stellar contaminants. The 5 objects listed below the line lack coverage in Pan-STARRS and SDSS, but are classified in other ways.

GRB	PM <i>WISE</i>	PM HSOY	PSF-Kron	W1- <i>J</i>	Type
050522	-	S	S	S	S
050716	S	-	S	-	S
050721	-	S	S	S	S
050724	-	-	G	-	G
060428B	-	-	G	-	G
061002	-	-	U	-	U
070208	-	-	G	-	G
070724A	-	-	G	-	G
080405	-	S	G	-	S
080517	-	-	G	G	G
090904B	S	S	S	G	S
100206A	-	-	U	-	U
110305A	-	-	S	S	S
111222A	-	S	S	S	S
120119A	-	-	G	-	G
120612A	-	-	S	S	S
130603B	-	-	G	-	G
131018B	-	-	S	S	S
140927A	-	-	-	S	S
150101B	-	-	G	G	G
150120A	-	-	U	-	U
160703A	-	S	S	-	S
161010A	S	-	G	S	S
161214B	-	S	S	-	S
070309	-	-	-	S	S
080623	S	S	-	S	S
150626A	-	S	-	S	S
161001A	-	S	-	-	S
161104A	S	-	-	-	S

G - galaxy. S - star. U - uncertain.



## 2.5 Previously Reported GRB Hosts and Observations

Many of the GRBs in this sample of 55 have previously been studied, providing useful information. In this section, I compile reported afterglow positions, detailed host studies and other noteworthy information. This rules out some IR sources as chance alignments, and adds some hosts to the sample for which the required observations were lacking. I split these into 3 categories: matched IR sources with an optical detection, those without, and those lying outside the optical surveys searched in this Chapter. A summary of the entire source selection and rejection process is provided as a flowchart in Figure 2.10.

### 2.5.1 Optical Survey Detections

*LGRB 060428B*: The candidate host represents a single IR source corresponding to what appears to be a single optical source. However, Perley et al. (2007) has suggested that a compact blue galaxy lies underneath the foreground elliptical’s light, at an offset of 2.6 arcsec. This corresponds to the foreground object’s Einstein radius, as such they claim that LGRB 060428B is likely a gravitationally lensed event originating from the higher redshift, bluer galaxy. While this work has not been fully published, it is a possible explanation. I therefore take a conservative approach and exclude this source from later analysis.

*LGRBs 070208 and 120119A*: Blanchard et al. (2016) report *HST* imaging of the burst locations in these cases, with the optical afterglow positions indicating that these may be chance alignments with the IR-bright sources. This is backed up by analyses in Section 2.6.

*LGRB 160703A*: Zheng et al. (2016) observed the afterglow with Keck-I in the *g* and *r* bands. The improved positional certainty over XRT suggests that the IR source is not the host. The object has proper motion (see Table 2.7), confirming this interpretation. I therefore remove the source from further analysis.

*LGRB 161214A*: The object associated with the matched *WISE* source was observed by Malesani et al. (2016), who obtained spectroscopy identifying it as a K or M star. There are cases where an improved burst localisation (e.g. in the optical) strengthens the IR source association, rather than ruling it out. There are also hosts where there is sufficient photometry for SED fitting, in addition to previously reported host parameters. This information is compared to the SED fitting results. These studies and observations are referenced for each burst in Table 2.8 of Section 2.6.

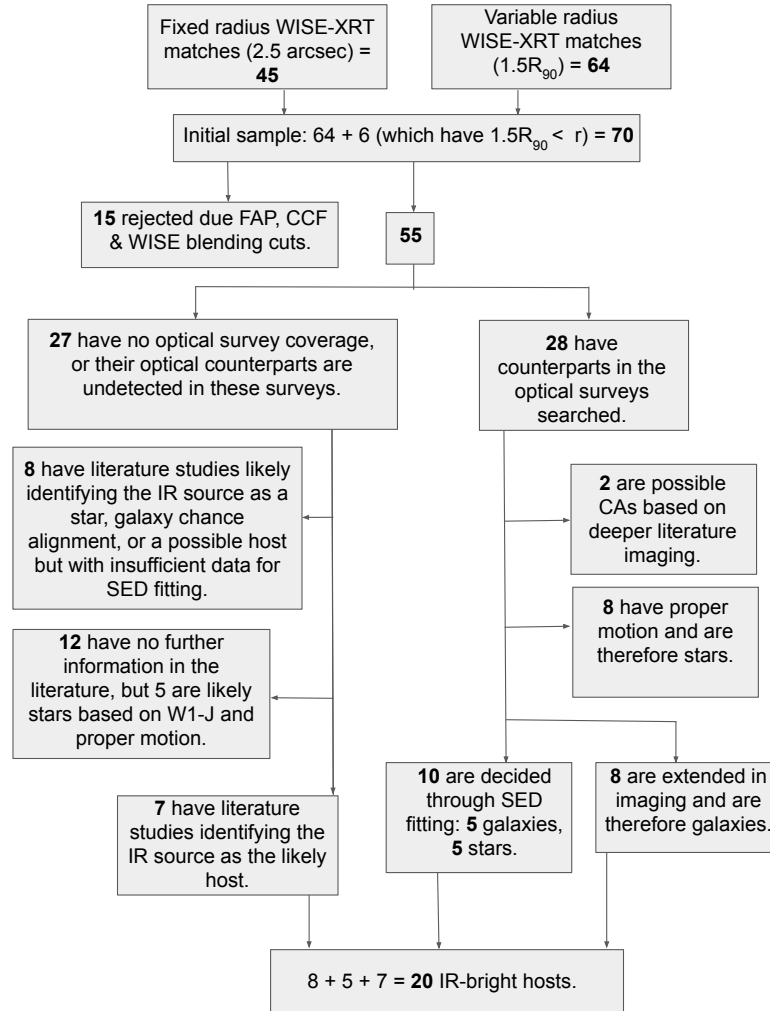


Figure 2.10: A flowchart depicting the process of selecting, and rejecting, IR sources matched to XRT afterglow coordinates. Chance alignments (CAs), sources rejected due to a high false alarm probability ( $FAP > 0.05$ ), crowding and confusion flags (CCF), blending, or evidence of being a star, are discounted, leaving 20 likely IR-bright hosts in the sample. Six sources which appear in the sample of 45 (fixed  $r = 2.5$  arcsec matching), but *not* in the sample of 64 ( $1.5 \times R_{90}$  matching), are re-added as they are close to an IR source (within  $r = 2.5$  arcsec) but have small X-ray uncertainties - which does not account for the angular size of the candidate host galaxy.



### 2.5.2 Optical Survey Non-Detections

*LGRB 050716*: No object is detected in optical imaging. Rol et al. (2007b) deduced a burst redshift  $> 2$  based on the optical to X-ray afterglow SED, however the matched *WISE* source has proper motion - assuming that the flux is entirely from this star, I reject this association as a chance alignment.

*LGRB 080207*: This host has been extensively studied in the literature (Hunt et al., 2011; Svensson et al., 2012; Hjorth et al., 2012; Krühler et al., 2012b; Arabsalmani et al., 2018; Hatsukade et al., 2019; Hashimoto et al., 2019) as an example of a red, dusty luminous infrared galaxy. There is a 1 arcsec separation between the *WISE* centroid and the Chandra position provided by Svensson et al. (2012), which itself is clearly placed over the galaxy in question. Therefore, I include the reported parameters for this galaxy in the analysis. The optical faintness of this galaxy shows that such sources can have steep optical to IR spectral slopes, and demonstrates that other optical non-detections could be similar in nature.

*LGRB 080307*: This burst has an X-ray detected AGN a few arcseconds away (Page et al., 2009). Both the *WISE* IR emission and X-ray flux have levels consistent with expectations for local AGN (Eckart et al., 2010). Therefore, the AGN is the most likely source of the IR flux. While it is possible that the AGN resides in the host galaxy (as is the case with SGRB 150101B, see Fong et al. (2016)), I use MAGPHYS for SED fitting in the next section, which does not have a prescription for AGN. Because the IR flux is consistent with being AGN dominated, this would lead to incorrect parameters when the SED is fitted by MAGPHYS. Therefore, I take a cautious approach and remove LGRB 080307 from further analysis.

*LGRB 080605*: In the imaging provided by Krühler et al. (2012a) and Blanchard et al. (2016), it can be seen that the *WISE* flux centroid is centred on a  $z = 1.64$  galaxy undetected in Pan-STARRS, rather than either of the two bright sources. The burst redshift of  $z = 1.64$  was determined from afterglow spectroscopy. Because this galaxy is therefore confirmed as the host, I reject the nearby bright objects and reclassify this host as a Pan-STARRS non-detection. Krühler et al. (2012a) provide estimated parameters for the host galaxy, which are employed.

*GRBs 100816A and 110918A*: For these sources I use the physical parameters reported by Pérez-Ramírez et al. (2013) and Elliott et al. (2013) respectively. In both cases, the IR bright source is aligned with the reported host galaxy.

*GRB 120224A*: This object is only marginally detected in the X-shooter spectroscopy, however Selsing et al. (2019b) found a  $2\sigma$  emission line in similar X-shooter data. If the line is  $H\alpha$ , this corresponds to a redshift of 1.1. I tentatively assume this to

be the case going forward, treating the source as an optically undetected galaxy at  $z = 1.1$ .

*LGRBs 130527A, 150323C and 161007A*: The positions of these bursts were observed in the optical. In each case, an extended object was seen, allowing galaxy classifications (Cano et al., 2013; Malesani et al., 2015; Heintz et al., 2016). There is insufficient photometry for SED fitting, so I continue to treat these as non-detections, but note that the IR flux likely originates from faint galaxies (rather than stellar contaminants).

*LGRB 130528A*: While undetected in Pan-STARRS, this source is revealed to be in a crowded region in deeper imaging, with multiple objects in a 10 arcsec region (Jeong et al., 2014b). Because the IR flux cannot be assigned to a single object with any certainty, I classify this burst as a potential chance alignment and do not consider it any further.

### 2.5.3 Lacking Coverage

*GRBs 050219A, 070429B, 100316D*: I use the host galaxy physical parameters reported by Rossi et al. (2014), Cenko et al. (2008) and Izzo et al. (2017) respectively. In these cases, I compare the reported host coordinates to the *WISE* positions. For all three, the IR flux is aligned with the galaxies identified as a potential hosts. Because these are good quality IR sources which satisfy the FAP cut, I include the reported host parameters in subsequent analysis.

*LGRB 130515A*: Levan and Tanvir (2013) observed the brightest source in the X-ray error circle with VLT/FORS2, finding it to be an M star. The position of the star is consistent with the *WISE* source, so I discount this association.

## 2.6 SED Fitting

### 2.6.1 Multiple Candidate Hosts

In this sample, there are cases where multiple optical sources lie inside the search radius used to match optical imaging to *WISE*. Visual inspection reveals 3 GRBs (141212A, 140331A and 150120A) where the candidate host IR flux is not uniquely associated with a single optical source. In these cases, the optical and IR images were aligned to check for astrometric offsets.

For LGRB 140331A, the IR emission originates from the fainter of two optical sources within the XRT error circle. Inspection of Chandra X-ray imaging with sub-arcsecond afterglow localisation suggests that the burst may not, in fact, be



associated with either optical galaxy, but this cannot be ruled out (see subsequent work in Chapter 3 and Chrimes et al., 2019a). The optical source aligned with the IR flux matched to LGRB 140331A does not reach the threshold for cataloguing in Pan-STARRS. Instead, and in addition to the WHT photometry (see Section 2.3.1), I measure magnitudes from Pan-STARRS cutouts. This photometry is available in Appendix A, and is used for SED fitting.

In the case of SGRB 141212A, the IR source centroid lies closest to the host identified by Malesani et al. (2014), although there may be some blending with neighbouring objects. I download and perform aperture photometry on the Pan-STARRS images in addition to the WHT images previously discussed. The photometry from both is in good agreement, and the Pan-STARRS measurements are again given in Appendix A.

The IR source associated with SGRB 150120A may have either of two optical counterparts, both catalogued in Pan-STARRS DR1. I fit their SEDs separately, in each case assuming that the entire IR flux is associated with the galaxy under consideration. The better of the two fits is used in the subsequent analysis.

## 2.6.2 Galaxy SED fitting with MAGPHYS

Spectral Energy Distribution (SED) fitting on this sample was performed by  $\chi^2$  minimisation using templates derived from MAGPHYS and its high-redshift update (da Cunha et al., 2008, 2015). MAGPHYS was chosen for fitting the sample due to its careful implementation of dust extinction and re-emission. Given that these sources are detected in the infrared, dust might be expected to be an important influence on their spectra. The population synthesis models of Bruzual and Charlot (2003) are employed, with the dust absorption and re-emission model of Charlot and Fall (2000). The stellar populations are built up by assuming a range of ages distributed evenly from 0.1 Gyr to the maximum age permitted at a given redshift (i.e. the age of the Universe). The star formation rate is modelled as declining proportional to  $e^{-\gamma t}$ , where  $\gamma$  is the star formation timescale and  $t$  is the time elapsed since the onset of star formation. Random constant SFR bursts are overlaid, with durations evenly distributed between  $3 \times 10^7$  yr and  $3 \times 10^8$  yr. The probability of a burst is such that 50 per cent of the model galaxies have experienced a starburst phase in the last 2 Gyr. The amplitude of these bursts  $A$  is defined as the ratio of stellar mass formed in the burst and all stellar mass assembled since the galaxy was formed at time  $t_{\text{form}}$ ; this parameter is distributed logarithmically from 0.03 to 4.00.

Many of the candidates already have confirmed or likely redshifts, either from afterglow absorption lines or from the host. These were used to fix the redshift

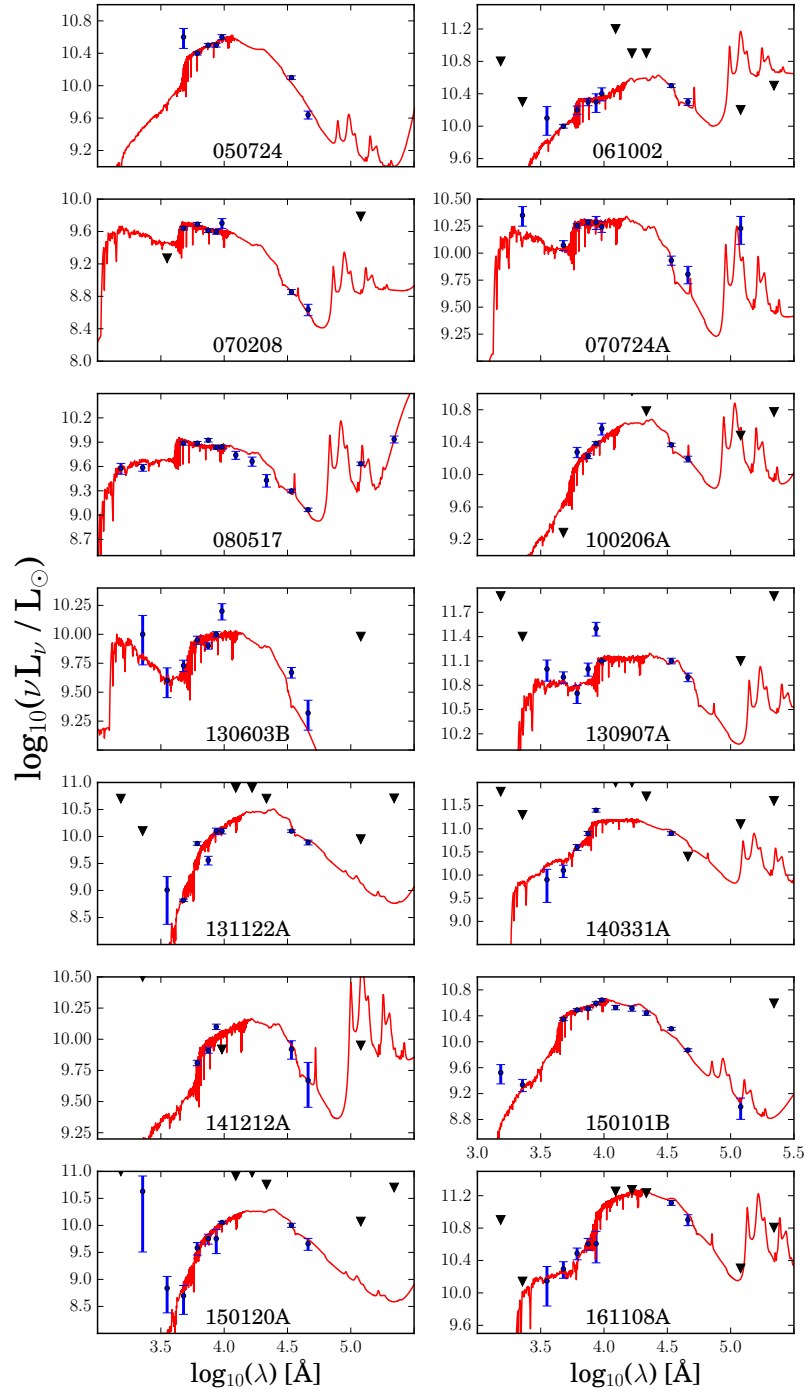


Figure 2.11: SEDs for the objects which were best-fitting (or else confirmed) as galaxies. Some upper limits are too high on this scale to be visible.



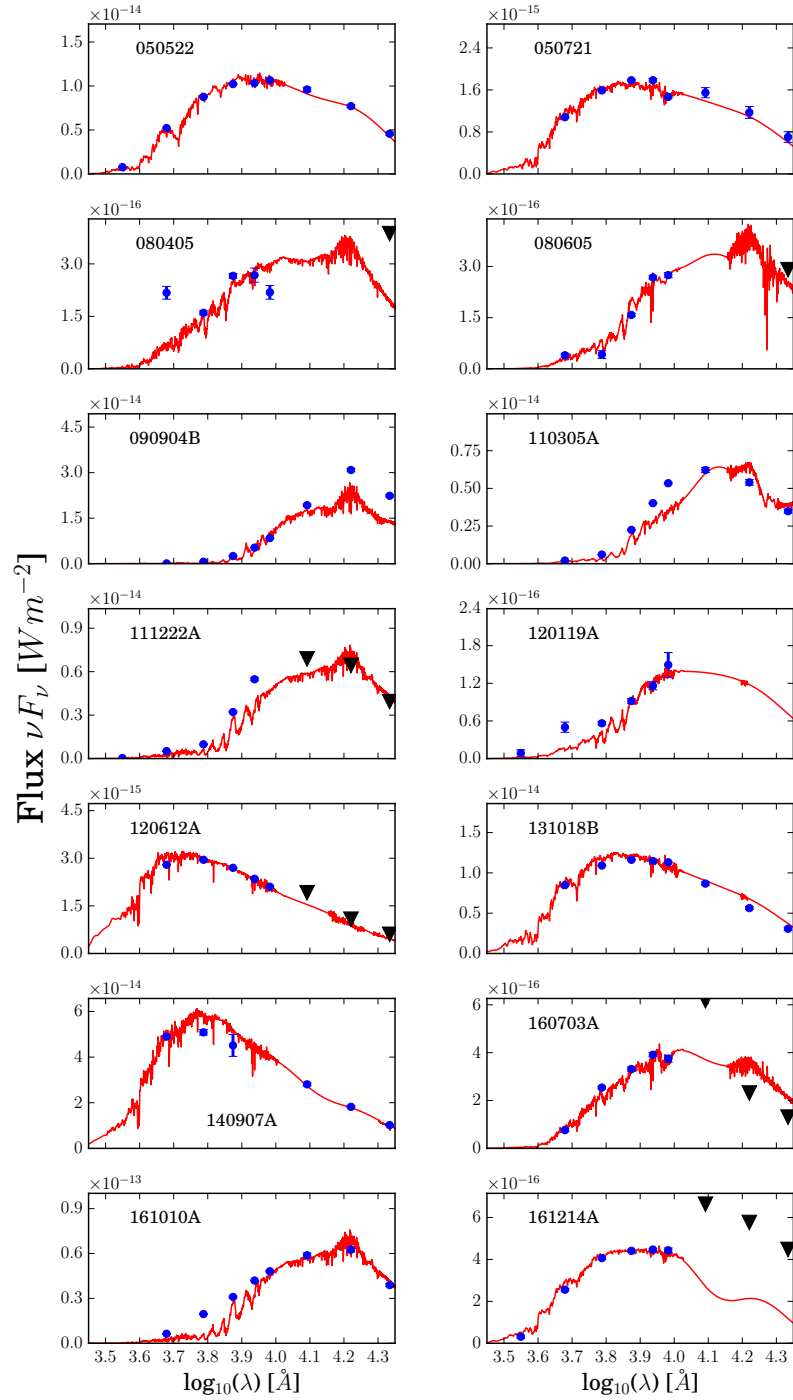


Figure 2.12: SDSS stellar templates for sources which were best-fitting (or otherwise confirmed) as stars. Some upper limits are too high on this scale to be visible.

where possible. I also derive a photometric redshift for each galaxy. At each step in a grid of trial redshifts, I make use of the internal Bayesian fitting code built into MAGPHYS to determine the redshift interval for which  $\chi^2 \leq \chi_{\min}^2 + \Delta\chi^2$  (Avni, 1976). I did this at redshift intervals of 0.05 over the range  $0 \leq z \leq 1$ , or up to  $z = 3$  if no acceptable solution is found at lower redshifts. The distribution of  $\chi^2$  over redshift is then minimised. In this way, MAGPHYS is effectively used as a photometric redshift code (da Cunha et al., 2015), with the redshift treated as an additional free parameter. The photometric redshifts are generally in agreement with spectroscopic redshifts where available, as shown in Table 2.8. Uncertainties on SED fitting parameters include the effect of photometric redshift uncertainty where a spectroscopic (or SDSS) redshift is not used.

MAGPHYS fits for stellar mass, current star formation rate, star formation history (age, timescale and burst amplitude), metallicity, and dust extinction, amongst other parameters. I caution that the number of free parameters is sometimes greater than the number of data points available for a given galaxy and that the fits may be over-constrained. MAGPHYS does not routinely report uncertainties on metallicity, as this is often a poorly constrained parameter, so I simply state the best-fitting metallicity given by MAGPHYS.

### 2.6.3 Galaxy SED fitting Summary

Of the 55 GRBs with candidate *WISE* counterparts, 29 have optical-NIR photometry (from Pan-STARRS, SDSS, APASS, 2MASS, WHT observations or some combination of the above) in addition to at least *WISE* band 1. I correct this observed photometry with the Galactic extinction maps of Schlafly and Finkbeiner (2011) and a Fitzpatrick reddening law with  $R_V = 3.1$ , using the IRSA dust reddening and extinction service<sup>4</sup> and the York Extinction Solver (YES, McCall, 2004). I fit 28 SEDs (excluding LGRB 060429B, as this has been rejected as probable chance alignment). For the host of SGRB 050120A, I fit the two optical components separately, assigning the entire *WISE* flux each time. 14 of the 28 objects are best-fitting, or otherwise confirmed, as galaxies. Objects identified as galaxies or stars solely through the quality of fitting to stellar or galaxy templates are classified as photometric galaxies or stars (‘PG’ or ‘Ps’) in Table 2.1. The limited number of stellar templates available makes it difficult to decide whether an object is best-fitting as a star or galaxy based on the reduced  $\chi^2$  alone. Therefore, the reduced  $\chi^2$  values for galaxy fitting are noted, but I make the assumption that a visually good star fit indicates that the object is a star, when the corresponding galaxy  $\chi^2$  value is poor.

<sup>4</sup><http://irsa.ipac.caltech.edu/applications/DUST/>



The data for the objects best-fitting as galaxies, together with the best-fitting galaxy templates, are shown in Figure 2.11 and Table 2.8. There are some instances where the FUV/NUV flux appears inconsistent with the SED. This might be because a different object has been matched to - the matching to *WISE* is independent for the UV, optical and NIR. However, this unlikely as a nearby UV source should also be seen in the optical. They might be UV upturns, a phenomena seen in otherwise red elliptical galaxies, or the fitting may simply be failing to properly account for complex stellar populations. Another explanation is that they are main sequence stars with a white dwarf companion, as this can produce remarkably similar SEDs (Parsons et al., 2016), however this is ruled out for extended sources, leaving only GRB 150120A as a main sequence-white dwarf (or other UV-bright star) candidate.

Some fits produced no clear minimum in  $\chi^2$ , and therefore lack a robust photometric redshift. In these cases, I use a spectroscopic or SDSS photometric redshift where available. For LRGB 061002, a photometric redshift of  $0.10_{-0.10}^{+0.45}$  is obtained. However, the more precise SDSS photometric redshift, which is calculated using machine learning techniques (Csabai et al., 2007), is  $z = 0.56 \pm 0.09$ . The redshift is therefore fixed to the SDSS value. Similarly, the photometric redshift for LGRB 131122A is unconstrained, likely because there is no clear Balmer or Lyman break evident from the photometric points. However, this object also has an SDSS photometric redshift, at  $z = 0.399$ . This produces a visually acceptable fit, so I employ this redshift.

Another object, the candidate host of LGRB 070208, is correctly identified as a galaxy but the photometric redshift of  $z = 0.16_{-0.16}^{+0.37}$  is inconsistent with a previous spectroscopic redshift of  $z = 1.165$  (Cucchiara et al., 2007). The foreground object is not detected in the spectroscopy reported by Cucchiara et al. (2007), but there is a marginally detected object seen offset from the foreground galaxy, nearer to the afterglow centroid. The *HST* imaging of Blanchard et al. (2016) confirms this interpretation. Given this information, I do not include LGRB 070208 any further.

#### 2.6.4 Stellar Fitting

I also perform fitting to a library of 131 stellar spectra (Pickles, 1998), with the expectation that a significant fraction of the objects will be best-fitting as stars. The spectra span the range 1150-25000Å, allowing fitting from the FUV to *K* bands. In most of the 14 cases where MAGPHYS does not provide a good fit, stellar fitting does. The best-fitting stellar templates for these sources are shown in Figure 2.12. Here, the SEDs for those objects with proper motion or other star diagnostics are shown, in addition to sources where a stellar SED is a better fit than a galaxy SED.

Note that the sources which fit best to stellar templates include all objects for which a spectroscopic or proper motion confirmation as a star is available.

## 2.7 Results and Discussion

### 2.7.1 SED Fitting Results

Table 2.8 presents the SED fitting results for the 13 candidate or confirmed GRB hosts that match best to galaxy templates (the 14 shown in Figure 2.11, excluding the likely interloper LGRB 070208), and also a compilation of information from the literature for seven of the GRB hosts discussed in Section 2.5.

In comparing the SED fit results to independent measures of the host properties, potential discrepancies arises between them. The SED derived SFR,  $\sim 0.15 M_{\odot}\text{yr}^{-1}$ , for the host of SGRB 150101B disagrees with the NVSS 1.4 GHz radio SFR,  $\sim 300 M_{\odot}\text{yr}^{-1}$  and the detection of this source at  $5.8\mu\text{m}$  in the W3 band. This is due to the presence of an AGN (Fong et al., 2016). Unlike LGRB 080307 which was rejected due to coincidence with a nearby AGN, the association of SGRB 150101B with this galaxy has been secured with spectroscopic observations. It is therefore kept in the analysis. Only two other sources in this sample are detected in the W3 band. While this is sometimes used as a SFR indicator or AGN discriminator, the two cannot be unambiguously differentiated without a reliable (and low) redshift (Davies et al., 2017).

### 2.7.2 Short GRBs

Before considering the redshift distribution and other properties of this sample, it is important to consider the selection effects that will shape any comparisons made. The first issue to consider is whether there may be a particular bias towards long or short bursts. Since their progenitor mechanisms differ, their host properties should also differ. As such it is essential to consider the short vs long divide. Of the 55 GRB locations identified as having a *WISE* counterpart, 11 of the associated bursts had an observed  $T_{90} < 2\text{ s}$ . Of these, 8 are reported in Table 2.8 as galaxies. Two are identified as a Galactic stars.

The lack of a clear divide between the two populations can lead to ambiguity (e.g. Berger, 2014, and references therein). Two targets have  $2 < T_{90} < 5\text{ s}$  and might be classified as short by some proposed criteria. Of these, one is identified in the galaxy sample, while one has insufficient photometry. In the following, I treat these “intermediate” sources as long bursts.



Table 2.8: SED fitting results for the IR-bright sources with photometry best-fitting to galaxy templates. Additionally, where there is a non-detections or no coverage, values for well studied host galaxies identified in the literature are listed in the last 7 rows. References are given below the table and provide spectroscopic redshifts in most cases, or additionally, parameter values for galaxies lacking the photometry needed for SED fitting.

GRB	$z_{phot}$	$z_{spec}$	SFR ( $M_{\odot} \text{yr}^{-1}$ )	$M_{*}$ ( $10^{10} M_{\odot}$ )	sSFR ( $10^{-10} \text{yr}^{-1}$ )	$A_V$	$Z/Z_{\odot}$	$\chi^2/\text{dof}$	Ref.
050724†	$0.05^{+0.60}_{-0.05}$	0.258	$21.4^{+6.8}_{-20.7}$	$8.1^{+0.8}_{-3.6}$	$2.7^{+15.1}_{-2.6}$	$2.45 \pm 0.13$	0.038	1.81	[1], [2]
061002*	$0.56 \pm 0.09$	-	$1.6 \pm 0.6$	$2^{+1}_{-1}$	$0.8^{+3.6}_{-0.5}$	$4.47^{+0.22}_{-0.22}$	1.46	1.90	[3]
070724A†	$0.50 \pm 0.23$	0.457	$8.4^{+0.6}_{-6.1}$	$1.8^{+2.8}_{-1.1}$	$4.8^{+11.2}_{-3.0}$	$0.43^{+5.81}_{-0.06}$	1.093	0.85	[4], [5]
080517	$0.01^{+0.20}_{-0.01}$	0.089	$9.8^{+1.4}_{-2.7}$	$0.26^{+0.10}_{-0.04}$	$37^{+7}_{-5}$	$3.3 \pm 0.1$	1	2.51	[6], [7]
100206A†	-	0.4068	$14^{+2}_{-2}$	$8.8^{+0.1}_{-0.7}$	$3.2^{+0.8}_{-0.8}$	$2^{+1}_{-1}$	1.15	1.34	[8]
130603B†	$0.36^{+0.12}_{-0.25}$	0.356	$1.070^{+0.708}_{-0.001}$	$1.1^{+0.7}_{-0.4}$	$1.0^{+1.2}_{-0.6}$	$0.03^{+0.85}_{-0.03}$	0.038	2.78	[9], [10]
130907A	$1.00^{+0.04}_{-0.15}$	1.238	$1.45 \pm 0.8$	$4.5^{+6.8}_{-2.7}$	$0.32^{+0.52}_{-0.26}$	$\sim 1.9$	1.9	2.54	[11], [12]
131122A*	0.399	-	$0.22^{+0.06}_{-0.04}$	$8.9^{+1.7}_{-1.8}$	$0.022^{+0.006}_{-0.004}$	$2.2 \pm 0.1$	0.038	1.25	-
140331A	$1.00^{+0.11}_{-0.04}$	-	$5.3^{+4.3}_{-2.4}$	$16.5^{+4.1}_{-6.4}$	$0.47^{+0.35}_{-0.39}$	$1.4^{+0.9}_{-1.0}$	$0.09^{+0.17}_{-0.06}$	6.49	[13]
141212A†	-	0.596	$0.65 \pm 0.4$	$1.4^{+0.8}_{-0.5}$	$0.46^{+0.39}_{-0.33}$	$1.4^{+1.3}_{-1.2}$	1	2.42	[14]
150101B†	$0.15^{+0.05}_{-0.04}$	0.134	$0.15 \pm 0.03$	$6.3^{+0.8}_{-1.5}$	$0.023 \pm 0.005$	$\sim 3.6$	0.4	2.59	[15]
150120A†	$0.1^{+0.2}_{-0.1}$	0.46	$0.71^{+2.11}_{-0.08}$	$5.6^{+8.5}_{-2.1}$	$0.11^{+0.17}_{-0.07}$	$1.7 \pm 0.3$	0.89	0.90	[16]
161108A	$< 1.3$	1.159	$0.25 \pm 0.11$	$11.2^{+0.2}_{-0.4}$	$0.022 \pm 0.010$	$0.3^{+0.3}_{-0.2}$	1.6	1.81	[17]
050219A	-	0.2115	$\sim 0.06$	$\sim 1$	$\sim 0.06$	$< 0.1$	-	-	[18]
070429B†	-	$\sim 0.9$	$\gtrsim 1.1$	$\gtrsim 440$	$\gtrsim 0.0025$	-	-	-	[19]
080207	-	2.086	$\sim 119$	$32 \pm 8$	$\sim 4$	$\sim 1.9$	$\sim 1$	-	[20], [21], [22], [23]
080605	-	1.64	$49^{+26}_{-13}$	$0.80^{+0.13}_{-0.16}$	$60^{+60}_{-20}$	$0.22^{+0.40}_{-0.22}$	$0.6 \pm 0.2$	-	[24]
100316D	-	0.0591	$1.20 \pm 0.08$	$\sim 0.0895$	$\sim 13$	0.86	0.3	-	[25], [26]
100816A	-	0.804	-	-	-	$\sim 0.2$	-	-	[27]
110918A	-	0.984	$\sim 40$	$10.68 \pm 0.16$	$\sim 3.7$	$0.10 \pm 0.16$	-	-	[28], [29]

† These are short bursts. ‡ This has extended emission but is likely a disguised short burst. \* Uses an SDSS photometric redshift.

References: [1] Prochaska et al. (2005), [2] Berger et al. (2005), [3] Alam et al. (2015), [4] Kocevski et al. (2010), [5] Berger et al. (2009), [6] Stanway et al. (2015a), [7] Stanway et al. (2015b), [8] Perley et al. (2012), [9] de Ugarte Postigo et al. (2014), [10] Frederiks (2013), [11] de Ugarte Postigo et al. (2013), [12] Golenetskii et al. (2013), [13] Littenjohns et al. (2014), [14] Chornock et al. (2014a), [15] Fong et al. (2016), [16] Chornock and Fong (2015), [17] de Ugarte Postigo et al. (2016), [18] Rossi et al. (2014), [19] Cenke et al. (2008), [20] Arabsalmani et al. (2018), [21] Hunt et al. (2011), [22] Svensson et al. (2012), [23] Svensson et al. (2012), [24] Krühler et al. (2012a), [25] Starling et al. (2011), [26] Michałowski et al. (2015), [27] Pérez-Ramírez et al. (2013), [28] Elliott et al. (2013), [29] Frederiks and Pal'Shin (2011)

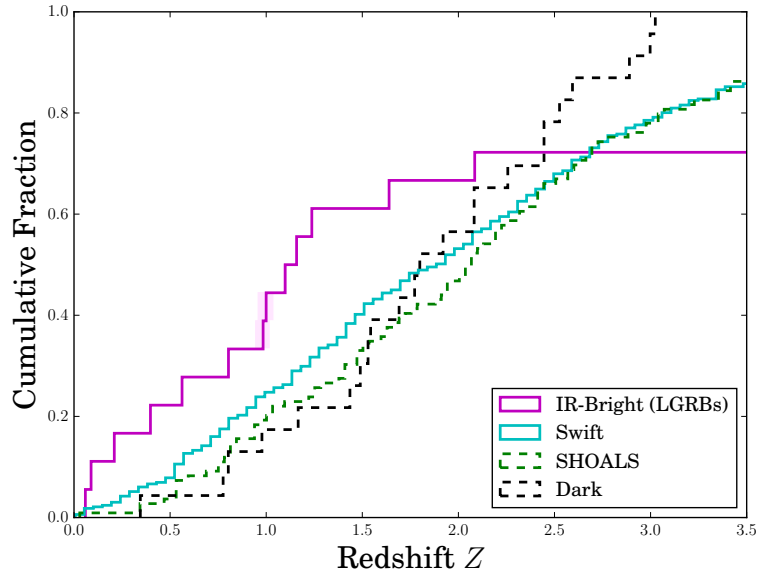


Figure 2.13: The redshift cumulative distributions of the IR-bright LGRB host sample, all *Swift* LGRBs with known redshift, the unbiased LGRB SHOALS host galaxy sample and the dark LGRB sample of Perley et al. (2013). I make the ‘worst case’ assumption that the 5 optical-non detections that have not been ruled out as stars are higher redshift galaxies.

Considering the 20 GRBs for which galaxy properties are assembled in Table 2.8, the fraction of SGRBs is 40 per cent (8/20) and would be as high as 50 per cent if the intermediate bursts were included. This compares to the short burst fraction in the entire GRB catalog of only 6 per cent (Berger, 2014), suggesting that short bursts are being preferentially selected. This may reflect the difference in the underlying redshift distribution of these sources, exemplified by the mean redshift of  $z = 0.45$  for the SGRBs. Short GRBs are typically of lower isotropic-equivalent luminosity and their distribution is biased towards low redshifts ( $\langle z \rangle < 0.8$ ) relative to long GRBs ( $\langle z \rangle \sim 2$ ), due to the differences in both their progenitors and detection probabilities (Berger, 2014). Given the relatively shallow depth of the W1 band imaging, a low redshift, and therefore SGRB excess, might be expected in the sample.

### 2.7.3 Redshift Distribution

I now consider the detailed properties of the IR-bright LGRB host population. Figure 2.13 shows the cumulative redshift distribution for the 13 candidate host galaxies that form the IR-bright LGRB host population (the 12 in Table 2.8 plus LGRB 120224A at  $z = 1.1$ ). I compared these to the SHOALS sample of LGRB



hosts (Perley et al., 2016a,b), all *Swift* LGRBs with a known redshift, and a sample of dark LGRB hosts (Perley et al., 2013). In each case I indicate uncertainty on the cumulative distribution by performing an analysis in which each value is permitted to vary by addition of its associated random error, drawn from a skewed Gaussian distribution, in order to account for asymmetric errorbars. The scale and alpha parameters are chosen in each case such that the asymmetric distributions are reproduced. The standard deviation of 1000 realisations of the perturbed cumulative distribution is shown as a shaded region (this is less apparent in Figure 2.13 than in subsequent distribution figures).

In this sample, 7 objects have survey coverage but are undetected, and lack extensive study in the literature. It is possible that some of these may be M, L or T dwarfs, which can be a few magnitudes brighter in the *WISE* bands than the optical (e.g., Best et al., 2013). Indeed, the optically undetected object associated with LGRB 050716 has significant *WISE* proper motion. Late L and T dwarfs have the reddest colours of these stars and would be most able to satisfy the criteria of W1 detection and optical non-detection, however these are also the rarest classes of these objects.

Alternatively, the optical non-detections could be intrinsically faint or higher redshift galaxies. This possibility has been demonstrated by several such examples in Section 2.5. Three of the optically undetected sources have been identified as extended sources in deeper imaging, as described in Section 2.5. One of the non-detections, LGRB 120224A, may be at  $z = 1.1$  (Selsing et al., 2019b). Figure 2.13 shows that the sample is biased towards low redshifts when non-detections are not included. Therefore, the most extreme scenario is that all 5 of the remaining non-detections are in fact galaxies at higher redshift than the highest confirmed LGRB in the sample. Setting these 5 non-detections to an arbitrarily high-redshift, it is still not possible to match the slower rise of the SHOALS and dark samples, demonstrating that there is a low  $z$  bias even in the ‘worst case’ scenario. In reality, their redshifts could well be lower, given that the optically undetected hosts of LGRBs 080605, 100816A, 110918A and 120224A all lie at  $z < 2$ .

The possibility that chance alignments remain in the sample must also be considered. LGRB 140331A is at high risk in this regard, since the XRT error circle position favours a different optical source, unaligned with the *WISE* flux. In general, foreground chance alignments preferentially select lower redshift or foreground objects, and this remains a possible explanation for the difference in cumulative distribution between this sample and others. However, all but three of these sources have spectroscopic redshifts, and it is unlikely that a spectroscopic redshift mea-

surement would be affected by a foreground interloper.

The effect of small number statistics in this sample is further quantified by bootstrap resampling of the SHOALS sample. I extract a subsample of sources from one of the reference samples matching the IR bright sample in size, and calculate its redshift distribution. This is done  $10^5$  times to explore the frequency with which the subsample realisation matched the observed distribution. I define a match as a scenario in which an appropriate fraction of the sample lies at  $z = 1.24$  (our highest optically detected galaxy redshift) or lower. In other words, how often is a sample of 20 bursts, exclusively at  $z < 1.24$ , drawn from SHOALS?

The Kolmogorov-Smirnov (KS) statistic is also considered for the same ( $z < 1.24$ ) distribution. As the results in Table 2.9 demonstrate, the KS-test is unable to reject the null hypothesis that IR-bright sample is drawn from the same population as SHOALS (when restricted to  $z < 1.24$ ), while the bootstrapping estimate gives a  $\sim 0.06$  per cent chance of drawing a sample (of 20) with the IR-bright redshift distribution from SHOALS. Assuming instead that the undetected sources are dusty, lower redshift galaxies, or that they are stars, only increases the disparity between the samples (see later).

The differences between the bootstrap and KS-test results are pronounced. The bootstrapping method supports a much stronger identification of IR-bright LGRB hosts being biased in redshift, compared to the KS-test. Fundamentally the two tests are exploring different aspects of the data. The KS-test is primarily sensitive to the relative *shapes* of the distributions, and at  $z < 1.24$  these are similar. However, the entire distribution for the IR-bright galaxies is shifted towards lower redshifts, producing the clear bootstrap results indicated in Table 2.9. The IR-bright hosts possess a biased distribution in redshift, but since the distribution shape is similar, this does not necessarily imply a distinct underlying population.

#### 2.7.4 Masses, Dust Extinction and SFR

I compare the stellar masses derived for the IR-bright LGRB host population (11 objects - 6 from SED fitting and 5 literature values), to existing samples over the same redshift range, in Figure 2.14. The IR-bright and SHOALS distributions yield a KS-test p-value that passes the  $2\sigma$  threshold for significance. This, and the corresponding bootstrap result, are given in Table 2.9. In comparing the mass distributions, I assume that the optically-faint subsample is not significantly biased in mass.

Given that selections have been made in the infrared, the dust extinction (and hence re-emission at long wavelengths) is a parameter of particular interest. A

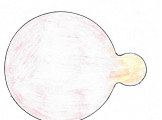


Table 2.9: Bootstrap and KS-test results for the LGRB redshift, stellar mass,  $V$ -band attenuation and star formation rate distributions, compared to unbiased samples over the same redshift range.

Property	Bootstrap Target	Bootstrap %age prob.	KS-test p-value <sup>1</sup>
$z$	0.61 by $z = 1.24$	0.056	0.45
$M_*$	0.50 by $\log_{10}(M_*) = 10.7$	0.001	0.004
$A_V$	0.50 by $A_V = 0.84$	20.2	0.07
$A_V$	0.75 by $A_V = 1.89$	0.09	0.07
SFR	0.50 by $\log_{10}(\text{SFR}) = 0.17$	50.1	0.62

<sup>1</sup>The KS test requires a p-value of less than 0.05 to pass the widely used threshold of  $2\sigma$  significance.

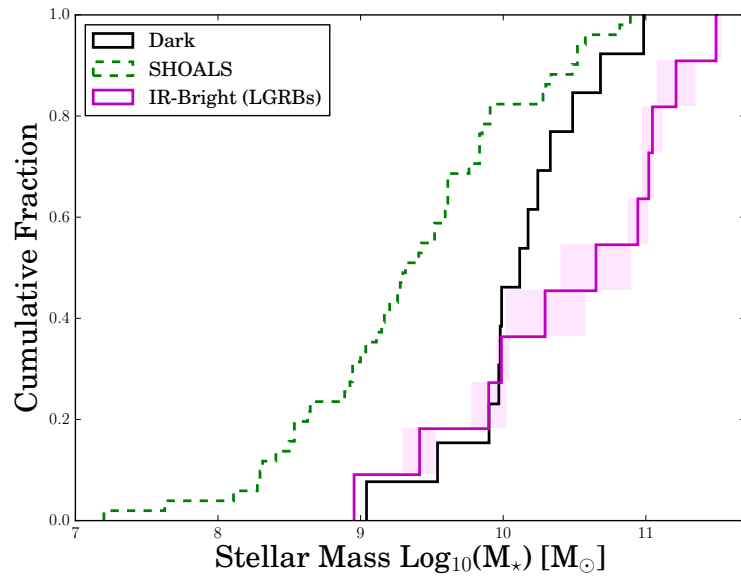


Figure 2.14: The cumulative distribution of stellar masses in the IR-bright host population, the SHOALS sample, and the dark burst sample. The IR-bright hosts appear to be more massive than even the dark burst population.

constraint on this is obtained from the SED fitting, parameterised by the  $V$ -band attenuation  $A_V$ . The cumulative distribution of  $A_V$  in the LGRB sample is shown in Figure 2.15. This is compared to the LGRB host distribution of  $A_V$  (where the sample is restricted to  $z < 2$ ), as determined by Perley et al. (2013) by correcting previous optically biased studies.

The bootstrap and KS-test results are again given in Table 2.9. 50 and 75 per cent bootstrap targets are provided to demonstrate the significance of the divergence of the distributions around  $A_V = 1$ . No *a priori* assumption is made about the extinction in optical non-detections. As in the case of the redshift distribution, it is appropriate to consider the possibility that the 5 optically undetected sources may, in fact, be biased and have very high dust extinction values. This would only strengthen the conclusion that IR bright sources are dustier than the typical host galaxy, while also making them more extreme outliers in redshift.

Regarding these comparisons, it should be noted that  $A_V$  is poorly constrained in a number of cases, in particular where (i) only UV upper limits are unavailable or (ii) where the best-fit SED diverges from the UV points. This is because MAGPHYS uses both the UV and IR, self-consistently, to estimate  $A_V$ . The lack of one of these bands, or a discrepancy between them, therefore results in large  $A_V$  uncertainties. Stellar masses, by comparison, are less affected since the optical/NIR better probes stellar mass - lower mass stars, which make up the bulk of a galaxy's mass, dominate emission in these bands.

Finally, I compare the population distribution in terms of the star formation rate in LGRB hosts. I compare the 7 IR-bright LGRB sources at  $z < 1$  for which there are SFR constraints (4 from SEDs, 3 from literature values) against the  $z < 1$  distribution reported by Salvaterra et al. (2009) and Japelj et al. (2016) for the BAT6 LGRB sub-sample in Figure 2.16. The KS-test p-value and bootstrap result in Table 2.9 fail to reject the null hypothesis that the IR bright sources are typical examples drawn from the underlying LGRB population.

### 2.7.5 Host Luminosity

Given a large range of source redshifts, any single photometric band samples a range of rest frame wavelengths, complicating an analysis of their rest frame magnitudes. Perley et al. (2016b) obtained *Spitzer*  $3.6 \mu\text{m}$  photometry for each of their targets in the unbiased SHOALS catalogue. The  $3.4 \mu\text{m}$  W1 and *Spitzer*  $3.6 \mu\text{m}$  apparent magnitudes are transformed to absolute magnitudes, without K-correction (these correspond to a rest-frame wavelength of  $\sim 3.5 \mu\text{m}/(1+z)$  in each case). The absolute  $W1/(1+z)$  magnitudes of the LGRB sample are shown in Figure 2.17, and are



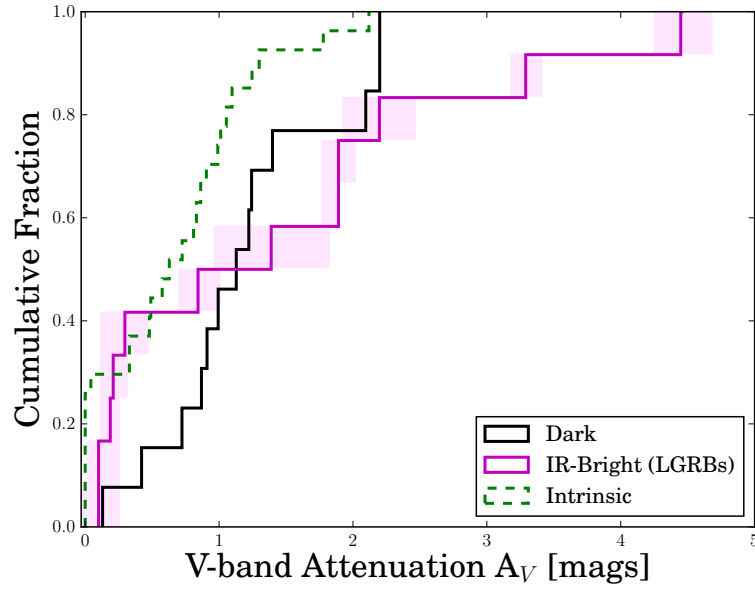


Figure 2.15: The cumulative distribution of  $A_V$  in the IR-bright host population, the dark sample and the derived ‘intrinsic’ distribution of Perley et al. (2013).

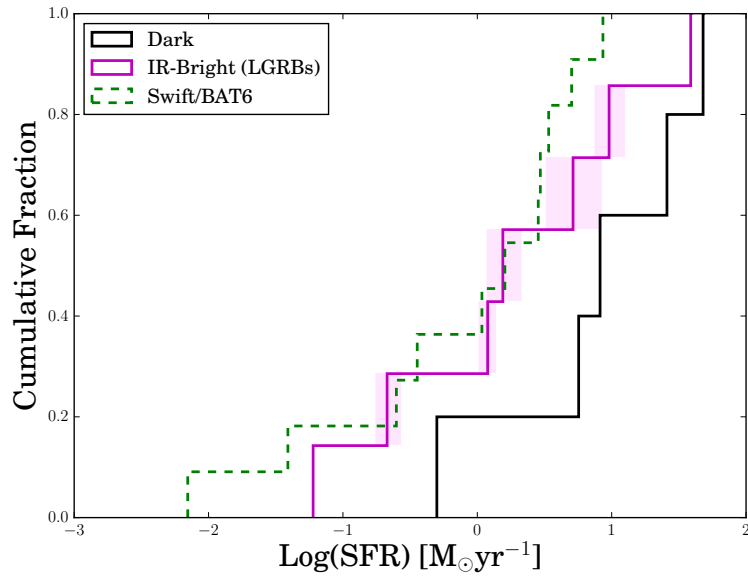


Figure 2.16: The cumulative distribution of SFR in the IR-bright LGRB host population, dark sample and the  $z < 1$  unbiased distribution of Japelj et al. (2016).

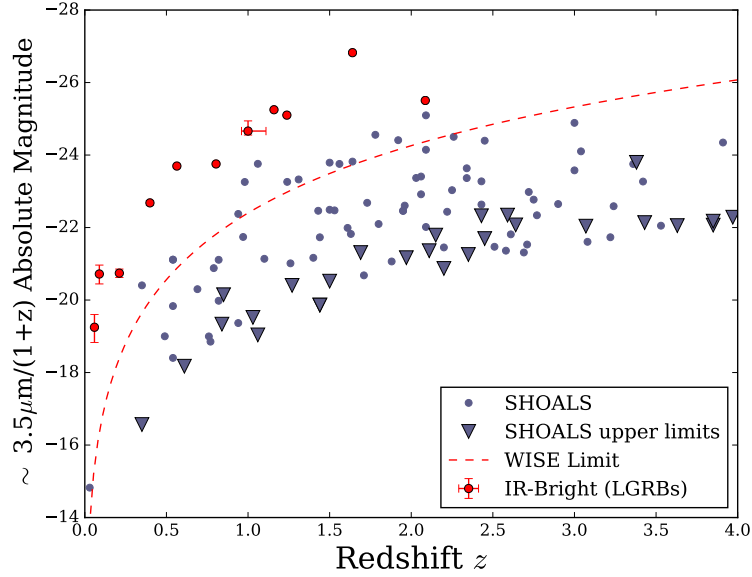


Figure 2.17: The absolute, rest-frame magnitude versus redshift for the IR selected hosts (red) and SHOALS. No K-correction is made to either sample. The absolute magnitude corresponding to the *WISE* apparent magnitude  $2\sigma$  limit is given by the dashed curve.

compared to the Perley et al. (2016b) distribution. Since this is a direct comparison with *Spitzer* data, the distribution in absolute magnitude at a given redshift is independent of the K-correction uncertainties. At low redshift ( $z \lesssim 0.6$ ), the W1 band is probing a fall off in the stellar flux and a rise in dust and PAH emission, rather than the stellar continuum. Above  $z \sim 0.6$  and below  $z \sim 3$ , the W1 magnitude is probing a fairly flat region of stellar emission and so is a good mass indicator. Again, the comparison to literature work is valid because the SHOALS magnitudes also suffer from this effect.

The faintest objects detected in *WISE* band 1 have an apparent magnitude  $m_{W1} \sim 20$ . Placing such a source at  $z = 2$  corresponds to a  $3.4\mu\text{m}/(1+z)$  absolute magnitude of  $\sim -24.5$ , which is at the very high end for GRB hosts as Figure 2.17 shows. The dashed line in Figure 2.17 indicates the  $2\sigma$  detection threshold for *WISE* as a function of redshift. It is clear that most SHOALS host galaxies, even at low redshift, fail to satisfy this threshold.

Matching is only against very bright sources, satisfying the cut-off for inclusion in the ALLWISE catalog. Perley et al. (2016b) obtained their  $3.6\mu\text{m}$  host galaxy fluxes by subtracting the flux from nearby bright sources to reveal an underlying host. This introduces the possibility that the IR flux may be overestimated.



However, in most cases no other optical source that might be the true origin of the *WISE* flux is seen. In other words, if the matched IR sources are simply chance alignments, then many of the GRB hosts would have to be too optically faint for detection in Pan-STARRS. In addition, it is known that IR-bright GRB hosts exist from previous work (Stanway et al., 2015b,a). Therefore, it is probable that the differences between the  $3.6\mu\text{m}$  magnitudes in this sample, and those of the SHOALS sample, are real.

The contrast between this sample and SHOALS is rather unsurprising, since the IR-bright sample is selected to be extreme in the W1 band. However, it does present the possibility that the bias towards low redshifts comes from sampling deeper into the host galaxy luminosity function. While the failure to identify higher redshift hosts may be a simple *WISE* data selection effect, the most luminous host galaxy would, theoretically, have been detectable out to  $z \sim 3$ . At these redshifts, the W1 band probes the rest-frame near-infrared and is unlikely to be strongly affected by dust, but the optical is probing the rest-frame ultraviolet, so dust extinction may account for observed optical non-detections.

### 2.7.6 Burst Luminosity

GRB studies have found a correlation between the rest-frame photon energy  $E_{p,i}$  at peak prompt emission, and the isotropic equivalent energy  $E_{\text{iso}}$ , known as the Amati relation (Amati et al., 2002; Amati, 2006). One member of the IR-bright host population, LGRB 080517, has already been identified as a sub-luminous low-luminosity GRB on this relation (Stanway et al., 2015a) due to its low  $E_{\text{iso}}$  and lower limit on  $E_{p,i}$ . I now consider whether other members of this population are low-luminosity bursts.

A number of targets in this sample have literature constraints on  $E_{\text{iso}}$  and  $E_{p,i}$ . Six bursts had  $E_{\text{iso}}$  and  $E_{p,i}$  estimates in the literature (see the references in Table 2.8 for details). For LGRBs 061002 and 050219A, I calculate  $E_{\text{iso}}$  and the rest frame peak energy  $E_{p,i}$  using the SDSS photometric redshift given in Section 2.6, the spectroscopic redshift presented by Rossi et al. (2014) and the bolometric fluence and observed peak energy provided by Butler et al. (2007). A cut-off power law is used to extrapolate from the gamma-ray band and infer  $E_{\text{iso}}$ . These eight GRBs with IR-bright hosts are placed on the Amati relation in Figure 2.18. Additional (non-IR bright) bursts are shown as grey circles in the background for reference, while the bursts from the IR-bright sample are shown in red (long bursts) and blue (short) with error bars. While LGRB 061002 lies in a similar region to LGRB 080517, towards the low-luminosity region of parameter space, the uncertainties cannot rule

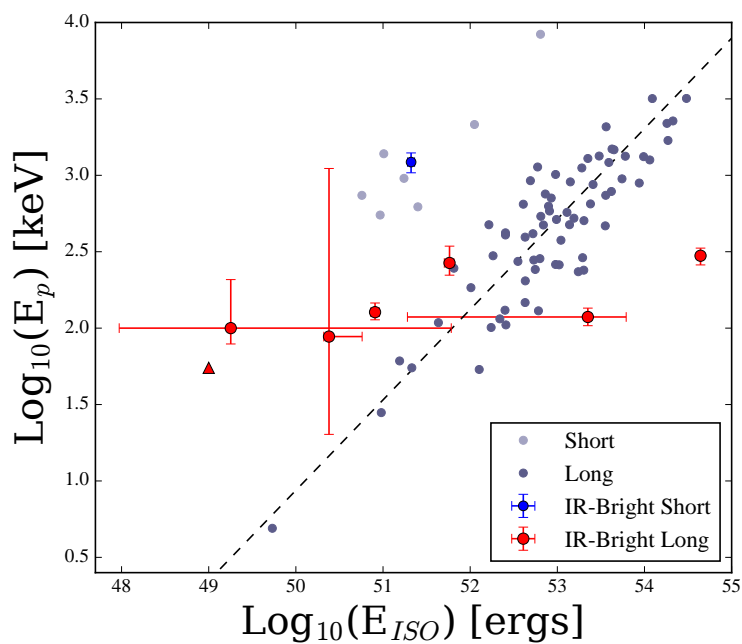


Figure 2.18: Placement of the GRBs on the Amati relation. The darker grey points are LGRBs and paler SGRBs. The long bursts with IR-bright hosts have red error-bars, the single short burst (SGRB 130603B) has blue. LGRB 080517 is indicated by the lower limit. I have calculated  $E_{iso}$  for LGRB 050219A and LGRB 061002, based on the  $E_p$  and  $S_{bol}$  values estimated by Butler et al. (2007).



out consistency with the Amati relation. Targets selected in the W1 band appear to cluster at the low  $E_p$  end of the distribution, consistent with expectations given the low redshift bias in this sample.

## 2.8 Interpretation

### 2.8.1 IR Sources with an Optical Counterpart

Our targets were selected to be bright in W1 imaging. At low redshifts, W1 lies above the bulk of stellar photospheric emission, while at intermediate redshift  $0.6 < z < 3$  it probes the bulk of the stellar mass. As Figure 2.17 makes clear, we are strongly limited by the shallow depth of W1 imaging in *WISE*. This introduces a Malmquist bias (Malmquist, 1922) which limits us to comparatively low redshift. Given that the star forming galaxy luminosity function favours less luminous systems, a larger fraction of the extant population at the lowest redshifts can be sampled, likely missing many of the galaxies in the more distant Universe.

However, many of the sources for which optical data is available are also extremely red (see Appendix A and Figures 2.11 and 2.12). Red colours can arise from either old stellar populations or dusty populations. The Balmer break, which appears in a galaxy spectrum after the death of hot young O stars, is an age indicator and so may allow us to distinguish between these two cases. In 2 of the 14 galaxy SEDs presented in Figure 2.11, there is no clear constraint on the Balmer break. In 5 cases there is a clear indication of a Balmer break. Even those galaxies with Balmer breaks have moderate star formation rates. Thus for the sources which are detected in the optical, old stellar populations can be ruled out as being dominant.

### 2.8.2 IR Sources without an Optical Counterpart

The population for which an IR-detection exists, but which remain undetected in optical surveys presents a slightly different challenge. It is possible that some of these may show a prominent  $4000\text{\AA}$  break, if the galaxy in question lies at  $z > 0.8$ . However, given the attenuation distribution presented in Figure 2.15, the failure to detect galaxies in the range  $1 < z < 3$  instead suggests that the rest-frame UV being probed at these redshifts has been attenuated by dust, resulting in observer-frame optical non-detections.

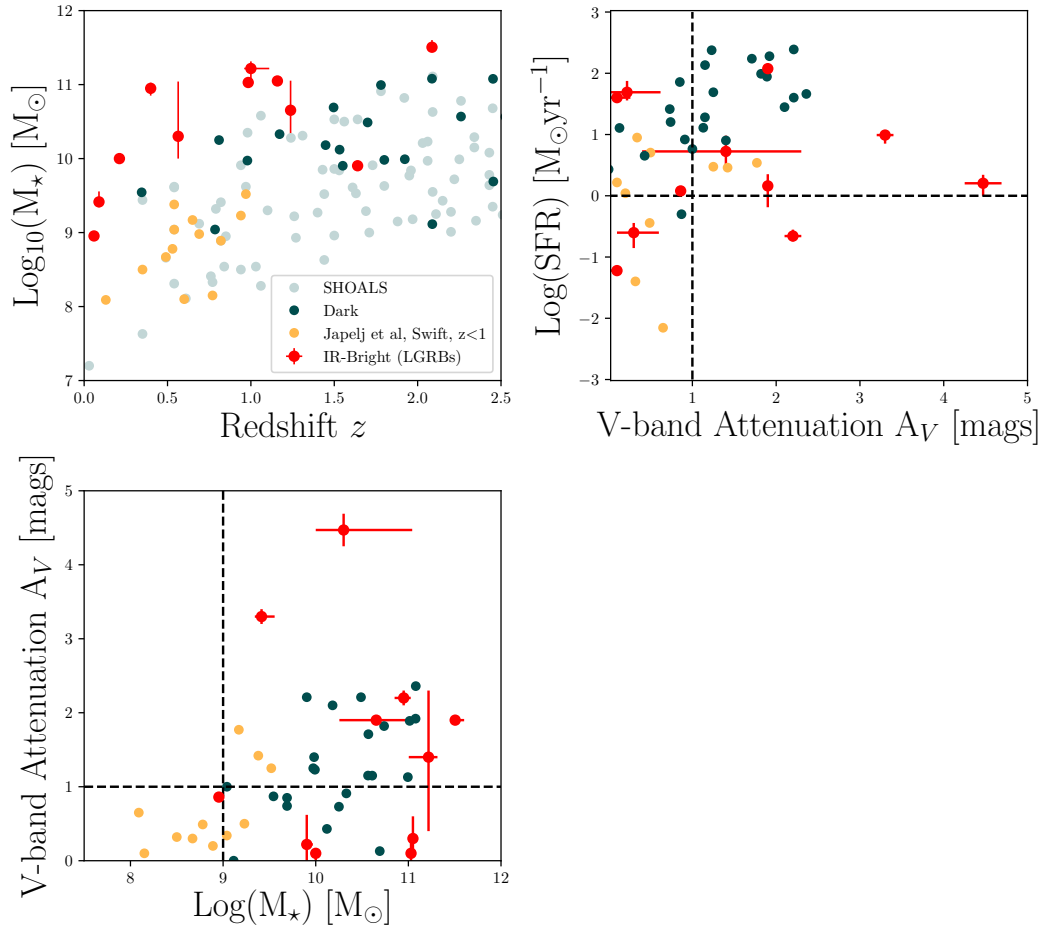
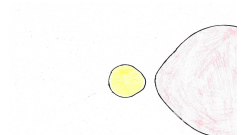


Figure 2.19: The distribution in physical property parameter space (mass, redshift, attenuation and SFR) of the IR-bright LGRB hosts with redshift estimates, as compared to the comparison samples discussed above. In each case, the IR-bright hosts are shown as red points with error bars. The dashed lines indicate regions of parameter space discussed in Section 2.8.



### 2.8.3 Host Galaxy Properties

In Figure 2.19 I present the multivariate distribution of properties for the LGRB hosts. While the W1 band magnitudes are bright by construction, the emission may arise for different reasons. The sources could be extremely dusty, or, if lying at  $0.6 < z < 3$ , may instead be very massive. Figure 2.19 indicates that these sources are amongst the most massive LGRB hosts known at their redshifts (Figure 2.19, left). In terms of attenuation and mass, mass appears to be the dominant factor (Figure 2.19, centre). Around half of the IR-bright sample are dusty for their star formation rate (Figure 2.19, right). In turn, this implies they have high mass for their SFR (Whitaker et al., 2017), or relatively low sSFRs for LGRB hosts (i.e. sit below what is known as the galaxy 'main sequence', Noeske et al., 2007). This is also seen in the sSFRs given in Table 2.8. While some hosts have high sSFRs of  $> 10^{-9} \text{ yr}^{-1}$ , as is expected from LGRB hosts generally, others have low values (e.g.  $6 \times 10^{-12} \text{ yr}^{-1}$  for LGRB 050219A and  $3.8 \times 10^{-11} \text{ yr}^{-1}$  for LGRB 080517).

This has implications for the supply and depletion of molecular gas in these systems. If the sample is preferentially selecting molecular gas (and therefore star formation) poor systems, this implies either that the hydrogen gas in these systems is in a different phase (i.e. heated by shocks, interactions or a large scale environment effect) or that there is very little gas, as might be seen in an old underlying system which accretes a small star forming satellite. This latter scenario has already been demonstrated in the most luminous example in this sample of IR-bright systems, the host of LGRB 080517 (Stanway et al., 2015b, and in prep). However a molecular gas detection has recently been reported for a second GRB host in the IR-bright selection, the dark burst LGRB 080207 (Arabsalmani et al., 2018), and two galaxies in the LGRB sample (080517 and 100316D) have detections of IR molecular hydrogen emission lines (Wiersema et al., 2018). Arabsalmani et al. (2018) find that the host of LGRB 080207 appears to follow the normal scaling relations for star forming galaxies and is not noticeably poor in molecular gas. It is however a dark burst, in a host which has already been noted for being relatively massive and dusty - criteria which bring it into the overall sample. This implies that molecular gas rich systems are not being preferentially selected.

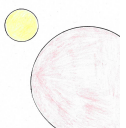
### 2.8.4 The Nature of the IR-bright population

Figure 2.19 shows that the IR-bright LGRB host sample may not have a single set of consistent properties. If sample is divided into dusty ( $A_V > 1$ ) vs non-dusty, and massive ( $\log_{10}(M_*/M_\odot) > 9$ ) vs less massive, I find that of 11 LGRB host galaxies in

the sample that have  $M_\star$  and  $A_V$  information, 6 would be classed as both massive and dusty, while 4 are simply massive, and one is on the border of being low in mass and not dusty.

A question thus arises: is this a distinct population, or is it sampling the tails of existing and known populations? The diversity of host galaxy properties favours the latter possibility. There is no clear separation between the IR luminous host galaxies and the bulk of the LGRB population in any projection of parameter space. While IR-bright sources are dustier than the bulk of the population over the same redshift range, they do not lie significantly outside of the range of typical LGRB host properties, with both  $A_V$  and another extreme property (e.g. high stellar mass, low redshift) required for selection. This suggests that the tails of previously established host distributions are being sampled. As such, it is unlikely that implications for LGRB progenitors can be derived from this sample. Nonetheless, selection in these relatively shallow infrared bands is useful for constraining the tails of existing distributions and therefore the full range of LGRB host properties.

This analysis has identified 2 new candidate GRB hosts. These are LGRB 080517, which has already been extensively studied (Stanway et al., 2015a,b) following selection with this methodology, and LGRB 061002. This burst has a false alarm probability for association with the IR-bright galaxy of only 0.0003. Existing host candidates have also been newly identified as being bright in the *WISE* bands. Generally, the low number of IR-bright GRB hosts found (only 20 from  $\sim 1000$  bursts), is consistent with expectations for the following reasons. First and foremost, a shallow survey such as *WISE* only allows us to sample low redshifts, covering a small cosmological volume. A secondary effect might be arising because the LGRB rate appears to be suppressed in the local Universe (e.g. Perley et al., 2016a), tracing the star formation rate density but also the increase in metallicity over cosmic time. Local and/or massive and dusty galaxies are typically detected in *WISE*, however massive and dusty galaxies are typically higher in metallicity and are less often seen to host LGRBs. SGRBs could be hosted by these classes of galaxy, however short bursts are intrinsically less luminous and have a much lower observed redshift distribution. Finally, by the time high enough redshifts are reached that the rest frame bands LGRB hosts are bright in (e.g. UV) are redshifted to W1, the emission is too faint for detection by shallow surveys such as *WISE*. These factors conspire to produce only small sample of GRB hosts that can be detected in *WISE*.



### 2.8.5 The Utility of IR-bright GRB host selection

In theory, using these data, it is possible to calculate the fraction of low redshift and massive, dusty GRB hosts that have been missed in previous follow up studies. This is primarily true for low redshift galaxies. As Figure 2.17 shows, the *WISE*  $2\sigma$  limit corresponds to absolute magnitudes of  $\sim -18$  at  $z = 0.1$ . This is well below the knee of the galaxy luminosity function, probing galaxies of  $\approx 0.1 L^*$  and above (Babbedge et al., 2006). Therefore, a naive expectation might be to see the majority of galaxies at  $z < 0.1$  in *WISE*.

However, the cross matching procedure fails to capture bursts at very large apparent offsets from their hosts, and this primarily affects short bursts and the lowest redshift galaxies in the GRB population. In fact, of the three known long bursts at  $z < 0.05$ , zero are identified as IR-bright. There are four long bursts known to be at  $0.05 < z < 0.1$ , of these two are detected and one was selected as low  $z$  purely on the basis of its *WISE* detection. The remaining two GRBs constitute one source at large offset from a very extended galaxy, and one source in a highly sub-luminous host. This demonstrates that 3.6 micron selection is not a highly efficient method for identifying low redshift bursts in all cases, but nonetheless that for typical galaxies in its redshift sweet spot, we would expect to have identified any source present in the archival data. Thus, while the continued presence of  $z < 0.05$  galaxies in the archival data set cannot be ruled out, it can be said with reasonable confidence that the fraction of GRB hosts without redshift identifications which lie at  $0.05 < z < 0.10$  is very low. With the exception of GRB 080517, which was selected as part of this sample, no further candidates in this range are identified. At least half of those present should have been found, unless the GRB host luminosity function has a steep faint end slope. This suggests that the total number of  $0.05 < z < 0.1$  hosts still remaining unidentified in the archival sample is of order a few, at most.

Note that deeper IR data, obtained for example with *JWST*, would detect galaxies further down the luminosity function, but would not overcome the issues of large projected offsets or galaxy sizes. It is therefore possible that future deeper infrared surveys will allow this analysis to be extended to slightly higher redshifts, and, for example, characterise the overlooked GRB hosts (if any) at  $0.1 < z < 0.3$ .

## 2.9 Conclusions

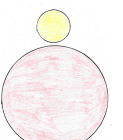
A population of infrared-bright GRB host galaxies has been identified by cross-matching X-ray afterglow positions to the ALLWISE catalogue. Selective cuts in apparent magnitude and catalogue quality flags, in addition to a false alarm prob-

ability analysis, yield 55 IR-sources that are convincingly associated with a GRB X-ray position. Compiling photometry from surveys and targeted observations, I perform SED fitting, finding that 14 sources fit well to galaxy templates and 14 are best-fitting to stellar SEDs. The remainder are either cut from the sample, optically undetected, lacking survey coverage or have been previously studied. Spectroscopy of 6 targets supplements the photometric data and allows us to rule out 3 stellar interlopers. The methodology described in this Chapter has identified the host of LGRB 080517, and potentially LGRB 061002. The former has already undergone extensive study, while the candidate host of LGRB 061002 is newly reported here. Focusing on LGRB hosts in particular, I find that the population is biased towards massive, dusty and low redshift galaxies, with respect to unbiased samples of LGRB hosts. The low redshift bias appears to be due to the depth of *WISE*, and within this low redshift population, galaxies with high stellar mass and dust content are selected. Dusty and local galaxies are the most frequently discovered hosts of dark and low-luminosity LGRBs respectively, classes of burst which are crucial to understand if we are to develop a full picture of the collapsar GRB phenomenon. I propose that the spatial association of an IR-bright galaxy with an LGRB is therefore a good indication that an unusual host system has been identified.

## 2.10 Subsequent Developments

The work described in this Chapter was published in the *Monthly Notices of the Royal Astronomical Society* in April 2018. Since then, there have been a number of new GRBs at prominently low redshifts. Most notably among these are GRBs 180720B ( $z = 0.654$ , Vreeswijk et al., 2018), 190114C ( $z = 0.42$ , Selsing et al., 2019a) and 190829A ( $z = 0.08$ , de Naurois, 2019, one of the closest ever GRBs), which are the first three GRBs to be detected at Very High Energy (VHE). Of these, a 2.5 arcsec cross-match with the ALLWISE catalogue using the *Swift* XRT positions yields 1 match - to GRB 190114C. The source has a W1 magnitude of  $20.1 \pm 0.1$ . There is no IR source in the vicinity of GRB 180720B out to at least 10 arcsec, while there is a match to GRB 190829A at 8.4 arcsec (W1 magnitude  $15.92 \pm 0.03$ ). Although outside the matching radius, this source is ostensibly the host galaxy given the low redshift and comparison to Pan-STARRS imaging. These results are broadly consistent with the findings described in this Chapter, that very low redshift hosts are missed by the matching process (because they are too extended) and high-redshift hosts are too faint unless particularly dusty.

These first TeV GRB detections are consistent with all long GRBs producing



TeV emission in the afterglow phase, as these bursts were both intrinsically energetic and low redshift. The results help to resolve a long standing energy budget problem in GRBs, that the prompt and afterglow total energies were discrepant. It now appears as though some energy is transferred to very high energy photons through inverse Compton scattering, after the initial prompt emission (based on a MAGIC detection of GRB 190114C and subsequent analysis, MAGIC Collaboration et al., 2019a,b).

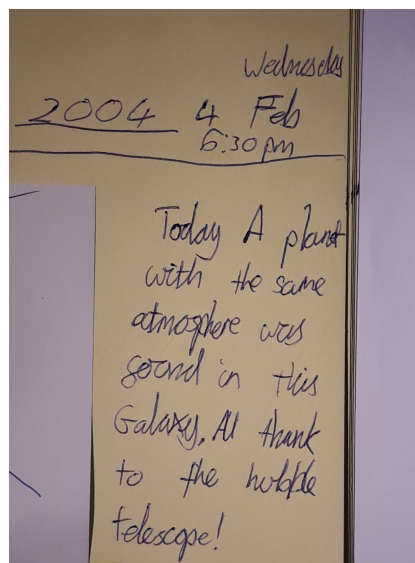
On the short GRB side, it is worth mentioning the multi-messenger neutron star merger event GW 170817. The host galaxy is bright in the WISE bands, thanks to its proximity (at  $z = 0.0098$ , it is the closest short GRB to date, Levan et al., 2017), with  $m_{W1} = 12.64 \pm 0.02$ . Again, as the galaxy is extended in WISE (and the burst was offset from the host centre), the burst and WISE catalogue position are 10.3 arcsec apart. The galaxy has a predominantly old stellar population (as expected for a short GRB host), a smooth morphology, and some dust lanes, however the burst site is in the outskirts of the galaxy and has a relatively low extinction of 0.2 magnitudes in the  $V$ -band. Overall, the galaxy is not particularly dusty and the brightness in WISE is due to its low distance.

It should be noted that the ALLWISE catalogue used for this work has recently been superseded by ‘unWISE’. This incorporates  $\sim 5$  years worth of NEOWISE (asteroid search) imaging to reach deeper limits (on average,  $5\sigma$  detections are reached 0.7 magnitudes fainter than in ALLWISE). Improvements to the handling of source crowding have also been made. The result is that the number of catalogued galaxies is doubled in the range  $0 < z < 1$  and tripled across  $1 < z < 2$  (Schlafly et al., 2019).

Finally, another survey dataset made public since this work is the second *Gaia* data release (Gaia Collaboration et al., 2018). This dataset contains proper motions, down to milliarcsecond precision, for  $\sim 1.5$  billion astronomical objects. Of the objects identified photometrically as stars and galaxies in Table 2.1 (tagged as *PS* or *PG*), 4 of the 5 stars were detected with significant proper motion (the fifth, the 120119A associated object, is too faint for *Gaia* detection). Matching was performed using a  $1.5R_{90}$  matching radius. The only galaxy to provide a match to the XRT afterglow coordinates was the host of GRB 150101B, for which no *Gaia* proper motion is reported. The other objects were again too faint for detection. The *Gaia* data is therefore consistent with the classifications made in this Chapter.

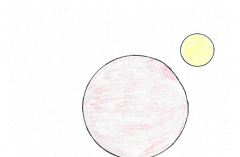
## Chapter 3

# Chandra and Hubble Space Telescope Imaging of dark gamma-ray bursts and their host galaxies



— The Author, school scrapbook

*“Little did 9-year-old me know that 14 years later, I would actually be using HST data. Also, I’m not sure that the exoplaneteers actually did discover a planet ‘with the same atmosphere’. I therefore retract my statement.”*



In this Chapter, I present a study of 21 dark GRBs and their host galaxies, observed with the *Chandra X-ray Observatory (CXO)* and *Hubble Space Telescope (HST)*. The sub arcsecond astrometric accuracy of *CXO* X-ray imaging, combined with deep *HST* optical and NIR imaging, facilitates the precise location of bursts and the identification of faint hosts down to magnitude  $\sim 27$ . As well as increasing the statistical certainty that dark GRBs favour luminous, dusty hosts, I exploit the spatial resolution of *HST* to examine the projected morphology of the GRB hosts. Crucially, these data also put constraints on the fraction of dark bursts arising from high-redshift ( $z > 5$ ). Hereafter in this Chapter, I use GRB to refer to long GRBs, and there is no discussion of the short duration bursts.

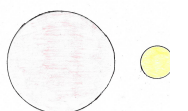
### 3.1 Introduction

Although most GRBs display a synchrotron afterglow in the optical bands if deep and early follow-up imaging is performed, a significant minority do not. The first example where this was found to be the case was GRB 970828 (Groot et al., 1998b), which showed no afterglow down to an  $r$ -band magnitude limit of  $\sim 23$  within 12 hours post-burst. Such events have subsequently become known as dark bursts (Fynbo et al., 2001, see also Section 1.5 and Chapter 4). A commonly used formal definition for dark GRBs is an X-ray to optical spectral slope  $\beta_{\text{OX}}$  of less than  $\sim 0.5$  (Jakobsson et al., 2004), effectively the limit allowed by standard synchrotron afterglow theory. Alternatively, the X-ray spectral slope can be extrapolated (Rol et al., 2005) according to a power of the form  $F_\nu \propto \nu^{-\beta_X}$ , and darkness defined as when  $\beta_{\text{OX}} < \beta_X - 0.5$  (van der Horst et al., 2009). It should be noted however that GRB emission can deviate from this simple synchrotron model, with plateaus, flares and variable decay rates often being seen (particularly in the X-ray, Evans et al., 2009; Gompertz et al., 2018). Estimates for the fraction of GRBs which are dark vary, but are typically around 25-40 per cent (e.g. Fynbo et al., 2009; Greiner et al., 2011; Perley et al., 2016a).

There are three possible explanations for darkness in GRBs (Greiner et al., 2011). Firstly, the burst may be intrinsically suppressed at optical wavelengths. Although this is disfavoured due to the difficulty in explaining such a spectral shape, it may be plausible in particularly low density environments, or if the spectral energy distribution is measured during a non-standard phase such as a flare or plateau. Second, the burst may be at high-redshift (defined as  $z > 5$ ), where observations in the optical correspond to rest frame wavelengths blue-wards of the Lyman break (noting also that the  $\text{L}\alpha$  forest may be dense enough to produce a comparable effect

at redshift  $4 < z < 5$ ). GRBs at  $z > 5$  are known to be rare in the spectroscopically confirmed sample (e.g. Kawai et al., 2006; Ruiz-Velasco et al., 2007; Salvaterra et al., 2009; Greiner et al., 2009; Tanvir et al., 2009; Cucchiara et al., 2011; Tanvir et al., 2018). Finally, the host galaxy (or Milky Way sight-line) might be dusty, so that the optical afterglow is reddened and attenuated. The last of these is favoured as the most frequent scenario, not least because the host galaxies of dark bursts are often detected at optical wavelengths, ruling out a high-redshift origin. The inferred rate of GRBs at high-redshift is therefore low (current estimates put  $\sim 10$ -20 per cent of dark GRBs at  $z > 5$ , Greiner et al., 2011; Jakobsson et al., 2012; Perley et al., 2016a).

The study of GRB host galaxies has provided additional insight into the environments capable of producing GRBs (Ramirez-Ruiz et al., 2002; Trentham et al., 2002), and by extension the nature of the progenitor systems. The GRB host population is overwhelmingly star forming and the burst locations trace this star formation, as measured through both projected, host normalised offsets and the fractional light  $F_{\text{light}}$  statistic (Bloom et al., 2002; Fruchter et al., 2006; Svensson et al., 2010; Blanchard et al., 2016; Lyman et al., 2017; Japelj et al., 2018). GRBs do not appear to be entirely unbiased tracers of star formation, however. Early studies of GRB hosts reported a strong bias against massive galaxies, implying some level of metallicity aversion in GRBs (Le Flocc’h et al., 2003; Fruchter et al., 2006; Savaglio et al., 2009) due to the mass metallicity relation (Tremonti et al., 2004). However, the first studies of this kind tended to use optical afterglows for host localisation, and therefore systematically omitted the hosts of dark GRBs from their samples. Subsequently, efforts have been made to account for this effect by specifically including dark hosts (Cenko et al., 2009; Krühler et al., 2011; Hjorth et al., 2012; Perley et al., 2013, 2016a), made possible by NIR afterglow imaging, or X-ray facilities such as the *Neil Gehrels Swift Observatory* (Gehrels et al., 2004) and its on-board X-Ray Telescope (XRT; Burrows et al., 2004). XRT provides  $\gtrsim 1$  arcsec localisation accuracy, sufficient in some cases to identify a probable host candidate. Because most dark GRBs are hosted by galaxies which are more massive, dustier and more chemically enriched than the wider population, their inclusion should weaken any bias relative to the underlying star formation distribution. Optically unbiased GRB host studies have shown this to be true, but despite the addition of more massive GRB hosts, some form of metallicity bias still appears to exist in the population (Perley et al., 2013; Krühler et al., 2015; Perley et al., 2016a,b). However, the precise value of this cutoff remains uncertain. There are a handful of cases with  $\sim$  Solar metallicity which suggest a hard cut-off is unlikely (Graham and Fruchter,



2017). If GRBs can genuinely be created at Solar metallicity, it is challenging for single star progenitor models which predict too much mass and angular momentum loss through winds at these metallicities (Vink et al., 2001; Hirschi et al., 2005). Solutions have been offered in the form of chemically homogeneous evolution, or binary pathways (e.g. Yoon et al., 2012; Szécsi et al., 2015; Song et al., 2016; Eldridge et al., 2017, and references therein). The exact nature of the host galaxy bias is still debated, with implications for both the progenitors and the usefulness of GRBs as tracers of star formation across cosmic time.

In this Chapter, I use the spatial resolution of *CXO* X-ray imaging, and the depth of *HST* imaging, to investigate the nature of dark GRB host galaxies as a population, probing their colours, morphologies, and the spatial distribution of dark GRBs within their hosts. The Chapter is structured as follows. In Section 3.2, I detail the observations and data reduction. Section 3.3 outlines the methodology, and in Section 3.4 I present results. This is followed by a discussion and conclusions in Sections 3.5 and 3.6.

## 3.2 Observations and Data Reduction

### 3.2.1 Target Catalogue

A total of 21 dark GRB positions were imaged with *HST* (PI: Levan)<sup>1</sup>. The criteria for inclusion was an X-ray to optical spectral slope,  $\beta_{\text{OX}}$ , of less than 0.5 (measured within 12 hours post-burst), and a Galactic foreground extinction of  $A_V < 0.5$  (determined from the dust maps of Schlegel et al., 1998). For *CXO* observations it was necessary that no more precise position (e.g. optical/radio) was available at the time of the *CXO* trigger. No further selection criteria were applied, although not all candidates in a given cycle could be followed up due to limits on the available observing time. For each burst, a  $\beta_{\text{OX}}$  limit is provided in Table 3.1. Where an analysis has not already been performed in the literature, these are determined from reported optical limits, and the extrapolated X-ray flux at the time of these observations assuming a simple power law<sup>2</sup>.

Because the optical afterglows of dark GRBs are by definition faint or undetected, they seldom yield absorption-line redshifts. Redshifts for dark bursts must therefore come from observations of a likely host candidate. Only 9 of the sample have redshifts (either photometric or spectroscopic) from the literature, these are listed in Table 3.5. In Figure 3.1, I compare the *known* redshifts in this sample to

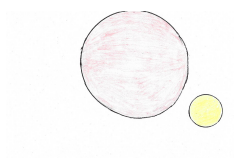
<sup>1</sup>Programmes 11343, 11840, 12378, 12764, 13117 and 13949

<sup>2</sup>[http://www.swift.ac.uk/xrt\\_curves](http://www.swift.ac.uk/xrt_curves)

Table 3.1: Approximate  $\beta_{\text{OX}}$  limits, calculated by extrapolation of the X-ray lightcurves out to the time of deep optical observations. I correct for Galactic foreground extinction with the updated dust maps of Schlafly and Finkbeiner (2011). Otherwise, where a detailed analysis of the afterglow has been carried out in the literature, that value is reported here.

GRB	$\beta_{\text{OX}}$	Reference
051022 <sup>†</sup>	<-0.1	Rol et al. (2007a)
080207 <sup>†</sup>	<0.3	Svensson et al. (2012)
090113 <sup>†</sup>	<0.3	Krühler et al. (2012b)
090404 <sup>†</sup>	<0.2	Perley et al. (2013)
090407 <sup>†</sup>	<0.4	Krühler et al. (2012b)
090417B <sup>†</sup>	<-1.9	Holland et al. (2010)
100205A	<0.3	Malesani et al. (2010)
100413A	<0.2	Filgas et al. (2010)
100615A	<-0.6	Nicuesa et al. (2010a)
110312A	<0.2	Nicuesa Guelbenzu et al. (2011)
110709B	<-0.1	Fong and Berger (2011)
110915A	<0.2	Malesani et al. (2011)
111215A <sup>†</sup>	<0.2	van der Horst et al. (2015)
120320A	<0.5	Chester and Markwardt (2012)
130131A	<0.4	Siegel and Grupe (2013)
130502B	<0.3	Malesani et al. (2013)
130803A	<0.5	Littlejohns et al. (2013)
131229A	<-0.3	Graham et al. (2013)
140331A	<0.2	Butler et al. (2014)
141031A	<0.1	Trotter et al. (2014)
150616A	<-0.4	Murphy et al. (2015)

<sup>†</sup> - These  $\beta_{\text{OX}}$  limits are obtained from the literature.



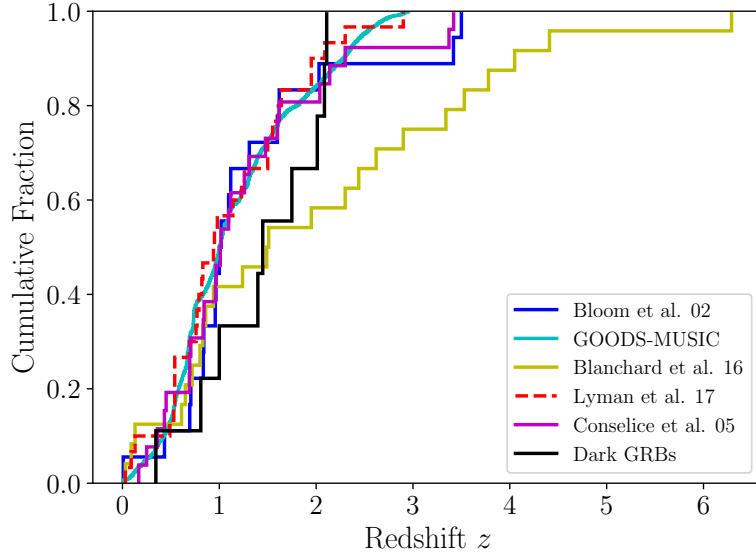


Figure 3.1: A comparison between the redshift distribution of the dark GRB sample, other similar studies and the GOODS-MUSIC galaxy survey. The dark hosts with redshifts have a distribution comparable to the other samples, however many of them do not have this information and may be biased towards higher  $z$ .

the redshift distributions from Bloom et al. (2002), Blanchard et al. (2016, with which there is sample overlap) and Lyman et al. (2017), who all provide burst-host galaxy spatial offsets for mixed (dark and bright) or exclusively optically-bright GRB samples. I also show the redshift distribution of Conselice et al. (2005), whose concentrations and asymmetries are compared to later, and the GOODS-MUSIC galaxy survey (Grazian et al., 2006b; Santini et al., 2009). The distributions are similar - with the exception of Blanchard et al. (2016) - and assuming that dark GRBs without redshifts are not significantly biased towards high  $z$ , these therefore represent fair comparison samples for the parameters of interest.

### 3.2.2 *Hubble Space Telescope*

Each burst location was imaged with *HST* in two bands, F160W ( $\lambda_{\text{eff}} \sim 15400\text{\AA}$ , IR) and F606W ( $\lambda_{\text{eff}} \sim 6060\text{\AA}$ , UVIS). An exception is GRB 080207 which has F110W imaging instead of F160W for the IR (Svensson et al., 2012). For all IR observations, and most UVIS, the Wide Field Camera 3 (WFC3) was used. For 4 UVIS observations, the Advanced Camera for Surveys (ACS) was employed, and the Wide Field Planetary Camera 2 (WFPC2) was used once (for GRB 080207). The details of these observations are given in Table 3.2.

The exposures for the *HST* targets were dithered, at least twice or up to 4 times depending on the exposure times. The charge transfer efficiency (CTE) corrected images were reduced with standard ASTRODRIZZLE procedures, available with the python package DRIZZLEPAC<sup>3</sup>. The PIXFRAC was chosen to be 0.8 in every case, while the final scale is 0.065 arcsec pixel<sup>-1</sup> for IR images and 0.02 arcsec pixel<sup>-1</sup> for UVIS. Exceptions are the ACS images where a 0.03 arcsec final pixel<sup>-1</sup> scale is used, the sole WFPC2 example where it is 0.07 arcsec pixel<sup>-1</sup>, and the three IR images in programme 13949 where only two dithers were available and the final scale is 0.085 arcsec pixel<sup>-1</sup>. A subset of these data were previously published in Blanchard et al. (2016), and similar results are obtained in these cases.

### 3.2.3 *Chandra*

Out of 21 burst locations observed with *HST*, 18 have been observed with *CXO* and its Advanced CCD Imaging Spectrometer (ACIS) instrument (all PI: Levan, with the exception of GRB 051022, PI: Kouveliotou). Standard CIAO (v4.9, with CALDB v4.7.6) procedures were used to reduce the data, including reprocessing, PSF map creation and energy filtering of the event files to the range 0.3-8 keV. WAVDETECT is then used to identify sources in the field. A list of the observations used is provided in Table 3.3.

## 3.3 Methodology

### 3.3.1 Astrometric Alignment

The default pipeline processing can result in astrometric offsets between *Chandra* and *HST* of order a few arcsec. Because the burst-host offsets are expected to be much smaller than this (e.g, Blanchard et al., 2016; Lyman et al., 2017), a refined astrometric solution was required to precisely locate the burst with respect to the host. This involved identifying sources in common between images, and computing the best transformation that maps one set of coordinates onto the other, a process referred to as astrometric tying. In almost all cases, there were insufficient sources in common between *HST* and *CXO* to perform a direct tie. For reference, the fields of view are 136×123 arcsec in the WFC3 IR channel of *HST* (162×162 in UVIS) and 8.3×8.3 arcmin for the field of view of *CXO*/ACIS in high-resolution mode.

Because *CXO*/ACIS has a much wider field of view, and a lower source den-

---

<sup>3</sup><http://drizzlepac.stsci.edu>

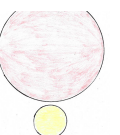


Table 3.2: Details of the *HST* observations.

GRB	Prog.	Date	Inst.	Filter	Exp. [s]
051022	11343	2009 Oct 12	WFC3	F160W	2397
051022	11343	2009 Aug 21	ACS	F606W	2080
080207	11343	2009 Dec 09	WFC3	F110W	1600
080207	11343	2008 Mar 18	WFPC2	F606W	1600
090113	11840	2009 Oct 17	WFC3	F160W	2612
090113	11840	2009 Oct 15	ACS	F606W	2208
090404	11840	2010 Jan 09	WFC3	F160W	2612
090404	11840	2010 Sep 02	ACS	F606W	2208
090407	11840	2010 Sep 15	WFC3	F606W	740
090407	11840	2010 Sep 15	WFC3	F160W	1209
090417B	11840	2009 Oct 17	WFC3	F160W	2612
090417B	11840	2011 Jan 22	ACS	F606W	1656
100205A	11840	2010 Dec 06	WFC3	F606W	1140
100205A	11840	2010 Dec 06	WFC3	F160W	1209
100413A	11840	2010 Aug 31	WFC3	F606W	752
100413A	11840	2010 Aug 31	WFC3	F160W	1209
100615A	11840	2010 Dec 16	WFC3	F606W	1128
100615A	11840	2010 Dec 16	WFC3	F160W	1209
110312A	12378	2011 Nov 17	WFC3	F606W	1110
110312A	12378	2011 Nov 18	WFC3	F160W	1209
110709B	12378	2011 Nov 12	WFC3	F160W	2612
110709B	12378	2011 Nov 08	WFC3	F606W	2480
110915A	12764	2011 Nov 03	WFC3	F160W	2612
110915A	12764	2011 Oct 31	WFC3	F606W	2508
111215A	12764	2013 May 13	WFC3	F160W	1209
111215A	12764	2013 May 13	WFC3	F606W	1110
120320A	12764	2013 Feb 20	WFC3	F606W	1110
120320A	12764	2013 Feb 20	WFC3	F160W	1209
130131A	13117	2014 Oct 09	WFC3	F160W	1059
130131A	13117	2014 Oct 09	WFC3	F606W	1101
130502B	13117	2013 Dec 30	WFC3	F160W	2412
130502B	13117	2013 Dec 30	WFC3	F606W	2400
130803A	13117	2014 May 28	WFC3	F160W	1209
130803A	13117	2014 May 28	WFC3	F606W	1125
131229A	13117	2014 Aug 14	WFC3	F160W	1209
131229A	13117	2014 Aug 14	WFC3	F606W	1125
140331A	13949	2016 Mar 28	WFC3	F160W	1209
140331A	13949	2016 Mar 28	WFC3	F606W	1137
141031A	13949	2014 Nov 29	WFC3	F160W	1209
141031A	13949	2014 Nov 29	WFC3	F606W	1395
150616A	13949	2016 Feb 29	WFC3	F160W	1209
150616A	13949	2016 Feb 29	WFC3	F606W	1329

Table 3.3: Details of the *CXO* observations. All imaging was performed with ACIS-S. The modified Julian Date (MJD) of the observation mid-point is provided, as is the mean count rate in the 0.3-8 keV energy range. The J2000 R.A. and Dec of the afterglow, in the *CXO* world coordinate system, is also listed.

GRB	Obsv. ID	Date	MJD	Exp. [ks]	Count Rate [s <sup>-1</sup> ]	R.A.	Dec.
051022	5536	2005 Oct 05	53668.88	18.72	$(2.83 \pm 0.03) \times 10^{-2}$	23:56:04.09	+19:36:23.90
080207	9474	2008 Feb 15	54511.97	14.83	$(6.00 \pm 0.93) \times 10^{-4}$	13:50:02.97	+07:30:07.60
090113	10490	2009 Jan 19	54850.52	14.85	$(2.09 \pm 0.17) \times 10^{-3}$	02:08:13.77	+33:25:43.30
090404	10491	2009 Apr 13	54934.35	14.85	$(6.53 \pm 0.22) \times 10^{-3}$	15:56:57.50	+35:30:57.50
090407	10492	2009 Apr 18	54939.79	14.96	$(2.66 \pm 0.17) \times 10^{-3}$	04:35:55.06	-12:40:45.10
090417B	10493	2009 May 11	54962.67	13.70	$(1.31 \pm 0.15) \times 10^{-3}$	13:58:46.63	+47:01:04.40
100413A	11772	2010 Apr 19	55305.05	14.94	$(3.51 \pm 0.18) \times 10^{-3}$	17:44:53.13	+15:50:03.70
100615A	12229	2010 Jun 21	55368.15	14.84	$(1.48 \pm 0.03) \times 10^{-2}$	11:48:49.34	-19:28:52.00
110312A	12919	2011 Mar 22	55642.95	14.86	$(7.63 \pm 0.22) \times 10^{-3}$	10:29:55.49	-05:15:44.70
110709B	12921	2011 Jul 23	55765.59	14.86	$(4.18 \pm 0.19) \times 10^{-3}$	10:58:37.11	-23:27:16.90
110915A	14051	2011 Sep 26	55830.66	14.86	$(1.25 \pm 0.15) \times 10^{-3}$	20:43:17.93	-00:43:23.90
111215A	14052	2011 Dec 28	55923.20	14.77	$(9.22 \pm 0.23) \times 10^{-3}$	23:18:13.30	+32:29:39.40
120320A	14053	2012 Mar 26	56012.55	15.07	$(4.62 \pm 0.13) \times 10^{-3}$	14:10:04.27	+08:41:47.60
130502B	15194	2013 May 13	56425.07	14.69	$(2.70 \pm 0.18) \times 10^{-3}$	04:27:03.07	+71:03:36.50
131229A	15195	2014 Jan 06	56663.12	15.05	$(1.06 \pm 0.15) \times 10^{-3}$	05:40:55.62	-04:23:46.50
140331A	16161	2014 Apr 08	56755.15	14.86	$(5.52 \pm 1.25) \times 10^{-4}$	08:59:27.51	+02:43:02.80
141031A	16162	2014 Nov 06	56967.30	10.19	$(4.58 \pm 0.26) \times 10^{-3}$	08:34:26.09	-59:10:05.80
150616A	17235	2016 Jun 24	57197.30	14.76	$(8.63 \pm 0.24) \times 10^{-3}$	20:58:52.00	-53:23:38.00

sity, an wide-field intermediate was used, which was in most cases a Pan-STARRS<sup>4</sup> cutout (Chambers et al., 2016). Again, due to the low number of sources detected by *CXO* and the faintness of their associated optical counterparts, there were only a handful of *CXO*-Pan-STARRS matches in each case. To tie these images, I performed a similarity transform on the *CXO* coordinates, placing them in the intermediate frame. This transform conserves the relative distances between points, and involves an  $x - y$  shift, scaling and rotation. The scaling between images was known and fixed, and if necessary to avoid over-fitting, the rotation obtained from the image headers was assumed to be correct. In this scenario, the root-mean-square uncertainties, whilst incorporating offsets due to any rotation errors present, were derived as if only  $x - y$  shifts were contributing. In this way, rotational uncertainties are still accounted for.

The next step, tying Pan-STARRS or an alternative intermediate to *HST*, provided many more tie objects allowing for a more sophisticated procedure. Tying was performed with the IRAF tasks GEOMAP and GEOXYTRAN, fitting for rotation, scaling in  $x$  and  $y$ ,  $x$ - $y$  shifts, and second or third order polynomial distortions.

The total tie uncertainty was estimated as the quadrature sum of the X-ray to intermediate, and intermediate to *HST* root-mean-square uncertainties. In turn,

<sup>4</sup>The Panoramic Survey Telescope and Rapid Response System, see <http://panstarrs.stsci.edu>



this was added in quadrature to the afterglow positional uncertainty, which is estimated as  $\text{FWHM}/(2.35 \text{ SNR})$  (where FWHM is the full-width at half maximum, and SNR is the signal-to-noise ratio, e.g. Birney et al., 2006). When measuring burst offsets, the uncertainty on the host centre was also considered, however this was usually at the sub-pixel level. Deviations from these standard procedures are as follows:

*GRB100205A*: No *CXO* data was available for this burst. Instead, the *HST* images were tied directly to a *K*-band Gemini-North image of the afterglow (Tanvir et al., 2010; Cucchiara et al., 2010). There was therefore no need for an intermediate image in this case.

*GRB130131A*: No *CXO* imaging is available. The *HST* images are tied directly to a *K*-band UKIRT image of the afterglow (Tanvir et al., 2013a). Again, no intermediate image was required.

*GRB130803A*: No *CXO*, optical or NIR afterglow was available, so I used the less-precise enhanced *Swift*/XRT position (1.5 arcsec)<sup>5</sup>.

*GRB141031A*: This source was too far south for Pan-STARRS coverage, and there were insufficient mutually detected objects between the *CXO* image and other available intermediates (e.g. 2MASS, SDSS) to perform a tie. Instead, I directly placed the *CXO* position onto the *HST* frame, after it had been astrometrically refined through cross-matching to the Hubble Source Catalogue (v3, Whitmore et al., 2016). The uncertainty on the burst position in the *HST* images was therefore given by the absolute astrometric accuracy of both *CXO* and the refined *HST* image, as well as the positional uncertainty of the *CXO* afterglow.

*GRB150616A*: This burst was too far south for Pan-STARRS coverage. Instead, I used a VLT/FORS2 image as the intermediate, from programme 095.B-0811(C) (PI: Levan).

Figure 3.2 shows the best position of the GRB in the *HST* frames for each burst. The larger, magenta error circles arise from the tie and afterglow uncertainties as described above. The smaller cyan and orange circles represent the host candidate brightest pixel and barycentre in each band respectively. I also show a zoomed out set of images for GRB 090113 in Figure 3.3, as there appears to be an offset between either the host galaxy or afterglow position between the two bands. Centring the images on the putative host’s barycentre in each band, we can see that the offset is primarily due to the difference in tie position with respect to the sources in the field. It should be noted that the error circles marked here and in Figure 3.2 enclose the  $1\sigma$  confidence regions, and so afterglow spatial offsets of this magnitude are not

---

<sup>5</sup>[www.swift.ac.uk/xrt\\_positions](http://www.swift.ac.uk/xrt_positions)

unexpected in a sample size of 21.

### 3.3.2 Host Measurement with SExtractor

Apparent magnitudes, enclosed flux radii and ellipticities were measured from the drizzled, charge-transfer-efficiency-corrected and filtered images with SExtractor (v2.19.5, Bertin and Arnouts, 1996). I resampled, registered and cropped the IR and UVIS images using SWARP (Bertin et al., 2002), allowing MAG\_AUTO to be used in dual-image mode. Flux is conserved in this process with variations due to re-sampling only occurring at the millimag level.

Object identification was performed on the F160W images, using a detection threshold of at least 5 connected pixels at  $1\sigma$  above the background. Non-detections are given as  $3\sigma$  limits. These are calculated from 0.4 arcsec apertures in the sole case that there is no detection in F160W, using the STScI tabulated zero points<sup>6</sup>. Every other non-detection is in F606W, and the aperture positions and sizes were determined in these cases by the MAG\_AUTO apertures used on the F160W image, through the use of SExtractor’s dual-image mode. A standard smoothing filter was used on all the images, with a radius of 3 pixels.

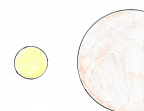
The cleaning parameter was also varied in order to remove spurious, spatially separated pixels which were mostly likely incorrectly attributed to a source. The appropriate zero points for each instrument, CCD and filter were obtained from the image headers and STScI<sup>7</sup>. The magnitude errors output by SExtractor are corrected for correlated noise following Casertano et al. (2000) and Fruchter and Hook (2002). Galactic dust attenuation is calculated using the York Extinction Solver (YES, McCall, 2004) with an  $R_V = 3.1$  Fitzpatrick reddening law (Fitzpatrick, 1999), effective filter wavelengths from the SVO filter profile service (Rodrigo et al., 2012, 2013), and the dust maps of Schlafly and Finkbeiner (2011). Enclosed flux fraction radii measurements were performed using SExtractor with the standard 3 pixel smoothing. Radii enclosing 20, 50 and 80 per cent of the flux were measured in each case.

### 3.3.3 Concentration and Asymmetry

The morphology and structure of a galaxy can provide insight into the nature of the constituent stellar populations. For example, it is well known that irregular or disturbed morphologies are associated with recent or ongoing star formation. Quantitative measures of galaxy morphology are provided by the concentration  $C$

---

<sup>6</sup>[http://www.stsci.edu/hst/wfc3/analysis/ir\\_phot\\_zpt](http://www.stsci.edu/hst/wfc3/analysis/ir_phot_zpt)



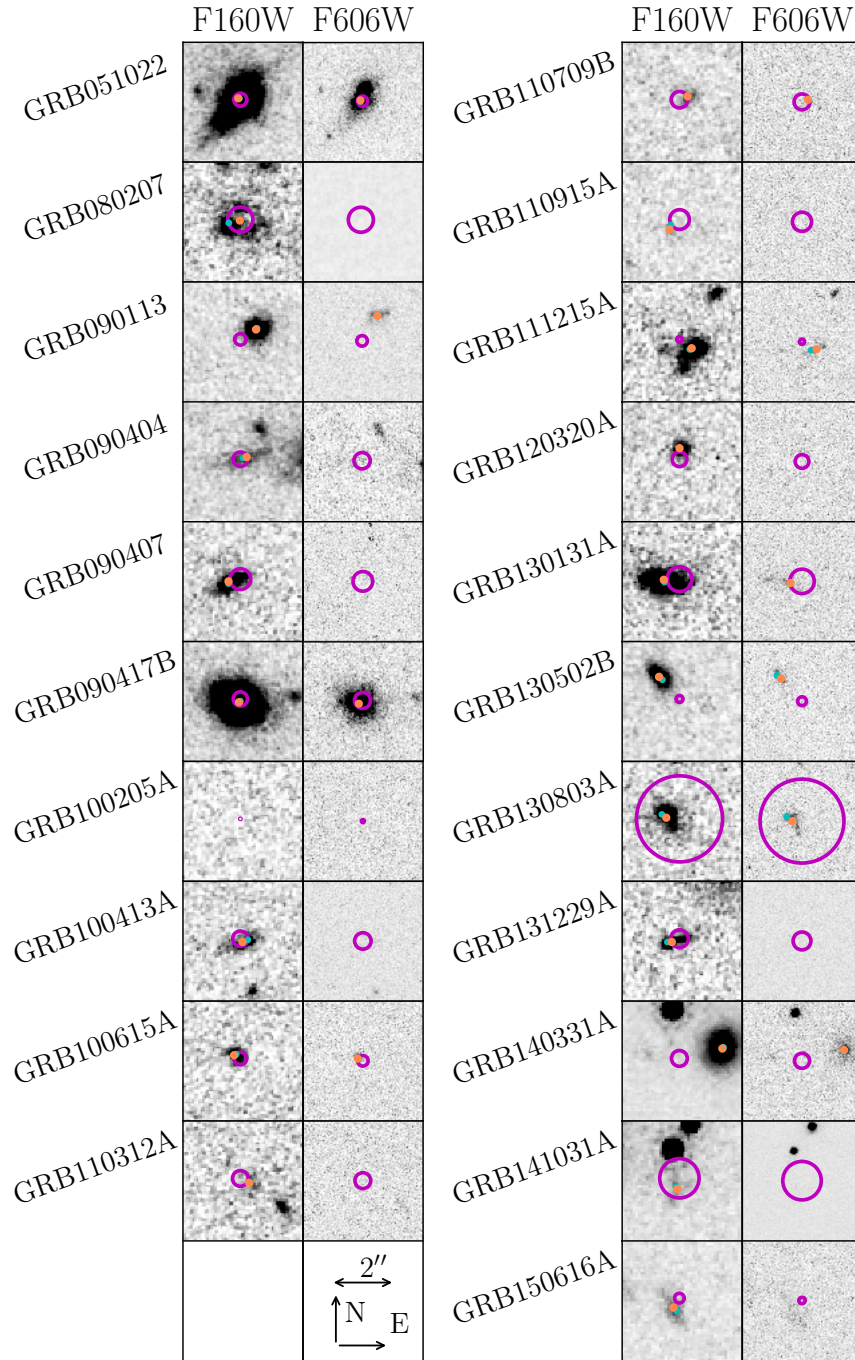


Figure 3.2: The positions of the best available afterglow localisations on their host galaxies after astrometric alignment. Magenta circles represent the *CXO* or other afterglow positions, and their sizes correspond to the  $1\sigma$  confidence region. Smaller cyan and orange circles correspond to the host galaxy brightest pixel and barycentre respectively. Note that the host of GRB 110915A is present but is largely obscured by the brightest pixel and barycentre markers.

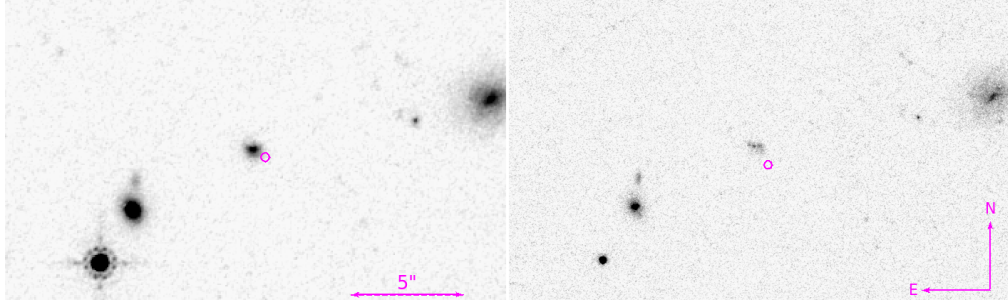


Figure 3.3: Zoomed out *HST* images in F160W (left) and F606W (right), for the host of GRB 090113 and surrounding sources. These have been centred on the host galaxy barycentre, rather than the tied *CXO* afterglow position as in Figure 3.2. There is a clear  $\sim 0.5$  arcsec offset between the afterglow position in these bands. However, given that these are  $1\sigma$  confidence regions, the probability of an alignment with the true location lying beyond  $1\sigma$  in each image is  $\sim 0.1$ . Given the sample size of 21, the occurrence of one such offset in the sample is not surprising.

and asymmetry  $A$  parameters (Kent, 1985; Abraham et al., 1996; Bershadsky et al., 2000; Conselice et al., 2000a,b; Conselice, 2003; Conselice et al., 2003; Lotz et al., 2004). Concentration is proportional to the log of the ratio of the radii enclosing 80 and 20 per cent of the total source flux, and measures the degree to which light is centrally concentrated within a galaxy. Asymmetry is obtained by rotating an image cutout through  $180^\circ$  around the barycentre of the galaxy of interest, followed by image subtraction, normalisation and summation. An identical process is carried out on blank sky regions for background asymmetry subtraction.

I employ the same division of  $CA$  parameter space as Conselice et al. (2005), categorising galaxies as ellipticals, spirals/irregulars, or mergers. Additionally, the ellipticity (i.e. one minus the ratio of semi-minor and semi-major axis length) is used to break the degeneracy in  $CA$  parameter space between objects with similar concentrations and asymmetries but different projected 2D light distributions. This issue arises because elongated objects can be symmetric through a  $180^\circ$  rotation, and the interest here is in the effect of viewing angle and the line of sight through the GRB host. For disk galaxies, ellipticity is a proxy for line of sight inclination, information that the  $CA$  parameters alone are not able to provide.

I do not perform an analysis of  $F_{\text{light}}$  (Fruchter et al., 2006) or the third ‘CAS’ parameter, clumpiness  $S$ . The reason for the former is that the positional uncertainties are sufficiently large that significant fractions (or in some cases, 100 per cent) of the hosts are enclosed by the error circle. Blanchard et al. (2016) showed that high error circle to galaxy area ratios produce  $F_{\text{light}}$  values which are significantly biased to lower values. Secondly, the clumpiness statistic  $S$  becomes

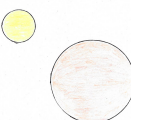


Table 3.4: Host properties for the entire sample of 21 GRB hosts. For brevity, the astrometric tie and morphological information shown here is for the IR images only (far more hosts are detected in F160W and so this band provides the most statistically robust sample). In most cases, tying is performed via a Pan-STARRS  $r$ -band intermediate (PS- $r$ ) as described in the text. The magnitudes have been corrected for Galactic extinction, listed in the final column, and non-detections are given as  $3\sigma$  limits.

GRB	Intermediate	$\sigma_{\text{tie}}['']$	$m_{160}$	$\sigma_{160}$	$m_{606}$	$\sigma_{606}$	$R_{\text{norm}}$	$R_{\text{n.bp}}$	$A$	$C$	$\epsilon$	$P_{\text{chance}}$	$A_V(\text{Gal})$ †
051022	PS- $r$	0.21	20.582	0.004	21.932	0.003	0.21	0.14	0.12	2.84	0.41	$4.16 \times 10^{-5}$	0.150
080207	PS- $r$	0.41	24.017	0.070	>26.5	-	0.06	0.65	0.17	1.98	0.27	$4.96 \times 10^{-5}$	0.057
090113	PS- $r$	0.19	22.705	0.022	24.225	0.017	2.25	2.41	0.16	2.57	0.16	$1.27 \times 10^{-2}$	0.205
090404	PS- $r$	0.24	23.334	0.043	>25.6	-	0.39	0.17	0.07	2.69	0.7	$2.32 \times 10^{-3}$	0.051
090407	PS- $r$	0.34	22.779	0.037	>26.7	-	1.23	1.29	0.2	2.71	0.5	$4.35 \times 10^{-3}$	0.168
090417B	PS- $r$	0.23	20.595	0.004	21.425	0.003	0.34	0.19	0.12	3.31	0.27	$8.92 \times 10^{-5}$	0.041
100205A	Direct GN	0.02	>26.7	-	>27.1	-	-	-	-	-	-	-	0.047
100413A	PS- $r$	0.25	23.667	0.077	25.947	0.134	0.42	0.83	0.16	2.33	0.03	$7.38 \times 10^{-4}$	0.281
100615A	PS- $r$	0.20	23.912	0.058	24.972	0.041	1.41	1.19	0.22	2.71	0.19	$2.10 \times 10^{-3}$	0.111
110312A	PS- $r$	0.26 †	24.806	0.204	>26.8	-	1.05	1.15	0.01	2.26	0.21	$6.58 \times 10^{-3}$	0.095
110709B	PS- $r$	0.27	24.829	0.010	26.549	0.181	1.25	1.12	0.19	2.71	0.18	$6.15 \times 10^{-3}$	0.121
110915A	PS- $r$	0.31	25.628	0.171	>27.5	-	1.92	1.42	0.23	2.61	0.24	$2.12 \times 10^{-2}$	0.142
111215A	PS- $r$	0.09	22.361	0.032	24.071	0.035	1.72	1.6	0.19	2.7	0.42	$5.99 \times 10^{-3}$	0.156
120320A	PS- $r$	0.24	23.940	0.069	>27.0	-	1.42	1.42	0.04	2.5	0.01	$4.63 \times 10^{-3}$	0.073
130131A	Direct UKIRT	0.40	21.889	0.022	24.089	0.037	1.85	1.77	0.15	2.84	0.51	$8.53 \times 10^{-3}$	0.038
130502B	PS- $r$	0.11	22.612	0.026	24.642	0.026	6.93	6.93	0.1	2.7	0.22	$1.52 \times 10^{-1}$	0.515
130803A	XRT only	1.40	22.740	0.037	23.730	0.026	-	-	0.19	2.69	0.21	-	0.140
131229A	PS- $r$	0.29 †	23.235	0.077	>25.8	-	0.87	1.31	0.19	2.41	0.69	$3.24 \times 10^{-3}$	0.671
140331A	PS- $r$	0.26	20.127	0.007	23.127	0.022	3.29	3.39	0.08	3.31	0.08	$7.32 \times 10^{-3}$	0.112
141031A	PS- $r$	0.64 †	22.812	0.032	>25.7	-	0.94	0.89	0.19	2.33	0.32	$4.47 \times 10^{-3}$	0.423
150616A	FORS2	0.16	22.870	0.051	24.250	0.051	1.11	1.09	0.2	2.43	0.47	$5.42 \times 10^{-3}$	0.093

† - These hosts have a barycentre uncertainty of more than 0.1 arcsec. ‡ - This is the F606W band Milky Way extinction.

increasingly unreliable as redshift increases, as demonstrated by Conselice (2003). Pixel-to-pixel variations caused by the *HST* PSF create high frequency power that is not due to spatial variation in the stellar populations, artificially boosting  $S$  for sources which are small in extent.

### 3.3.4 Morphological Uncertainties

Due to the drizzling process, there is correlated noise in the final *HST* images which is not accounted for in the [ERR] maps output by the data reduction. To address this issue, I resampled the pixels in the pre-drizzled FLC and FLT images by adding values sampled from their [ERR] extension uncertainty distribution, *before* drizzling. This process was repeated a few hundred times for each set of images, with measurements made on the new drizzled image each time. This produced distributions of SExtractor and CA output parameters (following the methodology of Lyman et al., 2017). The CA results use the mean of the drizzled image measurements, with uncertainties given by the  $1\sigma$  spread of the re-sampled distribution. The distributions for  $A$  and the three enclosed flux radii are available in Appendix B, for both the UV and IR images. In cases where the original, observed measurement

Table 3.5: GRB host properties for which a redshift is required. Uncertainties are given on the redshift of GRBs 140331A, as this is not spectroscopically determined.

GRB	$z$	$z$ ref	Scale [kpc/'']	$R_{20}$ [kpc]	$R_{50}$ [kpc]	$R_{80}$ [kpc]	$R_{\text{phys}}$ [kpc]	$M_{160}$	$M_{606}$
051022	0.809	[1]	7.536	1.48	2.94	5.47	0.63	$-22.177^{+0.004}_{-0.004}$	$-20.958^{+0.003}_{-0.003}$
080207	2.0858	[2]	8.328	3.21	5.09	7.98	0.30	$-20.778^{+0.070}_{-0.070}$	$>-18.4$
090113	1.7493	[2]	8.456	1.35	2.60	4.41	5.86	$-21.613^{+0.022}_{-0.022}$	$-20.279^{+0.017}_{-0.017}$
090407	1.4485	[2]	8.449	1.39	2.77	4.84	3.40	$-21.196^{+0.037}_{-0.037}$	$>-17.4$
090417B	0.345	[3]	4.894	0.87	1.87	3.61	0.64	$-20.355^{+0.004}_{-0.004}$	$-19.562^{+0.003}_{-0.003}$
100615A	1.398	[4]	8.431	0.71	1.45	2.49	2.04	$-20.042^{+0.058}_{-0.058}$	$-19.080^{+0.041}_{-0.041}$
110709B	2.109	[5] <sup>a</sup>	8.315	0.94	2.04	3.28	2.56	$-19.930^{+0.010}_{-0.010}$	$-19.419^{+0.045}_{-0.045}$
111215A	2.012	[6] <sup>b</sup>	8.364	1.31	2.67	4.54	4.60	$-22.275^{+0.032}_{-0.032}$	$-20.706^{+0.035}_{-0.035}$
140331A	$1.00^{+0.11}_{-0.04}$	[7] <sup>c</sup>	8.008	1.51	3.51	6.97	11.55	$-23.120^{+0.222}_{-0.088}$	$-20.222^{+0.223}_{-0.090}$

[1] Castro-Tirado et al. (2007), [2] Krühler et al. (2012b), [3] Berger and Fox (2009), [4] Kruehler et al. (2013), [5] Perley et al. (2016a), [6] van der Horst et al. (2015), [7] Chrimes et al. (2018)  
<sup>a</sup> - this is a tentative redshift based on one emission line, <sup>b</sup> - tentative and based on a single line, but consistent with the photometric redshift, <sup>c</sup> - this is a photometric redshift

falls outside this region, I use it as the upper or lower limit as appropriate. The quantities for which uncertainties are estimated in this way are the enclosed flux radii, host barycentre, asymmetry and ellipticity.

### 3.4 Results

Basic results, as measured from the photometric images are reported in tables 3.4 and 3.5. Where known, redshifts are used to calculate angular and luminosity distances, providing physical scales and absolute magnitudes. Where there is no redshift information, an upper limit on physical offsets and sizes can still be obtained since the angular diameter distance reaches a maximum at  $z \sim 1.6$ , for the adopted cosmological parameters. This also happens to be similar to the mean redshift of GRBs, and there is little evolution in the angular diameter over the redshift range  $1 < z < 3$ . These limits are listed in Table 3.6.

In order to judge whether an association between a burst and the nearest galaxy is genuine, I use the  $H$ -band galaxy counts of Metcalfe et al. (2006) and perform a false alarm probability analysis (e.g., Bloom et al., 2002; Levan et al., 2007). The probability  $P_{\text{ch}}$  of finding at least one unrelated source of magnitude  $m_g$  or brighter within an angular separation  $r$  is given by,

$$P_{\text{ch}} = 1 - e^{-\Sigma(m \leq m_g) \pi r^2}, \quad (3.1)$$

where  $\Sigma$  is the surface density of sources. Using a cut-off of  $P_{\text{ch}} < 0.05$ , which permits at most one interloper in the sample, 1 candidate (GRB 130502B) is rejected as a

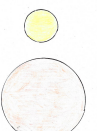


Table 3.6: Here, I provide upper limits on the physical separations,  $R_{\text{phys}}$ , and enclosed flux radii for those GRBs without redshifts. A redshift of  $\sim 1.6$  is assumed, which corresponds to the maximum angular diameter distance and (approximately) the mean GRB redshift. Note that GRB 100413A has an XRT-derived redshift of  $z \sim 4$  (Campana et al., 2010), but a lower  $z$  solution cannot be ruled out.

GRB	$R_{\text{phys}}$ [kpc]	$R_{20}$ [kpc]	$R_{50}$ [kpc]	$R_{80}$ [kpc]
090404	2.22	2.76	5.71	9.54
100413A	1.10	1.42	2.47	4.14
110312A	2.73	1.4	2.6	3.97
110709B	2.61	0.96	2.08	3.34
110915A	3.88	1.09	2.03	3.63
120320A	3.05	1.14	2.14	3.61
130131A	6.52	1.74	3.53	6.45
130502B	18.44	1.34	2.66	4.66
130803A	3.68	1.7	3.13	5.87
131229A	2.32	1.42	2.66	4.31
141031A	6.67	0.77	3.39	5.07
150616A	3.8	1.84	3.44	5.64

potential chance alignment based on this cut. All further analyses therefore omit GRB 130502B. If this is considered a chance alignment, the implication is that the true host is undetected, and possibly very distant. The X-ray brightness of this burst makes a high-redshift scenario unlikely, however (Evans et al., 2009; Melandri and Immler, 2013). While the burst and its candidate host are not included in this sample, the possibility that the nearby galaxy is associated but that the burst is at a large offset must be acknowledged. The probability of there being 1, 2 and 3 interlopers in the remainder of the sample (ignoring GRB 130803A whose positional uncertainty is too large for a meaningful  $P_{\text{ch}}$  estimate) is calculated using the Poisson Binomial distribution, giving 0.1,  $3.8 \times 10^{-3}$  and  $9.8 \times 10^{-5}$  respectively (Hong, 2013)<sup>7</sup>.

### 3.4.1 Host Colours and Luminosities

I use the F160W absolute magnitudes and F606W-F160W colours to further characterise the host population. Figure 3.4 compares a proxy for the absolute magnitudes of the hosts in this sample, calculated as  $m_{\text{F160W}} - \mu + 2.5 \log_{10}(1+z)$  (where  $\mu$  is the distance modulus), to those from Blanchard et al. (2016) and Lyman et al. (2017). For all the results, where there is overlap between samples, the measurements agree

<sup>7</sup><https://github.com/tsakim/poibin>

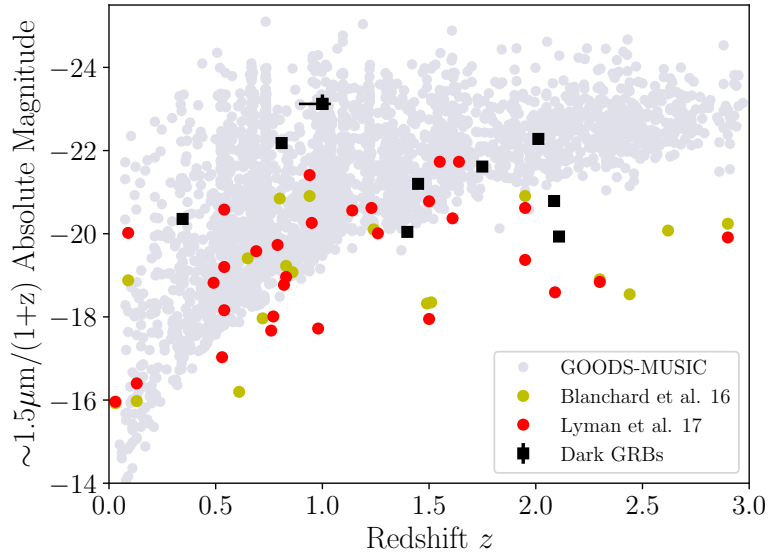
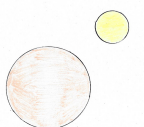


Figure 3.4: Redshift versus absolute magnitude for the dark GRB hosts, comparison galaxies hosting optically bright GRBs, and the GOODS-MUSIC galaxy catalogue. The hosts of dark GRBs are more luminous than bright GRB hosts over a wide range in redshift.

well (e.g. van der Horst et al., 2015; Blanchard et al., 2016). The dark hosts are more luminous than the hosts of optically bright GRBs, at all redshifts. They are also more representative of the general star forming galaxy population at their epoch; all galaxies reported by Grazian et al. (2006b) and Santini et al. (2009, labelled GOODS-MUSIC) are shown. Previous GRB hosts studies have found similar results (e.g., Hjorth et al., 2012; Perley et al., 2013), and attribute dark GRB host luminosities to greater stellar masses, consistent with a dust-extinguished afterglow scenario.

The colours of these hosts also provide information. Figure 3.5, is a colour-magnitude diagram plotting apparent F160W magnitudes against F606W-F160W colour. The points themselves are coloured according to redshift, if available, otherwise they are left black. Horizontal lines denote constraints derived from the luminosity function of high-redshift galaxies reported by Bouwens et al. (2015). At each of  $z = 4, 5$  and  $6$ , I use the reported  $M^*$  and faint end slope to determine the apparent (rest-frame UV) magnitude fainter than which 95 per cent of the UV star-forming galaxy population would be observed. At  $z > 4$ , the observed  $H$ -band lies below the Lyman break, and for star forming galaxies, the mean spectral energy distribution is approximately flat in  $F_\nu$  and therefore AB magnitude. This leads



to a zero colour term between the rest-UV and rest-optical (observed  $H$ -band). It is assumed that the luminosity function extends down to an absolute magnitude  $M_{UV} = -10$ . Note that the line shown at  $z \sim 5$  is within a few tenths of a magnitude of the brightest galaxy detected at  $z > 5$  in the GOODS-MUSIC moderately wide area photometric survey (Grazian et al., 2006b; Santini et al., 2009).

I use the set of 95<sup>th</sup> percentile limits discussed above, and the shallowest F606W limit in this imaging, to split the parameter space into 4 (redshift-dependent) regions. Objects in region A lie above both limits. They would have to be exceptionally bright if at  $z > 5$ , and are in fact detected in F606W suggesting that the Lyman break does not lie red-wards of the F606W band, which is centred around  $\sim 5700\text{\AA}$  (Rodrigo et al., 2012). Therefore, it can be said with confidence that all sources in region A are at  $z < 4$ , providing a limit for three galaxies without previous redshift information: GRBs 130131A, 130803A and 150616A. In region B of Figure 3.5, the lower bound of which is redshift dependent, the galaxies would have to be unusually bright in F160W to be at high-redshift but are nonetheless undetected or very faint in F606W. Such sources are most likely intrinsically red. Sources in region C, below both limits, are either undetected or faint in F606W, and faint enough in F160W to plausibly be at  $z > 4$  (or  $z > 5$  or  $z > 6$  depending on the adopted limit). While the F606W non-detections here could be attributed to the Lyman break, a faint and dusty scenario cannot be ruled out. Two sources lie clearly in region C. One of these, the non-detection of GRB 100205A in either band, is not shown. This burst has previously been suggested as a high-redshift candidate (Cucchiara et al., 2010). The other is GRB 110915A. An additional two objects lie in an ambiguous region, on the boundary between regions B and C at  $z = 4 - 5$ , and would have to be luminous if at high-redshift, although not exceptionally so. Of these, one is known to lie at  $z \sim 2$ . Finally, objects in region D would be detected in F606W and are thus very likely at  $z < 4$ .

### 3.4.2 Host Morphologies

Morphological measurements for each detected galaxy are also listed in Table 3.4. Figure 3.6 shows the  $CA$  results for the dark hosts in the F160W band, with equivalent measurements in the same band from Lyman et al. (2017) shown in grey. The dark population shows no statistically significant offset from the normal bursts. I also measure  $CA$  parameters in the F606W band. In two cases where there is a photometric detection, the galaxy appears sufficiently diffuse in F606W that meaningful  $CA$  measurements could not be made (i.e. the source is frequently undetected as an object when re-drizzling is performed, this occurred for GRBs 100413A and

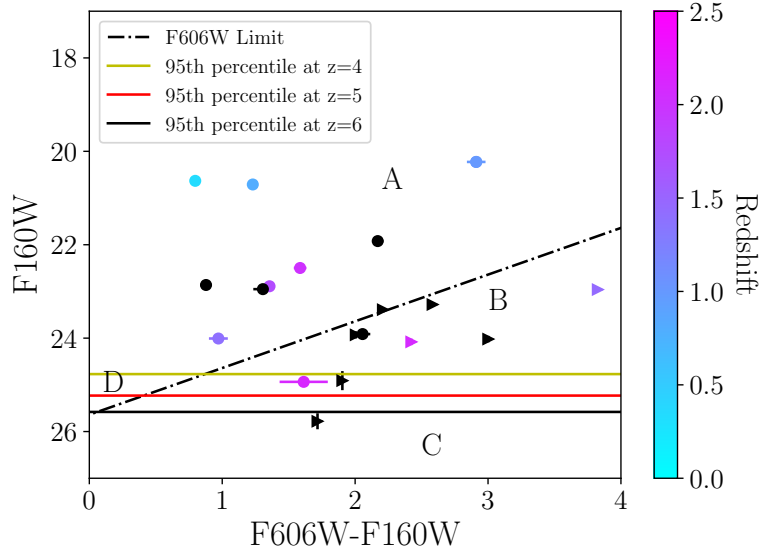


Figure 3.5: The F160W apparent magnitude of GRB hosts in this sample versus their observed F606W-F160W colour. Points which are coloured have a redshift, those in black do not. Horizontal lines denote the apparent UV magnitude fainter than which 95 per cent of the UV star-forming galaxy population would be observed (Bouwens et al., 2015). The dashed line represents the shallowest F606W limit in the sample. Sources to the left of the dashed line, in regions A and D, are detected in F606W and a high-redshift scenario is disfavoured. In region B, there are sources which are undetected in F606W but which are implausibly bright in F160W if they lie at  $z > 5$ . The two undetected sources in region C (depending on the redshift) are also faint in F160W, and are possible high  $z$  candidates. One source, GRB 100205A does not appear as it was not-detected in either band.

150616A). The true noise in the image is given by the pixel-to-pixel noise multiplied by a corrective factor (up to an order of magnitude) that accounts for correlated noise from drizzling (Fruchter and Hook, 2002). Due to this correlated noise, re-sampling produces more variation in the resultant re-drizzled galaxy pixel values and explains the large morphological uncertainties that are obtained with this method. Indeed, it is the dominant source of morphological (and photometric) uncertainty, particularly when dealing with sources that are associated with a small number of pixels.

The F606W results are compared to the optical measurements of Conselice et al. (2005). An Anderson-Darling (AD) test produces a p-value of 0.048 for concentration (providing marginal evidence that dark GRB hosts are more concentrated) and 0.25 (i.e. no significant difference) for asymmetry.

If dark GRB hosts are preferentially edge-on and disk-like, the average line-of-



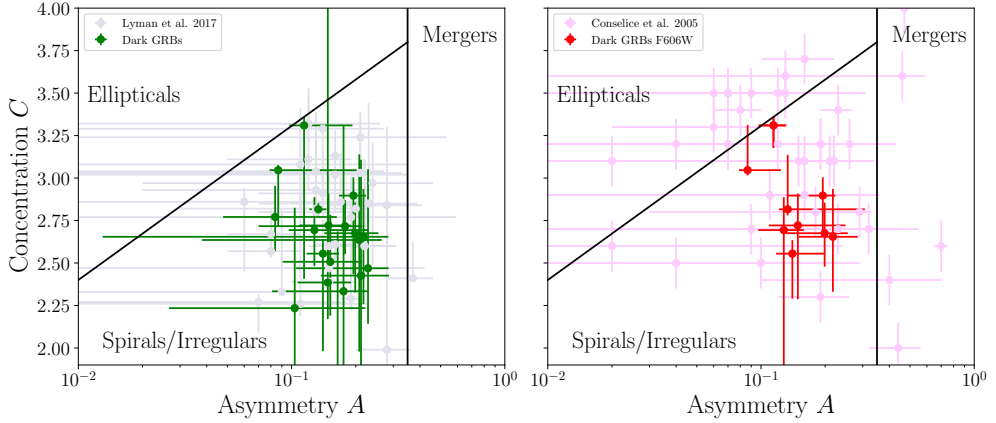


Figure 3.6: The position of the 19 F160W-detected dark GRB hosts in  $CA$  parameter space (left), and the 9 detected in F606W for which measurements could be made (right). Comparisons are made to Lyman et al. (2017, shown in grey) and Conselice et al. (2005, pink). The most significant difference occurs for concentration in the F606W band.

sight through the galaxy to the burst location would be longer and more prone to dust extinction in the plane of the disk. This would manifest as dark GRB hosts showing relatively elongated morphologies which are identified by the ellipticity  $\epsilon$  but not necessarily the asymmetry. Again, statistical comparison between this sample and that of Lyman et al. (2017) provides no grounds to reject the null hypothesis that the two populations have the same underlying ellipticity distribution. Comparing the physical half-light radius  $R_{50}$  of the dark GRB hosts with a known redshift from Table 3.5 to the samples of Lyman et al. (2017) and Blanchard et al. (2016), I find that the dark GRB hosts are physically more extended, with AD tests yielding p-values of 0.030 and 0.087 respectively. The median physical  $R_{50}$  of this sample is  $2.7 \pm 0.4$  kpc, versus  $1.8 \pm 0.1$  kpc for Blanchard et al. (2016) and  $1.7 \pm 0.2$  kpc for Lyman et al. (2017).

### 3.4.3 Burst Offsets

Out of the 21 bursts in the sample, one host candidate is rejected as a potential chance alignment, one host is undetected and one GRB has a positional uncertainty which is too large to measure a meaningful offset from the putative host. I therefore measure the offset of the burst from the host light barycentre ( $R_{\text{norm}}$ ) and brightest pixel ( $R_{\text{n,bp}}$ ) for the remaining 18 GRBs. The offset distribution, normalised by the host  $R_{50}$  radius, is shown for the F160W band in the upper left panel of Figure 3.7. This is compared to distributions drawn from the literature. The uncertainty on

Table 3.7: Statistical tests comparing the dark GRB host-normalised barycentre offset distribution to other samples, using bursts solely from this sample (upper set of statistics) and including optically/NIR detected dark bursts from Blanchard et al. (2016) (lower set). The first column is the significance of the difference between the median  $R_{\text{norm}}$  values. The second is the frequency with which randomly drawn offsets are less than the median of the comparison sample. The final column lists AD test results.

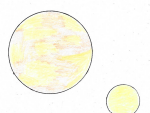
Sample	$R_{\text{norm}}$	$\sigma$	Bootstrap %	AD Test p-val
This work	$1.2 \pm 0.3$			
Bloom et al. (2002)	$0.8 \pm 0.3$	0.83	6.2	0.58
Blanchard et al. (2016)	$0.7 \pm 0.2$	1.24	2.3	0.56
Lyman et al. (2017)	$0.6 \pm 0.1$	1.70	0.5	0.03
Extended sample <sup>†</sup>	$0.9 \pm 0.2$			
Bloom et al. (2002)	$0.8 \pm 0.3$	0.35	83.9	0.34
Blanchard et al. (2016)	$0.7 \pm 0.2$	0.70	74.8	0.57
Lyman et al. (2017)	$0.6 \pm 0.1$	1.17	61.7	0.20

<sup>†</sup> - Includes these additional 13 GRBs: 050401, 060719, 061222A, 070306, 070508, 080325, 080605, 080607, 081109A, 081221, 090709A, 100621A, 120119A

each offset has contributions from afterglow, tie and host positional uncertainties. In order to quantify the uncertainty on the cumulative distribution, I follow the approach of Bloom et al. (2002) and Blanchard et al. (2016). In the case of a point source with approximately Gaussian uncertainties, offset from the host centre by a distance  $R$ , the frequency of occurrence at any given offset  $x$  is described by the Rice distribution. The upper right panel of Figure 3.7 shows the Ricean probability density functions for each GRB in the sample individually, and the summed distribution. 18 barycentre offsets are randomly drawn from the summed distribution 1000 times, and these are plotted in grey in the left-hand panel. This gives an indication of the uncertainty on the cumulative distribution.

Table 3.7 shows the results of statistical comparisons between the dark GRB, host-normalised offset distribution reported here, and other literature samples. The results vary from being statistically consistent to marginally inconsistent (if defined as a  $< 0.05$  probability of occurring by chance). Working instead with physical offsets produces comparable results. Interestingly, the dataset most inconsistent is the normal GRB sample of Lyman et al. (2017).

Because the dark burst sample size is modest, and *Chandra* determined positions typically have larger positional uncertainties, I now consider the effect of including additional optically or NIR detected dark GRBs in the offset comparisons. Specifically, dark bursts from Blanchard et al. (2016), whose data reduction



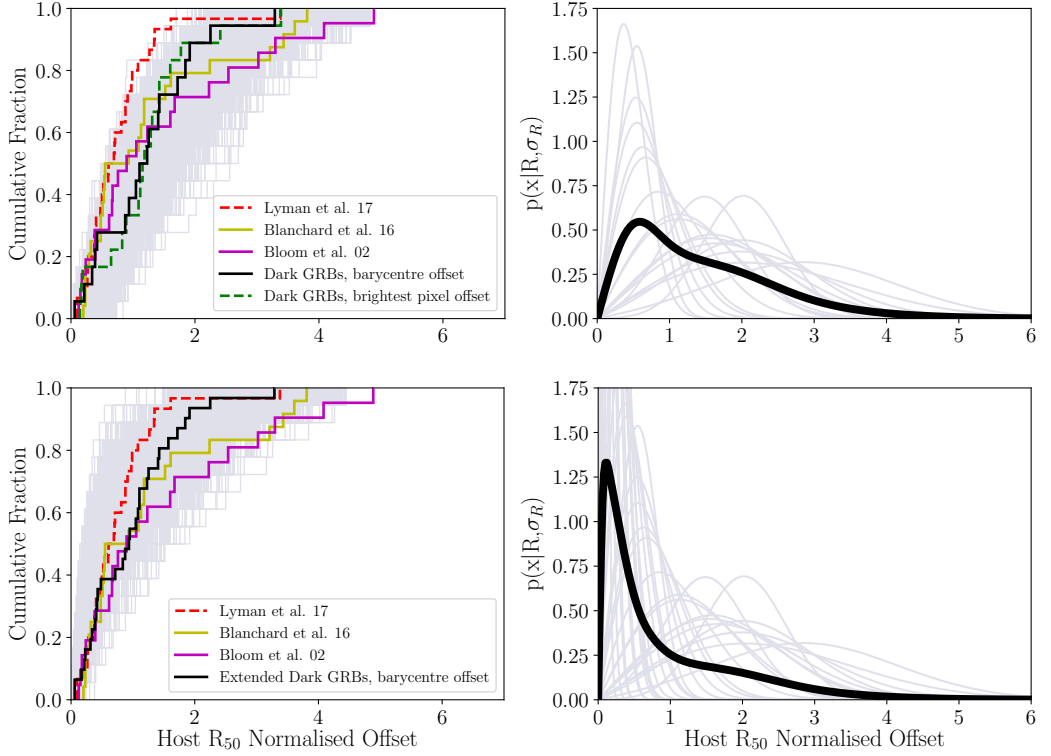


Figure 3.7: Upper left: The cumulative distribution of  $R_{50}$  normalised host offset for the dark GRBs and a selection of comparison data sets. The grey distributions in the background are Monte Carlo resamples, drawn from the summed Ricean distribution of the dark sample. Upper right: The individual Ricean probability distributions for the dark GRB normalised offsets are shown in grey, with the summed and normalised distribution overlaid in black. Lower panels: As above, but for the extended dark burst sample, including optically or NIR detected dark GRBs from Blanchard et al. (2016).

and analysis is similar to the methods I have employed, are incorporated. I choose bursts which have F160W (or similar) *HST* imaging, a  $\beta_{\text{OX}} < 0.5$  (see Perley et al., 2016a), a Galactic  $A_V < 0.5$  and an optical or NIR afterglow detection. The 13 host normalised offsets of those GRBs reported in Blanchard et al. (2016) which meet these criteria are added to the sample described in this Chapter, to create an extended dark burst offset sample. The same statistical comparisons are made between the extended sample, and the three literature datasets. The effect of including these optically or NIR detected dark bursts is shown in the bottom two panels of 3.7 - the extended sample is also consistent with the comparison samples.

## 3.5 Discussion

### 3.5.1 Host Colours and Magnitudes

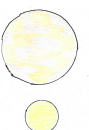
In common with previous work (Greiner et al., 2011; Hjorth et al., 2012; Perley et al., 2013), it is shown that dark GRB hosts are typically more luminous, and thus likely of higher stellar mass, than the hosts of GRBs with bright afterglows at the same rest-frame wavelength. They also show larger physical sizes. For these reasons, the darkness of most GRBs is now widely attributed to dust within the host. Perley et al. (2016a) estimate that no more than 2 per cent of GRBs with fluence greater than  $10^{-6}$  erg cm $^{-2}$  lie at  $z > 5.5$ . Based on the colours and magnitudes of the sample, I find that the fraction of dark GRBs in this sample which could feasibly be high-redshift is  $0.14 \pm 0.08$ . Allowing for Poisson uncertainties on the small number statistics, and assuming that 20 per cent of all GRBs are dark (Greiner et al., 2011; Jakobsson et al., 2012; Perley et al., 2016a), this puts  $< 4.4$  per cent of all GRBs at  $z > 5$ , in good agreement with previous estimates (2 – 3 per cent, Perley et al., 2009, 2016a). This is strictly an upper limit, as the non-detection of a number of targets as shown in Figure 3.5 might also be the result of moderate extinction at intermediate redshifts, particularly since the F606W band is increasingly affected by dust extinction as it probes further into the NUV.

### 3.5.2 Host Galaxy Morphologies

I find marginal evidence for dark GRB hosts being more concentrated in the F606W band, and no evidence for differences in asymmetry or ellipticity between this sample and those of Lyman et al. (2017) and Conselice et al. (2005). The ellipticity result implies that the dark GRB hosts are typically not edge-on disks. In both bands, a comparison is being made with a similarly observed and analysed dataset.

One might have expected that galaxies would appear to be more asymmetric in F606W, given that this corresponds to the rest frame UV at redshift  $\sim 2$ , and the irregularity of star forming clumps might be measurable. However, previous *CA* analyses have shown that this effect manifests itself primarily in the clumpiness parameter (Lee et al., 2013), with *A* and *C* unaffected. The dark host sample has very similar mean  $C \sim 2.6$  and  $A \sim 0.15$  values to the *H*-band,  $M_{\star} > 10^9 M_{\odot}$ , spectroscopically-selected star forming galaxy sample of Lee et al. (2013).

The most striking difference between this sample and those of Lyman et al. (2017) and Conselice et al. (2005) is that the Conselice et al. (2005) sample is significantly more spread out over *CA* parameter space in F606W, with mergers and ellipticals clearly identified. There is also a marginal trend for the dark hosts



to be more concentrated in this band, as the AD test p-value of 0.048 indicates. Despite some of the sources in this sample appearing to be visually disturbed, none are identified as mergers by the *CA* analysis. Conselice et al. (2000b) and Conselice (2003) show that while concentration is largely unaffected by increasing redshift, asymmetry is weakened to varying degrees, depending on the *HST* instrument used. For example, low redshift galaxies would typically have their asymmetries decreased by  $-0.10 \pm 0.10$  (for ACS) and  $-0.03 \pm 0.10$  (for WFPC2) if they were observed instead at  $z=2$ . These are not strong effects, but because the dark GRB host redshift distribution is shifted to slightly higher values with respect to Conselice et al. (2005, see Figure 3.1), it is worth considering the dilution of asymmetry as an explanation for the lack of *CA* mergers in this sample.

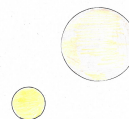
### 3.5.3 Host Galaxy – GRB Offsets

As demonstrated in Section 3.4.1, the majority of sources in this sample are consistent with dusty galaxies lying at intermediate redshifts. Their host-normalised offset distributions are similar to those of optically-bright GRBs. This has implications for how the extinguishing dust is distributed within the galaxies. If the dust were uniformly spread throughout the internal volume of the galaxy, there would be a tendency for dark bursts to occur at low projected offsets, where the column density of dust would be greater. This assumes, however, that the underlying form of the star formation distribution is the same in both dusty and non-dusty GRB hosts, and that the nature of the dust is the same throughout the galaxy. There are also uncertainties on the true galaxy centroids arising from the blurring effect of dust, and the irregular nature of the galaxy morphology in some cases. Nevertheless, the fact that no bias to low offsets is seen implies either that the extinction occurs in a foreground screen (difficult to arrange for every system) or that the dust has a clumpy component. This clumpiness is likely on galactic scales (hundreds to thousands of parsecs), not on the scale of the afterglow radiating region, as has been shown by studies of absorption lines in GRB afterglows (e.g. Prochaska et al., 2008; Chen, 2012) which put dense gas clouds at distances of a few hundred parsec from the burst (although I note these studies require optical afterglows and therefore do not use dark GRBs). Additionally, if the dust causing extinction were too close to the GRB and natal site of the progenitor, it would likely be destroyed (Waxman and Draine, 2000; Fruchter et al., 2001; Zafar et al., 2018b; Heintz et al., 2019a). The inference that clumpy dust is present is further supported by the ellipticity distribution: assuming that at least some of the hosts are spiral in morphology, the lack of a favoured edge-on orientation suggests that the line-of-sight depth through

the host is not the only factor in causing darkness in GRBs. However, it is important to note that the presence of dust - whether clumpy or not - is the primary factor in causing darkness in afterglows. A burst in a low- $A_V$  host will appear optically bright, whether or not the dust that is present is clumpy or uniform. The dust distribution is therefore a secondary effect.

There is a bias against the measurement of very small offsets when afterglow positional uncertainties are an appreciable fraction of the projected size of the galaxy (Blanchard et al., 2016). This issue is therefore more significant when *Chandra* X-ray positions are used, which although precise, are typically less so than optical, IR or radio localisations. One method of addressing this is to include more dark bursts with optical or NIR positions, as in Section 3.4.3. While still statistically consistent with the comparison samples, one can see from Figure 3.7 that the inclusion of extra optically/NIR detected GRBs shifts the dark offset distribution to smaller values, as expected. I caution that in this sample, only 3 dark bursts from 21 have an optical/NIR localisation - suggesting that such scenarios are rare. By artificially including more of these in the extended sample, it must be acknowledged that selection biases may be introduced. However, the redshift and physical host sizes are not significantly changed by their inclusion (mean  $z$  changes from 1.44 to 1.61, the mean  $R_{50}$  from 2.67 to 2.40). It therefore appears as though such biases are not a large concern. Overall, the inclusion of extra optically/NIR detected dark GRBs does not change the interpretation of the results.

There is mixed support for a clumpy dust model in the literature. Corre et al. (2018) studied the relationship between line-of-sight extinction curves derived from optically-bright GRB afterglows and the global dust properties of the host. They find that for more than half of their sample, a significant amount of clumpy dust is required. Some level of irregularity in the dust distribution would certainly be expected, as both supernovae and mature stellar populations are dust-production sites and these will each enrich a limited volume. Since star-forming galaxies tend not to have uniform distributions of star formation, the starburst regions will randomly sample dusty and dust-sparse sites. Indeed, Krühler et al. (2011) find examples of heavily extinguished bursts in otherwise blue, low mass galaxies, as might be expected given this model. Friis et al. (2015) and Heintz et al. (2017) also find evidence for local dust properties which differ from the galaxy wide average. Furthermore, as Figure 3.4 demonstrates, there is considerable overlap in absolute magnitudes between dark and bright GRB hosts. Hosts of similar absolute magnitude are capable of producing both bright and dark bursts, which suggests that the host luminosity and/or mass does not correlate directly with the dustiness of sight-lines through



the galaxy. There is also much uncertainty about the interstellar dust properties of GRB hosts (Zafar et al., 2018b,c), and variations in  $R_V$  between hosts and/or burst sites could help explain the overlap in dark and bright GRB host luminosities.

In argument against the clumpy dust scenario, the fact that hosts of the same absolute magnitude can produce both bright and dark GRBs could be explained by whether or not the burst occurs on the near or far side of the galaxy. Furthermore, previous studies have indicated that burst site properties such as  $A_V$  and metallicity are more typically similar to the properties derived from integrating over the entire host (Krühler et al., 2011). From the sample of 21, only 3 GRB hosts have metallicity determinations. These are GRBs 051022 ( $Z \sim 8.77$ , Graham et al., 2015), 090407 ( $Z \sim 8.85$  Krühler et al., 2012b) and 100615A ( $Z \sim 8.4$  Krühler et al., 2012b). The first two of these have  $\sim$  solar metallicity, which is particularly high for GRB hosts, and consistent with the presence of dust. This implies that, for the progenitors at least, the main difference between dark and bright GRBs may be their metallicity. The link between host and afterglow determined properties is by definition only measurable for bursts where the afterglow is detected, and it remains possible that the local  $A_V$  might be greater than the host average for dark GRBs. Nonetheless, Perley et al. (2013) and Perley et al. (2016b) concluded that an approximately uniform dust component can help explain the dark burst preference for massive hosts.

The true picture is likely not to be as simple as either purely homogeneously-distributed gas and dust, or entirely clumpy. Some combination of these extremes, with clumps occurring embedded within more diffuse dust is most likely, in agreement with the findings of Corre et al. (2018). Again, it is important to note that the results presented in this paper do not imply that dark bursts *require* clumpy dust. Rather, dark bursts occur in dusty galaxies first and foremost, and that within these hosts, a clumpy component is likely present. Ultimately, a study of how  $\beta_{\text{OX}}$  varies with host normalised offset would be able to distinguish the various dust distribution scenarios discussed here, but would likely require a level of astrometric precision not currently possible.

### 3.6 Conclusions

F606W and F160W imaging of a sample of 21 dark bursts is presented, where the burst location is known in 20 cases to significantly sub-arcsecond (typically  $\sim 0.1 - 0.3$ ) precision through *CXO* X-ray afterglow observations. Twenty of the bursts are robustly detected in the F160W band, and twelve at F606W. One source is

undetected in both bands. Where sources are undetected, deep *HST* imaging places stringent limits on host magnitudes, and thus the plausibility of a high-redshift interpretation for optically-faint afterglows can be evaluated. This analysis provides an upper limit of 22 per cent of dark GRBs arising from  $z > 5$ , or  $\sim 4.4$  per cent of all GRBs, consistent with previous estimates. I also consider the morphology of the detected hosts. A concentration and asymmetry analysis provides marginal evidence that dark GRB hosts are more concentrated than the hosts of optically-bright GRBs. Otherwise, the morphologies of these galaxies are consistent with the wider GRB host population. In agreement with previous studies, I have shown that dark gamma-ray bursts occur preferentially in galaxies which are larger and more luminous than those hosting optically bright bursts. Dark bursts trace their host light in a similar way to bright GRBs, with no evidence for a smaller offset bias. Combining ellipticities with the concentration and asymmetry parameters, I find that dark hosts do not show any evidence for a preferred edge-on orientation. This, and the offset distribution, may imply that a significant proportion of the extinguishing dust is clumpy on galactic scales. This does not, however, suggest that clumpy dust is a specific requirement for dark GRB production - dust in any configuration can achieve this. Rather, the results implies that the dust in galaxies more generally has clumpy component, wherever it is present.

### 3.7 Subsequent Developments

The work described in this Chapter was published in the *Monthly Notices of the Royal Astronomical Society* in April 2019. Since then, Higgins et al. (2019) modelled the afterglow of dark GRB 140713A with BOXFIT using X-ray and radio observations to determine the amount of optical and NIR flux that was missing, given non-detections in these bands. Host galaxy observations facilitated a determination of the stellar mass through SED fitting, which at  $2 \times 10^{10} M_{\odot}$  is typical of dark GRB hosts. The neutral hydrogen column density, as determined from the X-ray afterglow, implied extinctions that are consistent with the  $> 3$  magnitude deficit in optical-IR flux. The afterglow and host galaxy data therefore produce a consistent picture where dust is the cause of darkness in this, and likely most, dark GRBs - in agreement with the conclusions of this chapter.



## Chapter 4

# The case for a high-redshift origin of GRB100205A

*“Looking up into the night sky is looking into infinity – distance is incomprehensible and therefore meaningless.”*

— Douglas Adams, *The Hitchhikers Guide to the Galaxy*

In this Chapter, I present the case for dark GRB 100205A being a high-redshift event. It is undetected in the  $r$ -band, but well detected in the infrared, suggestive of the presence of the Lyman break between the  $r$  and  $J$  bands at a redshift  $z > 5$ .

### 4.1 Introduction

Long-duration gamma-ray bursts (GRBs) give rise to a synchrotron afterglow (see Section 1.2.2), detectable at optical wavelengths if sufficiently rapid and deep follow-up observations are made. A substantial fraction, however, lack such emission even when it would be expected from extrapolation of the X-ray spectral slope (Groot et al., 1998b; Fynbo et al., 2001). When the X-ray to optical spectral slope,  $\beta_{\text{OX}}$ , is below the recognised threshold of 0.5, the event is classified as ‘dark’ (Jakobsson et al., 2004, see also Section 1.5 and Chapter 3). This is typically evaluated at 11 hours post-burst to avoid contamination from early-time effects including X-ray flares and plateaus. An alternative method uses  $\beta_{\text{OX}} < \beta_{\text{X}} - 0.5$  to define darkness (van der Horst et al., 2009). There are two primary causes for darkness in GRBs: attenuation by dust, or rest frame ultraviolet HI absorption at high-redshift (e.g., Fruchter, 1999; Levan et al., 2006; Perley et al., 2009; Greiner et al., 2011; Svensson et al., 2012; Perley et al., 2013; Zauderer et al., 2013; Higgins et al., 2019; Chrimes

et al., 2019a).

The number of GRBs known at high-redshift ( $z > 5$ , in the epoch of reionisation) is small ( $\sim 15$ , from around 500 GRBs with a known or estimated redshift, Kawai et al., 2006; Cenko et al., 2006; Grazian et al., 2006a; Jakobsson et al., 2006; Ruiz-Velasco et al., 2007; Salvaterra et al., 2009; Greiner et al., 2009; Tanvir et al., 2009; Cucchiara et al., 2011; Afonso et al., 2011; Castro-Tirado et al., 2013; Laskar et al., 2014; Jeong et al., 2014a; Chornock et al., 2014b; Tanvir et al., 2018), and each one is valuable, as they provide insight into star formation in the low mass, low luminosity galaxies which power the epoch of reionisation. Because they have small projected offsets from their hosts, high-redshift GRBs with a detected afterglow uniquely allow us to place accurate, deep upper limits on the luminosities of the faintest, undetected galaxies, probing fainter galaxies than deep field studies (Berger et al., 2007; Tanvir et al., 2012; Trenti et al., 2012; McGuire et al., 2016). For those with the brightest afterglows, insight into the burst environment can be gained from absorption lines in their spectra (e.g. Kawai et al. 2006; Chornock et al. 2014c; Sparre et al. 2014; Hartoog et al. 2015).

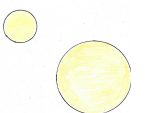
This Chapter explores the possibility that dark GRB 100205A, the only burst of the sample studied in Chapter 3 to lack detections in both *HST* bands, occurred at high-redshift.

## 4.2 Observations, Data Reduction and Results

GRB 100205A ( $T_{90} = 26$  s) was detected by the *Neil Gehrels Swift Observatory* (Gehrels et al., 2004) on 5 Feb 2010 (Racusin et al., 2010). The Burst Alert Telescope (BAT, Barthelmy et al., 2005) measured a fluence of  $(4.0 \pm 0.7) \times 10^{-7}$  erg cm $^{-2}$ , with a peak photon flux of  $(0.4 \pm 0.1)$  cm $^{-2}$  s $^{-1}$  (15-150 keV, 90 per cent confidence errors). The enhanced X-Ray Telescope (XRT; Burrows et al., 2004) position was RA. 09h 25m 33.08s, Dec.  $31^\circ 44' 24.3''$ , with a 90 per cent error radius of  $1.7''$  (Evans et al., 2009)<sup>1</sup>. The X-ray afterglow was rapidly identified, and ground based observations were taken in the first hour after the burst. However, none of these early optical observations revealed a candidate optical afterglow (see Malesani et al., 2010; Cobb et al., 2010; Tanvir et al., 2010; Cucchiara et al., 2010; Nicuesa et al., 2010b; Urata et al., 2010; Perley et al., 2010), marking GRB 100205A as a dark burst (Malesani et al., 2010), and motivating further follow-up.

---

<sup>1</sup>[http://www.swift.ac.uk/xrt\\_positions/](http://www.swift.ac.uk/xrt_positions/)



### 4.2.1 Gemini

Gemini-S/GMOS (Hook et al., 2004) observations in the  $r$ -band were obtained 40 minutes post trigger (PI: Fox). These observations were reduced in the standard fashion within the Gemini IRAF environment, and did not yield an optical afterglow to a  $3\sigma$  limit of  $R > 25.2$ , the deepest upper limit on the optical light available. Given this non-detection the burst location was subsequently imaged in the infrared by Gemini-N/NIRI (with the f/6 camera Hodapp et al., 2003) in the  $Y$ ,  $J$ ,  $H$  and  $K$  bands starting at  $\sim 2.4$  hours post-burst, as shown in Table 4.1 (PI: Tanvir).

The data were reduced with help from Klaas Wiersema, using standard Gemini IRAF package procedures. Care was taken to optimise bad pixel rejection. Cutouts of the reduced images around the GRB afterglow location are shown in Figure 4.1. Also shown is a wider-field view, which includes the *Swift* enhanced XRT position. The  $K$ -band numbering ( $K_{E1}$ ,  $K_{E2}$ ) refers to the first and second epochs of observation, which were approximately 1 day apart. The two epochs in  $H$  and  $J$  are sufficiently close in time that I combined the data from these, where that led to an improvement in signal to noise. Afterglow aperture magnitudes are listed in Table 4.1. The photometric aperture radii are equal to the seeing FWHM for each image, and background subtraction was performed using annuli around these apertures. The aperture positions were anchored to the same point, relative to field objects, in each image. The  $K_{E1}$  afterglow centroid was used as the reference position. Photometry was calibrated against UKIDSS (Lawrence et al., 2007) in  $J$ ,  $H$  and  $K$ , and Pan-STARRS (Chambers et al., 2016) in  $r$  and  $Y$ . All magnitudes are given in the AB system and are corrected for foreground Galactic dust extinction using a  $R_V = 3.1$  Fitzpatrick reddening law (Fitzpatrick, 1999) and the dust maps of Schlafly and Finkbeiner (2011), with  $E(B-V)=0.0165$ . An afterglow was securely detected in the  $J$ ,  $H$  and  $K$ -band images, at a location consistent with that of the X-ray afterglow detected by *Swift*/XRT.

### 4.2.2 Hubble Space Telescope

The burst region was observed with Wide Field Camera 3<sup>2</sup> in the F606W and F160W bands on 2010 Dec 06 (10 months post-burst, programme 11840, PI: Levan). These bands have effective wavelengths of 0.57 and  $1.52\mu\text{m}$  respectively. A three-point dither pattern was observed in each band, with total integration times of 1209s (F160W) and 1140s (F606W). ASTRODRIZZLE (part of the DRIZZLEPAC python

---

<sup>2</sup><http://www.stsci.edu/hst/wfc3>

Table 4.1: Gemini-S/GMOS ( $r$ -band) and Gemini-N/NIRI afterglow observations. Afterglow magnitudes (or  $3\sigma$  limits), corrected for Galactic extinction, and detection significance are listed in the final two columns.  $T_{\text{obs}}$  is the average time since burst trigger for the input exposures.

Filter	$\lambda_{\text{eff}}$ [ $\mu\text{m}$ ]	$T_{\text{obs}}$ [hrs]	$N_{\text{exp}}$	Tot. Int. [s]	FWHM [arcsec]	Mag	$\sigma$
$r$	0.62	0.68	5	602.5	1.44	$>25.2$	-
$Y$	1.02	3.22	10	600	1.15	$>23.5$	-
$K_{\text{E1}}$	2.20	3.88	30	1800	0.58	$23.45 \pm 0.09$	13.2
$H$	1.63	4.73	24	720	0.65	$23.63 \pm 0.26$	3.69
$J$	1.25	5.48	17	510	0.63	$24.29 \pm 0.29$	3.35
$K_{\text{E2}}$	2.20	30.32	28	1620	0.45	$24.42 \pm 0.16$	6.40

All observations were taken as part of program GN-2010A-Q-7 (PI: Tanvir) with the exception of the  $r$ -band data, which is associated with program GN-2010A-Q-5 (PI: Fox).

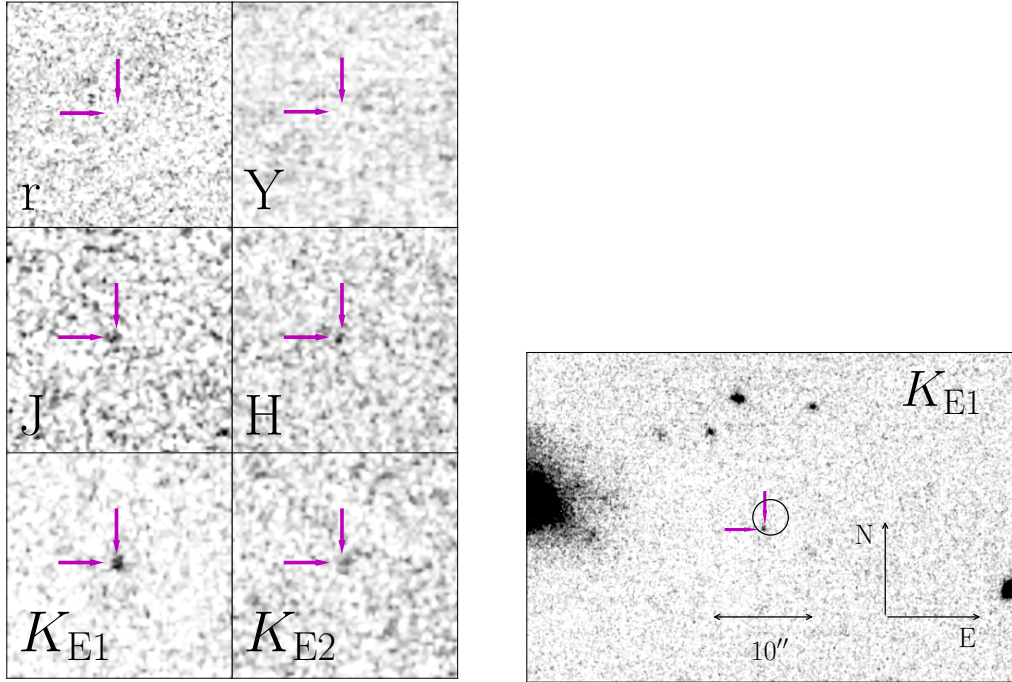
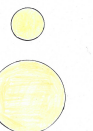


Figure 4.1: Left: Image cutouts ( $4 \times 4''$ ) around the afterglow position for each set of Gemini observations. The  $r$ -band pixel scale is  $0.073'' \text{ pixel}^{-1}$ , the other NIRI images have pixels that are  $0.1171''$  on a side. Numbering indicates whether data is from the first or second observation with that filter. Right: a wider area cutout to demonstrate the location of the burst with respect to a nearby large galaxy. Included here is the *Swift* enhanced XRT position, indicated by a black circle (with a 90 per cent error radius of  $1.7''$ ). All images have been smoothed with a  $3 \times 3$  pixel Gaussian filter.



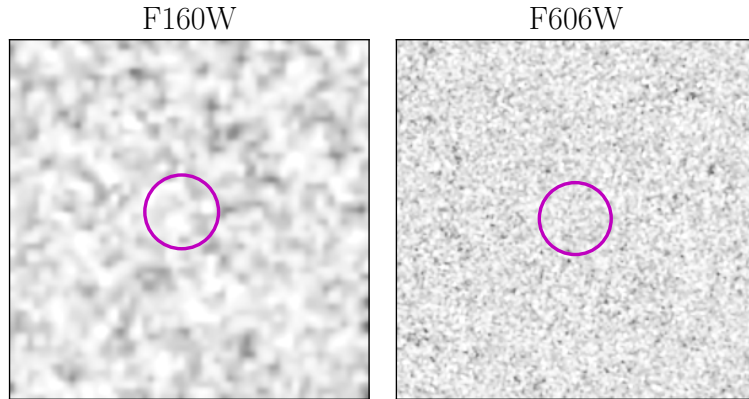


Figure 4.2: *HST* image stamps at the location of GRB 100205A, the images are smoothed with a  $3\times 3$  pixel Gaussian filter. The burst location is indicated in each image by a 0.4 arcsec radius circle. No host is detected down to  $3\sigma$  magnitude limits of 26.7 and 27.1 for F160W and F606W respectively.

package<sup>3</sup>) was used to reduce the images. The chosen PIXFRAC was 0.8, with final scales of  $0.065 \text{ arcsec pixel}^{-1}$  (F160W) and  $0.02 \text{ arcsec pixel}^{-1}$  (F606W).

Once again, the Gemini  $K_{E1}$  detection is used as a reference position, determining the burst location in the *HST* images by calculating a direct transformation based on six reference objects in the field. I used the IRAF tasks GEOMAP and GEOXYTRAN to fit for rotation, shifts and scaling in the  $x$  and  $y$  directions. The total positional uncertainty on the afterglow position in the *HST* frame has contributions arising from this transformation and the uncertainty on the afterglow position in the Gemini image, yielding a positional uncertainty of 18 mas in the F160W image and 49 mas in F606W. Figure 4.2 shows image cutouts centred on the burst location. The source is not detected in either band. At the position of the afterglow,  $3\sigma$  magnitude limits of 26.7 in F160W and 27.1 in F606W were measured (with a 0.4 arcsec aperture, for which STScI tabulate zero-points<sup>4</sup>). A similarly deep optical limit was obtained by Perley et al. (2010) two days post burst, using the Low Resolution Imaging Spectrometer on Keck (Oke et al., 1995) to place an  $r$ -band  $3\sigma$  limit of 26.7 on any host emission at the burst location.

<sup>3</sup><http://drizzlepac.stsci.edu>

<sup>4</sup><http://www.stsci.edu/hst/wfc3/analysis>

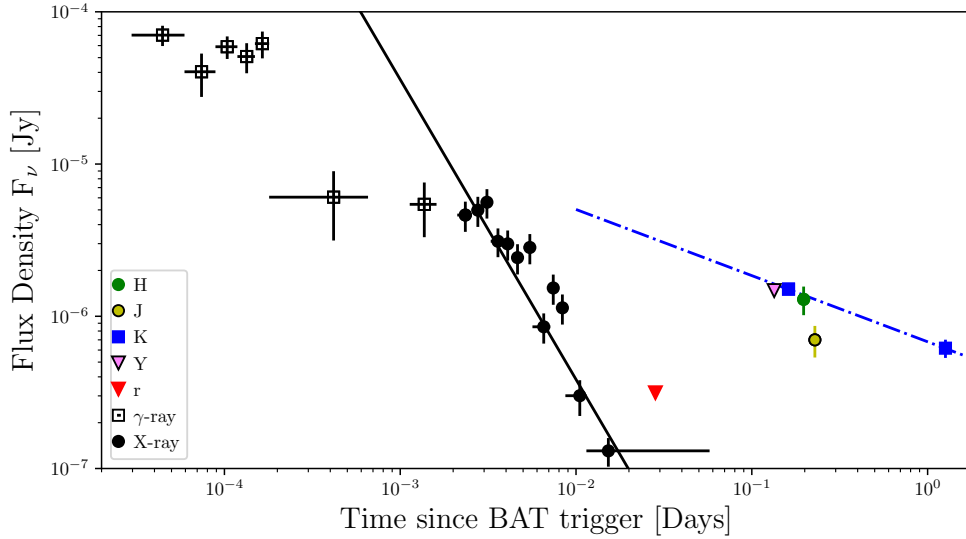
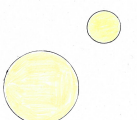


Figure 4.3: The gamma-ray, X-ray and NIR/optical light curve of GRB 100205A. Triangles represent  $3\sigma$  upper limits, circles and squares are detections. The X-rays were undetected by *Swift* XRT by the time of the first optical/IR follow-up observation. The solid black line is a power law fit to the X-ray data points, representing the X-ray temporal decay, while the dashed blue line is a fit to the two *K*-band observations, giving the NIR decay rate. The NIR fit is not extrapolated far beyond the *r*-band limit, as the prompt BAT lightcurve and NIR behaviour are likely driven by different physical mechanisms, making such a comparison misleading.

### 4.3 Interpretation

In Figure 4.3, I show the light curve for GRB 100250A, featuring the gamma-ray, X-ray, near-infrared (NIR) and *r*-band fluxes and limits. The prompt emission detected by the BAT instrument in gamma-rays shows some evidence for a short plateau followed by a decline after approximately 20 seconds. The X-ray lightcurve is monitored from a few minutes after the burst. It decays rapidly and becomes undetectable after about 30 minutes, before the first optical observation is made. The initial *r*-band non-detection lies chronologically between the X-ray monitoring and the start of NIR observations at about 3 hours post-burst. While the NIR data is sparse, it appears to show a less rapid decline in flux density than that seen in the X-ray. As a result, the X-ray to optical spectral energy distribution (SED) is difficult to reconstruct since there is no time overlap, and two different methods are considered for extrapolating between data points. In Figures 4.5 and 4.6, SEDs are constructed from the afterglow measurements. The first assumes that the NIR and optical flux decays at the same rate as the X-ray, the second derives a decay



rate from the two  $K$ -band points. Note that an extrapolation based on the prompt gamma-ray emission would lie between these, but is likely inappropriate for the late time afterglow. After considering the SED, I go on to discuss the burst energetics and the host non-detection.

### 4.3.1 X-ray based SED construction

Firstly, I assume that the flux in  $J$ ,  $H$ , and  $K$  bands shows the same time evolution as the X-ray flux, and that the flux decays according to  $F_\nu \propto t^\alpha$ . All detections and the  $r$ -band limit are extrapolated backwards or forwards to the mean time of the first epoch of observations (0.18 days, at which point there are contemporaneous NIR observations). The X-ray temporal slope  $\alpha = -1.97 \pm 0.14$  and X-ray photon spectral index  $\Gamma = 1.91_{-0.22}^{+0.25}$  are obtained from the *Swift* online database<sup>5</sup> (Evans et al., 2009, 90 per cent errors). The corresponding intrinsic neutral Hydrogen column density (at  $z = 0$ ) is  $(3_{-3}^{+6} \times 10^{20}) \text{ cm}^{-2}$ , a low value which disfavours a dusty, low-redshift explanation for the darkness of this GRB (Perley et al., 2010).

The X-ray flux is extrapolated to the optical (NIR) using a broken power law, with the two segments of the synchrotron spectrum given by  $F_\nu \propto \nu^{-\Gamma+1}$  and  $F_\nu \propto \nu^{-\Gamma+1+\Delta\beta}$ , where  $\Delta\beta$  accounts for a synchrotron spectral cooling break between the NIR and X-ray (Sari et al., 1998).  $\Delta\beta = 0.5$  provides a satisfactory fit in most GRBs (Greiner et al., 2011; Zafar et al., 2011).

The spectrum is fitted to the X-ray points, while the break frequency and break strength are allowed to vary. The parameter values which best fit the extrapolated NIR points are then obtained through the following procedure. A broken power law model is used, extrapolated from the X-ray using the *Swift*/XRT spectral slope, until a break frequency  $\nu_{\text{break}}$  is reached (Sari et al., 1998). At this break frequency, the spectral slope shallows by an amount  $\Delta\beta$ , allowed to vary between 0 and 1, covering a representative range (this break normally occurs between the X-ray and optical, see e.g. Greiner et al., 2011). A broken power law is fit from the X-ray to the  $J$ ,  $H$  and  $K$  points, covering a range of break frequencies and break strengths. Minimising  $\chi^2$  over this parameter space produces best fit values of  $\log_{10}(\nu_{\text{break}}) = 14.24$ , between the  $K$  and  $H$  bands, and a strength  $\Delta\beta = 0.73_{-0.73}^{+0.08}$ . The range of statistically acceptable fits within 67, 95 and 99.5 per cent confidence regions is shown in Figure 4.4.

The flux decrement between the (time-extrapolated)  $J$  and the  $r$ -band is independent of whether a simple  $\Delta\beta = 0$  spectral extrapolation is used (which is consistent within the uncertainties), or if the best fit from this procedure is used

<sup>5</sup>[http://www.swift.ac.uk/xrt\\_live\\_cat](http://www.swift.ac.uk/xrt_live_cat)

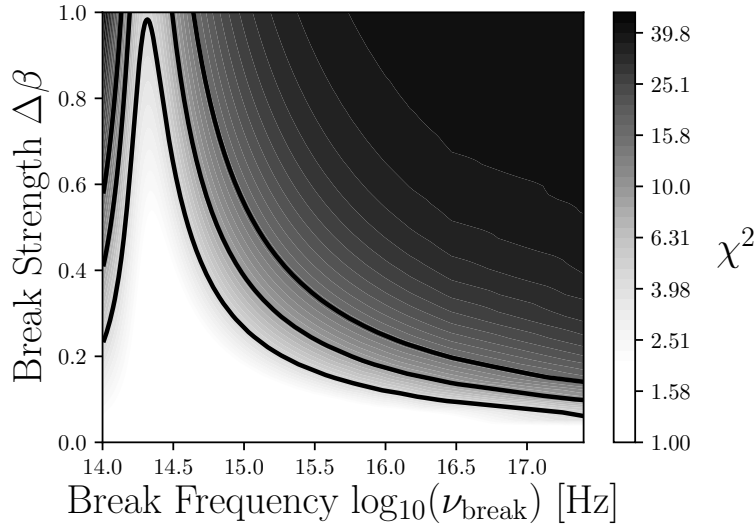
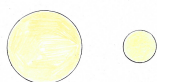


Figure 4.4: The result of fitting a broken power law to the  $J$ ,  $H$ ,  $K$  and X-ray fluxes through  $\chi^2$  minimisation. One, two and three  $\sigma$  contours are shown (Avni, 1976). The power law models are fixed to the X-ray data, but a range of break frequencies and strengths are allowed for at lower energies. A break in the NIR is favoured, and the possibility that the NIR and X-ray points lie on the same section of the synchrotron spectrum is not excluded.

(where a break is included long-wards of this filter). This suggests that the  $r$ -band non-detection is due to dust or the Lyman-break at high redshift, rather than an afterglow-related spectral break. In summary, the data are consistent either with an unbroken extrapolation ( $\Delta\beta = 0$ ), or an extrapolation which breaks in the infrared (i.e. not short-wards of the  $r$ -band).

The upper panel of Figure 4.5 illustrates the observed fluxes extrapolated in time as points with error bars and compares these against the  $\Delta\beta = 0$  spectral extrapolation from the X-rays. The uncertainty in the X-ray extrapolation is indicated by the shaded region, which is dominated by the uncertainty on the XRT spectral slope.

The NIR to X-ray spectral slope,  $\beta_{\text{IR-X}}$ , is  $\sim -0.92$ , compared to the XRT value of  $-0.91$  (where  $\beta = 1 - \Gamma$ ). Fit values for this interpretation of the data are listed in Table 4.2. The fit in this case is very good given the uncertainties, although it should be noted that the extrapolated  $K_{\text{E2}}$  point is not in agreement. Host contamination in the  $K$ -band is effectively ruled out by the deep  $HST$  non-detection in F160W, discussed in Section 4.3.4. Therefore, if the X-ray decay model is correct, then this epoch must have been contaminated by a flare or other non-



standard variability.

Dark GRBs are typically classified based on X-ray to optical (i.e.  $r$ -band) rather than X-ray to NIR spectral slopes. GRB 100205A was classified as a dark burst with  $\beta_{\text{OX}} < 0.28$ , due to the very deep  $r$ -band non-detection at early times (Malesani et al., 2010). Given a simple power law SED passing from the X-ray and through the optical limit, the NIR bands would also be expected to have a faint flux, inconsistent with the observations. In order to produce the observed  $r$ -band decrement relative to the X-ray to NIR fit described above, the spectrum would have to show a broken ( $\Delta\beta > 0.5$ ) extrapolation from the X-ray to the  $r$ -band, followed by another sharp steepening of the slope in the narrow frequency range between  $r$  and  $J$  and a return to the original slope at longer wavelengths (lower frequencies) - i.e. three intrinsic spectral breaks in the afterglow. This is not consistent with any model or observation of GRB afterglow behaviour.

For the purposes of investigating the darkness of GRB 100205A, I instead adopt a simple case where the X-ray and NIR lie on the same section of the synchrotron spectrum ( $\Delta\beta = 0$ , or no break). Indeed, the best-fit broken power law from Figure 4.4, and this simplified model, are both consistent with the data.

Since many dark GRBs are the result of dust extinction (see for example Perley et al., 2009; Greiner et al., 2011; Svensson et al., 2012; Perley et al., 2013; Zauderer et al., 2013; Jeong et al., 2014b; van der Horst et al., 2015; Higgins et al., 2019; Chrimes et al., 2019a), a first assumption may be that this apparent break is in fact due to spectral curvature induced by dust absorption within the host galaxy. The precise level of the relative dust correction between the observed  $r$  and  $J$  bands depends on the redshift of the source. Alternatively, the break could be due to the presence of the Lyman- $\alpha$  break between the  $r$  and  $J$  bands (e.g. Kawai et al., 2006; Tanvir et al., 2009).

In order to determine the likely cause of the factor 100 drop in flux to the  $r$ -band, a grid of afterglow models are compared to the extrapolated NIR data points and  $r$ -band flux (for the latter I use the  $1\sigma$  limit, see Table 4.2). The models consist of unbroken power laws with a range of  $\beta$  values given by the uncertainty on the XRT spectral slope. Each model is then placed at a range of redshifts ( $0 < z < 7$ ), subject to a range of rest-frame dust attenuation ( $0 < A_V < 3$ , with an SMC-like attenuation law), and normalised to best fit the extrapolated NIR and  $r$ -band fluxes using  $\chi^2$  minimisation. Because the  $r$ -band encroaches on the Lyman break from around  $z \sim 4$ , the filter profile<sup>6</sup> is accounted for and the effect of line-of-sight averaged HI absorption as a function of redshift (Madau, 1995; Madau and Haardt, 2015) is

---

<sup>6</sup><http://svo2.cab.inta-csic.es/svo/theory/fps>

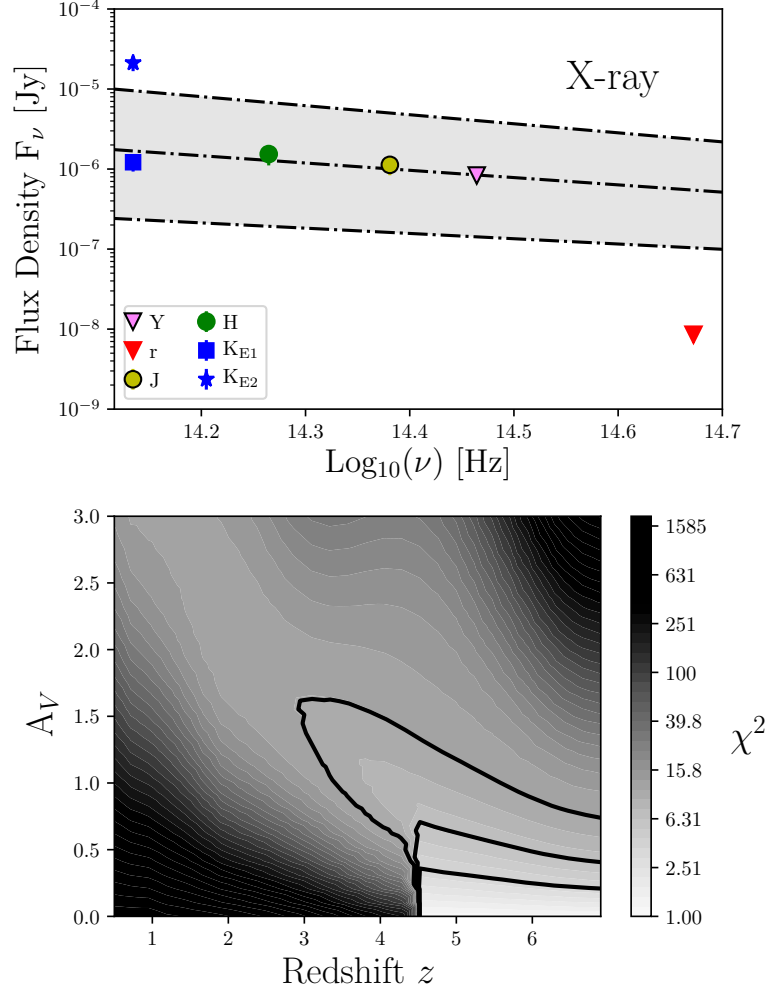


Figure 4.5: Upper panel: the afterglow SED for GRB 100205A, where the  $J$ ,  $H$ ,  $K$ ,  $Y$  and  $r$ -bands (triangles are  $3\sigma$  upper limits) have been extrapolated to the midpoint of the first epoch of observations, assuming the same rate of dimming as measured in the X-rays. Flux uncertainties include the contribution from the uncertainty in temporal evolution. An extrapolation of the X-ray spectral slope with  $\Delta\beta = 0$  at the same epoch is shown, with the 90 per cent confidence region shaded and bounded by dot-dash lines. A strong break occurs between  $r$  and  $J$ . Lower panel:  $\chi^2$  minimisation over a grid of power law models. Contours representing the 67, 95 and 99.5 per cent frequentist probability intervals are overlaid in black.

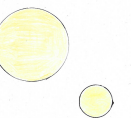


Table 4.2: Values of the parameters obtained from fitting power laws to the X-ray or temporally extrapolated NIR and optical data, assuming the fading rate of either the X-rays or  $K$ -band. Included are the temporal index  $\alpha$  and spectral index  $\beta$  (with 90 per cent errors), extrapolated  $r$ -band limits, and the flux decrement  $F_d$  between the observed  $r$ -band (for which I use the  $3\sigma$   $r$ -band constraint) and the model.

	$\alpha$	$\beta$	Extrapolated $r$ -band 1 (3) $\sigma$ limit [Jy]	$F_d$
X-ray	$-1.97 \pm 0.14$	$-0.91^{+0.25}_{-0.22}$	$2.92 (8.50) \times 10^{-9}$	$> 64$
$K$ -band	$-0.43 \pm 0.16$	$-0.51 \pm 0.26$	$0.47 (1.40) \times 10^{-7}$	$> 5.5$

included. The results of minimising  $\chi^2$  across the grid of parameters is shown in the lower panel of Figure 4.5. The  $K$ ,  $H$ ,  $J$  and  $r$ -bands are used for the fitting of four variables, however these variables are not independent. Therefore, only one degree of freedom is assumed as a conservative estimate, which defines the contours given the minimum in  $\chi^2$  (e.g. Avni, 1976).

The result of this analysis is that the only region of parameter space producing acceptable fits is at high-redshift, and low dust extinctions. Because there is no evidence of the Lyman break entering the  $J$  band, the short-wavelength edge of this band is used ( $\lambda \sim 1.17 \mu m$ ) to infer an upper redshift limit of  $\sim 8$ . This places GRB 100205A in the range  $4.5 < z < 8$ , at the high end of the GRB redshift distribution.

Another possibility is that molecular Hydrogen, vibrationally excited by a strong ultraviolet (UV) flux, could produce absorption at rest-frame UV wavelengths (shortwards of  $1650 \text{ \AA}$ , Draine, 2000; Sheffer et al., 2009; Wiersema et al., 2018). However, molecular to atomic Hydrogen ratios are sufficiently low in GRB hosts, even when  $H_2$  lines are detected, that it effectively rules out this scenario (Bolmer et al., 2019).

### 4.3.2 NIR based SED construction

This analysis also suffers from uncertainty due to the assumed fading rate of the afterglow. For an alternative approach, the temporal decay of the afterglow in the  $K$ -band can be used instead. The NIR temporal index  $\alpha = -0.43 \pm 0.16$  (90 per cent error) is substantially different from the X-ray temporal index, warranting an alternative interpretation of the data using this decay rate instead.

In the upper panel of Figure 4.6, I extrapolate the  $r$ -limit and NIR fluxes to the epoch 1 mean time of 0.18 days using the  $K$ -band decay rate, and fit a spectral slope to the NIR points at that epoch. The best fit NIR spectral slope has the value

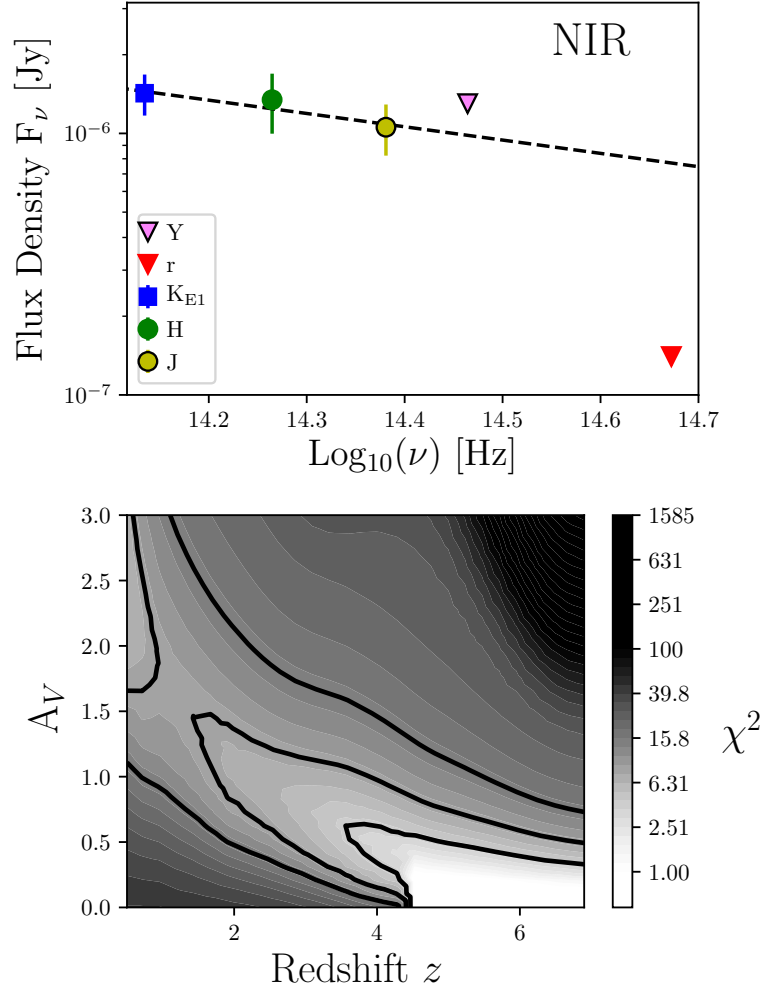
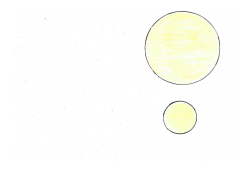


Figure 4.6: Upper panel: As in Figure 4.5, but the fluxes and limits are extrapolated using the decay rate as seen in the  $K$ -band. The  $K_{E2}$  point is not shown as it overlaps with  $K_{E1}$  by construction. The best fit NIR spectral slope is given by the dashed line. Lower panel:  $\chi^2$  minimisation as in Figure 4.5, with data extrapolated according to the  $K$ -band decay rate.



$\beta_{\text{NIR}} = -0.51 \pm 0.26$  (90 per cent error). The break between  $r$  and  $J$  is less strong in this scenario, with a flux decrement of factor  $\sim 5$ . Fit parameters are listed in Table 4.2, for ease of comparison to the X-ray decay interpretation.

A single spectral break between the  $J$  and  $r$  bands could, in this case, explain the photometric data. In order to do this, however, extremely low environmental densities would be required to produce such a blue break frequency at  $\sim 4$ -5 hours post burst, and would be highly unusual (e.g. Wijers and Galama, 1999; Greiner et al., 2011).

As for the X-ray hypothesis, afterglow models are compared to the extrapolated NIR data points and  $r$ -band flux in order to determine the possible cause of this spectral break. The models are once again power laws with a spread of  $\beta$  values, bounded by the uncertainty on the NIR spectral slope. The models are subject to a range of redshifts ( $0 < z < 7$ ), dust attenuations ( $0 < A_V < 3$ ) and normalisations. Neutral hydrogen absorption and the filter profile are accounted for as before. The lower panel of Figure 4.6 shows the results of minimising  $\chi^2$  over this parameter space. Although dusty and low redshift scenarios cannot be ruled out, the 67 per cent confidence region is nearly entirely limited to  $z > 4$  and  $A_V < 0.5$ , indicating a preference for low-dust, high-redshift solutions. The presence of emission in the  $J$ -band, as with the X-ray case, places an upper limit of  $z < 8$  on the burst, putting it in the range  $4 < z < 8$ .

Variability in the NIR cannot be ruled out, particularly as there are only two epochs available in the  $K$ -band. Note that the disagreement between the X-ray and NIR temporal slopes might indicate that there is non-afterglow activity occurring in either band. We can likely be confident that the correct decay rate and spectral slope lie somewhere between the NIR and X-ray cases. The non-standard X-ray afterglow argument is strengthened if the burst is indeed at high-redshift - given that the X-ray observations finished at  $t \sim 40$  minutes, this corresponds to only a few minutes post burst in the rest-frame (for  $4 < z < 8$ ). Such early times often show non-standard afterglow activity, including flares, the decay of which could produce the steep X-ray decline seen in this burst (Nousek et al., 2006).

The result that the burst lies in the range  $4 < z < 8$  is independent of the method chosen to interpret these data as Figures 4.5 and 4.6 demonstrate.

### 4.3.3 High energy properties

The high energy properties of a burst also has the potential to offer redshift constraints. In particular, a bright burst may become a significant outlier in energetics at higher redshift, disfavouring such a distance indication. Figure 4.7 shows the

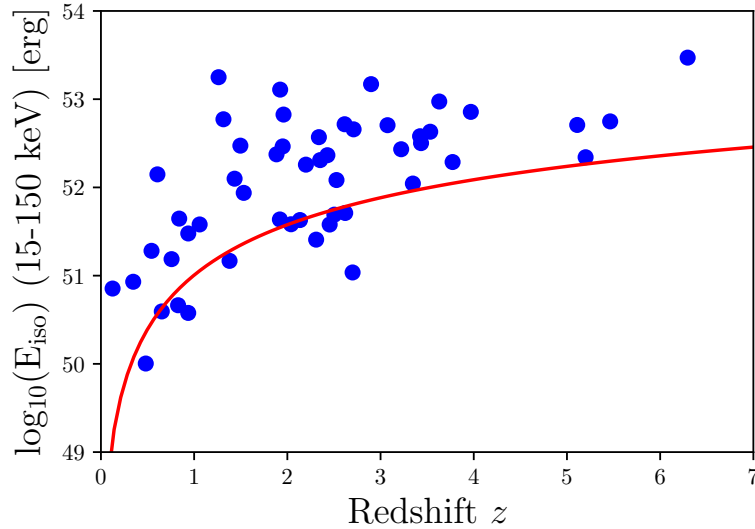


Figure 4.7: The isotropic equivalent energy  $E_{\text{iso}}$  of *Swift* GRBs from the optically unbiased TOUGH sample versus redshift. GRB 100205A (indicated by the red line) is not unreasonably under-luminous at any redshift  $\gtrsim 0.5$ , and not unreasonably luminous at any redshift. Energetics considerations therefore cannot rule out a high-redshift interpretation.

distribution of isotropic energy inferred for *Swift* GRBs from the optically unbiased TOUGH sample against redshift (Hjorth et al., 2012). GRB 100205A is unremarkable if placed any redshift  $\gtrsim 0.5$ , although it is at the fainter end of the luminosity distribution. The energetics of GRB 100205A therefore do not preclude a high-redshift interpretation.

#### 4.3.4 Non-detection of the host

Finally, the extremely deep limit obtained for the galaxy host flux in the *HST* F160W band strongly favours a higher redshift origin. This is not due to the Lyman break - this feature is not redshifted into the F160W filter until  $z \sim 11 - 12$ , and at redshifts this high no *J* or *H*-band afterglow detection would be expected. The NIR afterglow detections in fact provide a firm upper limit on the redshift of  $z \sim 8$ . Instead, the host non-detection implies a very low host flux rather than HI absorption in the intergalactic medium.

In Figure 4.8, I show F160W apparent magnitudes for GRB hosts with known redshift (either from host emission or afterglow absorption lines, Blanchard et al., 2016; Lyman et al., 2017, and Chapter 3). Three high-redshift data points are also

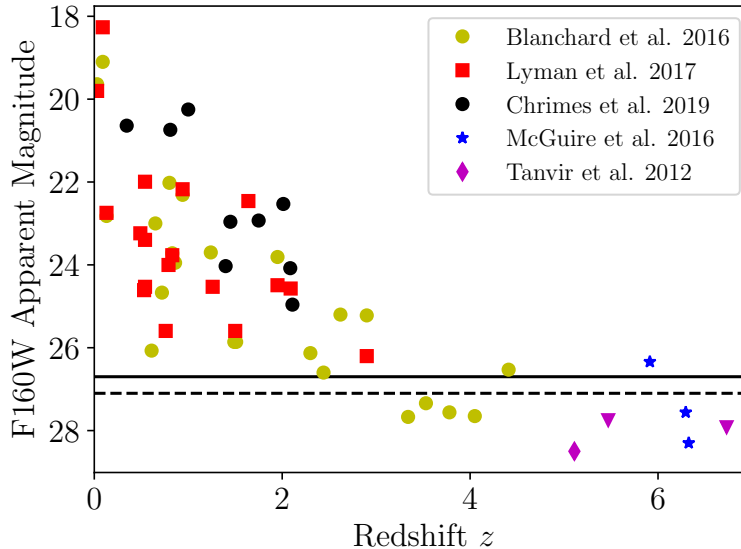


Figure 4.8: GRB host galaxy apparent magnitudes, measured in the *HST* F160W band (Blanchard et al., 2016; Lyman et al., 2017; Chrimes et al., 2019a). Four high-redshift GRB host detections in the *J* and F140W bands, and two  $2\sigma$  upper limits (F160W, triangles), are also shown (McGuire et al., 2016; Tanvir et al., 2012). The  $2\sigma(3\sigma)$  limit at the position of GRB 100205A is indicated with a dashed (solid) line.

included in F140W - GRBs 130606A, 050904 and 140515A (McGuire et al., 2016) - in addition to one detected host (GRB 060522, *J*-band) and two deep limits (F160W) from Tanvir et al. (2012). The Lyman et al. (2017) sample is composed exclusively of optically bright (thus  $z < 3$ ) bursts. The sample from Chapter 3 is composed exclusively of dark bursts. The other samples include a mixture of bursts. For redshifts  $z \lesssim 3$ , an apparent  $1\text{-}2\mu\text{m}$  (observed) magnitude of  $> 26.7$  is uncharacteristically faint for GRB hosts, and at these lower redshifts essentially all are detected. Conversely, at  $z \gtrsim 3$ , such faint hosts become the norm, with most host galaxies undetected at this level. Note that in the sample of Chapter 3, GRB 100205A is the *only* burst for which no host is detected in F160W. If we assume that GRB 100205A occurred at  $z = 5$ , the rest-frame UV absolute magnitude of the host is  $M_{\text{UV}} > -19.74$ , placing it at least one magnitude fainter than  $M_*$  at that redshift (Bouwens et al., 2015) - demonstrating the ability of GRBs to select low mass star forming galaxies in the distant Universe.

## 4.4 Conclusions

In this Chapter, I have presented Gemini and *HST* imaging of the afterglow and host galaxy location of the dark GRB 100205A. The lack of a detected host at  $m_{\text{AB}}(\text{F160W}) > 26.7$  ( $3\sigma$ ), combined with a strong spectral break in the afterglow SED between  $r$  and  $J$ , suggests a high-redshift ( $4 < z < 8$ ) origin for this burst, adding it to the small sample of GRBs known to have occurred in the early Universe. Despite the limited photometric coverage and lack of co-eval multi-wavelength data, this conclusion stands independent of the spectral and temporal extrapolation methods assumed. It was only identified thanks to rapid and deep optical observations that could place meaningful constraints on the darkness of a burst with an apparently faint X-ray afterglow, and subsequently inform infrared observations. This highlights that such deep observations, beyond the range of modest aperture telescopes at any epoch, may well be necessary to significantly increase the sample of known high-redshift GRBs. Furthermore, this work demonstrates the importance of having deep multi-wavelength data at several epochs, so that spectral and temporal slopes can be less ambiguously determined.

## 4.5 Subsequent Developments

The work described in this Chapter was published in the *Monthly Notices of the Royal Astronomical Society* in July 2019. Since then, no further GRBs have been reported at  $z > 5$ , and only two have been discovered at  $z > 3$  since the start of 2019<sup>7</sup>. This demonstrates the scarcity of high-redshift events, the necessity of rapid and deep multi-wavelength follow-up observations to identify them, and the value in investigating overlooked archival events.

---

<sup>7</sup>[https://swift.gsfc.nasa.gov/archive/grb\\_table/](https://swift.gsfc.nasa.gov/archive/grb_table/)



## Chapter 5

# The progenitors and event rates of long-duration gamma-ray bursts with BPASS

No endemic New Zealand creatures were harmed in the making of this Chapter.

In this Chapter, I explore the possibility that massive stars in binaries, without undergoing quasi-homogeneous evolution, can produce GRBs given the right evolutionary history, even at moderate to high metallicities (see e.g. Podsiadlowski et al., 2004; Izzard et al., 2004; Petrovic et al., 2005; Detmers et al., 2008; Trenti et al., 2015). This route is particularly promising as binary interactions are likely responsible for the rapid rotation of massive stars (de Mink et al., 2013). To investigate, I introduce a tidal interaction post-processing algorithm to the BPASS (Binary Population and Spectral Synthesis) stellar evolution models in order to account for angular momentum transfer between orbital and stellar rotation. I investigate subsets of the resultant high mass, rapidly spinning, stripped envelope population, and explore the consequences of matching synthetic GRB rates arising from selection criteria to observations.

### 5.1 Introduction

It is known that long GRBs require a stripped envelope progenitor with a large reserve of angular momentum at core-collapse. However, the evolutionary pathways which lead to these progenitors are not well constrained (see Levan et al., 2016;

Fryer et al., 2019, and references therein). Models invoking single stars struggle to maintain enough angular momentum over the stellar lifetime, while simultaneously losing the outer envelope through winds (Vink et al., 2001; Hirschi et al., 2005; Vink and de Koter, 2005; Woosley and Bloom, 2006; Vink et al., 2011a; Modjaz et al., 2016). Furthermore, the central engines are unknown. GRBs could be ‘collapsars’, (Woosley, 1993; Woosley and MacFadyen, 1999), in which a collapsing star powers a rapidly spinning black hole central engine, which launches relativistic jets. If the jets produced can escape the envelope (a requirement which might explain the association with stripped envelope supernovae, since these stars do not have a thick hydrogen envelope which may stifle a jet e.g. Modjaz et al., 2016), and we are aligned along the jet axis, the event is observable as a relativistically-beamed GRB (MacFadyen and Woosley, 1999; MacFadyen et al., 2001; Woosley and Bloom, 2006; Hjorth, 2013). Alternatively, the central engine could be a rapidly spinning neutron star with a strong magnetic field (a magnetar, Wheeler et al., 2000; Mazzali et al., 2014), which powers relativistic jets as it spins down.

One promising pathway is through chemically homogeneous evolution. In the later stages of binary evolution, the primary can expand and fill its Roche lobe, triggering accretion onto the secondary star. This can spin up the secondary, and if sufficient angular momentum is transferred, rotational mixing can occur within the star (Cantiello et al., 2007; de Mink et al., 2009; Eldridge et al., 2011; de Mink et al., 2013). If the star becomes fully mixed, it evolves chemically homogeneously, becoming smaller, hotter and hydrogen deficient, and evolving blue-wards on the Hertzsprung-Russell diagram. If this process occurs at low metallicity, the secondary can retain the angular momentum gained from mass transfer, and end its life as a rapidly spinning, massive type Ic progenitor - a good candidate for producing a GRB. Eldridge et al. (2019a) calculated the volumetric event rate of GRBs as a function of redshift, assuming that they arise solely from a quasi-homogeneous evolution (QHE) pathway (Yoon et al., 2006; Cantiello et al., 2007), using the BPASS stellar evolution and population synthesis code (Eldridge et al., 2017). They found that although QHE stars could account for the observed GRB rate, there are significant uncertainties arising from luminosity function and beaming corrections. Additionally, BPASS only implements QHE pathways at metallicities  $Z < 0.004$ . GRBs are not exclusively found at such low metallicity, with observed examples arising in environments exceeding Solar abundance (e.g. Graham et al., 2009; Schady et al., 2015; Michałowski et al., 2018b; Hashimoto et al., 2018). QHE cannot therefore be the sole contributing pathway. One mechanism not considered in Eldridge et al. (2019a) is angular momentum transfer through tidal interactions in binaries.

This Chapter details the use of the population synthesis code BPASS to investigate the plausibility of tidally spun-up massive stars as GRB progenitors. The Chapter is structured as follows: In Section 5.2, I outline the categorisation of models into different classes of core-collapse progenitor, producing updated BPASS classifications for the properties of supernova progenitors. Section 5.3 describes the implementation of tides within BPASS, and the effect of their inclusion. A comparison to observations is presented in Section 5.4, with a Markov Chain Monte Carlo (MCMC) analysis used to infer the most likely parameter values in a two-progenitor pathway model. Section 5.5 details the results, including predictions for progenitor properties such as their position on the Hertzsprung-Russell diagram, and the interior angular momentum at core-collapse. A discussion of the physical interpretation of these models follows in Section 5.6, with conclusions presented in Section 5.7.

## 5.2 Classification of Core-Collapse Progenitor Models

GRBs, when close enough (typically within  $\sim 1$  Gpc) and followed up with prompt and deep optical-NIR observations, typically show evidence for an associated broad-lined type-Ic supernova (Ic-BL SN). The preference for stripped-envelope supernovae of this type is likely a jet escape requirement, as a thick envelope of helium or hydrogen around the star may prove an insurmountable barrier to the ejection of fast-moving material and hence stifle any incipient jet. It appears as though not every Ic-BL SN has an accompanying GRB, although in some cases the jet might be choked, as may have been the case in SN 2008D (Mazzali et al., 2008; Piran et al., 2013; Modjaz et al., 2016; Sobacchi et al., 2017; Barnes et al., 2018). Nevertheless, the minimum requirement for a stripped envelope is an observational constraint on the progenitor stars of GRBs. Using the binary stellar evolution models of BPASS (Tuatara v2.2.1, Stanway and Eldridge, 2018), the first step in identifying GRB pathways is to find models which likely produce type Ic-SNe.

At each step in the BPASS models, stellar properties such as mass, interior structure and chemical composition are calculated. When core carbon burning ends, the stellar model is assumed to progress rapidly through the final stages of core burning (if massive) before ending its life (Woosley et al., 2002). If a supernova occurs, the stellar model is then replaced by a neutron star or black hole based on the final stellar mass and the amount of mass that could be removed by energy injection from a supernova of  $10^{51}$  erg. Because supernovae are observationally classified according to their spectral properties, which reflect the chemical composition of the

ejecta and circumstellar medium (Filippenko, 1997), we can predict which supernova type each model will produce based on its chemical properties immediately before core-collapse.

Our first task is to identify stars which produce supernovae. The fate of stars with final masses  $< 2M_{\odot}$  is uncertain. They might produce weak, faint and fast core-collapse supernovae (Moriya and Eldridge, 2016), or, depending on the central carbon abundance, type Ia supernovae. Alternatively, they could form white dwarfs without a supernova. Supernovae from these stars would in any case be rare events (Eldridge et al., 2017).

I find models that likely experience a supernova by two methods, based on the BPASS v2.1 specifications described in Eldridge et al. (2017). First, if at the end point of a model the CO core mass is greater than  $3M_{\odot}$ , a supernova occurs. Second, at lower masses, due to the complexity of second dredge-up and carbon burning in super-AGB stars, we require that the final total mass exceeds  $2M_{\odot}$ , the CO core mass is greater than  $1.38M_{\odot}$  and core carbon burning has occurred (when the ONe core is greater than  $> 0.1M_{\odot}$ ). Then, if the remnant mass is in the range  $\sim 1.4-3M_{\odot}$ , a neutron star results. Above this remnant mass, black holes are created, and supernovae in this regime are uncertain, with ‘islands of explosability’ in mass (e.g., Sukhbold et al., 2016; Auchettl et al., 2019; Woosley, 2019; Sukhbold and Adams, 2019). It is believed that most stars above a zero-age main sequence mass of  $20M_{\odot}$  will create a black hole remnant and have their explosion engulfed within the Schwarzschild radius, thus producing no visible display. This picture is increasingly backed up by a lack of high mass stars seen in pre-explosion imaging (the Red Supergiant problem, Smartt, 2009, 2015), possible tension between star formation and SN rates (Horiuchi et al., 2011), and the direct observation of a quietly disappearing massive star (Adams et al., 2017). As such, any model which produces a remnant mass greater than  $3M_{\odot}$  (i.e. a black hole) is initially disregarded and classified as a vanishing event (see Eldridge and Tout, 2004, for a description of how remnant and ejecta masses are calculated).

Otherwise, if the stellar structure at the end of the model still satisfies the carbon-oxygen, oxygen-neon and total mass conditions listed above, it is assumed that a visible supernova will be produced. I then split these models into three categories, types Ib, Ic, and II, based on their chemical composition (as described by Eldridge et al., 2011, 2013, 2017).

The type I/type II divide is defined by the total mass of hydrogen in the star; observationally this is probed by the presence of hydrogen lines in the SN spectrum, or lack thereof. Theoretically, a small residue of hydrogen may still be present



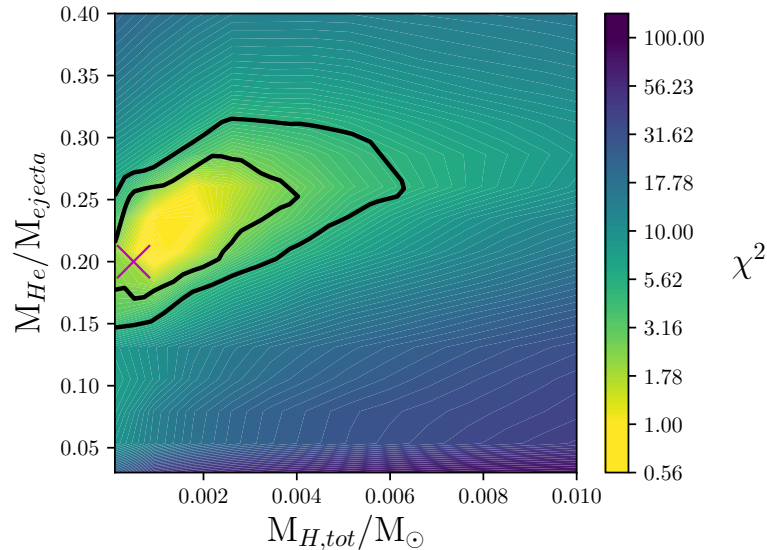


Figure 5.1: The result of matching type II, Ib and Ic SN relative fractions to observations, by minimising  $\chi^2$  over  $M_{H,tot}$  and  $F_{He,ejecta}$  parameter space. The best fit classification thresholds, assuming that black hole producing events do not go supernova, are marked by a cross. Solid contours represent the 68 and 90 per cent confidence regions for one degree of freedom.

without leaving observational evidence, as long as it is below some threshold. This threshold is varied, labelling models with a total hydrogen mass less than  $M_{H,tot}$  as type I and those with more as type II. The type Is are further divided into Ibs (which have visible helium lines) and Ics (with no helium or hydrogen in their spectra). This is decided by the fraction of helium in the ejecta,  $F_{He,ejecta}$ , and this threshold is also varied. The total hydrogen mass is used, rather than the fraction of hydrogen in the ejecta, because (unless QHE is underway) the majority of the hydrogen should be on the surface of the star and therefore mixed into the ejecta upon supernova.

The models in each category are then assigned a weighting, which corresponds to the estimated occurrence frequency of each model in a star formation episode, assuming  $10^6 M_{\odot}$  of metal enriched gas were allowed to collapse and form stars with 100 per cent efficiency. The weightings are informed by observations of stars in terms of binary fractions, mass distributions, binary orbital periods and mass ratios (Moe and Di Stefano, 2017) and correspond to the weightings from v2.2 of the BPASS spectral synthesis models (Stanway and Eldridge, 2018). The standard BPASS initial mass function (IMF) is used. This is parameterised as a power-law in  $\frac{dN}{dm}$ , and has a slope of -1.3 in the range 0.1-0.5 $M_{\odot}$ , and -2.35 from 0.5

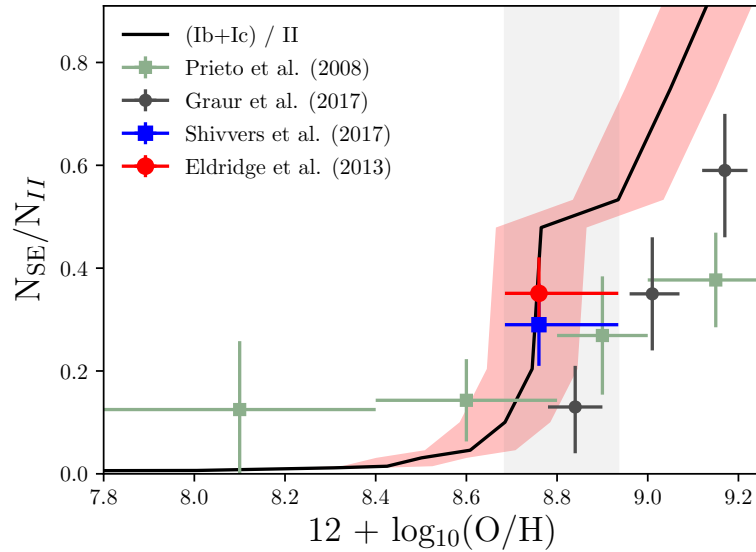


Figure 5.2: The ratio of stripped envelope (SE) to hydrogen-rich (type II) supernovae as a function of metallicity, using the best fit  $M_{\text{H,tot}}$  and  $F_{\text{He,ejecta}}$  thresholds (black line), assuming that supernovae only occur if a black hole is not produced. Metallicities in the range 0.008 to 0.02 by mass fraction are indicated by a grey shaded band. The red shaded region is a 0.1 dex uncertainty, intended to give an indication of the discrepancies between different metallicity scales (Eldridge et al., 2017). Where a dataset metallicity range is not explicitly defined, I assume that it samples the local metal mass fraction spread of 0.008 to 0.02. Observed ratios from Prieto et al. (2008), Graur et al. (2017), Shivvers et al. (2017) and Eldridge et al. (2013) are used as comparison data.

to a maximum of  $300M_{\odot}$ .

For a  $10^6M_{\odot}$  stellar population, at each metallicity  $Z$  ( $12 + \log_{10}(\text{O}/\text{H})$  over the range  $10^{-4}$  to 0.04 by metal mass fraction) I calculate the relative contribution to the total number of supernovae from each type (II, Ib and Ic), summed over 10 Gyr from  $t = 0$ . The average of the fractions over the  $Z = 0.008, 0.010, 0.014$  and  $0.020$  metallicities are then compared to observed fractions from volume limited supernova studies. The metallicity range used for comparison is broadly representative of the range seen in the local Universe. For the type I/type II ratio we refer to Eldridge et al. (2013), which is a volume-limited sample and therefore representative of the intrinsic ratio. Shivvers et al. (2017) is used for the Ib/Ic ratio, due to their careful reclassification of a number of stripped envelope SNe from the Lick Observatory Supernova Search (LOSS).

In using the LOSS data, I have classified type IIb events as Hydrogen-rich

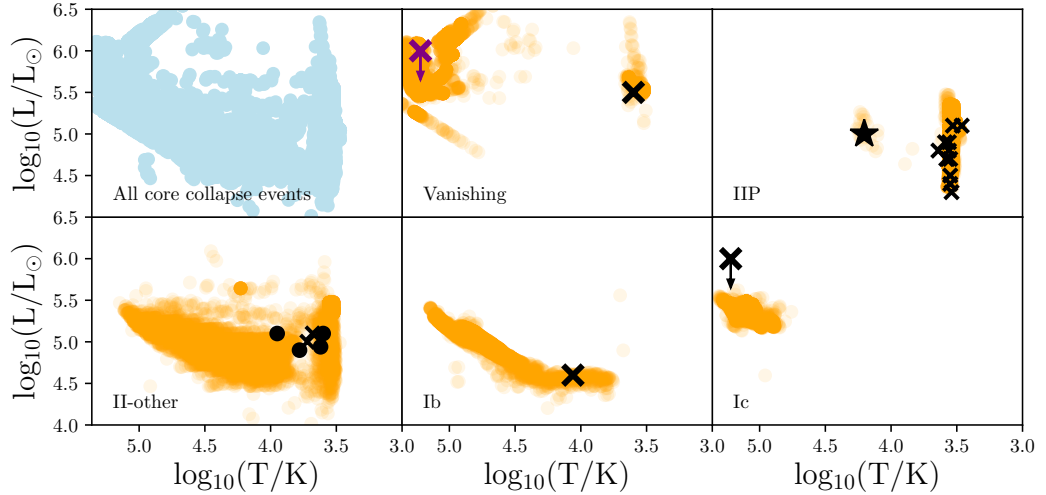


Figure 5.3: Following the categorisation of BPASS model such that the observed supernova relative rates are reproduced, I place the pre-explosion properties of these models on the HR diagram (in orange) according to core-collapse type. The shading represents the number density of models. Observed progenitors (in black) include the vanishing star N6946-BH1 (marked by a cross, Adams et al., 2017), for which the luminosity has been adjusted to reflect an updated distance estimate (Eldridge and Xiao, 2019), SN 1987A (marked by a star in the IIP section, Walborn et al., 1987), several IIP SNe from Smartt (2015), type IIb and IIL SNe (both classified as II-other, and marked by dots and crosses respectively, Smartt, 2015), SN 1993J (also a IIb event, Aldering et al., 1994), the Ib progenitor of SN iPTF13bvn (Eldridge and Maund, 2016) and finally the candidate Ic progenitor of SN 2017ein (Van Dyk et al., 2018). The marked luminosity for 2017ein is an upper estimate, assuming that it was a single star (Kilpatrick et al., 2018). This progenitor system is also indicated on the ‘vanishing’ panel (in purple) for reference.

(so that they are in the type II category), and regular, peculiar and broad-line Ic SNe are grouped together. Type IIs can be subdivided into IIP (plateau) and II-other classes, but this is not used for constraining the pre-core-collapse properties as there would be too many degrees of freedom. Instead, I use the selection criteria of Eldridge et al. (2017), where type IIPs are defined to have  $M_{\text{H,tot}} > 1.5M_{\odot}$  and a hydrogen to helium ratio greater than 1.05.

I use the difference between the BPASS weighted fractions and the observed fractions to calculate  $\chi^2$ , which is then minimised by varying  $M_{\text{H,tot}}$  and  $F_{\text{He,ejecta}}$  across parameter space. The results of this process are shown in Figure 5.1. The best fitting values are  $M_{\text{H,tot}} = 5 \times 10^{-4}M_{\odot}$  and  $F_{\text{He,ejecta}} = 0.20$ , with SN types II, Ib and Ic making up 75, 14 and 10 per cent of the local Universe supernova rate respectively. This compares to the Eldridge et al. (2013) and Shivvers et al. (2017)

combined percentages of  $74 \pm 7.6$ ,  $14.5 \pm 2.6$  and  $11.5 \pm 2.0$ . The differences correspond to a  $\chi^2$ , equivalent to a reduced  $\chi^2$  in this case, of 0.27. The large uncertainties on the observed fractions, taken together with the large number of free parameters, allows for a range of values above these best fitting thresholds. Hydrogen masses up to 0.0022, and  $F_{\text{He,ejecta}}$  values in the range 0.17-0.26, are permitted within the 68 per cent confidence interval. Nonetheless, there is a clear preference for lower values, with the upper end of the explored parameter space firmly excluded.

The best-fit values for  $M_{\text{H,tot}}$  and  $F_{\text{He,ejecta}}$  found here differ from previously reported BPASS values (Eldridge et al., 2013, 2017). For the helium threshold, the difference is primarily due to our use of the reclassified type Ib/Ic supernova ratio from LOSS (Shivvers et al., 2017). The hydrogen threshold differs because (i) the previous BPASS values were an ansatz, informed by synthetic spectra results reported in the literature, and (ii) varying the He threshold also affects the type I/II cut-off. This is evidenced by the correlation between the two thresholds in Figure 5.1. Furthermore, the best-fit value is only a factor of two smaller than previously assumed. This is within the uncertainties of the fit, and in terms of the stellar evolution models (which vary by a factor of  $\sim 100$  in metallicity mass fraction) represents only a small change.

Dessart et al. (2011) predicted the supernova spectra from Wolf-Rayet stars, and found that hydrogen lines are initially visible if more than  $10^{-3} M_{\odot}$  of hydrogen is present, likely making such events type IIb. This is consistent with a  $M_{\text{H,tot}} = 5 \times 10^{-4} M_{\odot}$  type I/II threshold. Dessart et al. (2012b) then showed that helium ejecta fractions as low as 0.2-0.3 can produce visible helium lines in the spectrum, again consistent with these results.

Using the selection criteria determined from comparison to the local Universe supernova rates, I apply these cuts over the entire BPASS metallicity range. The predicted stripped envelope to hydrogen-rich ratio as a function of metallicity is shown in Figure 5.2, with the ratios as reported by various observational studies also shown. The BPASS metallicity scaling used in this Chapter includes modifications to the previous scale used (Xiao et al., 2018), to improve agreement with the data at low metallicities (see Figure 44 of Eldridge et al., 2017, and Table 5.1). Note that the stellar evolution is driven primarily by iron abundance and bulk metallicity mass fraction, rather than the oxygen abundance (Hashimoto et al., 2018). The BPASS relative rates generally agree with observation, including with those studies listed in (Smartt, 2009), which are not shown on the Figure for clarity. However, at the highest metallicities, there are discrepancies. The models appear to over-predict the rate of stripped envelope events relative to Hydrogen-rich events at significantly



Table 5.1: The BPASS metallicity scaling used in this work, adapted from Xiao et al. (2018). For a detailed discussion of metallicity scales and uncertainties, please refer to Eldridge et al. (2017).

Metal fraction by mass	Previous	New	
	12+log(O/H)	12+log(O/H)	12+log(Fe/H)
0.0001	6.60	7.00	5.23
0.001	7.61	8.00	6.24
0.002	7.91	8.31	6.54
0.003	8.09	8.43	6.72
0.004	8.21	8.51	6.84
0.006	8.39	8.61	7.02
0.008	8.52	8.69	7.15
0.010	8.62	8.75	7.25
0.014	8.77	8.77	7.40
0.020	8.93	8.93	7.57
0.030	9.13	9.05	7.76
0.040	9.27	9.13	7.90

super-Solar metallicities. In this regime the remnant mass and ejecta composition are strongly sensitive to the assumed mass loss rates on the asymptotic giant branch and immediately preceding the explosion. Small adjustments in the assumed wind prescription may have a significant effect on the supernova type ratio and further work is required to explore this further.

Using the derived classification criteria, I place every pre-core-collapse model (in the metallicity range 0.08-0.020) on a Hertzsprung-Russell diagram in Figure 5.3. I also show known or candidate progenitors, identified from pre-explosion imaging. In most cases, there is good agreement. The only candidate which could be in tension is that of the type Ic progenitor, SN 2017ein (Van Dyk et al., 2018; Kilpatrick et al., 2018), although it is currently unclear how much of the pre-explosion stellar light was from the progenitor, rather than a possible binary companion, and so this data represents an upper limit. Note that increasing the remnant threshold for supernova production (i.e. assuming lower supernova mass-ejection energies or less efficient black-hole stifling of any core-collapse event) would improve the agreement here. The physical properties of observed Wolf-Rayet stars are similarly more typical of the most luminous Ic progenitor models in this classification, with luminosities around  $\log_{10}(L/L_{\odot}) \sim 5.6$  (Neugent and Massey, 2019), although there is no observational constraint on whether these stars will go supernova or not.

A possible resolution to the type Ic tension is that SN 2017ein may have produced a supernova *and* a black hole remnant. Modelling of pre core-collapse stellar

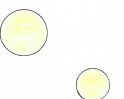
structure shows that some black-hole producing events can successfully explode if the core has a low compactness parameter (Sukhbold et al., 2016), although this is just one of several relevant quantities (Mapelli et al., 2019). Furthermore, work in this area has typically focused on red supergiants, since these are the class of stars which we would have expected to see in pre-explosion imaging - stripped envelope supernovae are typically too distant to expect to see the progenitor. Therefore, we have few constraints on the explodability of such stars, and the generic vanishing threshold applied might not be applicable to stripped envelope stars. Another possibility is that supernovae can occur in stars that would otherwise implode thanks to energy injection from a rotationally powered central engine. This could be from disc winds (e.g. MacFadyen and Woosley, 1999) or a jet (for example, type Ic-BL SNe might harbour choked jets, Mazzali et al., 2008; Piran et al., 2013; Modjaz et al., 2016; Izzo et al., 2019). I refer the reader to Piran et al. (2019) for a review of these ideas.

Regardless of the mechanism, it is likely that some black hole producing events cause visible supernovae, and that these have been classified as vanishing in this analysis so far. One example are pair-instability supernovae (PISNe, Heger and Woosley, 2002), which are classified as occurring in stars with helium cores between 64 and 133  $M_{\odot}$  at core-collapse in this work (following Eldridge et al., 2017). However, these particular events likely disrupt the star leaving no remnant. They are also exceptionally rare and do not significantly impact the analysis thus far.

It is likely that GRBs do indeed require such a black hole central engine, but these events are also luminous and associated with supernovae. In order to decide which BPASS models end their lives as GRBs, we therefore need to consider the rotation of stars which are Ic-like in their chemical composition, but which also produce black holes at core-collapse. Note that these additional black hole producing SNe are rare, given that they have higher mass progenitors. They make a small difference to the relative SN rates in the local Universe, therefore having a minimal impact on the supernova categorisation - this is demonstrated later, see for example Figure 5.14.

### 5.3 Introducing Complex Tidal Interactions to BPASS

The surface composition and structure of the pre-explosion progenitor allows us to identify the subset of BPASS models which produce Ic SNe and black holes. In order to produce a GRB, however, rapid rotation is also required. BPASS accounts



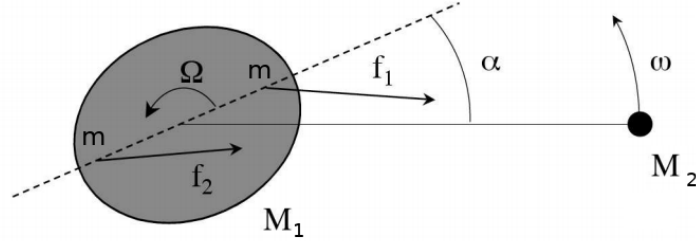


Figure 5.4: A schematic diagram representing the operation of the equilibrium tide. Tidal bulges induced on the primary (mass  $M_1$ ) can be modelled as diametrically opposed smaller masses  $m$ . The forces  $f_1$  and  $f_2$  produce a torque which always act to either spin-up the primary (moving the secondary to a lower orbit) or vice versa, tending towards synchronisation where the orbital angular velocity  $\omega$  equals the primary rotational velocity  $\Omega$ . The secondary mass  $M_2$  is treated as a point mass. This figure is adapted from Zahn (2008).

for the first order effects of mass loss and mass transfer on the spins of stars in binaries, but we must also consider the transfer of angular momentum between the orbit and stellar spins due to tidal interactions. BPASS currently only invokes tidal interactions when Roche lobe overflow occurs (Eldridge et al., 2017), however tides may have a substantial impact at all stages of stellar evolution. In this Section I describe the first-order application of tides to the BPASS output models.

### 5.3.1 Tidal forces

Tidal interactions arise because (i) astrophysical bodies such as galaxies, stars and planets are not point masses and (ii) because the components of a binary orbit a common centre of mass. Refer to Figure 5.4. The gradient of the gravitational potential across the primary due to the secondary results in the formation of two tidal bulges, one facing the secondary and one opposing (which can be described as being due to a centrifugal force).

The primary can be modelled as a large mass  $M_1$  with two smaller masses  $m$  on opposite sides, representing the bulges. In Figure 5.4, the forces  $f_1$  and  $f_2$  act on these small masses. Because  $f_1 > f_2$ , there is a torque  $\Gamma$  which acts to slow the rotation of the primary (if  $\Omega > \omega$ ) such that the semi-major axis aligns with the line joining the primary centre of mass to the secondary. The imbalanced forces  $f_1$  and  $f_2$  also have a component which drags the secondary ahead in its orbit, widening the

orbit. If the secondary were already ahead of the semi-major axis of the primary, then the opposite occurs: the secondary is dragged back, moving it to a lower orbit, while the torque on the primary acts to spin it up. The effect of this tidal torque, therefore, is to push the system towards synchronisation (i.e.  $\Omega = \omega$  and  $\Gamma \rightarrow 0$ ).

For the following I assume that the tidal lag angle  $\alpha$  is small (the weak friction approximation). Friction between the bulges and the main body of the star is how the torque is able to slow or increase the primary rotation. The net components of  $f_1$  and  $f_2$  acting along the tangential direction of motion of the secondary can be approximated as  $(f_1 - f_2) \sin(\alpha)$ . It can be shown (Zahn, 2008; Eldridge and Tout, 2019) that the resultant torque is given by,

$$\Gamma \approx -\left(\frac{R}{a}\right)^6 GM_2 \alpha \quad (5.1)$$

where  $M_2$  is the secondary mass, and the apsidal motion constant  $k$  (which accounts for the deformability of the star) has been set equal to 1. The lag angle can be written in terms of the difference between the primary rotational ( $\Omega$ ), and orbital ( $\omega$ ), angular velocities,

$$\alpha = (\Omega - \omega) \tau_{\text{lag}} \quad (5.2)$$

where  $\tau_{\text{lag}}$  has dimensions of time to return  $\alpha$  as an angle. We would like to estimate what this lag time is. Physically, from the reference frame of the primary surface, this lag time is the delay between a bulge (or small mass  $m$  in the model) and the secondary passing overhead. Again thinking in terms of the primary ( $M_1$ ) reference frame, bulges on the surface will appear to rise and fall at any fixed location (as Earth's ocean tides appear to). The rate of change of energy, when a mass  $m$  falls from a height  $z$ , is approximately,

$$\frac{E_{\text{tide}}}{\tau_{\text{damp}}} \approx \frac{mv^2}{\tau_{\text{damp}}} \approx Fv \approx \left(m \frac{dg}{dz} z\right) v \quad (5.3)$$

where  $\tau_{\text{damp}}$  is the time taken for the bulge to dissipate. It also takes time  $\tau_{\text{lag}} = z/v$  for the bulge to rise and fall. The local gravitational acceleration  $g = GM_1/(R+z)^2$ , so that

$$F \approx m \frac{dg}{dz} z \approx m \frac{GM_1}{R^3} z \approx m \frac{GM_1}{R^3} v \tau_{\text{lag}} \quad (5.4)$$

referring back to equation 5.3 this leads us to,

$$m \frac{GM_1}{R^3} v^2 \tau_{\text{lag}} \approx \frac{mv^2}{\tau_{\text{damp}}} \quad (5.5)$$



and hence,

$$\tau_{\text{lag}} \approx \frac{R^3}{GM_1} \frac{1}{\tau_{\text{damp}}} \quad (5.6)$$

so that the lag timescale, and therefore the strength of the tidal torque, depends on the damping timescale  $\tau_{\text{damp}}$  over which the bulges are dissipated (Eldridge and Tout, 2019).

### 5.3.2 Convective damping of the equilibrium tide

There are two mechanisms for tidal dissipation within stars. The first is convective damping of the equilibrium tide, the equilibrium tide being due to persistent (from the observers reference frame) tidal bulges as discussed above. Tidal forces are strongly dependent on radius, whatever the dissipation mechanism, and so the nature of the stellar envelope (rather than the core) determines which mechanism is dominant. For lower mass stars on the main sequence, convection dominates the envelope. Convection leads to turbulent viscosity, which provides the necessary friction to couple torques on the bulges to the rest of the star. The damping timescale due to convection can be approximated as,

$$\tau_{\text{damp}} \approx \tau_{\text{convective}} \approx \left( \frac{M_{\text{env}} R_{\text{env}} R}{3L} \right)^{\frac{1}{3}} \quad (5.7)$$

where ‘env’ denotes the envelope and  $L$  is the stellar luminosity (Hurley et al., 2002; Eldridge and Tout, 2019).

### 5.3.3 Radiative damping of the dynamical tide

Given that we are interested in stars with masses greater than  $2M_{\odot}$ , which have radiative envelopes for the majority of their lives, I employ the second mechanism - radiative damping of the dynamical tide (Zahn, 1975, 1977; Hut, 1981; Goldreich and Nicholson, 1989; Hurley et al., 2002) - and assume that convective damping is negligible. The mass and orbit of a companion star introduces a time-varying external gravitational potential. In the radiative regime, this variation couples to  $g$ -modes (where buoyancy is the restoring force) within the radiative envelope. The density within this zone is not constant, and the frequencies corresponding to orbital motion preferentially drive  $g$ -modes deeper within the radiative zone, near the convective core, because the Brunt-Väisälä oscillation frequency is density dependent. The induced  $g$ -modes distort the star, allowing gravitational torques to act. The excited waves would be standing waves if they were reflected at the stellar surface, but because the radiative timescale there is short, they are only partially reflected,

undergoing a phase shift. Angular momentum is therefore transported from the core to the surface, or vice versa, by the induced  $g$ -modes (Zahn, 1975; Goldreich and Nicholson, 1989).

### 5.3.4 Implementation of tides

The BPASS stellar models are not recalculated to include tides at each time-step, as this would be extremely computationally expensive. Instead, the approach is analogous to the rapid population synthesis models of Hurley et al. (2002). I choose a subset of the BPASS output models and implement a post-processing algorithm as described below. First, I identify every primary and secondary star model which produces a black hole remnant and has the chemical properties of a Ic progenitor immediately before core-collapse. In this model subset, the lowest initial mass, at any metallicity, is  $10M_{\odot}$ . Using this to inform the strategy, I opt to consider every primary and secondary model in BPASS with Zero Age Main Sequence (ZAMS) masses greater than  $7M_{\odot}$ , expecting that binary interaction, enhanced by tides, might cause some slightly lower mass stars to move onto black hole/type-Ic pathways.

For each model, over each time-step, the expected change in the orbital semi-major axis  $\Delta a_{\text{tides}}$  due to tides is calculated. The change in  $a$  and corresponding change in the stellar rotational angular velocity  $\Omega$  are given by,

$$\Delta a_{\text{tides}} = \frac{6ka}{t_{\text{damp}}} q(1+q) \left(\frac{R}{a}\right)^8 \left(\frac{\Omega}{\omega} - 1\right), \quad (5.8)$$

and

$$\Delta \Omega = -\frac{3k}{t_{\text{damp}}} \frac{q^2}{r_g^2} \left(\frac{R}{a}\right)^6 (\Omega - \omega) \quad (5.9)$$

where  $k$  is an apsidal motion constant (typically in the range 0.01-0.1, 0.05 is adopted, Zahn, 1975),  $q$  is the ratio of secondary mass to primary mass,  $R$  is the stellar radius,  $\omega$  is the orbital angular velocity and  $r_g = I^{0.5} M^{-0.5} R^{-1}$  (Zahn, 1977; Hut, 1981; Hurley et al., 2002; Eldridge and Tout, 2019). The moment of inertia  $I$  is assumed to be that of a solid sphere,  $\frac{2}{5}MR^2$ , using the total stellar mass  $M$  (and assuming solid body rotation). This approximation is made for the current study as detailed calculations using stellar structure models would be computationally expensive. Most stars show only a small differential rotation gradient while still on the main sequence, although post-main sequence stars may show a significant disconnect between envelope and core rotation (Heger et al., 2000). The final term left undefined is the damping timescale,  $t_{\text{damp}}$ . For radiative damping, it can be

shown that the damping timescale is,

$$t_{\text{damp}} = \frac{ka^5}{(1.9782 \times 10^4) MR^2 (1+q)^{5/6} E_2} \text{ yrs} \quad (5.10)$$

where  $M$ ,  $R$  and  $a$  are in Solar units (Hurley et al., 2002), and  $E_2$  is a second-order dimensionless coefficient, parameterising the strength of the tidal interaction given the internal structure of the star.  $E_2$  was calculated for a limited number of stellar models by Zahn (1975). Subsequently, Hurley et al. (2002) fitted a functional form to these values, producing a prescription for  $E_2$  as a function of mass. Kushnir et al. (2017) significantly improves upon this, however their implementation relies on knowledge of the radial structure of the star - information which is not readily available in the standard BPASS output files, and would again make this process computationally expensive. A full implementation would require recalculating 250,000 individual detailed BPASS stellar evolution models, which is far beyond the scope of this Chapter. Comparing a handful of  $E_2$  parameters calculated by Kushnir et al. (2017) to the form assumed by Hurley et al. (2002) gives results that are in broad agreement. I caution that the  $k$  parameter, which directly scales  $t_{\text{damp}}$ , is more susceptible to large revisions. This is also taken into account by the formalism of Kushnir et al. (2017), where it is calculated based on the stellar structure. These uncertainties are discussed further in section 5.6.3.

Observations of massive stars, for example the VLT-FLAMES Tarantula survey (Ramírez-Agudelo et al., 2015, 2017), suggest that they are born spinning with initial stellar rotational velocities typically around 30-40 per cent of their critical break-up velocity. Dufton et al. (2019) construct a probability density function for the rotational velocities of (apparently) single O stars in the Tarantula Nebula (Large Magellanic Cloud, LMC) and NGC 346 (Small Magellanic Cloud) and again find a median rotation around 40 per cent of critical. By contrast, Stevance et al. (2018) used spectropolarimetry of galactic WO stars to show that their rotational velocities are less than 10 per cent of critical, however these stars are unambiguously at a late stage of evolution, suggesting that the spins of these massive stars evolve significantly during their lifetime. However, in low metallicity environments, the spin-down is likely reduced. Vink et al. (2011a) and Vink and Harries (2017) report the detection of young Galactic and LMC Wolf-Rayet stars which have surface rotations that could be conducive to GRB production.

For primary models, initial equatorial rotational velocity that is 0.4 of the critical rotation is adopted. This is faster than previously assumed in BPASS and its predecessors. The current prescription, first used by Hurley et al. (2000), gives early-

type stars (specifically, those that end their lives as black holes) initial rotational velocities which are 10-20 per cent of the equatorial break-up velocity. The 0.4 ansatz is much faster, but consistent with the observations described above.

The tidally driven change in orbital separation,  $\Delta a_{\text{tides}}$ , is added to the orbital change due to stellar evolution processes which have already been accounted for, such as mass loss, so that  $\Delta a_{\text{total}} = \Delta a_{\text{tides}} + \Delta a_{\text{BPASS}}$ . The BPASS and tidal changes can act against each other. The orbital evolution from this point forward may correspond more closely to that of a BPASS model at the same stellar evolution stage which began life with a slightly different orbital separation. If the new orbit is now closer to a different BPASS model (with the same stellar masses, at the closest matching time step), the models are switched and the parameters updated, continuing from there. The semi-major axis  $a$ , orbital angular velocity  $\omega$  and stellar rotational angular velocity  $\Omega$  vary smoothly and are not updated when a model change occurs. Otherwise, the model is not changed.

This process is continued until a significant event happens in the system - this is defined as either a common envelope phase or Roche lobe overflow. At this point, the primary spin is synchronised to the orbital period and synchronisation is maintained until core-collapse. Because tidal forces are strongly dependent on radius, any post-main sequence expansion is likely to result in synchronisation (Hurley et al., 2002). Since it is assumed that most high mass systems are synchronised before the end of the primary model, each secondary model is started in a synchronised state, where the rotational angular velocity of the secondary equals the orbital angular velocity of the compact object companion. The percentage of model outcomes changed by the influence of tides is around  $\sim 5$  per cent, out of  $\sim 7000$  models considered per metallicity. Most of these changes do not alter the final event categorisation, as many models are shifted onto a slightly different evolutionary track which still results in the same class of transient.

An example of the methodology is shown in Figure 5.5, demonstrating the process of jumping between BPASS models when tidal interactions significantly alter the binary orbit. The synchronisation of the binary is also shown when the common envelope phase occurs at  $t \sim 35$  Myr.

### 5.3.5 The effect of tides on high-mass stars

The number of models which now produce either Ic SNe with a neutron star remnant, or direct collapse to a black hole, is compared to the previous numbers from before tides were considered. I find that models are both added to, and removed from, the pool of models which produce Ic SNe and black holes. The overall effect is shown



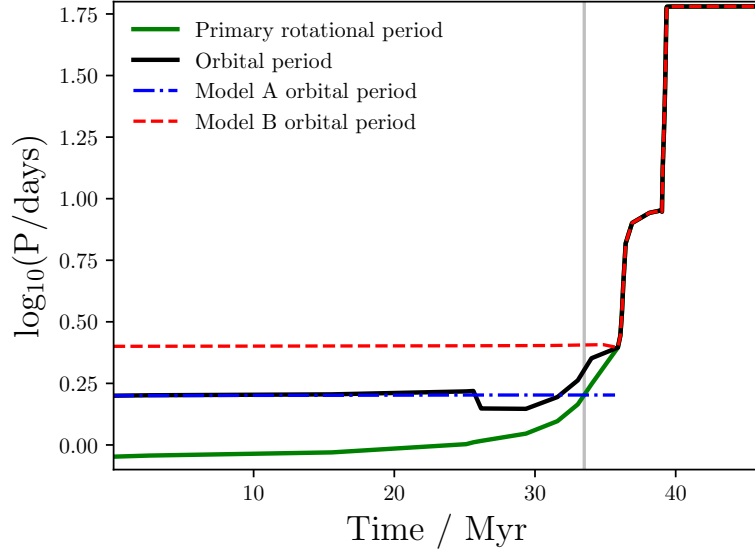


Figure 5.5: An example of the tidal methodology. The blue dashed line indicates the orbital period evolution of the initial model (labelled Model A). The red dashed line shows the orbital period of the model at the time of core-collapse (Model B). Other models can be passed through in between these. The solid green line is the primary star’s rotational angular velocity, which starts at 40 per cent of critical, and the solid black line is the orbital angular velocity. A vertical grey line indicates when the model switch occurs. The system in this example is at a metallicity of  $Z = 0.014$  and consists of a  $M_{\text{ZAMS}} = 8 M_{\odot}$  star with a  $7.2 M_{\odot}$  companion, and an initial orbital period of  $\log_{10}(P/\text{days}) = 0.2$ . The system starts in a state where the primary is spinning faster than the orbit of the companion, and so the system moves apart as angular momentum is transferred. Tidal forces get stronger as the primary expands, leading to synchronisation at  $\sim 35$  Myr. In this case, the added orbital angular momentum gained from tidal interactions is sufficient to eject the common envelope, and consequently the binary moves apart. Without tides, the system would retain more mass, shortening the primary lifetime, such that it explodes in  $< 40$  Myr without significant evolution in orbital period.

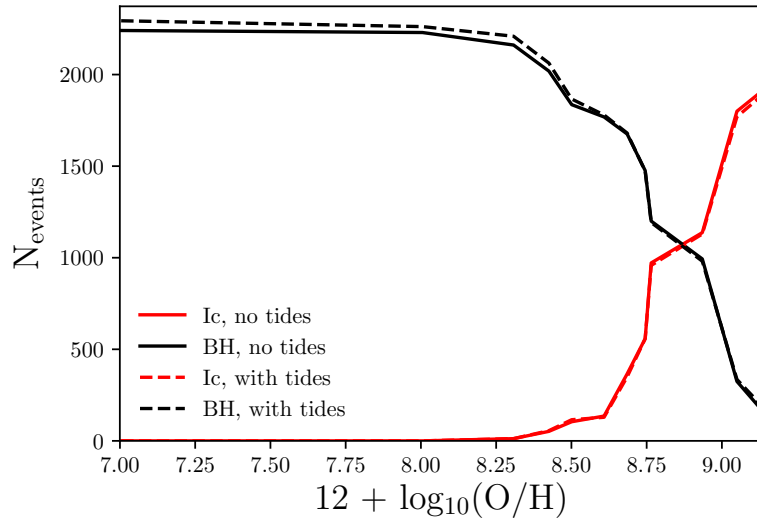


Figure 5.6: The change in the number of Ic SNe and black holes produced per  $10^6 M_{\odot}$  of star formation, as a function of metallicity, due to the inclusion of tidal interactions.

in Figure 5.6.

For a more complete breakdown of the changes due to tides, refer to Figures 5.7 and 5.8. This shows the number of high-mass stellar death events (Ib, Ic, PISN and vanishing) per  $10^6 M_{\odot}$  of star formation for each metallicity and BPASS model type, both before and after tides. Initial distributions in mass, mass ratio, period and binary fraction are drawn from BPASS v2.2.1. The effect of tides is complex and depends on the specific system in question. In most systems, given the initial rotational velocities, the binary is pushed apart, leading to reduced envelope mass loss from the primary (and a shorter main sequence lifetime). However, this same transfer of angular momentum to the orbit can make the ejection of a common envelope more efficient. These effects are roughly balanced, such that the overall change in the number of stripped envelope progenitors is small, as Figure 5.6 shows. In order for a stripped-envelope star to produce a GRB, it must also launch jets. A key parameter of interest in jet production is the angular momentum of the star at core-collapse. Woosley (1993) and Woosley and MacFadyen (1999) calculated that the specific angular momentum of material just outside the newly formed black hole should be  $> \sim 10^{16} \text{ cm}^2 \text{ s}^{-1}$  in order for accretion to occur, otherwise material directly infalls and energy extraction is inefficient.

In Figure 5.9, the effect of tides on the final angular momentum of Ic-SN and black hole progenitors is visualised. For the evolution without tides, the spin

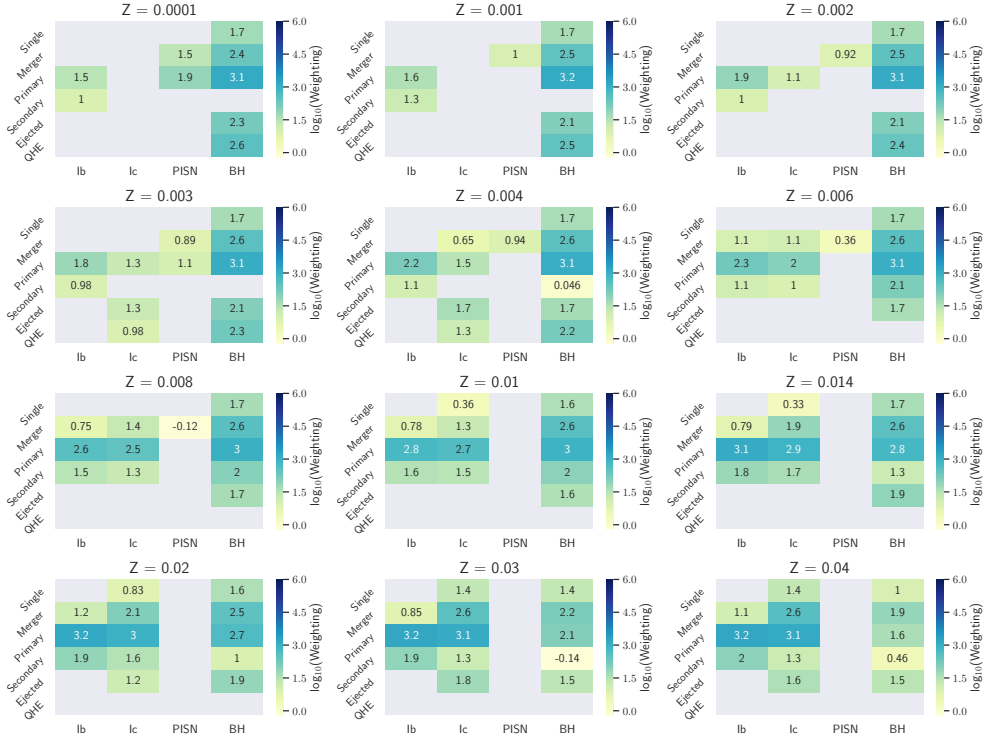


Figure 5.7: The number of high-mass progenitor core-collapse events arising from each BPASS model type, weighted by the relative occurrence rates of each model. Higher BPASS weightings indicate that the model occurs more frequently. This figure shows the weightings before tides were added. Figure 5.8 shows the weightings including the effects of tidal evolution.

of the star in question is synchronised to the orbit in the final time-step in order to obtain an estimate of the specific angular momentum  $j$ . The resultant distributions of  $j$ , with and without tidal evolution over the stellar lifetime, are binned, and the difference in the normalised fraction contributing to each  $j$  bin is shown. Notably, it is the high metallicity models which are predominantly affected by the inclusion of tides. The evolution of these systems was previously dominated by wind-driven mass loss, however tidal interactions are acting to maintain angular momentum in the primary when it would otherwise be lost. Although tides typically push binaries apart over the main sequence lifetime, they tend to end their lives spinning more rapidly due to synchronisation in the mass transfer and common envelope phases. Figure 5.9 also shows a high- $j$  spike due to tides, which is mostly populated by low metallicity systems. Inspecting the mass distribution of these high angular momentum stars, they are typically very high mass. The assumed initial mass function (IMF) in this work allows for ZAMS masses up to  $300M_{\odot}$ . Because tidal

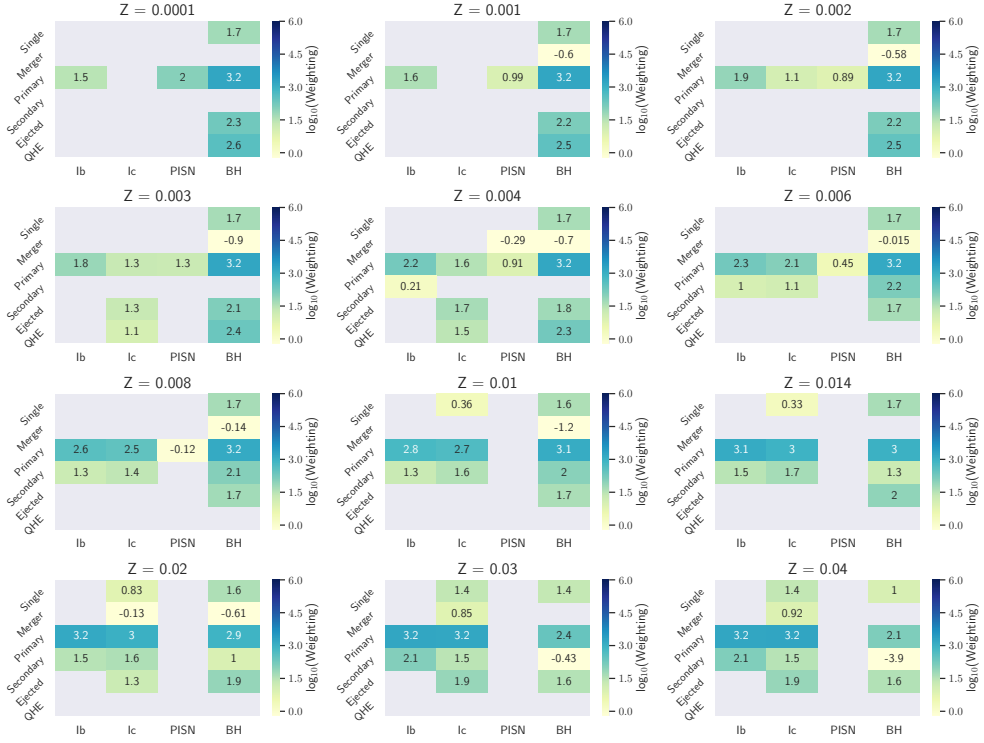


Figure 5.8: As for Figure 5.7, with the addition of tidal interactions in post-processing

forces are extremely radius sensitive (proportional to the eighth power in  $R$  in the prescription used), and because low  $Z$  stars are more likely to maintain very high masses all the way to core-collapse, the highest  $j$  bins are naturally populated by the lowest  $Z$  stars.

Another effect of introducing tides to BPASS is that the delay times, the intervals between star formation and core-collapse, are changed. In general, over the main sequence lifetime, tides act to push binaries apart, therefore decreasing the mass lost to a companion. This means that stars leave the main sequence with higher masses than before tides were considered, which typically shortens lifetimes and therefore delay times. However, if the stars are further apart, the orbital angular momentum is greater and common envelopes are more efficiently ejected, therefore reducing the system mass (and increasing delay times). These two effects, which act to add and remove mass respectively, dominate equally as often. In Figure 5.10, as in Figure 5.9, I show the change of the contribution to each delay time bin from the Ic-SN and black hole progenitor population, before and after tides are included. The overall effect of tides on the delay time distributions is a small shift to



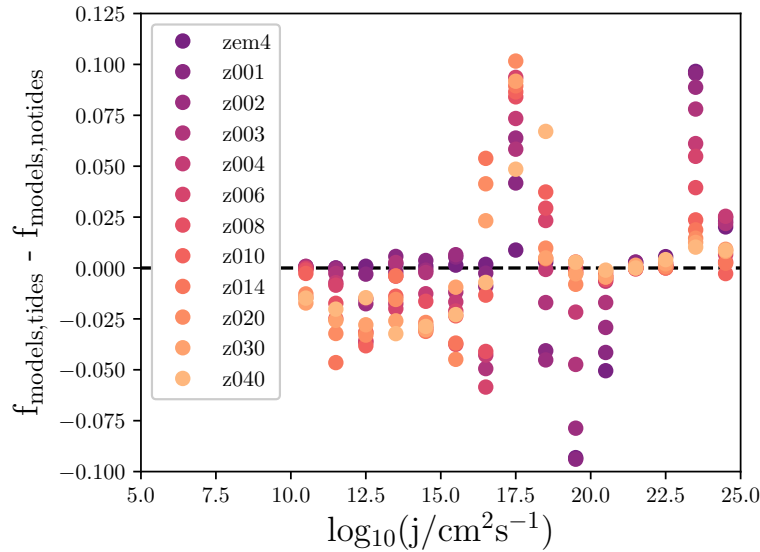


Figure 5.9: The difference in each specific angular momentum bin between the number of stellar models producing Ic-SNe and black holes at core-collapse, before and after tides are considered. Metallicity is indicated by the colour gradient. The  $y$ -axis represents the bin heights for the number of models after tides, subtracted from the bins heights before tides were considered, where the histograms are normalised so that the enclosed area of each is equal to unity. This therefore provides an indication of changes in the  $j$  distribution due to tides.

shorter delays. Because the application of this tidal algorithm changes the frequency with which primary models end in different configurations, the weightings of the secondary models are changed. These are calculated based on the primary model endpoints and follow the evolution of post-supernova systems to later time-steps. Using the IMF and initial binary population parameters of the primary models, and the associated new binary end points, the secondary models are re-weighted to account for the tidal evolution. All subsequent analyses use these new weightings.

## 5.4 Calculation of long GRB volumetric event rates and inference of progenitor properties

### 5.4.1 Transient population synthesis

The search for additional, tidally-induced GRB pathways (referred to hereafter as ‘tidal GRBs’) is motivated by the observed metallicity distribution of GRB progenitor environments (see e.g. Trenti et al., 2015; Palmerio et al., 2019), but the addition

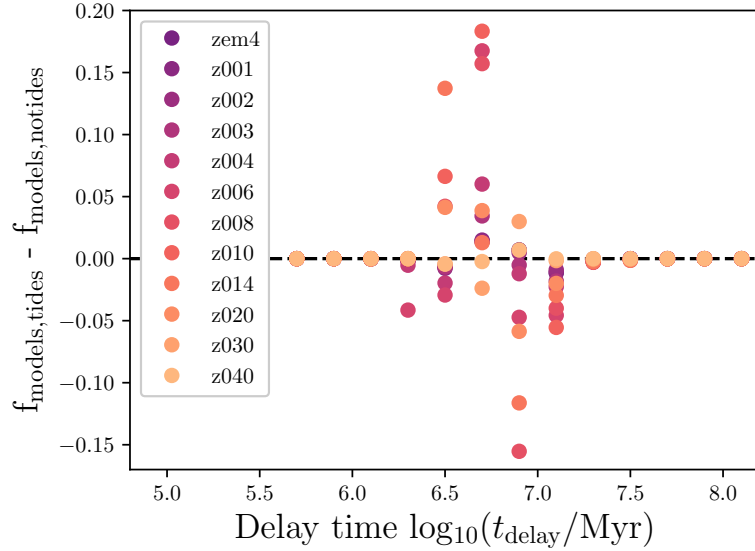


Figure 5.10: The change in the number of models falling in each delay time bin, for black hole and Ic-SN producing models. Delay times are measured from the zero age main sequence. The overall effect of tides on the delay time distribution of massive stars is small, since model lifetimes are both shortened and lengthened by decreased mass transfer and more efficient common envelope ejection respectively. The  $y$ -axis is calculated in the same way as Figure 5.9.

of any such pathway must also be consistent with observed long GRB volumetric event rates. For the existing QHE pathway, any stars with a remnant mass  $> 3M_{\odot}$ , which accrete  $> 5$  per cent of their initial mass at  $Z < 0.004$ , fulfil the composition and spin requirements for a GRB (Eldridge et al., 2019a). The BPASS models which are rapidly spinning at core-collapse, at all metallicities, and which would produce a type Ic-SN if collapse to a black hole did not hamper the escape of emission from an explosion, are now identified. We expect a currently-undefined subset of these to also launch GRBs and hypothesise that the principle determinant of whether they do so is whether they exceed a threshold in specific angular momentum,  $j_{\text{cut}}$ . I will assume that these two pathways are the only contributors to the GRB population and now turn to deciding which of the tidally spun models produce GRBs, and whether the observed GRB rate and its evolution over cosmic history can be recreated using plausible selection criteria.

The specific angular momentum threshold is varied to define sets of plausible GRB progenitors. The model weightings are used to determine, for a given mass of stars formed at metallicity  $Z$ , how many GRBs we would expect. We also know the delay times of these models. In order to construct the GRB rate as a

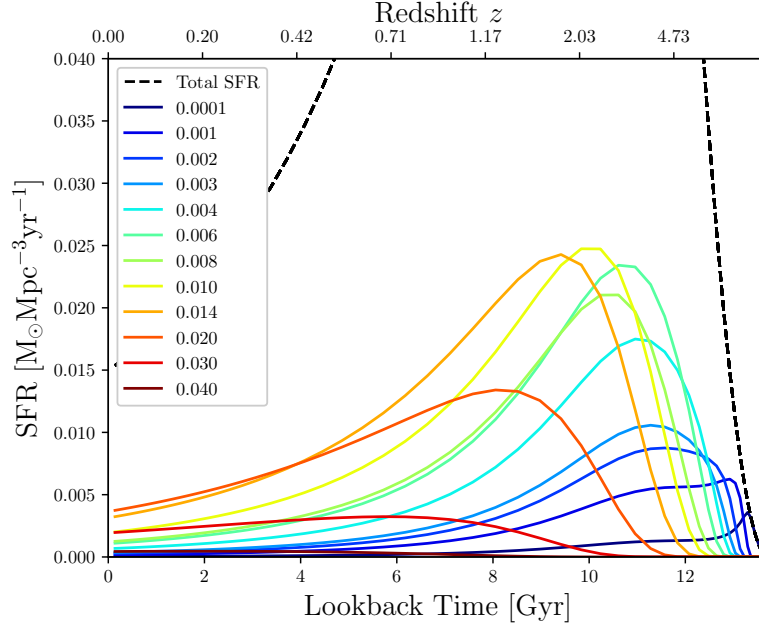


Figure 5.11: The cosmic star formation rate history employed, decomposed into 12 constituent metallicities.

function of redshift, I follow the methodology of Eldridge et al. (2019a) to apply a metallicity-dependent cosmic star formation rate history. The star formation rate density (SFRD, Madau and Dickinson, 2014) as a function of redshift is given by,

$$\psi(z) = 0.015 \frac{(1+z)^{2.7}}{1 + ((1+z)/2.9)^{5.6}} M_{\odot} \text{yr}^{-1} \text{Mpc}^{-3}, \quad (5.11)$$

and this used in conjunction with the formalism of Langer and Norman (2006), which decomposes the SFRD into contributions from different metallicities as a function of redshift. The SFRD at or below a metallicity  $Z$ , at redshift  $z$ , is given by,

$$\Psi \left( z, \frac{Z}{Z_{\odot}} \right) = \psi(z) \frac{\hat{\Gamma}[0.84, (Z/Z_{\odot})^2 10^{0.3z}]}{\Gamma(0.84)}, \quad (5.12)$$

where  $\hat{\Gamma}$  and  $\Gamma$  are the incomplete and complete Gamma functions. 0.020 is used for Solar metallicity  $Z_{\odot}$ , which corresponds to  $12 + \log(O/H) = 8.93$  in the abundance distribution pattern adopted by BPASS (see Eldridge et al., 2017).

Figure 5.11, shows how star formation varies with lookback time at each BPASS metallicity. Low metallicities dominate star formation only in the very early Universe, with the peak of Solar-metallicity star formation at around  $z \sim 1$ , and the

overall peak in star formation at  $z \sim 2$ . By applying the GRB progenitor model rate per  $10^6 M_\odot$  to the SFR at each redshift and metallicity, and accounting for the delay times, the intrinsic (and hence estimate the observed) GRB rate can be constructed. This requires, however, the application of an angular momentum cut-off  $j_{\text{cut}}$  for the tidal GRB pathways, and rate corrections due to jet beaming and the GRB luminosity function.

#### 5.4.2 Bayesian parameter estimation

In order to investigate whether a two-pathway model is plausible, four model parameters are allowed to vary, and their values are inferred by comparison to observational data. The parameters are,

1. the jet half-opening angle  $\theta$ ,
2. the lower limit on the isotropic equivalent energy of GRBs,  $E_{\text{low}}$ ,
3. the specific angular momentum  $j_{\text{cut},\odot}$ , at Solar metallicity, above which GRBs can occur in the black hole producing, stripped envelope, rapidly rotating models,
4. the index  $n$ , which allows for a metallicity dependence of this angular momentum cut (as  $j_{\text{cut}} \propto j_{\text{cut},\odot} (Z/Z_\odot)^n$ ).

The first two parameters determine whether a GRB is likely to be seen in the observed sample, while the latter two determine whether an event is likely to launch a jet at all. For observed GRB rates, I use the Swift Gamma-Ray Burst Host Galaxy Legacy Survey (SHOALS) sample (Perley et al., 2016a). This is the largest unbiased sample of GRBs with identified hosts (and hence redshift and metallicity estimates) consisting of bursts with isotropic equivalent energies,  $E_{\text{iso}}$ , greater than  $10^{51}$  erg.

Of the four model parameters, two are corrective and change the number density of events equally across redshift ( $\theta$ ,  $E_{\text{low}}$ ). The other two ( $j_{\text{cut}}$ ,  $n$ ) may also affect how the rate varies with redshift. The half-opening angle  $\theta$  is used to account for the fact that GRBs are strongly beamed, and therefore most events are seen off-axis and not detected, so that the observed rate is much lower than the intrinsic one. This correction is given by  $[1 - \cos \theta]^{-1}$  for bipolar jets, and assumes that within a viewing angle  $\theta$ , we are equally likely to detect the burst whatever the orientation. The second factor corrects for the GRB luminosity function (actually an isotropic-equivalent energy  $E_{\text{iso}}$  function). This is required because the SHOALS comparison data is comprised exclusively of high-energy bursts, above  $10^{51}$  erg, which creates a



luminosity-unbiased sample over a wide redshift range. However, we want to know the total number of bursts which are occurring. The assumed GRB luminosity function is taken from Pescalli et al. (2016). This has a power law slope of -1.2 below, and -1.92 above, a break energy of  $5 \times 10^{50}$  erg. The SHOALS data gives us the number of events per redshift bin above  $10^{51}$  erg, to obtain the total number at each redshift for comparison with modelled rates I integrate over the function down to a lower limit  $E_{\text{low}}$ . Finally, models are selected as GRB candidates if they have a specific angular momentum at core-collapse greater than  $j_{\text{cut}}$ , which is proportional to  $(Z/Z_{\odot})^n$ .

An MCMC analysis is performed to infer the probability density functions of  $\theta$ ,  $E_{\text{low}}$ ,  $j_{\text{cut}}$  and  $n$ . The Python package EMCEE is used to perform MCMC sampling (Goodman and Weare, 2010; Foreman-Mackey et al., 2013). The posterior distribution of the parameters,  $P(\theta, L_E, j_{\text{cut}}, n|D, M)$  is given by the product of the log likelihood and log prior,

$$P(\theta, L_E, j_{\text{cut}}, n|D, M) \propto P(D|\theta, E_{\text{low}}, j_{\text{cut}}, n, M) \times P(\theta, E_{\text{low}}, j_{\text{cut}}, n) \quad (5.13)$$

where  $D$  denotes the data (in this case the SHOALS rates and their quoted uncertainties), and  $M$  is the two-pathway model as previously described. The priors assumed,  $P(\theta, E_{\text{low}}, j_{\text{cut}}, n)$ , are as follows:

1. For the half opening angle, I simply limit  $\theta$  to the range  $0 < \theta < 22.5$ , the least informative prior that can be used whilst ruling out very weakly beamed (total opening angle  $> 45$  deg) or isotropic emission.
2. We have limited prior knowledge on the lowest possible GRB luminosity. I therefore restrict  $E_{\text{low}}$  to the range  $45 < \log_{10}(E_{\text{low}}/\text{erg}) < 50.7$ , where the upper bound is the break in the assumed luminosity function, and the lower bound is arbitrarily low. Although events are seldom seen at  $\log_{10}(E_{\text{iso}}) < 50.7$ , we are trying to apply a minimal prior and allow for a small number of outliers in  $E_{\text{iso}}$  (Ajello et al., 2019).
3. I use a top-hat prior which covers the range  $16 < \log_{10}(j_{\text{cut}}/\text{cm}^2\text{s}^{-1}) < 19.3$ . The lower bound corresponds to the theoretical minimum  $j$  required for GRB production by a black hole central engine (e.g., Woosley, 1993; MacFadyen and Woosley, 1999). The upper bound is simply the maximum value of  $j$  obtained from the tidal calculations, the lack of any models with a  $j$  value higher imposes this hard cut-off.

4. For the index  $n$ , I again use a uniform prior, covering all physically realistic values ( $0 < n < 15$ ). Unlike for  $j$ , the prior is not bounded (at least not until a extremely large value), allowing for more spread in the posterior distributions towards the higher values. GRBs are rarer at high metallicity, and high stellar envelope opacity could help to impede jet propagation. Because opacity scales approximately as  $Z$  (e.g. Vink et al., 2001), we might expect  $n = 1$  to be most probable, however this is not favoured by the prior. Including a prior that favours  $n = 1$  would weight the posterior distributions towards this value.

Initialising the MCMC with 100 walkers, 2000 steps, and a burn-in of 50 steps (checked by visual inspection), the joint marginalised distributions and correlations shown in the corner plot of Figure 5.12 are obtained.

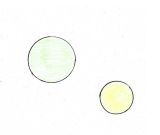
## 5.5 Predicted long gamma-ray burst rates and progenitors

### 5.5.1 MCMC results

The marginalised probability distribution in the half-opening angle  $\theta$  is similar in form to those found by Racusin et al. (2009), and the well-fit sample of Ryan et al. (2015). The posterior distribution in  $E_{\text{low}}$  favours a critical isotropic equivalent energy of  $10^{48.1}$  erg. This result arises despite a minimal prior which allows for all physically reasonable values below the break in the assumed luminosity function. The cutoff is in good agreement with observations, which have yielded bursts with  $\log_{10}(E_{\text{iso}}) < 48$  on only a few occasions, despite such events being theoretically detectable at low redshift (e.g. Racusin et al., 2009; Ajello et al., 2019). However, the possibility that there is a population of even fainter bursts, beyond the detectability limits of current instruments, cannot be ruled out.

The posterior distribution of the angular momentum cutoff  $\log_{10}(j_{\text{cut},\odot})$  has its median at 18.74. Finally, the distribution of the power-law index  $n$  drops away at very high values, with a peak and median at  $\sim 4$ . The mean, median, and percentiles of all four posterior distributions are listed in Table 5.2.

In Figure 5.13 I show the posterior probability density for this model, compared with the observed  $E > 10^{51}$  erg SHOALS rates. The model (as a function of  $j_{\text{cut}}$  and  $n$ ) predicts an intrinsic rate, which is converted to an observed rate by the  $\theta$  and  $E_{\text{low}}$  parameters as described above. The probability density shown in Figure 5.13 therefore represents the posterior distribution for the correction to the intrinsic rate, which is a convolution of the corrections arising from the opening angle and



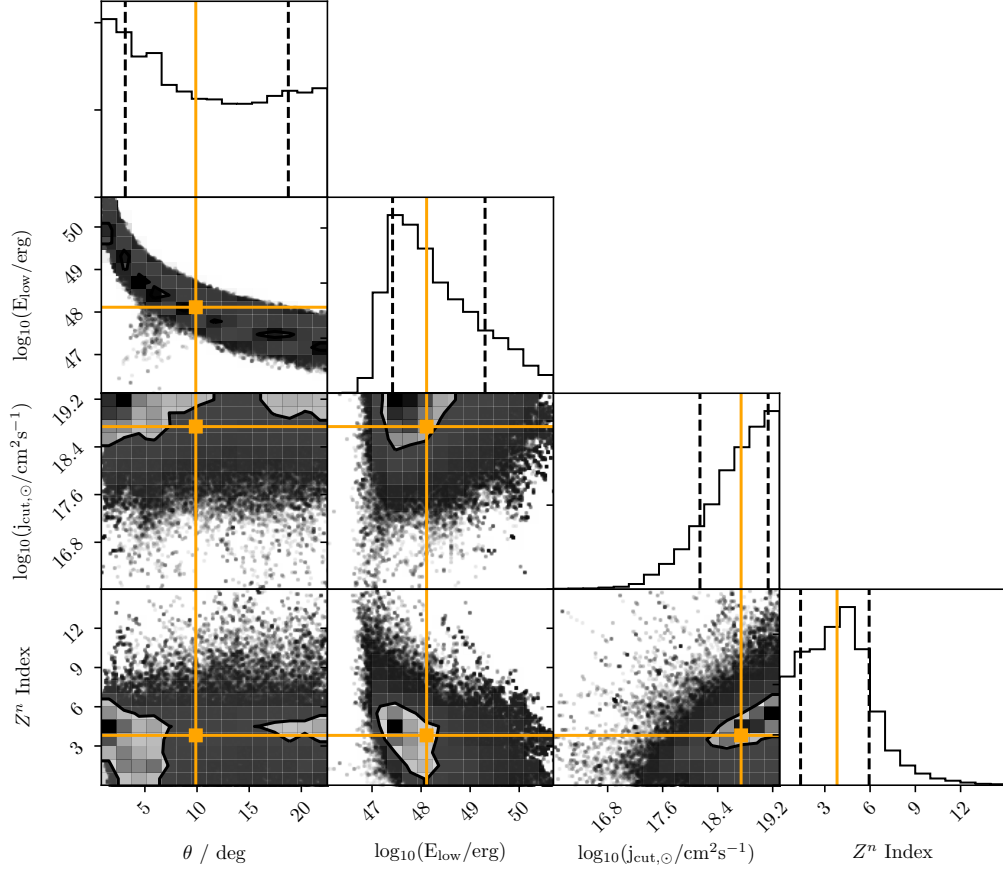


Figure 5.12: Covariances between the four fitted parameters in the two-pathway GRB model, and the marginalised posterior probability density distributions for each. Vertical dashed lines mark the 16<sup>th</sup> and 84<sup>th</sup> percentiles, and the orange crosshairs indicate the distributions medians. 1D histograms at the top of each column represent the marginalised distribution of the parameter indicated on the  $x$ -axis for that column.

Table 5.2: Properties of the parameter posterior distributions, obtained from the MCMC analysis carried out in Section 5.5.

Parameter	Mean	16 <sup>th</sup> Percentile	Median	84 <sup>th</sup> Percentile
$\theta / \text{deg}$	10.62	3.12	9.88	18.75
$\log_{10}(E_{\text{low}}/\text{erg})$	48.31	47.42	48.11	49.30
$\log_{10}(j_{\text{cut},\odot}/\text{cm}^2\text{s}^{-1})$	18.64	18.14	18.74	19.13
$Z^n \text{index}$	3.87	1.39	3.81	5.94

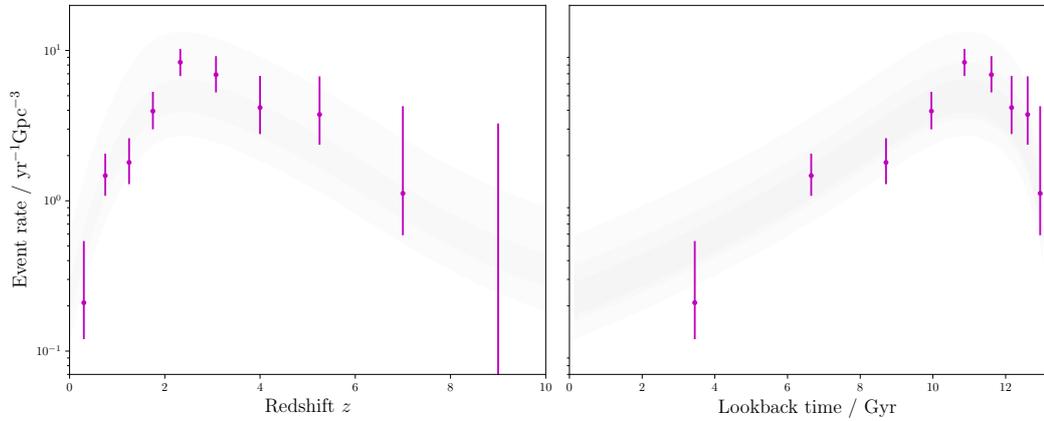


Figure 5.13: The distribution of observed GRB rates, as a function of redshift (or lookback time). Darker shading represents higher probability density. The observed SHOALS rates are shown with their uncertainties. BPASS produces intrinsic rates, these have been corrected using the distributions of  $\theta$  and  $E_{\text{low}}$  which are output as posteriors from the MCMC run.

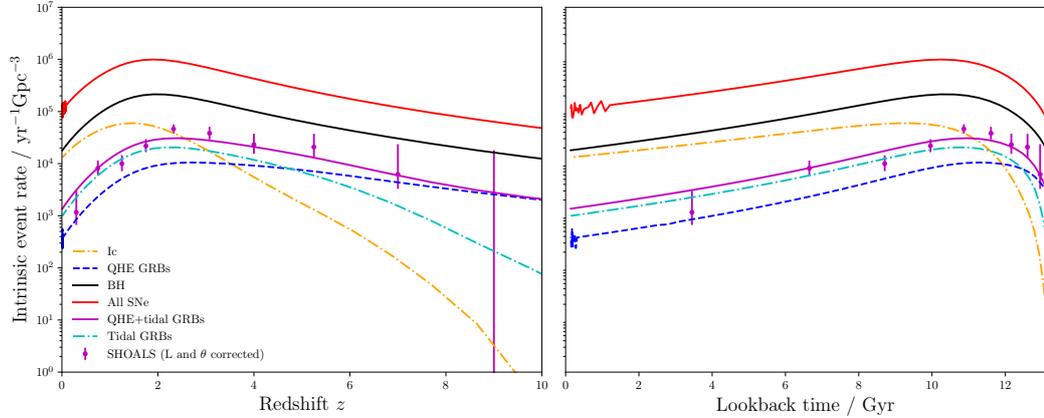


Figure 5.14: The BPASS prediction for the intrinsic volumetric rate of GRBs arising from both QHE and tidal pathways, shown by the solid purple line. The dashed dark blue line below is the contribution from QHE progenitors, and the dashed orange line represents bursts from the tidal influence pathway. These rates were obtained by selecting black hole-producing, stripped envelope progenitors with a specific angular momentum cut that best reproduces the evolution of the rate over cosmic time. The SHOALS rates have then been corrected for beaming and a luminosity function, using the medians of the  $\theta$  and  $E_{\text{low}}$  MCMC posterior distributions.



lower luminosity limit.

For best estimates of the parameters values, I use the posterior medians and 68 per cent credible intervals given by the 16<sup>th</sup> and 84<sup>th</sup> percentiles. This gives  $\theta = 9.9_{-6.8}^{+8.9}$  degrees,  $\log_{10}(E_{\text{low}}/\text{erg}) = 48.1_{-0.7}^{+1.2}$ ,  $\log_{10}(j_{\text{cut},\odot}/\text{cm}^2 \text{ s}^{-1}) = 18.7_{-0.6}^{+0.4}$  and  $n = 3.8_{-2.4}^{+2.1}$ . Using the median values gives the fit shown in Figure 5.14 (the highest redshift SHOALS point, which gives an event rate consistent with zero, is not included in the fit). Note that the fitting just the QHE pathway can produce similarly good results given different assumptions for  $\theta$  and  $E_{\text{low}}$ , as demonstrated by Eldridge et al. (2019a), but we know that GRBs occur above  $0.2Z_{\odot}$  metallicity, and therefore the QHE pathway cannot be the sole contributor.

### 5.5.2 Metallicity distribution

An independent test is to compare the metallicity distribution predicted for the tidal and QHE GRB progenitors, to that of observed host galaxies. In Figure 5.16, I show the synthetic metallicity distribution of the GRB-producing stars at two redshifts,  $z = 0.2$  and  $z = 1.5$ . Also shown are host galaxy metallicity distributions from Japelj et al. (2018), Modjaz et al. (2019), Graham et al. (2019) and Palmerio et al. (2019).

To draw comparisons between metallicity distributions, we need to ensure that the scales being used do not have significant offsets. Graham et al. (2019) used the metallicity diagnostic and scaling of Kobulnicky and Kewley (2004), with Solar metallicity defined at  $12+\log(\text{O}/\text{H}) = 8.69$  (Allende Prieto et al., 2001). This corresponds in their scale to a metal mass fraction of 0.014. In the BPASS scaling, a mass fraction of 0.014 corresponds to  $12+\log(\text{O}/\text{H}) = 8.76$ . To reconcile this with Kobulnicky and Kewley (2004), 0.07 dex is added to each value in the Graham et al. (2019) distribution, bringing the scales into better alignment in the Solar range (see Figure 5.15).

The other three comparison data sets use a Maiolino et al. (2008) scaling (Modjaz et al. (2019) provide a variety, I choose the same scaling for consistency), where Solar is again at  $12+\log(\text{O}/\text{H}) = 8.69$ , but this now corresponds to 0.0134 by mass fraction (Asplund et al., 2009). Again, these data sets are shifted by 0.07, which brings the 0.0134 Solar value into agreement with BPASS at  $12+\log(\text{O}/\text{H}) = 8.76$ . For a discussion of metallicity scaling issues, and their impact within BPASS, refer to Eldridge et al. (2017) and Xiao et al. (2018).

Interestingly, there appears to be little evolution of the metallicity distribution in GRBs predicted by the BPASS models with redshift, with an overall shift to lower values of only  $\sim 0.2$  dex between redshifts 0 and 5. The data similarly shows

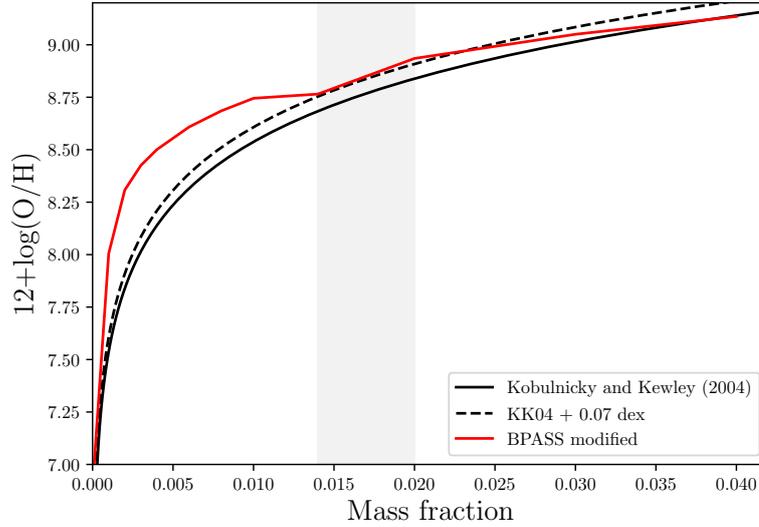
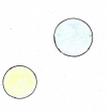


Figure 5.15: Metallicities are often measured in terms of the relative strength of oxygen to hydrogen emission lines, quantified as  $12+\log_{10}(\text{O}/\text{H})$ . There are various prescriptions for converting this value to a metallicity mass fraction. The BPASS conversion is shown here (as in the ‘new’ column of Table 5.1), along with the scaling of Kobulnicky and Kewley (2004) which is employed by Graham et al. (2019). By adding a 0.07 dex offset to  $12+\log_{10}(\text{O}/\text{H})$  values reported in the Kobulnicky and Kewley (2004) scale, the two scales agree at the Solar metallicity mass fraction of 0.014 (where the grey shaded region is the range of metallicities that might be considered Solar, but 0.014 is adopted as the reference point).

a lack of variation in the observed fraction of high metallicity bursts out to redshift 2.5 (Graham et al., 2019). The observed samples nonetheless span a wide redshift range, and I compare each to the closer of the two redshift curves shown on Figure 5.16. Anderson-Darling tests between the BPASS results and the data fail to reject the null hypothesis (i.e.  $p > 0.05$ ) that they are drawn from the same distribution, in every case except for Graham et al. (2019).

### 5.5.3 Delay-time distribution

In Figure 5.17, the delay-time distribution for the QHE and tidal progenitors are shown. In the tidal case this is for all metallicities considered, whereas the QHE distribution is limited to  $Z < 0.2Z_{\odot}$  by construction. The new tidal pathways have shorter delay times, decreasing the mean temporal offset between star formation and GRB events. Note that these times are technically only until the end of core carbon burning. However, the final stages of core burning before core collapse occupy  $\ll 1$  Myr (e.g. Groh et al., 2014). The GRB progenitors have among the



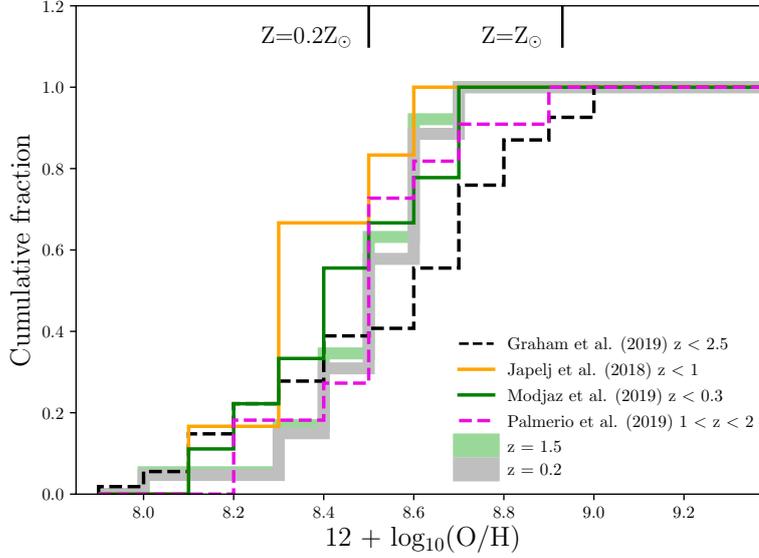


Figure 5.16: Cumulative metallicity distributions of the GRB progenitors at  $z = 0.2$  and  $z = 1.5$ , marked by shaded grey and green lines, compared with observed host galaxy distributions from Japelj et al. (2018), Modjaz et al. (2019), Palmerio et al. (2019) and Graham et al. (2019). The comparison data has been shifted so that at the mass fraction used to define Solar metallicity in their scale,  $12 + \log(\text{O}/\text{H})$  is the same as the BPASS value at that mass fraction. Marked on the plot are  $0.2Z_{\odot}$  and  $Z_{\odot}$  metallicities in the (modified) BPASS scaling.

shortest delay times of any stars, particularly so for the tidal GRBs. This implies that they will be also be among the most luminous main sequence stars. Unlike the QHE pathway, in which it is lower mass secondary stars that produce GRBs, in the tidal pathway the progenitor will usually not have been subject to a supernova kick, or will have received a smaller kick. The progenitor stars would therefore be preferentially formed in the brightest regions of their host galaxies, and stay there, leading to a GRB distribution that is concentrated on these regions - a trend which has been previously been observed (e.g. Fruchter et al., 2006; Eldridge et al., 2011; Lyman et al., 2017).

#### 5.5.4 Progenitor systems

Table 5.3 shows distribution statistics for the tidal progenitor systems in mass ratio, orbital period, initial mass, final mass and delay time parameter space, over the metallicity range  $Z = 0.008 - 0.020$ . Stars with final masses of  $\sim 20M_{\odot}$ , in tight binaries with large mass ratios, are the most frequent progenitors. A corner plot showing this information, and covariances between parameters, is available in Figure

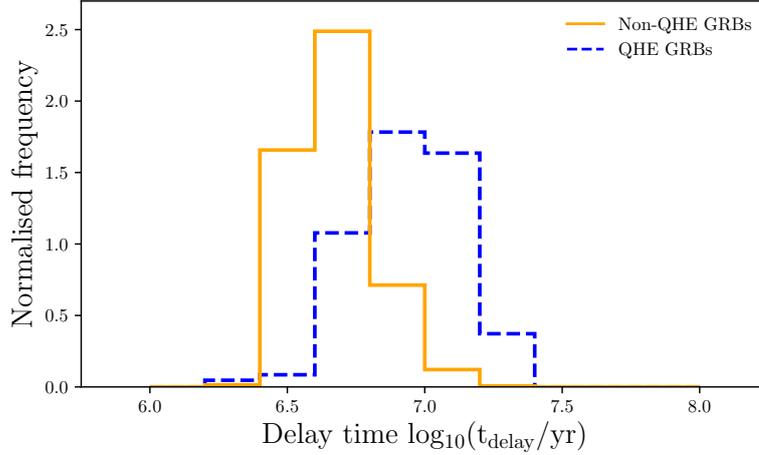


Figure 5.17: Delay time distributions (DTDs) for QHE and tidal GRB progenitors, across all metallicities considered in this work. QHE pathways are limited to  $Z < 0.2Z_{\odot}$  by construction. The contribution from each model is weighted according to the (tide adjusted) BPASS weightings, and delays are measured from zero-age main sequence. The total area of each distribution is normalised to unity.

5.18. There are signs of an excess in the number of twin systems (i.e. systems with mass-ratio near unity) which give rise to GRBs, however this is simply reflecting the increased likelihood of twin systems in all massive binaries, and is not specific to GRB progenitors.

### 5.5.5 Core angular momentum

Finally, we turn our attention to the angular momentum distribution of the tidally spun models selected as GRB progenitors. The angular momentum cut applies to  $j = \Omega \times R^2$ , where  $R$  is the radius of the star, however the quantity of interest for GRBs is the interior specific angular momentum. Theoretical modelling (Woosley, 1993; MacFadyen and Woosley, 1999) suggests that to launch a jet,  $\gtrsim 16 \text{ cm}^2 \text{ s}^{-1}$  is required at the innermost stable orbit around the newly formed black hole. To estimate these  $j$  values in the tidal GRB models, I make two assumptions. First, that the star has a constant rotational angular velocity  $\Omega$  throughout its structure at the end point of the models. Secondly, that initial radius of the material which will form the accretion disk of the nascent black hole is at  $R_{\text{boundary}}$  - the radius in the pre-collapse star which encloses the post-collapse remnant mass. This material is assumed to retain its specific angular momentum during core-collapse.

To calculate  $R_{\text{boundary}}$ , I use the files output directly from the BPASS version of the STARS code, which includes information on the radial structure of the stellar



Table 5.3: Properties of the tidal GRB progenitors over the metallicity range 0.008-0.020. For GRBs arising from the primary star (the majority), mass ratio  $q$ , initial mass and  $\log(P)$  are all given at ZAMS. For GRBs arising from the secondary star in a binary, values are given immediately after the supernova of its primary companion. The minimum, maximum, mean and standard deviation  $\sigma$  of the parameter distributions for the population are listed. The whole population (primary and secondary explosions) is given in the top section, solely for primaries below that, and solely for the secondaries in the lower section. A visual representation of this information is provided in Figure 5.18.

Property	Min	Max	Mean	$\sigma$
Mass ratio $q$	0.03	0.90	0.48	0.28
$\log_{10}(P/\text{days})$	0.00	2.20	0.45	0.50
Initial mass / $M_{\odot}$	15.0	300.0	84.7	67.6
Final mass / $M_{\odot}$	8.5	46.6	18.7	8.6
Delay time / Myr	2.5	16.0	4.5	2.1
Primary initial mass / $M_{\odot}$	15.0	300.0	81.6	69.9
Primary final mass / $M_{\odot}$	8.8	46.6	18.2	8.0
Primary delay time / Myr	2.5	16.0	4.6	2.1
Secondary initial mass / $M_{\odot}$	40.0	200.0	108.9	35.7
Secondary final mass / $M_{\odot}$	8.5	42.1	22.4	11.8
Secondary delay time / Myr	2.8	5.4	3.4	0.8

models<sup>1</sup>. The boundary radius is calculated by summing shells of mass until the remnant mass is enclosed, from  $r = 0$  to  $r = R_{\text{boundary}}$ . The specific angular momentum at this radius is then given by,

$$j_{\text{boundary}} = \frac{J_{\text{shell}}}{M_{\text{shell}}} = \frac{2}{3}\Omega R_{\text{boundary}}^2 \quad (5.14)$$

where the angular momentum and mass of the shell just outside the boundary radius are  $J_{\text{shell}}$  and  $M_{\text{shell}}$ . An example of the enclosed radial mass profile is shown in Figure 5.19, calculated using the STARS model and assuming a polytropic profile ( $P = K\rho^{1+\frac{1}{n}} \propto \rho^{\gamma}$ , where  $n$  is the polytropic index).

In Figure 5.20, I show the specific angular momenta, evaluated at the remnant-ejecta boundary  $r = R_{\text{boundary}}$ , for the tidal GRB models immediately before core-collapse in three metallicity bins. The angular velocity assumed in all cases is  $j_{\text{cut}}/R^2$ , the minimum value allowed by the metallicity-dependent surface momentum cut. Two cases are shown, the first has a  $Z^{3.8}$  dependence on this cut (the favoured value from the MCMC run), the other has  $n = 1.4$  (this is the lower,  $1\sigma$

<sup>1</sup>Note: these detailed output files do not form part of the standard BPASS stellar model data release due to their data volume and technical complexity.

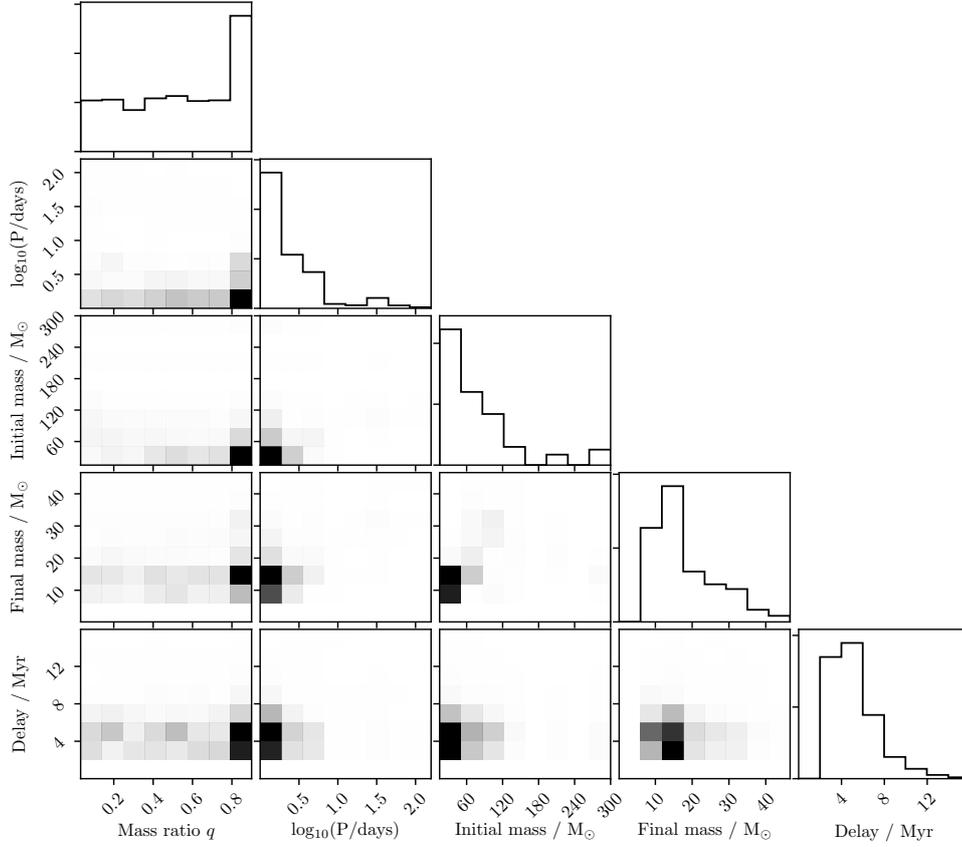
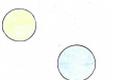


Figure 5.18: A corner plot showing the relative occurrence of the predicted non-QHE progenitors over the metallicity range  $Z = 0.008$  to  $0.020$ , for various system parameters. Distribution statistics are available in Table 5.3.

equivalent bound). We might expect no strong metallicity dependence on the angular momentum that a new-forming black hole requires to launch a jet, although an index of  $\sim 1$  may be expected for jet escape if envelope opacity is solely responsible for suppressing jets and hence dominates any  $Z$  dependence (Vink et al., 2001; Vink and de Koter, 2005).

The distributions shown in Figure 5.20 represents lower limits in that the angular momentum of any specific GRB progenitor may exceed the fitted cut level for the population. The distributions show scatter around  $10^{13} - 10^{17} \text{ cm s}^{-1}$  (a wide spread,  $n = 3.8$ ) and  $10^{14.5} - 10^{16.5} \text{ cm s}^{-1}$  (more peaked,  $n = 1.4$ ). Note that using a  $n \sim 1$  metallicity dependence preferentially shifts the low  $Z$  models to greater specific angular momenta, and brings the three metallicity bins into good agreement.



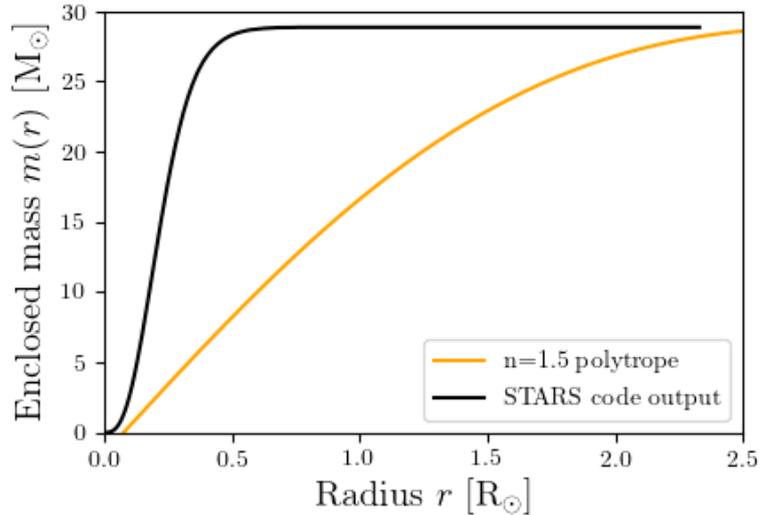


Figure 5.19: The enclosed mass as a function of radius for a  $100M_{\odot}$  star, shortly before core-collapse, calculated two ways. First, the Lane-Emden equation is solved numerically for the  $n = 1.5$  case (in orange). This form is often used to describe a fully convective star, such as a red giant (Eggleton, 2006). However, we can see that it does not reproduce the STARS model structure (in black) very well. The binary model used in this case has initial parameters  $M= 100M_{\odot}$ ,  $m= 10M_{\odot}$ ,  $\log_{10}(P_{\text{init}}/\text{days})=0.4$ , and is shown at the last time-step before the end of core carbon burning. The STARS model is more concentrated, demonstrating the importance of using detailed STARS outputs in this instance.

## 5.6 Discussion

### 5.6.1 The production of GRBs

We have identified the subset of probability weighted stellar evolution models which are likely to generate a GRB through either quasi-homogenous evolution or the results of tidal interactions modifying the angular momentum of the progenitor star. The location of the tidal GRB progenitors on the Hertzsprung-Russell diagram is shown in Figure 5.21, for all models in the metallicity range  $Z = 0.008$  to  $Z = 0.020$ . Purple stars indicate the predicted total optical light from the binary (i.e. both primary and secondary star, or secondary plus remnant in rare cases) immediately before the supernova explosion, where the more luminous component is assumed to dominate the temperature measurement. The yellow stars indicate the properties of the surviving binary companion expected to be observable after the GRB has faded. Grey circles represent the properties of individual progenitor stars immediately before core-collapse. In some cases, this progenitor is the secondary in the original

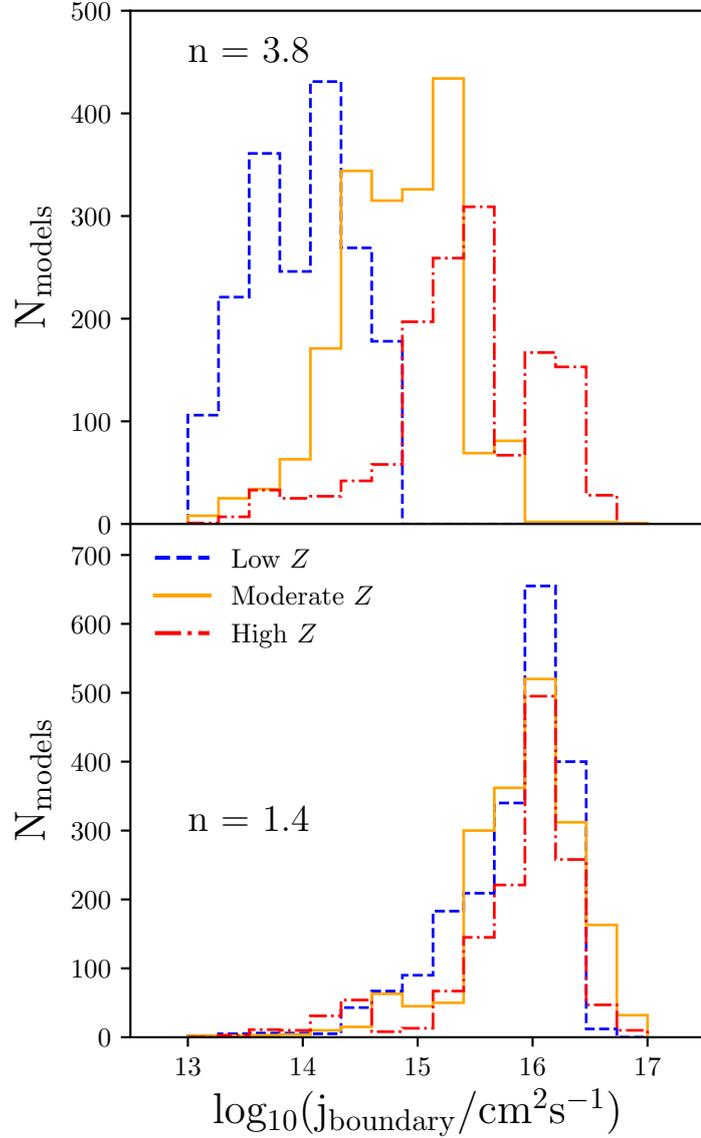


Figure 5.20: The minimum specific angular momenta required for a GRB, measured at the remnant-ejecta boundary of each model at the point of collapse. These correspond to collapsing stars with minimum surface specific angular momenta  $j_{\text{cut}}$ . The upper panel assumes a  $Z^{3.8}$  metallicity dependence, and the lower assumes that  $j_{\text{cut}} \propto Z^{1.4}$ . Detailed stellar interior models are used to calculate  $j_{\text{boundary}}$  as discussed in the text. The models, which include primary and secondary stars, are binned into three metallicity ranges: low ( $10 \times 10^{-4} \leq Z \leq 0.004$ ), moderate ( $0.006 \leq Z \leq 0.008$ ) and high ( $0.010 \leq Z \leq 0.040$ ). The typical boundary momenta required are in the range  $\log_{10}(j_{\text{boundary}}/\text{cm}^2\text{s}^{-1}) \sim 13-17$  for  $n = 3.8$ , and  $14.5-16.5$  for  $n = 1.4$ , although these are minimum values and could easily be  $\sim 100$  times greater (see discussion in Section 5.6.1).



ZAMS binary.

The GRB progenitor binary component is often not responsible for all the light coming from an observed progenitor system; this is particularly true for the twin systems identified above, in which the secondary is likely to be very nearly as bright and evolved as the primary. Immediately prior to core-collapse, 5 per cent of progenitor systems between  $0.4Z_{\odot}$  and  $Z_{\odot}$  metallicity have a secondary star that is more luminous than the pre-explosion primary.

Progenitors end in the hot and bright region on the upper left, as luminous or more luminous than typical Wolf-Rayet stars seen in the Local Group (Neugent and Massey, 2019). Figure 5.21 and Table 5.3 indicate that main sequence stars are the most frequent companions left behind after a primary star goes GRB in the models considered here. This is consistent with earlier findings. Zapartas et al. (2017b) predict the companions expected for stripped envelope (type IIb, Ib and Ic) supernovae using the BINARY\_C rapid population synthesis code. They found that at  $0.3Z_{\odot}$  metallicity, given their assumed IMF and binary parameters,  $\sim 68$  per cent of the progenitors should have a main sequence companion at the point of explosion, and the remainder have compact object companions.

The modelled intrinsic GRB rate shown in Figure 5.14 is around  $\sim 10$  per cent of the type Ic SN rate expected in the local Universe ( $z < 1$ ). This is consistent with previous estimates of this fraction (Fryer et al., 2007) from observational data, corrected for selection effects.

The key model property determining whether or not a massive stripped envelope star produces a GRB is its internal specific angular momentum. Estimates (using  $n = 3.8$ ) for the minimum boundary specific angular momentum required to launch a GRB,  $\log_{10}(j_{\text{boundary}}/\text{cm}^2\text{s}^{-1}) \sim 13 - 17$ , drop well below that expected from theory. This is also lower than the values found from detailed modelling of massive star interiors (Heger et al., 2000; Yoon et al., 2012; Fryer et al., 2019). The BPASS models rapidly evolve through their final stages, and do not track the end phases of evolution in detail. The core properties used are therefore more representative of stellar structure at the end of core carbon burning, rather than at collapse, and stellar cores can contract further by around two orders of magnitude in density after carbon burning (Eldridge et al., 2019b), potentially raising the specific angular momentum of a given shell. During this time, the assumption of solid body rotation almost certainly breaks down, but circumstances in which the envelope rotates faster than the core are highly unlikely. The  $j$  values shown in Figure 5.20 are already lower limits since the  $\log_{10}(j_{\text{cut}})$  minimum value has been adopted. Actual model values extend up to  $\log_{10}(j) \sim 19$ . If a further core contraction occurs, as expected,

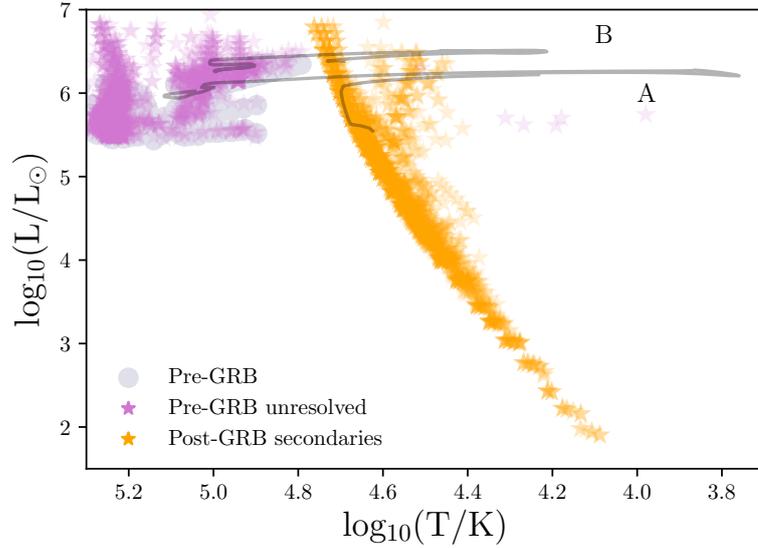
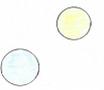


Figure 5.21: Every model (primary and secondary) which produces a GRB via the tidal pathway, in the metallicity range  $Z = 0.008$  to  $Z = 0.020$ , shown on the HR diagram. The model values for the individual pre core-collapse stars that go GRB are marked by grey circles. Also marked are the secondary stars left behind after a primary goes GRB (orange stars) and the unresolved systems that would be seen in pre-primary explosion imaging (purple stars). The shading represents the number density of models. Two example evolutionary tracks are overlaid. Track (A) is for a  $50 M_{\odot}$  primary with a  $45 M_{\odot}$  companion, starting with an orbital period of 0.2 days at a metallicity of  $0.5 Z_{\odot}$ . Track (B) follows a  $150 M_{\odot}$  secondary star with an  $11 M_{\odot}$  black hole companion, starting with an orbital period of 1.4 days, at  $0.4 Z_{\odot}$ .

the true values may be higher still by several orders of magnitude (e.g. Heger et al., 2000). Even a modest cumulative increase of 2 dex would push the distribution towards  $\log_{10}(j_{\text{boundary}}/\text{cm}^2\text{s}^{-1}) \sim 15 - 19$ , in better agreement with theoretical predictions (Woosley, 1993; Woosley and MacFadyen, 1999). This is the first time this critical threshold has been derived from observational data, albeit through fitting with stellar models. It arises naturally, without fine tuning, from the two-pathway model and associated assumptions.

### 5.6.2 The metallicity dependence of GRBs

GRBs show a deficit with respect to the cosmic volume-averaged star formation rate density at low-redshift, but occur in proportion to it at  $z \sim 3$  and above (Eldridge et al., 2019b). This is reflecting the well documented high-metallicity aversion of GRBs (Fruchter et al., 2006; Graham and Fruchter, 2013; Greiner et al., 2015b;



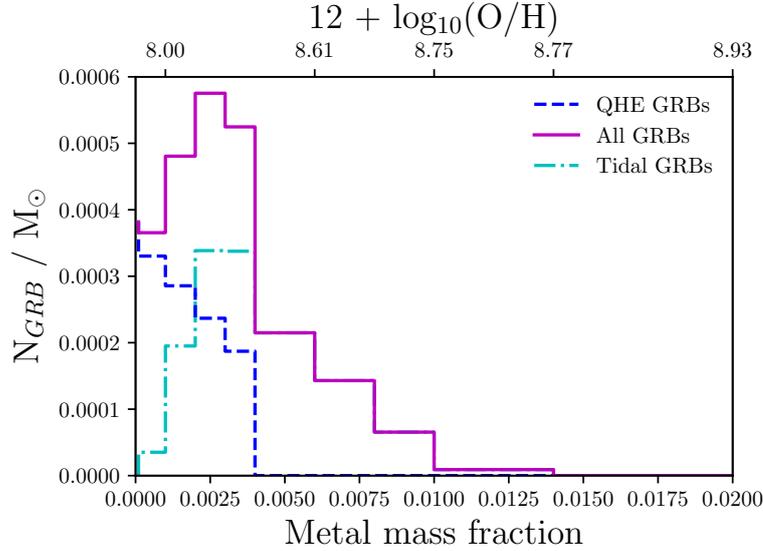


Figure 5.22: The efficiency of GRB progenitor production across metallicity. For a given mass of gas at a single metallicity, we would expect  $N_{\text{GRB}}$  progenitors to be formed per Solar mass of gas. I show this number for all GRB progenitors, and separately for the QHE pathway. QHE progenitors show a smooth decline in occurrence rate as metallicity increases, before the  $0.2 Z_{\odot}$  cut-off is reached. The tidally-induced pathways, however, peak around this metallicity.

Modjaz et al., 2019), which is demonstrated further in Figure 5.22. Here I show the GRB progenitor production efficiency, defined as GRB progenitor fraction per unit star formation at each metallicity, given the assumed IMF and binary parameters. There is a clear aversion to high metallicity. The QHE pathway becomes increasingly scarce as metallicity increases, until the  $Z = 0.004$  mass fraction cut-off implemented by BPASS is reached. Tidal pathways, on the other hand, peak at around 20 per cent of Solar. This is likely due to a trade-off between tides being more effective when the stellar envelope is extended, and increasing angular momentum loss through winds.

This can be tested further by examining the metallicity distribution of predicted progenitors. In Figure 5.16 I compared the synthetic GRB metallicity distributions to those from observed host galaxies, making the assumption that the metallicity of the host stellar population changes by a negligible amount over the lifetime of a GRB progenitor. The resultant distribution accounts for the cosmic star formation history and model weightings, and is broadly consistent with the observed host galaxy population.

Given that the predicted metallicity distribution and volumetric rate evolution is in good agreement with observations, using the best-fit Bayesian analysis

values, thought must be given to the strong metallicity dependence suggested by that analysis,  $Z \propto Z^n$  where  $n = 3.8_{-2.4}^{+2.1}$ . The uncertainties on this parameter are large, and at their upper end suggest a far stronger metallicity dependence for GRBs than seen in earlier work (e.g. Trenti et al., 2015).

In this analysis, the metallicity dependence has been placed as a modifier of the angular momentum threshold. However, the minimum angular momentum threshold at the remnant-ejecta boundary (i.e. at the point at which a jet is launched) should be independent of metallicity. Thus the effective threshold encodes information not on jet launching but rather on the metallicity dependence of whether the jet, once launched, can escape the stellar envelope or is stifled before producing a GRB.

Successful jet break-out relies on a number of different properties of the collapsing star. In principle, it will depend on the column density of the material through which the jet must tunnel (i.e. the density and thickness of the stellar envelope at point of collapse), the probability of photons interacting with that material (i.e. the envelope opacity), and also the timescale for jet escape (i.e. if the central engine deactivates before breakout is achieved there will no visible event).

I calculate the envelope column density for each GRB progenitor model by summing the density of mass shells from the core-envelope boundary out to the surface, multiplying by the shell thickness at each stage. The detailed STARS outputs are again used. Although high metallicity stars do have some of the highest columns, there is no distinct trend across the full metallicity range. The high  $Z$  dependence suggested by the model fitting analysis therefore cannot be confidently attributed to a column density effect.

The opacity of the ejecta which must be tunnelled through is also dependent on the metal content of the stellar material. For each photon, its probability of interaction scales with the number of possible electron energy level transitions which it may be able to excite. Heavier metallic elements, with their extended electron shells, dominate this probability, and so the opacity scales broadly linearly with the abundance of iron group elements. For higher opacities, more energy is dissipated from the jet in exciting electrons and so an initially more relativistic, more collimated jet is required. This corresponds to a greater reservoir of angular momentum also required to successfully tunnel through the envelope. Opacity is roughly proportional to metal mass fraction  $Z$  (Vink et al., 2001; Vink and de Koter, 2005), and would lead to  $n \sim 1$  in this formalism. It therefore cannot reproduce the  $n = 3.8$  dependence that results as a best fit from the Bayesian inference.

If instead the lower  $1\sigma$  bound from this analysis ( $n = 1.4$ ) is assumed, the



resultant  $j$  distribution in Figure 5.20 is good agreement with theory and removes any clear metallicity dependence at the point where the jet launches. A lower  $n$  index also introduces bursts at  $Z_{\odot}$  and above, improving the metallicity distribution agreement with observations. The question then is why  $Z^{3.8}$  was favoured by the Bayesian inference. In Figure 5.14, a model which tracks the assumed cosmic star formation history overestimates the GRB rate at low redshift and underestimates it at high-redshift. Larger powers of  $Z$  rectify this, allowing more bursts to occur at low metallicity (fewer at high values) - boosting the high-redshift rate (diminishing it at low redshift). However, a  $Z^n$  dependence that is too strong begins to remove too many bursts and makes it difficult to reproduce the observed population numbers with plausible  $E_{\text{iso}}$  and  $\theta$  corrections. The  $n = 3.8_{-2.4}^{+2.1}$  best fit arises from the combination of these factors, and inherits all their uncertainties. In particular, neither the substantial uncertainty on the cosmic volume-averaged metallicity evolution and its scatter as a function of redshift, nor uncertainties in the somewhat better constrained cosmic star formation rate density history, have been explicitly considered. The inclusion of other progenitor pathways, which could have a different occurrence rate over cosmic history, may also affect the best fit index  $n$ . Thus while a non-zero metallicity dependence is clearly favoured, over-interpretation of the best-fit value is warned against, whilst noting that an  $n \sim 1$  dependence is both permitted and explained by a physically plausible mechanism.

Note that the derived metallicity dependence arises from a fit to the evolution in the inferred GRB production rate. The fraction of very low metallicity (i.e.  $Z < 0.001$ ) models contributing to the volume averaged rate is very low and so the derived  $Z^n$  dependence is likely poorly constrained or not applicable at these very low metallicities. Indeed, it is possible that below a minimum metallicity threshold non-iron group opacities begin to dominate and the metallicity-dependence will plateau. There is very little difference in the stellar atmosphere opacity tables used by BPASS in this regime (Eldridge et al., 2017).

### 5.6.3 Uncertainties in the stellar modelling

Throughout this Chapter, assumptions and simplifications have been made with regards to the tidal evolution of binary systems, and the structure of high mass stars. For each model an initial weighting was selected from the IMF and binary parameter distributions, and assigned a value for an initial spin. The default BPASS IMF incorporates stars up to  $300M_{\odot}$  at ZAMS, in order to accommodate the rare but important Very Massive Star population seen in the Local Group (Hainich et al., 2014; Crowther et al., 2016; Schneider et al., 2018). However the occurrence of such

stars and the distribution of binary parameters may well be metallicity-dependent. This is unconstrained by observations and so not accounted for in the current version of BPASS (v2.2.1, Stanway and Eldridge, 2018, 2019).

The initial stellar angular velocity chosen for every primary model was 40 per cent of the Keplerian value at the equator (a typical value for OB stars, Dufton et al., 2019). While a distribution of velocities could be sampled, the exact choice of  $\Omega$  does not have a significant impact on tidal evolution (also seen by Zapartas et al., 2017a), as there is typically much more angular momentum stored in the orbit than in stellar spins. It is also assumed that the binaries start in circular orbits with their spin vectors aligned, so that only  $\dot{a}$  and  $\dot{\Omega}$  need be considered.

Given that most significant changes due to tides occur with the onset of mass transfer (Hurley et al., 2002), changes to evolution before that stage of factor a few are unlikely to have a major impact on these results. This is relevant to assumptions concerning stellar structure. I take the value of the apsidal motion constant,  $k$  (which depends on internal structure) to be 0.05 for every model. The theoretical modelled range of values is 0.01-0.1 (Zahn, 1975).  $\Delta\Omega$  and  $\Delta a$  both scale with  $k^{-1}$ . Varying  $k$  by a factor of a few will have similarly small effects on these parameters. For the system shown in Figure 5.5, varying  $k$  from 0.01 to 0.1 makes no difference to the size or timing of the model jump made by the tidal algorithm, and the system ends in the same state independent of  $k$ . I leave a full estimation of the impact of this systematic bias to future work, along with an improved estimation of both the  $k$  and  $E_2$  parameters.

The secondary star in the tidal prescription is treated as a point mass. For evolved binaries, where this object is a compact remnant, the approximation is reasonable. Otherwise, tidal distortion of the secondary may play a role in the system evolution, even if it remains inside its Roche lobe. One possible outcome of spin-orbit interactions is a merger. For this to occur, the total system angular momentum - the sum of the orbital and spin components - must be less than a critical value. Angular momentum is then transferred from the orbit to the spin, but the stars merge before synchronisation can occur (Eldridge and Tout, 2019). Given the starting velocity of  $0.4\Omega_{\text{crit}}$ , mergers solely due to tides are rare in this model set, only occurring in very tight binaries. These systems, which are doomed to merge due their initial  $\Omega$  and  $\omega$  conditions, are said to undergo a Darwin Instability (Darwin, 1879).

Finally, a major assumption in this analysis is that most black hole producing core-collapse events do not produce a visible supernova. The picture is more complex than there being a simple mass cutoff, as Dessart et al. (2012a) discuss in their work



on black hole production in GRBs, with other factors including the rotationally-driven magnetic field and envelope structure. Core compactness is also important criteria for successful supernovae (Sukhbold et al., 2016; Ertl et al., 2019), leading to so-called ‘islands of explodability’. The core compactness issue is addressed by assuming that the radius of interest within the pre-collapse star is that which encloses the eventual remnant mass. This is a reasonable approximation, provided that there is negligible fallback accretion. It is also assumed that the core and envelope co-rotate, with a flat angular velocity profile throughout the entire star. As previously discussed, any deviation from this will likely result in the core spinning faster than assumed. Such an increase in core spin would increase the number of rapidly spinning cores, and therefore increase the inferred  $j_{\text{cut},\odot}$  threshold, improving agreement with collapsar theory.

#### 5.6.4 Magnetars as GRB central engines

Although it has been assumed in this Chapter that GRBs operate under the collapsar mechanism, which requires black hole formation upon core-collapse, it is possible that newly formed magnetars might be able to launch jets too. Indeed, there is some evidence from GRB-SN energetics that this is the case (Mazzali et al., 2014). Therefore, I relaxed the remnant mass constraint to  $1.4M_{\odot}$ , allowing for the possibility that neutron stars are formed in core-collapse GRBs, and re-performed the MCMC analysis as described in section 5.4.2. It can be seen from Figure 5.6 that while black holes form readily at low  $Z$ , type Ic SNe with neutron star remnants are rare. By including neutron star producing Ic events, models are being added preferentially at high metallicity. Because these end their lives spinning slower, most of those added are then rejected by the angular momentum cut. Therefore, neutron star forming events can contribute, but are not an important pathway if black hole forming GRBs are also considered. The small difference their inclusion makes is demonstrated in Figure 5.23, which is a version of Figure 5.14 where GRBs have been restricted to occurring only in supernovae which produce neutron star remnants.

An extreme case would be that GRBs can *only* occur if a neutron star is formed in core-collapse. An MCMC run under this assumption, as described in section 5.4.2, yielded  $\theta = 12.8_{-4.6}^{+6.4}$  degrees,  $\log_{10}(E_{\text{low}}/\text{erg}) = 49.6_{-0.5}^{+0.6}$ ,  $\log_{10}(j_{\text{cut},\odot}/\text{cm}^2 \text{ s}^{-1}) = 18.8_{-0.4}^{+0.3}$  and  $n = 2.2_{-1.3}^{+1.0}$ . Because stripped envelope, fast-spinning, neutron star forming progenitors are rarer (than the equivalent black hole forming events), the best-fit parameter values are naturally quite different, as shown in Figure 5.23. The most notable among them is  $E_{\text{low}}$  - the minimum isotropic equivalent energy is nearly two orders of magnitude higher than the faintest GRBs

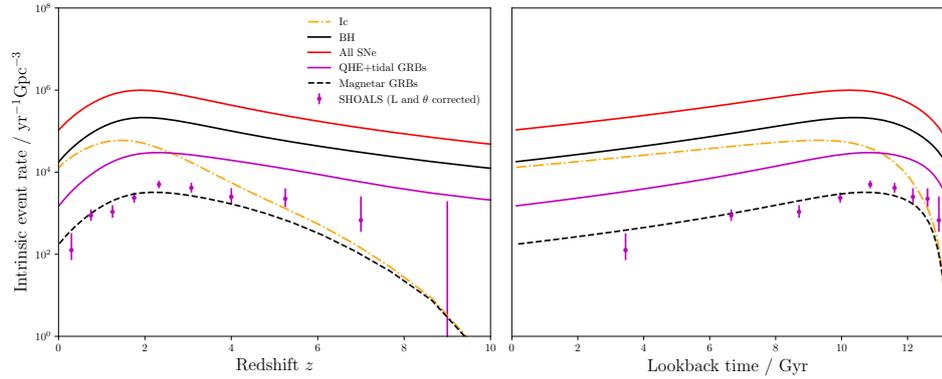


Figure 5.23: The intrinsic GRB rate, if only magnetar central engines are allowed, is shown by the black dashed line (to which the SHOALS data have been fitted). Although magnetars can be used to recreate the GRB rate, the inferred minimum GRB energy that results is  $\sim 100$  greater than the faintest bursts observed.

observed. Therefore, barring strong co-variances between the four model parameters which have not been considered, or a very different luminosity function than that assumed, this appears to disfavour magnetars as the sole central engines capable of launching GRBs. Furthermore, the metallicity distribution assuming just magnetar engines is inconsistent with the host galaxy data (see Figure 5.24, which is the equivalent to Figure 5.16 in the case where GRBs have been restricted only to events which produce neutron stars). There is narrow range of metallicity in which stars lose enough mass to produce neutron star remnants, but retain enough to not fully spin-down. Anderson-Darling  $p$ -values between the synthetic distribution and the hosts data sets are all  $< 0.05$ , rejecting the null hypothesis that they are drawn from the same distribution at the  $2\sigma$  level.

### 5.6.5 Future possibilities

In Figure 5.21, it is predicted that the progenitors of GRBs induced through tidal evolution are amongst the most luminous stripped envelope stars. They are also extremely hot. Thus despite their high luminosities they may be challenging to observe, requiring ultraviolet, or very blue-sensitive optical, detectors. Supernova 2017ein, the only SN Ic to have a progenitor system identified so far, occurred at a redshift  $\sim 0.0027$ , with the candidate identified in archival *Hubble Space Telescope* (*HST*) imaging (Van Dyk et al., 2018; Kilpatrick et al., 2018). The star, if single, had an absolute F555W magnitude of  $-7.5$ . The nearest GRB confirmed so far is GRB 980425, associated with SN 1998bw. This occurred at  $z \sim 0.0085$  (Galama et al., 1998), corresponding to a luminosity distance which is approximately three times



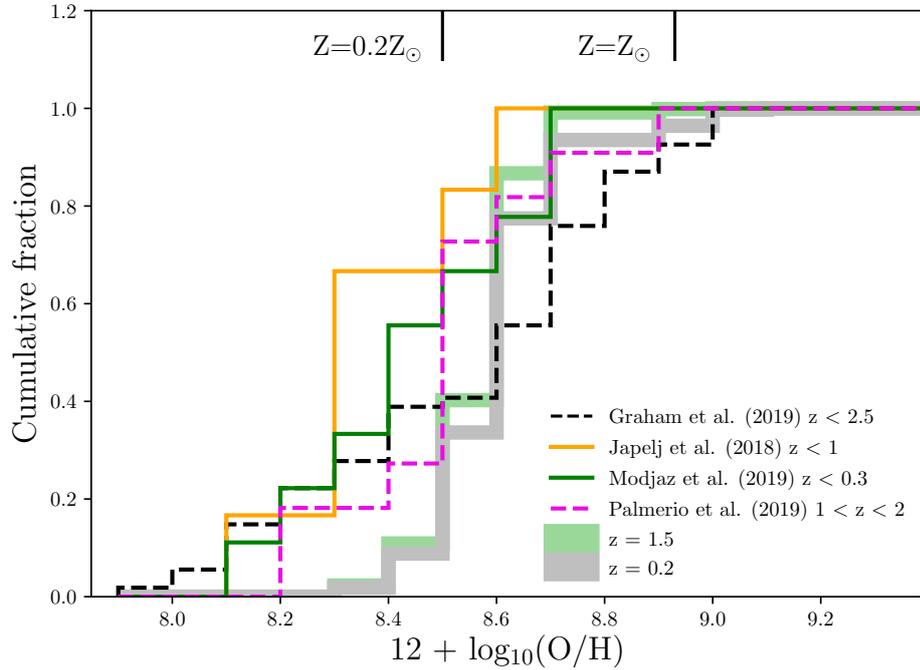


Figure 5.24: The synthesised host metallicity distribution, if GRBs are limited to magnetar central engines only. None of the comparison data sets are consistent (at the  $2\sigma$  level, according to Anderson-Darling tests).

greater than SN 2017ein. If SN 2017ein had occurred at the distance of SN 1998bw, the progenitor (or unresolved progenitor system) would have had an apparent magnitude of  $\sim 25.5$  (in the F555W band).

It is also interesting to consider the possibility of surviving companions being seen once the supernova and GRB afterglow have faded. The companions have been identified as main sequence stars (most-likely), with a slight preference for large mass ratios or twin systems. Such stars are faint, but not beyond the realms of possibility for *HST* or upcoming facilities such as the *European Extremely Large Telescope (E-ELT)* or the *James Webb Space Telescope (JWST)*. The low metallicity QHE pathway is restricted to high-redshifts where these kind of observations are unfeasible. However, the tidal GRB pathways identified, where tides maintain spin in a stripped envelope progenitor, are a plausible target if a sufficiently close example is identified for both detection and spatial resolution of the star.

## 5.7 Conclusions

I have used the binary stellar evolution models of BPASS to investigate the nature of supernova and core-collapse gamma-ray burst progenitors. By considering tidal interactions, and applying a prescription for the cosmic star formation rate history, I have shown that two binary pathways can explain the bulk of the observed GRB population. The first involves secondary stars spun up by accretion into a quasi-homogeneous state, and the second occurs when massive stars in binaries have their envelope removed while tides maintain the required angular momentum for jet production. This two pathway model can reproduce the rates as a function of redshift and the observed host metallicity spread, using reasonable parameter distributions for the jet opening angle and isotropic equivalent energy. The model predicts minimum angular momentum requirements which are in general agreement with collapsar GRB theory. Finally, predictions are made for the nature of the progenitor systems and their companions, which may be testable with next generation facilities. The exploratory work presented in this Chapter does not represent a definitive or unique solution to the GRB progenitor problem, and there are several areas which need to be further explored or developed in future work. None the less, this approach can simultaneously reproduce several aspects of long GRB theory and observation, demonstrating the utility of population synthesis models in transient progenitor studies.

## 5.8 Subsequent Developments

The work described in this Chapter was published in the *Monthly Notices of the Royal Astronomical Society* in January 2020, first appearing on arXiv in November 2019.

I now discuss other recent studies that may have implications for this Chapter. Callingham et al. (2019) observed the dust and gas in a colliding-wind Wolf-Rayet binary. They find that the dust pattern and measured wind speeds are inconsistent with isotropic wind models, and resolve this tension by invoking anisotropic winds which are stronger along the polar axis. This is observational evidence that massive single stars (or stars in non-interacting binaries) may still be able to retain angular momentum up to core-collapse, even with strong mass loss rates. If all fast-spinning Wolf-Rayet stars lose their mass preferentially along the polar axis (as has been suggested before, Groh et al., 2008), then the single star GRB scenario cannot be so easily ruled out, offering another pathway to be explored in future population



synthesis studies.

Part of this Chapter involved categorising models as progenitors of different supernovae types, based on their chemical composition and remnant mass. Since the publication of this work in MNRAS, Davies and Beasor (2020) have published a study on the Red Supergiant (RSG) problem. They compared the observed luminosities of RSGs in the SMC and LMC, to those known to be type II supernova progenitors. They find that the progenitor sample is indeed biased to lower luminosities (suggesting that the more massive examples collapse directly to black holes without supernovae). Furthermore, they find that a steep luminosity function, combined with small number statistics, can explain the observations if RSGs with initial masses  $> 20M_{\odot}$  collapse without supernovae. However, they caution that the effect is weaker than previously estimated, at only the  $1-2\sigma$  level. Only larger sample sizes of pre-supernova RSGs will constrain the maximum progenitor mass that produces a supernova, and corroborate the result of Adams et al. (2017), that some stars undergo failed supernovae. Furthermore, Farrell et al. (2020) find that  $T_{\text{eff}}$  and  $L$  measurements alone are not sufficient to deduce the final mass of star in pre-collapse imaging, due to degeneracies, and therefore that inferred progenitor positions in  $T - L$  parameter space (as in Figure 5.3) should be treated with caution.

## Chapter 6

# Conclusions and future prospects

*The very ability of human beings to make sense of the night sky “is a thought so compelling that it will surely drive us forward in our search for answers”— NSC Creative, We Are Aliens, narrated by Rupert Grint and adapted by the Author<sup>a</sup>*

<sup>a</sup><https://wearealiens.nsccreative.com/>

In this final Chapter, I summarise the findings of this thesis, and the conclusions that can be drawn about GRB host galaxies and progenitors as a result. I then discuss the prospects for future work, both in the field of GRBs, and more widely in transient astronomy, using the methods described in this thesis and the data that will come from next generation observatories. I end with an overview of the contributions of this thesis to GRB science, and the key questions in the field going forward.

Prior to this thesis, the key science questions for long GRBs concerned (i) the nature of their progenitor systems, beyond likely involving a massive, fast spinning star, and (ii) the variety of their host environments - a strong preference for low-metallicity star-forming environments was seemingly at odds with numerous examples that defied this trend (in particular, the presence of GRBs in dusty environments). The work presented in this thesis to characterise these unusual hosts galaxies had begun several years previously, with observing programmes to pinpoint dark GRBs within their hosts (with *HST* and *CXO*, PI: Levan) and to study IR-bright hosts following the identification of GRB 080517’s host (with the VLT and WHT, PI: Stanway). Using these datasets, and building on the body of literature



in the field, the key aims of this thesis were to:

- Improve our knowledge of the galactic environments capable of producing long-duration, core-collapse gamma-ray bursts.
- Advance our understanding of the dark GRB population, particularly the nature of their host galaxies, and what the implications are for the progenitors.
- Determine the most likely GRB progenitor channels based on their occurrence rates, host properties and theoretical considerations for the jet production mechanisms.

I now describe the main findings of this thesis in greater detail in the following section.

## 6.1 Summary of results

### 6.1.1 The nature of infrared-bright gamma-ray burst host galaxies

In Chapter 2, I identified a population of galaxies selected in the IR *WISE* all sky survey that are coincident with *Swift* GRB X-ray afterglows. I used imaging and spectroscopic data from WHT/ACAM and VLT/X-Shooter, along with archival GALEX, Pan-STARRS, 2MASS, *WISE* and other imaging to fit the SEDs for these galaxies, demonstrating that around 50% of X-ray-*WISE* matches were likely to be genuine host galaxy alignments, with the other half comprised mainly of nearby M-stars. Of the IR-bright long GRB host galaxies that were identified, I showed that they constitute the nearby and dusty tails of the GRB host distributions, and are not a distinct class of host. This suggests that the wide variety of environments capable of hosting long GRBs is not due to fundamental differences in the progenitors and mechanisms, and that the tails of the host parameter distributions arise because the progenitor scenarios themselves, while preferring low-metallicity, have some tolerance for higher metallicity situations.

### 6.1.2 Dark gamma-ray bursts and their host galaxies

In Chapters 3 and 4, I explored the properties of dark GRB host galaxies and the nature of dark GRBs themselves. Chapter 3 used *HST* imaging in two bands to show that  $\sim 20\%$  of dark GRBs have their optical emission diminished by rest-frame neutral hydrogen absorption of Lyman continuum emission, placing them at  $z > 5$ . This same imaging, coupled with precise afterglow locations from *CXO* and NIR

observations, demonstrated that dark GRBs trace their host light in a similar way to optically bright GRBs. The dark GRB hosts are morphologically similar to bright GRB hosts, consistent with the findings of Chapter 2 that the overlapping classes of IR-bright and dark GRB hosts are not a fundamentally different population. Ellipticity measurements showed that the higher line-of-sight attenuation in dark bursts is not due to them being viewed through an edge-on disc (assuming disc-like morphologies), and that the dust required for attenuation may have to be clumpy and local to the burst site. This disfavours scenarios where GRBs solely occur in low metallicity pockets, in otherwise enriched galaxies. In Chapter 4 I studied a single dark burst, drawn from the sample of Chapter 4, in more detail. Gemini/GMOS and Gemini/NIRI imaging, plus *Swift* data, was used to model the afterglow. A high-redshift origin in the range  $4 < z < 8$  was most favoured for GRB 100205A, consistent with the *HST* host galaxy non-detections in both F606W and F160W. The previous omission of this burst from high-redshift samples demonstrated the need for rapid, deep multi-wavelength follow-up if more high-redshift events are to be identified, and subsequently exploited for the study of high-redshift stellar populations.

### 6.1.3 Core-collapse gamma-ray burst progenitors via binary evolution pathways

Finally, Chapter 5 presented a population synthesis study using the Binary Population and Spectral Synthesis (BPASS) code to reproduce the observed GRB rate by (i) selecting stellar evolution models that might produce GRBs, (ii) determining how often these events should occur across cosmic time by assuming a metallicity-dependent star formation density history, and (iii) correcting the intrinsic rate to account for jet opening angles and the GRB luminosity function. This method showed that a two-pathway model, with accretion-driven QHE and tidally-interacting stripped-envelope stars, could match the observed redshift-dependent, volume averaged GRB rates. It simultaneously reproduces the host metallicity distribution, which was not used to constrain the model. The results therefore provide an explanation for the usual preference - but not requirement - for low-mass, low-metallicity hosts. Furthermore, this analysis matched theoretical estimates for the specific angular momentum of accretion discs around black hole central engines in the collapsar model. Although subject to various assumptions and not excluding other pathways, this was the first time that population synthesis had reproduced these aspects of GRB observation and theory. The methodology also makes falsifiable predictions for the progenitor systems of core-collapse GRBs, demonstrating its potential applications not just for



GRBs, but also for a wide range of other extragalactic transients.

## 6.2 Future prospects

Although this thesis has contributed to our understanding of the core-collapse GRB phenomena, open questions remain. Furthermore, the techniques and methods used in this thesis are plausibly applicable to a wider range of extragalactic transients, particularly those whose progenitors are currently uncertain. I now describe the prospects for future work, building on the findings of this thesis and taking advantage of new instrumentation we might expect to see operational within the next decade.

### 6.2.1 Core-collapse GRB synthesis: additions and improvements

The theoretical study presented in Chapter 5 has both the greatest potential for future expansion and the widest range of limitations and input physics to be tested and improved. For example, there are various improvements that can be made to more realistically model stellar rotation, supernova and GRB rates. These include,

- Use of an improved tidal implementation, in which values such as the apsidal motion constant  $k$  are not assumed, but calculated based on the stellar structure at each time-step (Kushnir et al., 2017).
- Incorporation of tidal interactions in the BPASS stellar evolution models themselves, rather than estimating their effect in post-processing. As a result of the study presented in this thesis, this is now a planned element of the BPASS v3 upgrades.
- Use of a more physically motivated NS-BH mass threshold (e.g.  $\sim 2.2M_{\odot}$ , as inferred from GW170817, Margalit and Metzger, 2017; Rezzolla et al., 2018).
- Consideration of supernova islands of explodability. Allowing for the possibility of successful explosions that produce black holes, when determining supernova classification thresholds based on their relative rates. PISNe could also be taken into account, given predictions for the final mass ranges where these occur (Heger and Woosley, 2002; Sukhbold et al., 2016; Ertl et al., 2019).
- Consideration of magnetic braking effects and their influence on orbital evolution.

In addition, although the observed GRB rate was reproduced using mass-transfer QHE and tidally spun-up pathways, it is worth considering other possibilities. A number of such pathways have been identified in the literature, including the

merger of helium stars with a companion (Fryer and Heger, 2005; Detmers et al., 2008; de Mink et al., 2013, 2014), binary-driven hypernovae (Rueda et al., 2019) and white dwarf-compact object mergers (Fryer et al., 1999; Caito et al., 2009) - all of which are testable with BPASS.

Another scenario not considered in Chapter 5 is that tidally spun-up stars could enter the QHE regime (de Mink et al., 2013; Song et al., 2016; de Mink and Mandel, 2016; Mandel and de Mink, 2016; Song et al., 2016; Marchant et al., 2016, 2017) - in the formalism currently used, the only way to induce QHE is through mass transfer at very low metallicity. Tidally induced QHE has received significant attention in the literature as a route to producing massive black hole binaries. However, because the low-metallicity, low mass-loss GRB requirement holds even if QHE is tidally induced, such events will not significantly contribute to the overall observed GRB rate. The analysis in this thesis produced a good match to the observed volumetric rates and properties of known GRBs, without assuming exotic or extremely rare progenitor pathways. I therefore leave a full BPASS study of the viability and occurrence rates of rarer alternative pathways for future consideration.

### 6.2.2 Core-collapse GRB synthesis: other observables

In Chapter 5, synthetic rates (as a function of redshift) were fitted to observations, with secondary output observables including the pre-explosion temperatures and luminosities of the progenitor stars, (host) metallicities and the delay time distributions (related to the host star formation rate). Angular momenta are also predicted, however these are not measurable (either directly or indirectly) in the same way.

There are other observable properties of GRBs that may corroborate, or disfavour, the dual pathway model determined as most likely in Chapter 5. One test is the synthesis of supernova lightcurves from the pre-explosion stellar structure models selected as GRB progenitors: do they look like type Ic-BL GRB-SNe? Similar work has already been carried out for type II SNe (CURVEPOPS, Eldridge et al., 2018, 2019b). A second test regards the mass loss history of the progenitor systems, and the effect that the resultant circumstellar medium has on afterglow lightcurves. Using a sample from *Fermi*, Gompertz et al. (2018) found that long GRBs can be separated into having wind-like or ISM-like circumstellar media, based on their lightcurve behaviour (first suggested by Chevalier and Li, 1999). The existence of two classes of afterglow is intriguing, given the dual pathway result of Chapter 5. An investigation into the model mass-loss histories may strengthen the case for these progenitor pathways, and provide a natural explanation for the ob-



served lightcurve dichotomy. A first step is to compare the synthesised relative rates and environments (metallicities) of the QHE and tidal GRBs to the observed rates and environments of the Wind and ISM GRBs, and this work is now underway.

### 6.2.3 Population synthesis of other transients

Many classes of transient still have poorly understood origins. These include engine-driven transients, like superluminous supernovae, and transients that may have binary star origins, such as fast radio bursts (The CHIME/FRB Collaboration et al., 2020). A similar methodology to that applied in Section 5 can be used to probe the likelihood of different progenitor scenarios for these transients. By searching for stellar systems within BPASS that satisfy a range of theoretical requirements, it will be possible (for each theory) to make predictions for the occurrence rates and galactic environments as a function of redshift. Comparison to observations then allows us to probe the plausibility of each theory, or combination of theories. If event rates as a function of redshift are reproduced, *and* the predicted galaxy properties (e.g. star formation rate, metallicity) are in agreement with observation, then the case is strong that the origin of a particular transient has been correctly identified. However, it is important to note that these studies are critically dependent on the assumed cosmic star formation rate history as a function of metallicity. Next generation telescopes such as *JWST* will help to constrain this fundamental component of transient synthesis methodology in the coming years.

### 6.2.4 Opportunities from next-generation facilities

The coming decade will see a plethora of new telescopes and instruments entering service, providing many opportunities for new GRB science. I will now give an overview of these next-generation facilities, and their expected role in GRB and transient astronomy.

Rapidly slewing gamma-ray and X-ray telescopes have driven GRB science ever since their inception. There is currently one notable new gamma-ray/X-ray satellite imminent, and two that are in the planning stages. Firstly, the Space Variable Object Monitor (SVOM, Paul et al., 2011) is due to launch in 2021 and will be the successor to *Swift*. *Swift* has far outlived its initial 2 year programme lifetime (having launched in 2004), in large part because there are no consumables onboard. It is currently funded until 2022<sup>1</sup>. SVOM's mission aim is similar to *Swift*'s: to provide rapid, well localised GRB positions in X-rays, refined by optical

---

<sup>1</sup>[https://science.nasa.gov/science-pink/s3fs-public/atoms/files/NASA\\_Response\\_SR2019\\_Final.pdf](https://science.nasa.gov/science-pink/s3fs-public/atoms/files/NASA_Response_SR2019_Final.pdf)

detections with an on-board red-sensitive telescope. SVOM's wide-field detection telescope, ECLAIRS, performs a similar role to *Swift*/BAT and has a comparable energy range (4-120 keV for SVOM versus 15-150 keV). The position is refined to  $\sim 20$  arcsec-1 arcmin precision with the Microchannel X-ray Telescope (MXT), which has the same 0.2-10 keV range as *Swift*/XRT. The first major difference between SVOM and *Swift* comes from its Gamma-ray Burst Monitor (GRM), a 50 keV to 5 MeV spectrometer, more comparable in energy range to *Fermi*/GBM and allowing early spectral characterisation of the GRB afterglow. *Fermi* and INTEGRAL currently provide GRB spectral information in the  $\sim$ MeV energy range, which is often where the peak of the afterglow spectrum lies at early times: measuring the position of  $E_p$  is crucial for afterglow modelling. *Swift*/BAT is too low energy to regularly capture this peak, and so SVOM represents an important improvement in this respect, combining the high energy range of INTEGRAL and *Fermi* with the wide-field detection (ECLAIRS will have an  $89 \times 89^\circ$  field of view) and fast-slewing abilities of *Swift* (SVOM will slew to observe with MXT within minutes of detection). Another difference between *Swift* and SVOM is the wavelength range of the onboard visible telescope (VT) - while *Swift*'s UVOT has UV capability, SVOM/VT will not, with a range of 400-950nm. This choice will make SVOM more sensitive to highly redshifted GRB afterglows, and will not jeopardise UV-bright afterglow detection as such events are also optically bright. The VT observations will be backed up by two ground-based robotic telescopes (visible to IR), with the aim of providing rapid photometric redshift estimates. However, the lack of UV capability reflects a wider trend in the community - once *Swift* retires, *HST* will be the sole (non-Solar) space telescope remaining that can observe in the UV.

While SVOM is an immediate successor to *Swift*, the Transient High-Energy Sky and Early Universe Surveyor (THESEUS, launch if selected 2032, Amati et al., 2018) is a proposed European Space Agency X-ray/IR mission that will succeed *Swift*, SVOM and *Fermi*, with a focus on high-redshift GRBs. Similar in design to *Swift* and SVOM (with a gamma-ray detection telescope, XGIS, soft X-ray imager for positional refinement, SXI, and an IR imager and spectroscope reaching  $1.8 \mu\text{m}$ , IRT), THESEUS will be an order of magnitude more sensitive in the X-ray than SVOM and *Swift*. The aim is to perform deep X-ray monitoring and surveys for transient detection, and particularly to spectroscopically identify high-redshift GRB afterglows for use in distant Universe studies. Finally, for precise GRB X-ray localisation without an optical-IR counterpart, the Advanced Telescope for High Energy Astrophysics (ATHENA, launch circa 2031, Nandra et al., 2013) is a natural successor to *Chandra*, providing an order of magnitude improvement in both spatial



resolution and sensitivity.

The study described in Chapter 2 relied heavily on the availability of deep, all-sky, multi-wavelength data. Upcoming optical surveys that will add to this sky census include the Large Synoptic Survey Telescope (LSST, Ivezić et al., 2019), which will produce a 18000 deg<sup>2</sup> sky map, reaching a  $5\sigma$  depth of 27.5 in the  $r$ -band, over the 10 year mission duration. LSST will provide the deepest, widest and fastest sky survey of this kind ever undertaken, and promises to catalogue 20 billion galaxies and discover transients at a rate  $\sim 100$  times greater than current surveys (such as the Zwicky Transient Factory, Bellm et al., 2019). Prior to LSST operations, BlackGEM is set to image the entire sky south of  $+30^\circ$  down to 22<sup>nd</sup> magnitude (the South All Sky Survey, Bloemen et al., 2015). These surveys will provide well sampled lightcurves, and improved classification with lightcurve data alone. Furthermore, for the first time thanks to BlackGEM, there will be optical imaging of the entire southern sky to a depth of at least AB mag  $\sim 22$ . All-sky imaging to this depth or greater will aid transient studies by facilitating more host identifications without the need for dedicated follow-up observations. The caveat associated with large survey programmes, and in particular LSST, is that the number of transient candidates per night will be extremely large. Aside from the challenges of processing such large data-sets, transient classification typically requires spectroscopic follow-up. While LSST will provide a goldmine of transient data, the vast majority of this data will be of limited use owing to the much smaller combined spectroscopic follow-up capacity on other telescopes around the world.

In cases where follow-up is required to detect a faint transient host, to characterise a host or study the transient itself, there are a number of new 30m-class and space-based telescopes under construction that represent a step change in observational capability. The James Webb Space Telescope (JWST), set to launch in Spring 2021 at the time of writing, is regarded as a successor to *HST* and will push galaxy imaging and spectroscopy to higher redshifts and greater depths than previously possible (thousands of galaxies are expected to be discovered at  $z > 6$ , Williams et al., 2018). In terms of GRB science, the NIR sensitivity of *JWST* makes it ideal for the follow-up imaging and characterisation of dark bursts and their hosts in particular. GRBs are excellent probes of the low-mass, low-metallicity galaxy population at high redshift - their afterglows bear the imprint of their host environment, and they pin-point the positions of their hosts (Tanvir et al., 2012; McGuire et al., 2016). GRB follow-up with *JWST*, and ground-based 30m-class telescopes will therefore facilitate their full potential in high-redshift, galaxy evolution and reionisation studies. These ground-based observatories include the Thirty Metre Telescope (TMT,

first light circa 2027 subject to site approval, Skidmore et al., 2015), Giant Magellan Telescope (GMT, first light circa 2029, Johns et al., 2012) and the European Extremely Large Telescope (E-ELT, for which construction is underway and first light is expected 2025, Gilmozzi and Spyromilio, 2007). At lower redshifts, the greater signal to noise spectroscopy of these telescopes permits, for example, direct measurements of the iron abundance in GRB hosts, rather than relying upon metallicity scaling relations (Hashimoto et al., 2018). These facilities will all have spatial resolutions  $< 0.01$  arcsec in the optical, while *JWST* will have  $< 0.1$  arcsec resolution in the NIR, allowing us to resolve stellar populations within more galaxies, out to greater distances, and further down the luminosity function.

In the radio regime, towards the end of the coming decade, the Square Kilometre Array (SKA) will be operational (In the form of SKA-MID, Macquart et al., 2015), building on the currently operational pathfinders MeerKAT (Karoo Array Telescope, Booth et al., 2009) and the Australian SKA pathfinder (Johnston et al., 2008, ASKAP). The volume of data expected from the SKA is unprecedented, and it will provide deeper, high spatial resolution radio imaging of transients in the time domain, covering everything from late-time GRB afterglows (revealing jet physics and structure) to fast radio bursts. This science is already underway with the precursor arrays, however the observing modes and response times for the full SKA are still to be decided. As with large scale, deep optical surveys, a serious challenge facing the SKA is the sheer scale of the datasets produced: both in terms of processing and the limited follow-up capability of other facilities around the world.

At very high energy (VHE), the Cherenkov Telescope Array (CTA, under construction in La Palma, Actis et al., 2011; Nandra et al., 2013) will provide sensitivity to photons in the energy range 20 GeV to 300 TeV, with a spatial resolution of 1 arcmin and an order of magnitude better sensitivity than MAGIC and H.E.S.S at 1 TeV (Cherenkov Telescope Array Consortium et al., 2019). There are already suggestions from the first three GRBs detected at VHE that these photons originate from inverse Compton scattering (Fraija et al., 2019; Abdalla et al., 2019); the larger sample sizes provided by the CTA will help to constrain the prevalence and nature of this emission.

Beyond the electromagnetic spectrum, new neutrino observatories such as the Deep Underground Neutrino Experiment (DUNE, Acciarri et al., 2016) will be capable of detecting  $\sim 3000$  neutrinos from a Galactic supernova at 10 kpc (5 times closer than SN 1987A, which occurred in the Large Magellenic Cloud, Hirata et al., 1987). It is not unfeasible that within 10 years, we will have the capability to detect a Galactic supernova not only in electromagnetic radiation, but with neutrinos and



gravitational waves too, providing insight into the mechanics and nuclear physics of massive star core-collapse.

On the short GRB side, there are several facilitates and programmes dedicated to finding the electromagnetic counterparts to binary merger gravitational wave events, with the aim of starting multi-messenger population studies within the next few years. These include robotic survey telescopes such as the Gravitational Wave Optical Transient Observer (GOTO, Steeghs et al., in prep) and BlackGEM, and larger follow-up collaborations such as ENGRAVE (which coordinates European Southern Observatory facilities, Ackley et al., 2020). LIGO/VIRGO (LVC) observing run O3 is due to end in May 2020, and O4 due to commence Spring 2022 (alongside KAGRA, Abbott et al., 2018b), with an increased binary neutron star merger detection horizon of 330Mpc.

### 6.3 Final conclusions

Much progress has been made in understanding GRBs over the last  $\sim 20$  years. The origins of the short and long duration sub-populations have been traced back to compact object mergers and massive star core-collapse respectively, through studies of their host galaxies and lightcurves. In 2017, multi-messenger astronomy spectacularly confirmed the merger origin for short bursts with GW 170817 / GRB 170817A / AT 2017gfo. Despite a large body of evidence derived from their star-forming host environments and association with type Ic-BL supernovae, the exact nature of long GRB progenitors has, perhaps surprisingly, proven more difficult to constrain. Their interpretation may have been simpler, had their *preference* for low mass, low metallicity host galaxies been an absolute *requirement* instead. Long GRBs have continued to surprise, with numerous examples occurring in metal-rich and dusty environments that seemingly do not fit the rapidly-spinning, low-metallicity progenitor star scenario. Furthermore, their association with stripped envelope supernovae appears at first glance inconsistent with the need for a large reservoir of angular momentum at core-collapse - if only single star progenitors and wind-driven mass loss processes are invoked.

Reconciling these observations with theory was the principle aim of this thesis. In Chapter 2, the IR-bright GRB host population was shown to represent the nearby and dusty tails of the GRB host parameter distributions, offering useful insight into the extreme ends of the distributions, and allowing us now to use IR luminosity as a quick diagnostic tool when a GRB host is identified. Chapter 3 confirmed that the majority of optically dark GRBs are dark due to dust extinc-

tion within their hosts, and provided an independent estimate for the high-redshift fraction among dark GRBs (and therefore the whole population). Dark GRB-host offsets were measured in a statistically significant sample size for the first time, and along with morphological information, this thesis has shown the attenuating dust likely has a clumpy component local to the burst site - disavouring an interpretation where long GRBs are offset from metal enriched regions within their hosts. Chapter 4 added GRB 1000205A to the modest list of events known at high-redshift, and demonstrated the need for deep, multi-wavelength follow-up if more high-redshift events are to be identified in future. Finally, in Chapter 5, this thesis has demonstrated that binary stars can explain both the observed long GRB rate as a function of redshift, and the host metallicity distribution, if (i) tidal interactions maintain stellar spins at the latest stages of stellar evolution or (ii) accretion spins up a massive star into a quasi-homogeneous state at low metallicity. This is the first time that a population synthesis code, incorporating the effects of binary interactions in detailed stellar evolution models, has been used to simultaneously reproduce the observational constraints (rates and metallicities) *and* theoretical estimates (collapsar angular momentum requirements) associated with collapsar GRBs. This work was publicly disseminated in a press release<sup>2</sup>, and has achieved an Altmetric score of 1011, the fourth highest attention score of any MNRAS output tracked by Altmetric to date. This demonstrates the high level of public interest in transient astronomy, and the ability of this topic to reach a wide range of audiences. An artist's impression of a tidally-driven GRB, commissioned for the press release, is shown in Figure 6.1.

During the course of this research being carried out, there have been a number of significant developments, including the first detection of very high energy photons from GRBs, the birth of gravitational wave multi-messenger astronomy, and significant advances in the theoretical modelling of stellar populations. Despite this, and the contributions made in this thesis to the reconciliation of collapsar GRB and theory, there is still much to learn. Some key science questions still remaining are:

- What does the GRB metallicity bias look like in terms of iron-group metallicity? There has traditionally been a heavy reliance on oxygen-based metallicities in GRB studies, or even simply using the mass-metallicity relation, which is now warned against (Graham et al., 2019). High signal-to-noise spectroscopy, for example with the 30m class telescopes and *JWST*, will make direct iron-line measurements feasible in GRB hosts.

---

<sup>2</sup>[https://warwick.ac.uk/newsandevents/pressreleases/stars\\_need\\_a](https://warwick.ac.uk/newsandevents/pressreleases/stars_need_a)



- What is the role of long GRBs in the chemical enrichment of galaxies? Specifically, do they dominate r-process enrichment? GW170817 / AT2017gfo demonstrated, thanks to an intense follow-up campaign, that neutron star mergers produce r-process elements in kilonova explosions (Tanvir et al., 2017). Deep IR searches for bumps in GRB-SN lightcurves (with *JWST* and the 30m-class telescopes) will be able to test whether long GRBs also produce large quantities of r-process ejecta - if this is not tested before then with current facilities (Siegel et al., 2019).
- What can long GRBs, and their afterglows, tell us about galaxy evolution and reionisation at high-redshift? The new GRB-hunting satellites SVOM (due 2021) and THESEUS (proposed) are biased toward the discovery and localisation of high-redshift GRBs; their afterglows can be used to measure the chemical properties of high-redshift stellar populations and to constrain the ionising photon escape fraction in  $z > 5$  host galaxies (Tanvir et al., 2019).
- Can we observationally test predictions for the nature of long GRB progenitor systems? The explosion of an extremely nearby long GRB, sufficiently close that pre-explosion imaging of the progenitor is available, may provide constraints (Chapter 5, Chrimes et al., 2020). However, given that this is unlikely to happen, other constraints may come from spectroscopy of Galactic and Local Group Wolf-Rayet stars. What are the fastest spinning stripped envelope stars observed at  $0.5-1 Z_{\odot}$ ? Are the fastest examples in binaries (or can rapid rotation in single stars be achieved thanks to anisotropic inds Callingham et al., 2019)? And can a star undergoing quasi-homogeneous evolution be unambiguously identified (there are already candidates, e.g. Martins et al., 2009)?
- What is the physics behind successful supernovae - are the explosions neutrino driven? And which classes of star undergo successful explosions? Observational tests of core-collapse models will soon be possible thanks to multimessenger astronomy - both in terms of neutrinos (e.g. DUNE) and gravitational waves (LIGO,VIRGO,KAGRA), both of which are produced in core-collapse events. However, this is contingent on a nearby (Galactic) supernova occurring, and the progenitor being identified in pre-explosion imaging. The existence of the ‘islands of explodability’, and the premise that some stars undergo a failed supernova, may also be tested in this way: the disappearance of a nearby star, temporally and spatially consistent with a core-collapse GW signal, would be strong evidence for a failed supernova.

- Can NS-BH mergers produce GRBs? Given that NS-BH mergers have already been detected in LIGO/VIRGO O3, it is only a matter of time before one occurs close enough - and is well localised enough - for a short GRB and/or kilonova to either be detected or ruled out (Ackley et al., 2020).
- What are the central engines driving GRBs, and are they the same for short and long bursts, despite their different progenitors? This may be answerable within the next decade for short GRBs, if the gravitational wave merger ring-downs are detected with high enough signal-to-noise (Margalit and Metzger, 2017; Rezzolla et al., 2018). The greater distance and weaker GW signals expected from core-collapse GRBs, however, will likely mean that their central engines cannot be determined in this way.
- What is the physics behind successful jet launch in these events? This has been a theoretical challenge for decades, and despite progress in understanding the propagation of jets once they are launched (see for example work on the afterglow of GRB170817A, Troja et al., 2019), their formation mechanism looks set to remain an active area of research for many years to come.

As we go forward into the next decade, new theoretical work coupled with observations across the electromagnetic spectrum and beyond will bring answers to these questions, and pose many more. In the 50 years since their discovery, our understanding of the GRB phenomena has gone from nothing to the large body of literature to which this thesis has contributed. We can only expect the next 50 years to be just as enlightening.



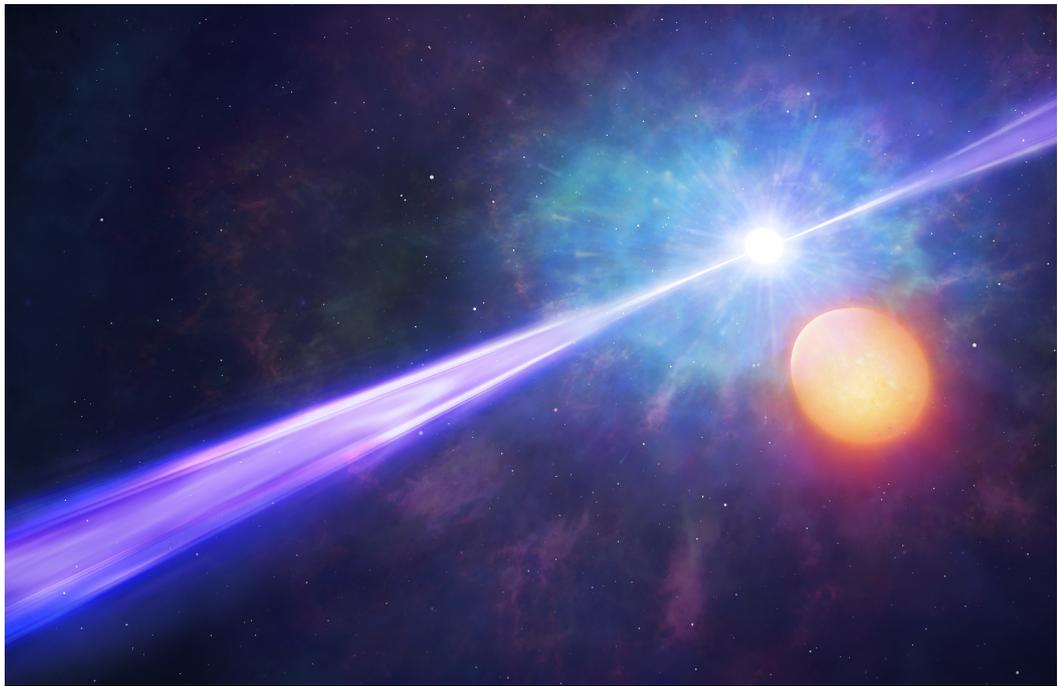


Figure 6.1: An artist's impression of a gamma-ray burst in a binary star system.  
*Credit: University of Warwick/Mark Garlick.*

## Appendix A

# IR-bright GRB hosts: additional information

In Chapter 2, a study into the nature of the IR-bright GRB host population was performed. These galaxies were detected in the *WISE* IR all-sky survey, and their properties determined through SED fitting using data from across the electromagnetic spectrum (UV to mid-IR). In this appendix, I provide the photometric data used to fit these SEDs, and image cut-outs at the location of each GRB-matched IR source in the W1, *J* and *r* bands.

### Photometric Compilation

In Table A.1, archival photometric data for the 30 GRBs with reliable *WISE* detected counterparts and detections (or limits) in archival optical photometry is compiled. One target is listed twice, since two plausible optical counterparts are detected. All magnitudes, including those for *WISE* are given in the AB magnitude system.

### Candidate Host Image Stamps

In Figure A.1 archival imaging postage stamp cut-outs in the W1, *J* and *r* bands are provided. Overlaid are the X-ray  $R_{90}$  error circles (blue, varying size) and the *WISE* source centroids (red, fixed diameter). The images are 30 arcsec on each side and are centred on the GRB location. The Figure extends over seven panels.



Table A.1: The full table of archival photometry for 30 GRB locations with reliable *WISE* detected counterparts, where optical data was available. No Galactic dust correction has been applied. If a magnitude is entered without an associated error, it is a  $2\sigma$  upper limit (all magnitudes are in the AB system). If no value is entered, then photometry in that band was unavailable. GRB 150120A has two sets of photometry, one for each component (see section 2.6.1).

GRB	FUV	$\delta$ FUV	NUV	$\delta$ NUV	u	$\delta$ u	g	$\delta$ g	r	$\delta$ r	i	$\delta$ i	z	$\delta$ z	y	$\delta$ y	J	$\delta$ J	H	$\delta$ H	K	$\delta$ K	W1	$\delta$ W1	W2	$\delta$ W2	W3	$\delta$ W3	W4	$\delta$ W4
050522	20.89	-	21.79	-	19.01	0.02	16.60	0.00	15.77	0.00	15.38	0.00	15.21	0.00	15.07	0.00	14.91	0.03	14.82	0.02	15.11	0.04	15.96	0.02	16.59	0.03	17.19	-	15.67	-
050721	20.89	-	21.79	-	-	-	18.31	0.01	17.62	0.00	17.28	0.01	17.12	0.02	17.22	0.02	16.89	0.07	16.87	0.11	17.14	0.17	17.99	0.06	19.36	0.26	16.72	-	14.59	-
050724	20.89	-	21.79	-	-	-	20.75	0.35	20.21	0.05	19.48	0.03	18.99	0.06	18.74	0.08	18.02	-	17.88	-	18.03	-	18.03	0.05	18.74	0.13	17.61	-	15.02	-
060428B	20.89	-	21.79	-	23.37	0.81	21.34	0.15	19.91	0.04	19.46	0.02	19.25	0.03	18.86	0.09	17.79	-	17.37	-	17.36	-	18.58	0.04	19.08	0.08	18.05	-	16.04	-
061002	20.89	-	21.79	-	22.60	0.53	22.27	0.06	21.67	0.14	21.13	0.12	20.81	0.33	20.40	0.22	17.44	-	17.80	-	17.53	-	18.88	0.05	19.08	0.11	17.45	-	15.87	-
070208	20.89	-	21.79	-	23.29	-	20.00	0.02	19.60	0.04	19.57	0.03	19.43	0.08	19.06	0.16	17.99	-	17.67	-	19.04	-	19.80	0.08	20.00	0.19	18.08	-	16.14	-
070724A	20.89	-	21.79	0.25	-	-	21.52	0.12	20.79	0.04	20.48	0.06	20.32	0.16	20.31	0.13	17.39	-	17.37	-	17.84	-	19.71	0.11	19.69	0.22	17.58	0.37	15.73	-
080307	20.89	-	21.79	-	23.29	-	24.30	-	20.88	0.16	21.65	0.19	23.90	-	22.30	-	17.79	-	17.77	-	17.64	-	20.32	0.21	19.97	-	17.60	-	15.70	-
080405	19.85	0.18	19.54	0.07	-	-	20.05	0.10	20.11	0.04	19.35	0.03	19.18	0.09	19.29	0.10	17.63	-	17.51	-	17.79	-	17.50	0.03	17.21	0.04	16.90	0.24	15.27	0.36
080517	20.85	0.18	20.46	0.11	-	-	18.31	0.01	17.94	0.03	17.56	0.01	17.37	0.03	17.45	0.03	17.37	0.13	17.22	0.15	17.50	0.21	17.33	0.03	17.57	0.04	15.09	0.05	13.67	0.11
080605	20.89	-	21.79	-	-	-	21.90	0.18	21.57	0.34	19.91	0.03	19.18	0.02	19.04	0.03	17.82	-	17.80	-	18.10	-	18.60	0.05	19.30	0.17	17.80	-	15.12	-
090904B	20.89	-	21.79	-	-	-	21.04	0.08	18.56	0.02	16.90	0.01	15.94	0.01	15.32	0.01	14.15	0.02	13.32	0.02	13.38	0.02	14.09	0.04	15.21	0.05	17.21	0.44	15.49	-
100206A	20.89	-	21.79	-	-	-	24.30	-	21.26	0.17	20.94	0.08	20.22	0.05	19.68	0.20	17.63	-	17.51	-	17.79	-	18.39	0.05	18.47	0.09	16.55	0.18	15.16	-
110305A	20.89	-	21.79	-	-	-	20.10	0.03	18.67	0.02	17.03	0.01	16.24	0.01	15.82	0.01	15.38	0.03	15.21	0.04	15.40	0.04	15.98	0.05	16.48	0.05	16.65	-	15.01	-
111222A	20.89	-	21.79	-	22.34	0.30	19.25	0.01	18.10	0.01	16.68	0.00	15.98	0.00	15.61	0.00	15.27	0.03	15.02	0.03	15.27	0.04	15.94	0.02	16.48	0.03	17.69	-	15.51	-
120119A	20.89	-	21.79	-	23.85	1.00	21.65	0.19	21.25	0.06	20.50	0.05	20.09	0.06	19.70	0.15	17.64	-	17.43	-	17.25	-	19.32	0.08	20.24	0.37	17.93	-	15.57	-
120612A	20.89	-	21.31	0.25	-	-	17.28	0.00	16.95	0.01	16.83	0.01	16.82	0.01	16.83	0.01	16.66	0.07	16.96	0.13	17.31	0.24	18.32	0.05	19.03	0.12	17.88	-	15.38	-
130603B	20.89	-	21.99	0.66	22.46	0.37	21.78	0.13	20.92	0.09	20.81	0.07	20.32	0.06	19.84	0.19	18.00	-	17.87	-	17.84	-	19.73	0.12	20.27	0.37	17.77	-	15.51	-
130907A	20.89	-	21.79	-	22.09	0.38	22.21	0.19	22.29	0.31	21.38	0.22	19.88	0.23	20.80	0.01	17.64	-	17.43	-	17.25	-	19.57	0.09	19.50	0.14	17.93	-	15.46	-
131018B	20.89	-	21.79	-	-	-	16.07	0.00	15.53	0.00	15.25	0.00	15.10	0.00	15.00	0.00	15.02	0.03	15.16	0.04	15.54	0.06	18.83	0.03	16.75	0.03	17.88	-	15.58	-
131122A	20.89	-	21.79	-	24.13	1.59	24.30	-	21.42	0.09	21.94	0.22	20.52	0.15	20.25	0.19	18.05	-	17.56	-	17.81	-	19.00	0.06	19.13	0.12	17.89	-	15.33	-
140331A	20.89	-	21.79	-	23.78	1.00	23.65	0.38	21.99	0.17	21.08	0.12	19.67	0.10	20.18	-	17.63	-	17.51	-	17.79	-	19.44	0.10	20.20	-	17.47	-	15.66	-
140927A	20.89	-	18.65	0.05	-	-	14.49	0.02	14.09	0.03	13.98	0.15	0.01	0.01	0.01	0.01	13.95	0.03	14.13	0.03	14.58	0.03	15.32	0.02	15.97	0.03	17.45	0.33	15.30	-
141212A	20.89	-	21.79	-	-	-	22.81	-	22.80	0.02	22.26	0.01	21.70	0.05	20.85	-	17.38	-	17.43	-	17.56	-	20.44	0.20	20.72	0.54	18.02	-	15.83	-
150101B	21.42	0.44	21.46	0.26	-	-	17.90	0.01	17.24	0.02	16.94	0.02	16.55	0.03	16.31	0.06	16.30	0.09	16.02	0.11	15.90	0.09	16.11	0.03	16.50	0.03	17.63	0.49	15.38	-
150120A	20.89	-	21.76	2.82	25.34	1.14	25.25	0.86	22.68	0.33	21.97	0.25	21.76	0.70	21.21	0.01	18.05	-	17.56	-	17.81	-	19.57	0.10	20.07	0.31	17.62	-	15.31	-
150120A	20.89	-	21.76	2.82	25.59	0.87	22.81	0.19	21.95	0.15	21.75	0.18	20.53	0.23	20.80	0.01	18.05	-	17.56	-	17.81	-	19.57	0.10	20.07	0.31	17.62	-	15.31	-
160703A	20.89	-	21.79	-	-	-	21.19	0.09	19.61	0.03	19.11	0.03	18.77	0.02	18.71	0.04	17.89	-	18.63	-	18.97	-	19.49	0.07	21.03	0.50	18.28	-	15.68	-
161010A	20.89	-	21.79	-	-	-	16.39	0.00	14.90	0.01	14.18	0.02	13.70	0.00	13.43	0.01	12.94	0.03	12.55	0.03	12.78	0.03	13.43	0.03	14.27	0.02	16.49	-	15.45	-
161108A	20.89	-	22.36	0.48	24.19	0.77	23.46	0.28	22.70	0.20	22.18	0.20	21.90	0.59	22.09	-	18.08	-	17.71	-	18.48	-	19.25	0.08	19.42	0.18	17.47	-	15.55	-
161214A	20.89	-	21.79	-	22.48	0.29	19.88	0.02	19.10	0.01	18.79	0.01	18.62	0.01	18.52	0.03	17.81	-	17.64	-	17.63	-	19.46	0.11	19.82	0.29	17.03	-	15.48	-

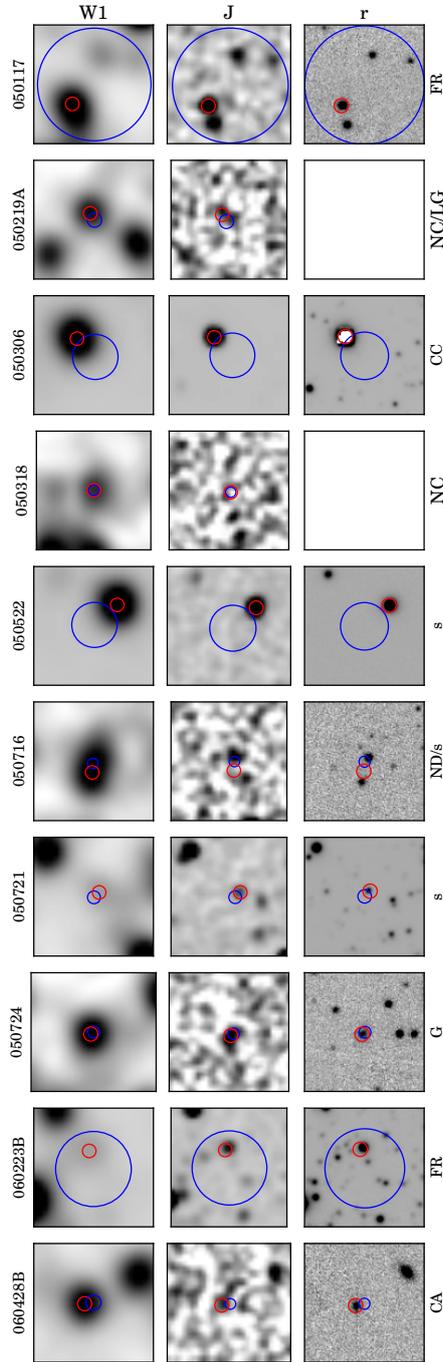


Figure A.1: Archival imaging in the W1,  $J$  and  $r$  bands (from top to bottom of each column). Overlaid are the X-ray  $R_{90}$  error circles (blue, varying size) and the *WISEc* source centroids (red, fixed diameter). The images are 30 arcsec on each side and are centred on the GRB location. The classification of each object, as defined in table 2.1 is shown at the bottom of each column. This figure extends over seven panels, the first is shown here.



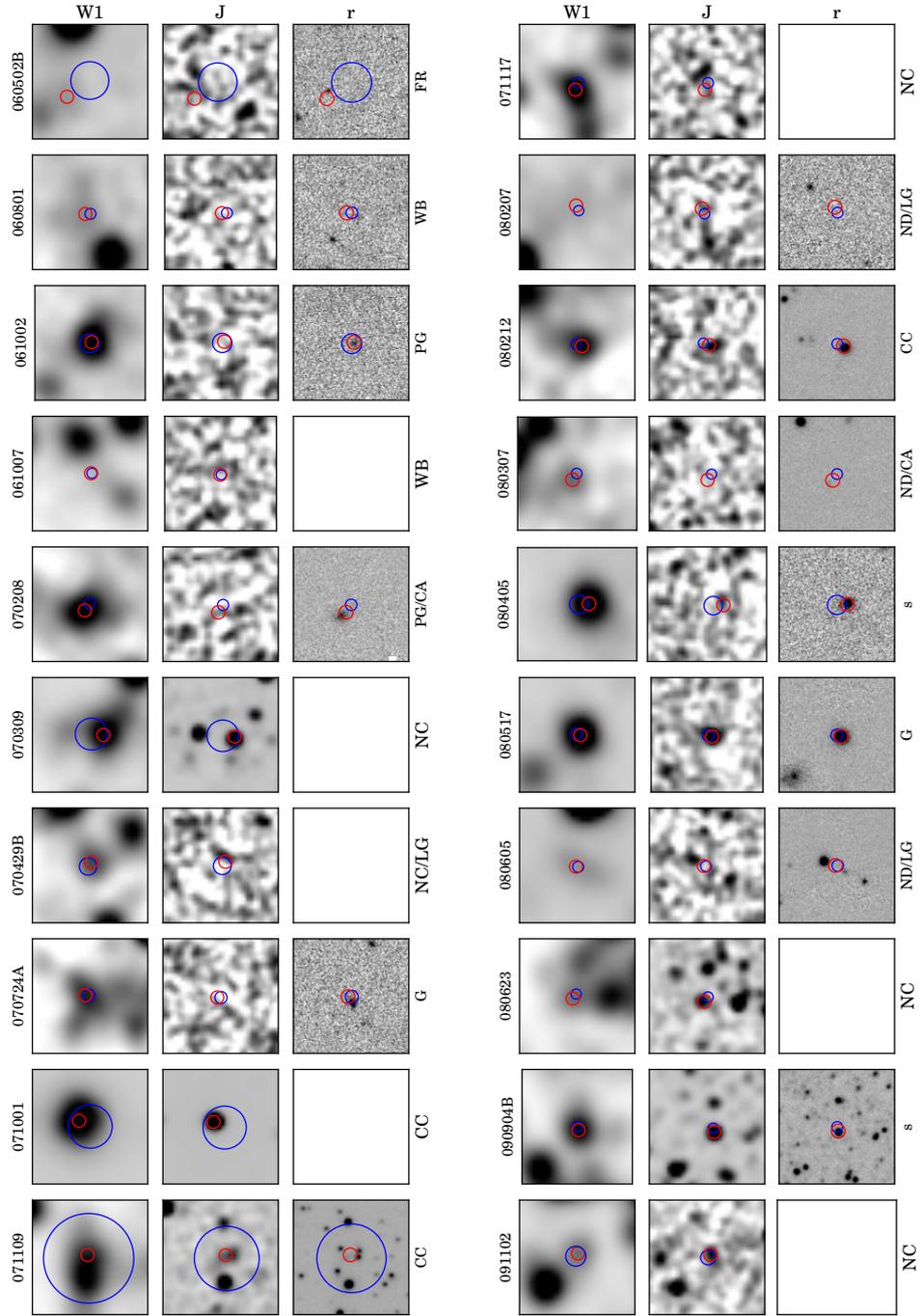


Figure A.1 continued (panels 2 and 3).

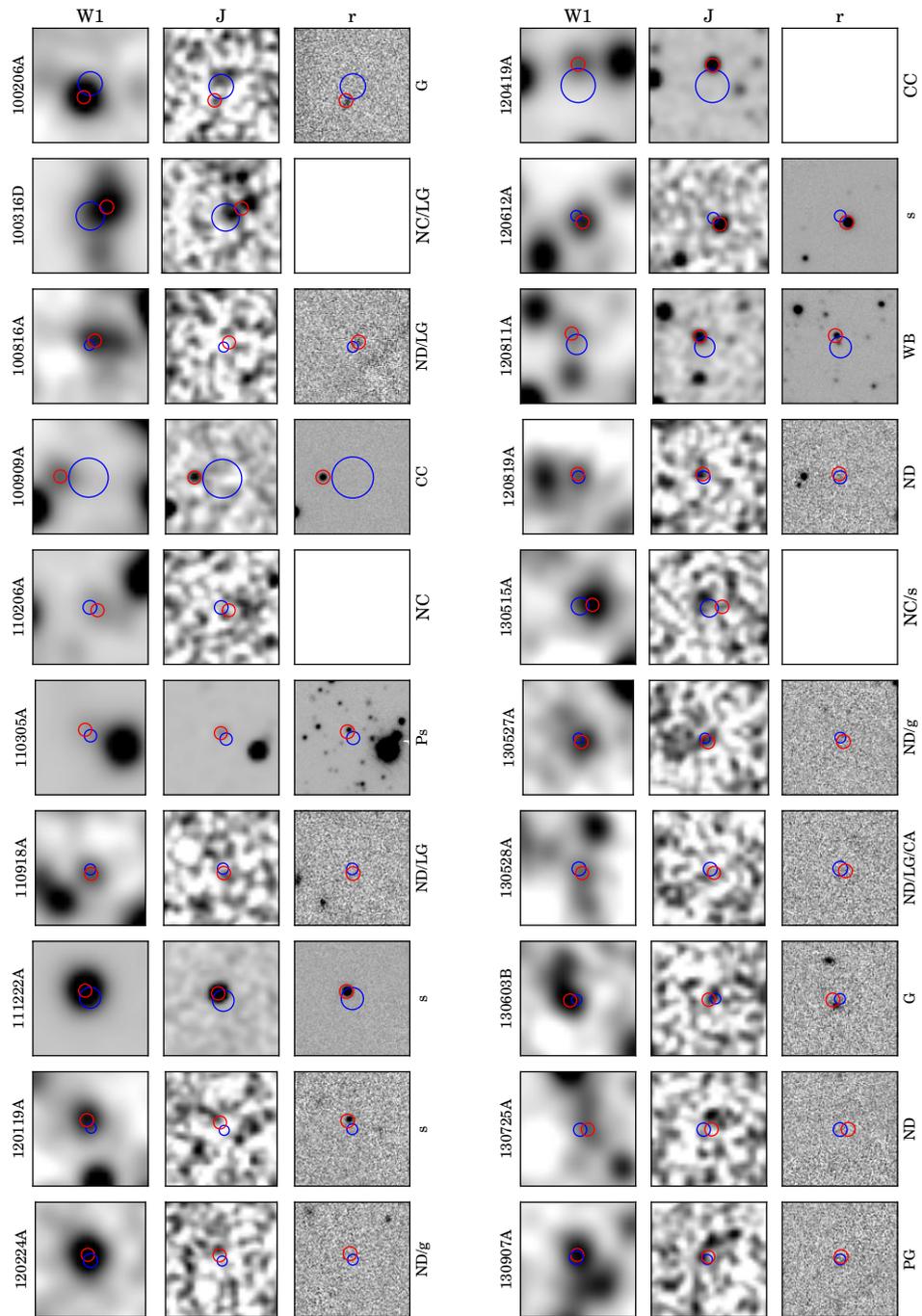
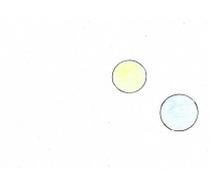


Figure A.1 continued (panels 4 and 5).



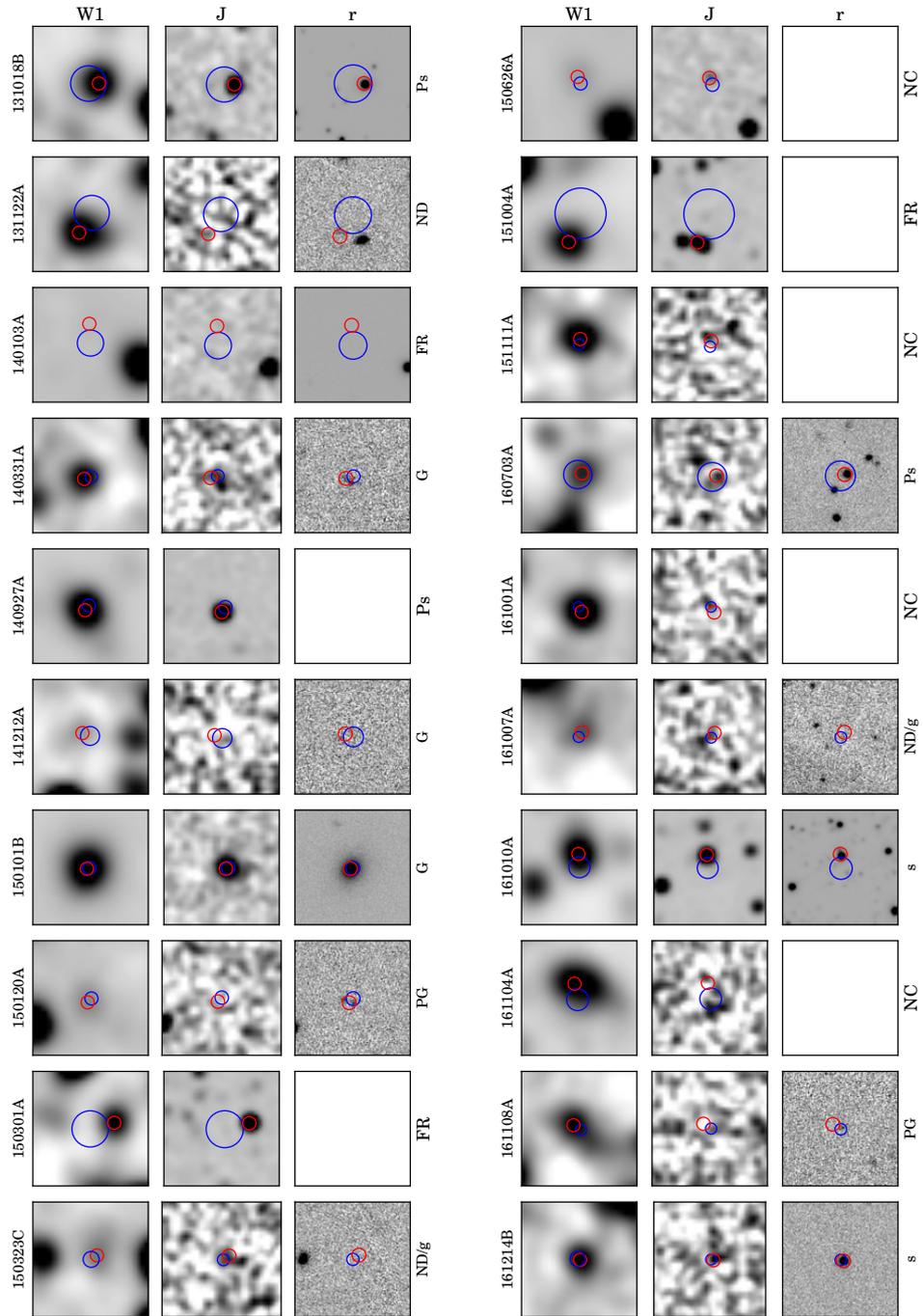


Figure A.1 continued (panels 6 and 7).

## Appendix B

# CXO and HST Dark GRBs: additional information

In Chapter 3, I perform a morphological investigation of a sample of dark GRB host galaxies, identified using  $\sim$  arcsec resolution X-ray afterglow imaging with *CXO* and deep *HST* imaging in the F606W and F160W bands. The morphological properties of these galaxies were measured in terms of the concentration  $C$  and asymmetry  $A$  parameters. The uncertainties on these parameters were calculated from the distribution of measured  $A$  and enclosed flux radii following 300 pixel re-samplings (where each pixel in the image is varied by according to their uncertainties) as described in section 3.3.4. This appendix provides the parameter distributions that result from this process, in Figures B.1 and B.2. These distributions were used to determine the uncertainties shown in Figures 3.6 and 3.7. Where the original image measurement lies outside the  $1\sigma$  re-sampled range, I use the original measurement as the upper or lower limit instead. The enclosed flux radii are provided here, as these are directly measured, but note that concentration is defined as  $C = \log_{10}(R_{80}/R_{20})$ , where  $R_{80}$  and  $R_{20}$  are the radii containing 80 and 20 per cent of the galaxy flux, respectively.



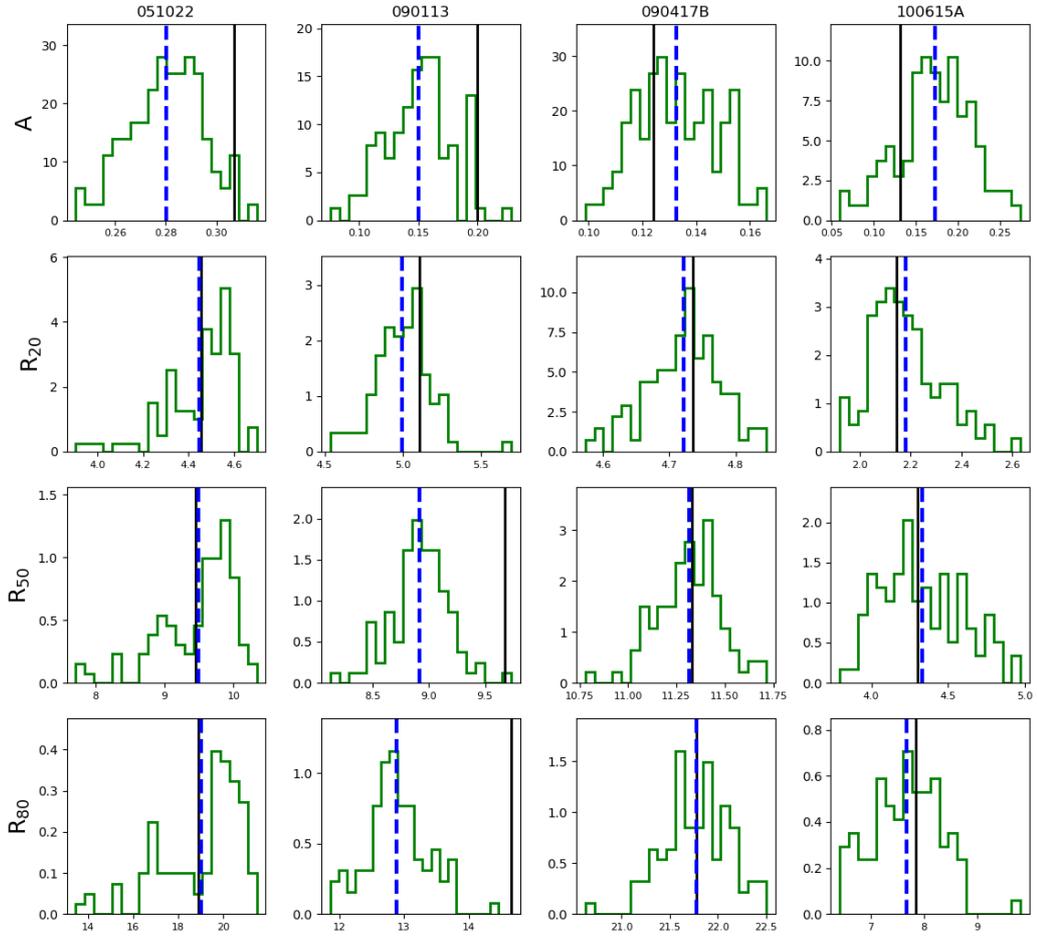


Figure B.1: The  $y$  axis is the normalised frequency that the  $A$  and enclosed flux radii parameters are measured, the  $x$  axes are the values of these parameters. This figure is for the parameters as measured in the F606W band. The vertical black lines are the morphological parameters as measured from the original drizzled image, the dashed blue lines are the medians of re-sampled distributions. The figure continues onto a second panel below.

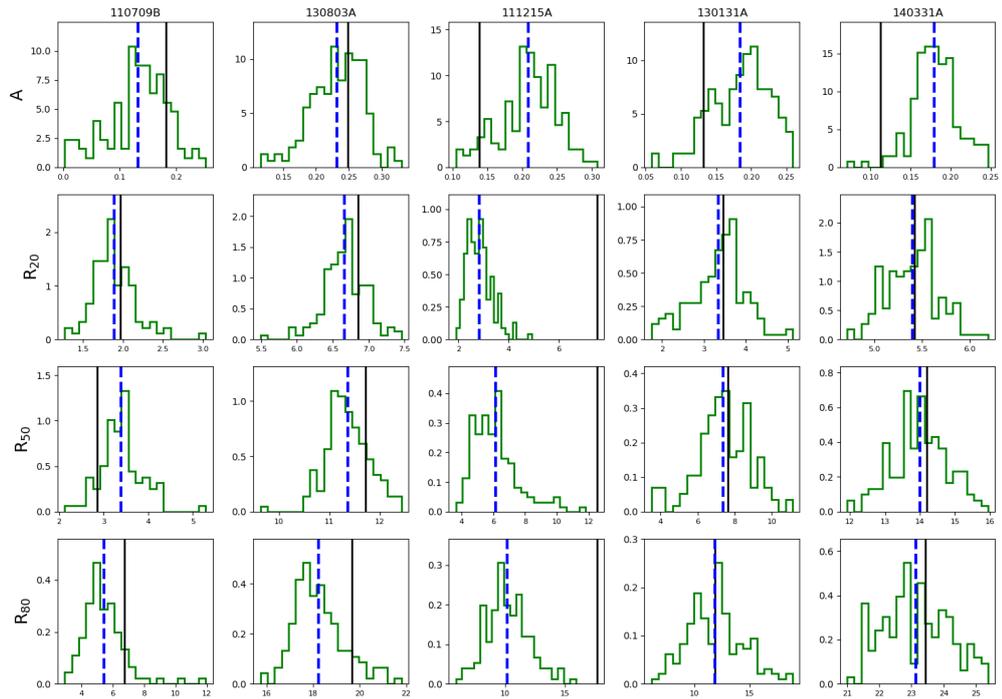


Figure B.1 continued.

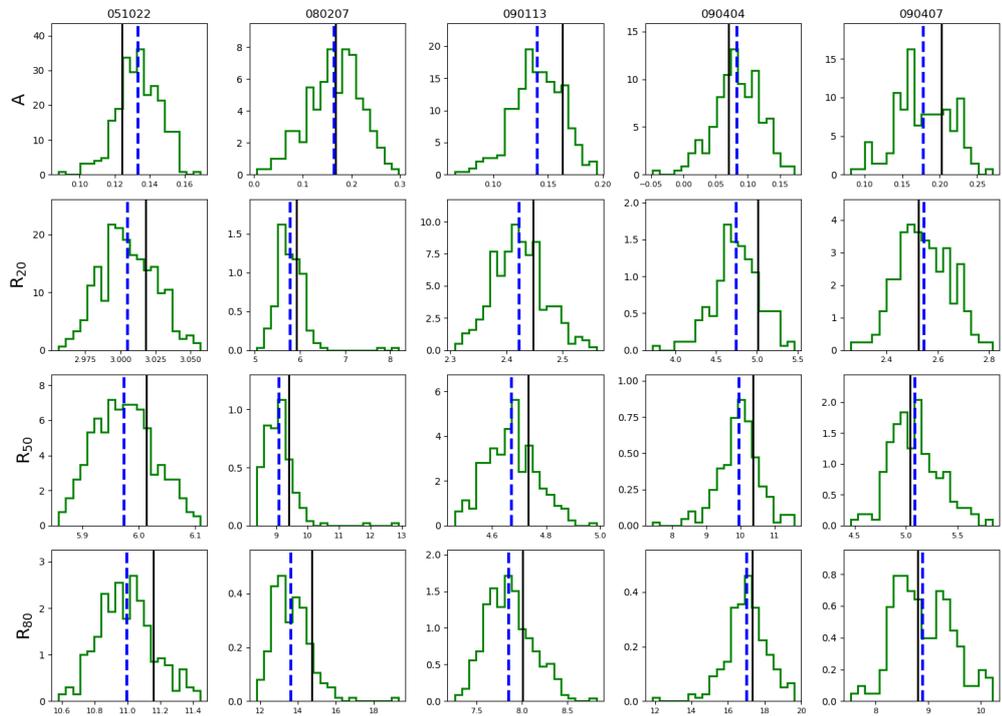


Figure B.2: As in Figure B.1, but for the parameters as measured in the F160W band. The figure continues onto 3 further panels below.



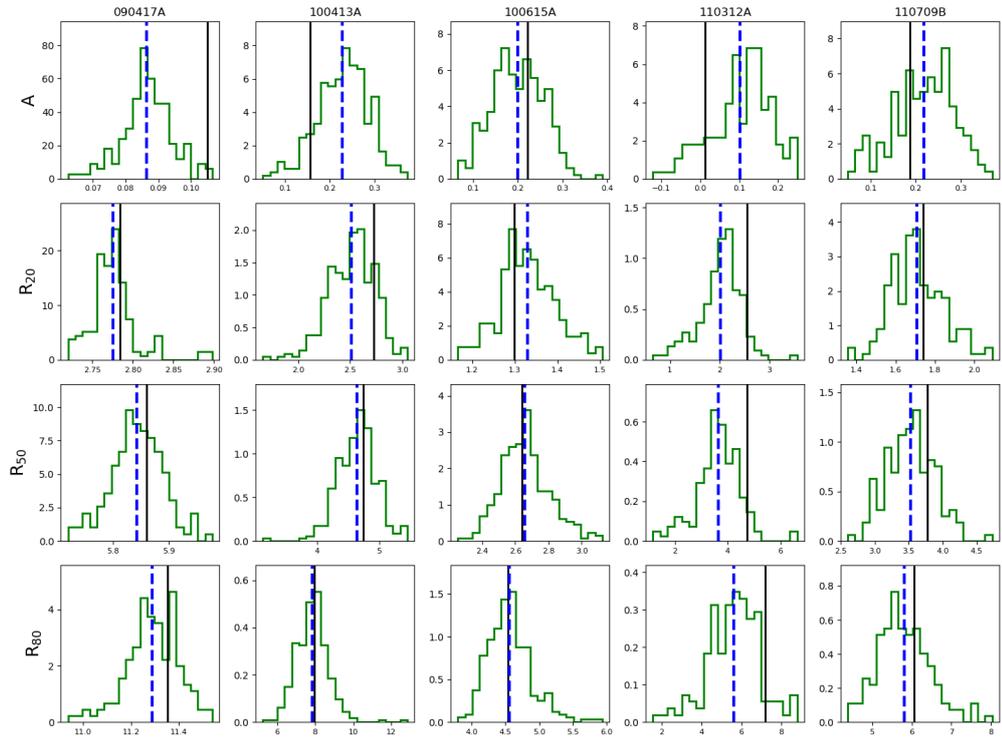


Figure B.2 continued (panel 2).

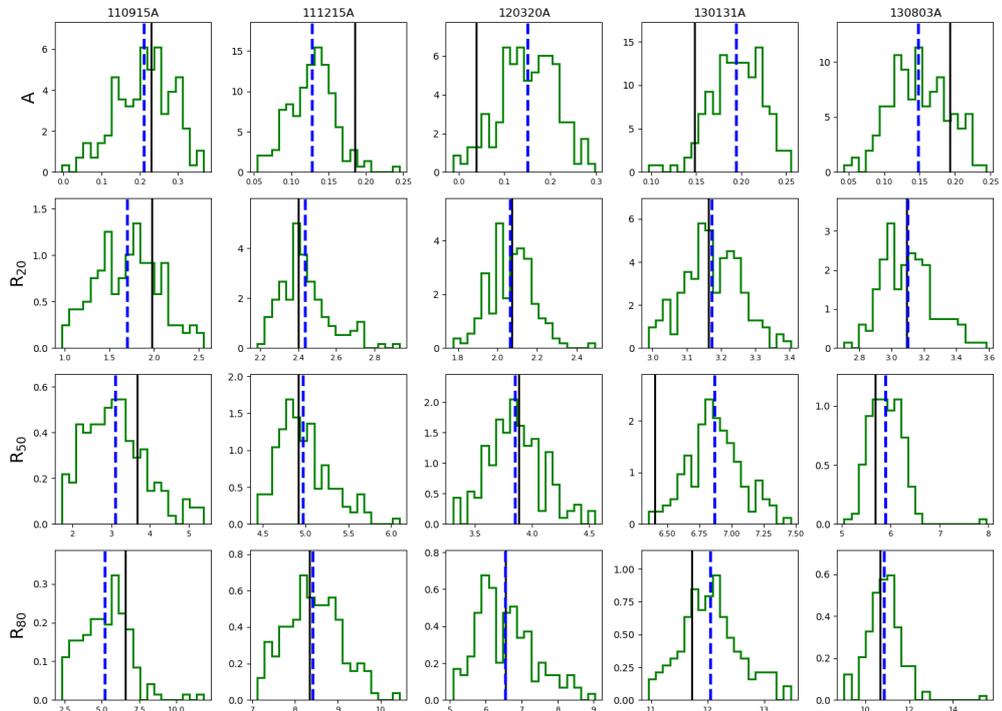


Figure B.2 continued (panel 3).

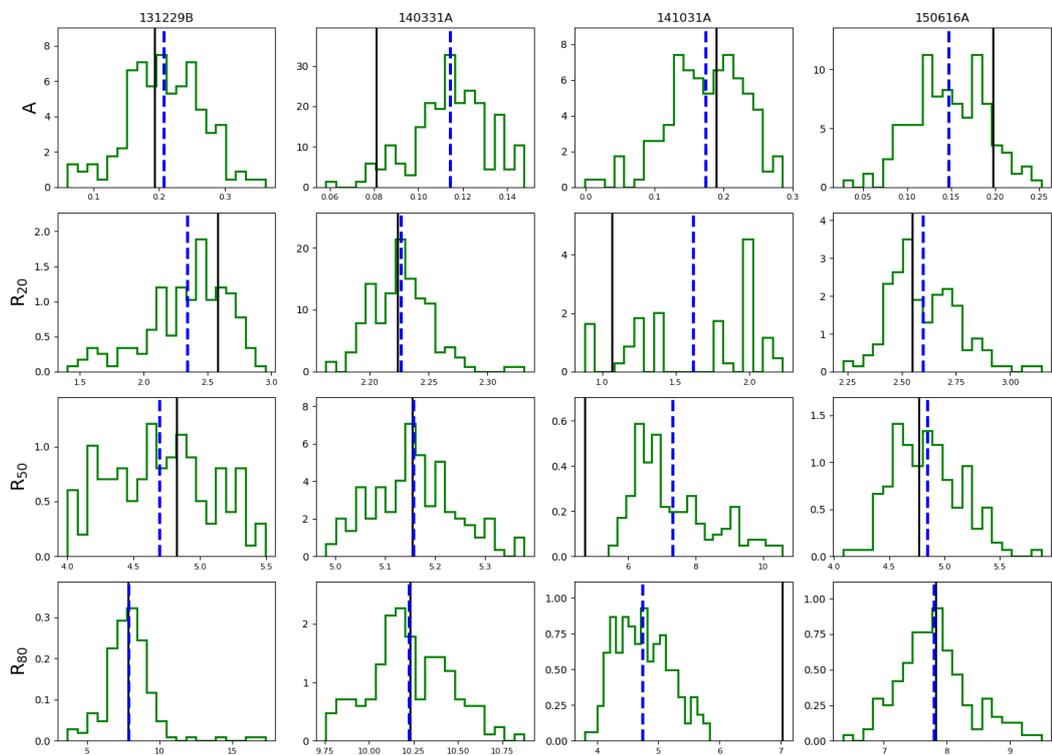


Figure B.2 continued (panel 4).



# Appendix C

## Data and funding acknowledgements

AAC has been supported by PhD studentship 1763016 from the UK Science and Technology Facilities Council (STFC). AAC also thanks the William Edwards Educational Charity.

ERS, AJL and PJW have been supported by STFC consolidated grant ST/P000495/1. AJL acknowledges support from the European Research Council.

I acknowledge the use of Ned Wright and James Schombert's online and Python-based cosmology calculators (Wright, 2006). IRAF is distributed by the National Optical Astronomy Observatory, which is operated by the Association of Universities for Research in Astronomy (AURA) under a cooperative agreement with the National Science Foundation. This research has made use of the SVO Filter Profile Service (<http://svo2.cab.inta-csic.es/theory/fps/>) supported from the Spanish MINECO through grant AyA2014-55216. I acknowledge the use of Patricio Cubillos' incredibly useful BIBMANAGER software.

### Chapter 2

*Collaborators on this chapter:* E. R. Stanway (data, comments, analysis), A. J. Levan (comments), L. J. M. Davies (data), C. R. Angus (data) and S. M. L. Greis (data)

CRA acknowledges receipt of a studentship from the Midlands Physics Alliance. SMLG is funded by a research studentship from the UK STFC. This paper contains original results based on observations taken at WHT and ATCA. The Australia Telescope Compact Array is part of the Australia Telescope National Facility which

is funded by the Australian Government for operation as a National Facility managed by CSIRO. The William Herschel Telescope is operated on the island of La Palma by the Isaac Newton Group of Telescopes in the Spanish Observatorio del Roque de los Muchachos of the Instituto de Astrofísica de Canarias. This Chapter makes use of archival data. The PanSTARRS Surveys and the PS1 public science archive have been made possible through contributions by the Institute for Astronomy, the University of Hawaii, the Pan-STARRS Project Office, the Max-Planck Society and its participating institutes. Funding for SDSS-III has been provided by the Alfred P. Sloan Foundation, the Participating Institutions, the National Science Foundation, and the U.S. Department of Energy Office of Science. The SDSS-III web site is <http://www.sdss3.org/>. SDSS-III is managed by the Astrophysical Research Consortium for the Participating Institutions of the SDSS-III Collaboration. I use observations made with the NASA Galaxy Evolution Explorer. GALEX is operated for NASA by the California Institute of Technology under NASA contract NAS5-98034. This Chapter makes use of data products from the Wide-field Infrared Survey Explorer, which is a joint project of the University of California, Los Angeles, and the Jet Propulsion Laboratory/California Institute of Technology, funded by the National Aeronautics and Space Administration. I acknowledge the use of public data from the Swift data archive. This research has made use of the APASS database, located at the AAVSO web site. Funding for APASS has been provided by the Robert Martin Ayers Sciences Fund. This Chapter makes use of data products from the Two Micron All Sky Survey, which is a joint project of the University of Massachusetts and the Infrared Processing and Analysis Center/California Institute of Technology, funded by the National Aeronautics and Space Administration and the National Science Foundation. This research has made use of the NASA/ IPAC Infrared Science Archive, which is operated by the Jet Propulsion Laboratory, California Institute of Technology, under contract with the National Aeronautics and Space Administration. Based on observations collected at the European Southern Observatory under ESO program 096.D-0260(A).

I thank the anonymous referee for their constructive feedback on the paper which became the basis for this Chapter.

### **Chapter 3**

*Collaborators on this chapter:* A. J. Levan (data, comments), E. R. Stanway (comments), J. D. Lyman (comments), A. S. Fruchter (comments), P. Jakobsson (comments), P. O'Brien (comments), D. A. Perley (comments), N. R. Tanvir (comments), P. J. Wheatley (comments) and K. Wiersema (comments)



Based on observations made with the NASA/ESA Hubble Space Telescope, obtained from the data archive at the Space Telescope Science Institute. STScI is operated by the Association of Universities for Research in Astronomy, Inc. under NASA contract NAS 5-26555. These observations are associated with programs GO 11343, 11840, 12378, 12764, 13117 and 13949 (Levan). Based on observations collected at the European Southern Observatory under ESO programme 095.B-0811(C). The scientific results reported in this article are based on observations made by the Chandra X-ray Observatory. This research has made use of software provided by the Chandra X-ray Center (CXC) in the application of the CIAO package. The Pan-STARRS1 Surveys (PS1) and the PS1 public science archive have been made possible through contributions by the Institute for Astronomy, the University of Hawaii, the Pan-STARRS Project Office, the Max-Planck Society and its participating institutes, the Max Planck Institute for Astronomy, Heidelberg and the Max Planck Institute for Extraterrestrial Physics, Garching, The Johns Hopkins University, Durham University, the University of Edinburgh, the Queens University Belfast, the Harvard Smithsonian Center for Astrophysics, the Las Cumbres Observatory Global Telescope Network Incorporated, the National Central University of Taiwan, the Space Telescope Science Institute, the National Aeronautics and Space Administration under Grant No. NNX08AR22G issued through the Planetary Science Division of the NASA Science Mission Directorate, the National Science Foundation Grant No. AST-1238877, the University of Maryland, Eotvos Lorand University (ELTE), the Los Alamos National Laboratory, and the Gordon and Betty Moore Foundation.

Finally, I thank the anonymous referee for their valuable feedback on the paper which became the basis for this Chapter.

#### **Chapter 4**

*Collaborators on this chapter:* A. J. Levan (data, comments), E. R. Stanway (comments), K. Wiersema (comments, analysis), E. Berger (comments), J. S. Bloom (comments), S. B. Cenko (comments), B. E. Cobb (comments), A. Cucchiara (comments), A. S. Fruchter (comments), B. P. Gompertz (comments), J. Hjorth (comments), P. Jakobsson (comments), J. D. Lyman (comments), P. O'Brien (comments), D. A. Perley (comments), N. R. Tanvir (data, comments), and P. J. Wheatley (comments)

Based on observations obtained at the Gemini Observatory, acquired through the Gemini Observatory Archive and processed using the Gemini IRAF package. The Gemini Observatory is operated by the Association of Universities for Research in Astronomy, Inc., under a cooperative agreement with the NSF on behalf of the

Gemini partnership: the National Science Foundation (USA), National Research Council (Canada), CONICYT (Chile), Ministerio de Ciencia, Tecnologia e Innovacion Productiva (Argentina), Ministerio da Ciencia, Tecnologia e Inovacao (Brazil), and Korea Astronomy and Space Science Institute (Republic of Korea). Based on observations made with the NASA/ESA Hubble Space Telescope, obtained from the data archive at the Space Telescope Science Institute. STScI is operated by the Association of Universities for Research in Astronomy, Inc. under NASA contract NAS 5-26555. This work made use of data supplied by the UK Swift Science Data Centre at the University of Leicester. The UKIDSS project is defined in Lawrence et al. (2007). UKIDSS uses the UKIRT Wide Field Camera Casali et al. (WFCAM; 2007). The photometric system is described in Hewett et al. (2006), and the calibration is described in Hodgkin et al. (2009). The pipeline processing and science archive are described in Hambly et al. (2008). The Pan-STARRS1 Surveys (PS1) and the PS1 public science archive have been made possible through contributions by the Institute for Astronomy, the University of Hawaii, the Pan-STARRS Project Office, the Max-Planck Society and its participating institutes, the Max Planck Institute for Astronomy, Heidelberg and the Max Planck Institute for Extraterrestrial Physics, Garching, The Johns Hopkins University, Durham University, the University of Edinburgh, the Queens University Belfast, the Harvard-Smithsonian Center for Astrophysics, the Las Cumbres Observatory Global Telescope Network Incorporated, the National Central University of Taiwan, the Space Telescope Science Institute, the National Aeronautics and Space Administration under Grant No. NNX08AR22G issued through the Planetary Science Division of the NASA Science Mission Directorate, the National Science Foundation Grant No. AST-1238877, the University of Maryland, Eotvos Lorand University (ELTE), the Los Alamos National Laboratory, and the Gordon and Betty Moore Foundation. IRAF is distributed by the National Optical Astronomy Observatory, which is operated by the Association of Universities for Research in Astronomy (AURA) under cooperative agreement with the National Science Foundation. I acknowledge the use of Jochen Greiners GRB website (<http://www.mpe.mpg.de/jcg/grbgen>).

I thank the referee Bruce Gendre for their useful feedback on the paper which formed the basis of this Chapter.



## Chapter 5

*Collaborators on this chapter:* E. R. Stanway (data, comments, analysis) and J. J. Eldridge (data, comments)

JJE acknowledges support from the University of Auckland and also the Royal Society Te Apārangi of New Zealand under Marsden Fund grant UOA1818. I acknowledge use of Python algorithms including the CORNER module (Foreman-Mackey, 2016), and the excellent Python-based introduction to Bayesianism by VanderPlas (2014). I thank the anonymous referee for their feedback on the paper which became the basis for this Chapter.

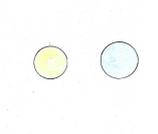
# Bibliography

- Abadie J. et al., 2010. *ApJ*, 715(2):1453–1461.
- Abbott B.P. et al., 2016. *Phys. Rev. Lett.*, 116(6):061102.
- Abbott B.P. et al., 2017a. *Phys. Rev. Lett.*, 119(16):161101.
- Abbott B.P. et al., 2017b. *ApJ*, 848(2):L12.
- Abbott B.P. et al., 2018a. *Phys. Rev. Lett.*, 121(16):161101.
- Abbott B.P. et al., 2018b. *Living Reviews in Relativity*, 21(1):3.
- Abbott B.P. et al., 2019. *Physical Review X*, 9(3):031040.
- Abdalla H. et al., 2019. *Nature*, 575(7783):464–467.
- Abraham R.G. et al., 1996. *MNRAS*, 279:L47–L52.
- Acciarri R. et al., 2016. *arXiv e-prints*, arXiv:1601.05471.
- Ackley K. et al., 2020. *arXiv e-prints*, arXiv:2002.01950.
- Actis M. et al., 2011. *Experimental Astronomy*, 32(3):193–316.
- Adams N.J. et al., 2019. *arXiv e-prints*, arXiv:1912.01626.
- Adams S.M. et al., 2017. *MNRAS*, 468:4968–4981.
- Afonso P. et al., 2011. *A&A*, 526:A154.
- Ajello M. et al., 2019. *ApJ*, 878(1):52.
- Alam S. et al., 2015. *ApJS*, 219:12.
- Aldering G., Humphreys R.M., and Richmond M., 1994. *AJ*, 107:662.
- Allende Prieto C., Lambert D.L., and Asplund M., 2001. *ApJ*, 556(1):L63–L66.



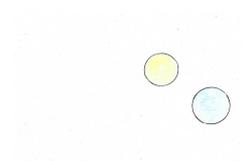
- Almeida L.A. et al., 2015. *ApJ*, 812(2):102.
- Altmann M. et al., 2017. *A&A*, 600:L4.
- Amati L., 2006. *MNRAS*, 372:233–245.
- Amati L. et al., 2002. *A&A*, 390:81–89.
- Amati L. et al., 2018. *Advances in Space Research*, 62(1):191–244.
- Anchordoqui L.A., Meckmann C., and Soriano J.F., 2019. *arXiv e-prints*, arXiv:1910.07311.
- Angus C.R. et al., 2016. *MNRAS*, 458(1):84–104.
- Angus C.R. et al., 2019. *MNRAS*, 487(2):2215–2241.
- Arabsalmani M. et al., 2018. *MNRAS*, 476(2):2332–2338.
- Arabsalmani M. et al., 2019. *MNRAS*, 485(4):5411–5422.
- Arnouts S. et al., 1999. *MNRAS*, 310(2):540–556.
- Asplund M. et al., 2009. *ARA&A*, 47(1):481–522.
- Atwood W.B. et al., 2009. *ApJ*, 697(2):1071–1102.
- Auchettl K. et al., 2019. *ApJ*, 871(1):64.
- Avni Y., 1976. *ApJ*, 210:642–646.
- Babbedge T.S.R. et al., 2006. *MNRAS*, 370:1159–1180.
- Baldry I.K. et al., 2006. *MNRAS*, 373(2):469–483.
- Band D. et al., 1993. *ApJ*, 413:281–292.
- Bannister K.W. et al., 2019. *Science*, 365(6453):565–570.
- Barnes J. et al., 2018. *ApJ*, 860(1):38.
- Barthelmy S.D. et al., 2005. *Space Sci. Rev.*, 120:143–164.
- Becker R.H., White R.L., and Helfand D.J., 1994. In D.R. Crabtree, R.J. Hanisch, and J. Barnes, editors, *Astronomical Data Analysis Software and Systems III*, volume 61 of *ASP Conference Series*, 165.
- Behroozi P.S., Wechsler R.H., and Conroy C., 2013. *ApJ*, 770(1):57.

- Bellm E.C. et al., 2019. *PASP*, 131(995):018002.
- Berger E., 2010. *ApJ*, 722(2):1946–1961.
- Berger E., 2014. *ARA&A*, 52:43–105.
- Berger E., Fong W., and Chornock R., 2013. *ApJ*, 774(2):L23.
- Berger E. and Fox D.B., 2009. *GRB Coordinates Network, Circular Service, No. 9156*, 9156.
- Berger E. et al., 2005. *Nature*, 438:988–990.
- Berger E. et al., 2007. *ApJ*, 665:102–106.
- Berger E. et al., 2009. *ApJ*, 704:877–882.
- Bershady M.A., Jangren A., and Conselice C.J., 2000. *AJ*, 119:2645–2663.
- Bertin E. and Arnouts S., 1996. *A&AS*, 117:393–404.
- Bertin E. et al., 2002. In D.A. Bohlender, D. Durand, and T.H. Handley, editors, *Astronomical Data Analysis Software and Systems XI*, volume 281 of *Astronomical Society of the Pacific Conference Series*, 228.
- Best W.M.J. et al., 2013. *ApJ*, 777:84.
- Bestenlehner J.M. et al., 2011. *A&A*, 530:L14.
- Bhandari S. et al., 2018. *MNRAS*, 475(2):1427–1446.
- Birney D.S., Gonzalez G., and Oesper D., 2006. *Observational Astronomy*. Cambridge University Press, 2 edition. ISBN 0521853702. Pp. 322.
- Blanchard P.K., Berger E., and Fong W.f., 2016. *ApJ*, 817:144.
- Blandford R.D. and Znajek R.L., 1977. *MNRAS*, 179:433–456.
- Bloemen S. et al., 2015. *The BlackGEM Array: Searching for Gravitational Wave Source Counterparts to Study Ultra-Compact Binaries*, volume 496 of *Conference Series*, 254. Astronomical Society of the Pacific.
- Bloom J.S., Djorgovski S.G., and Kulkarni S.R., 2001. *ApJ*, 554:678–683.
- Bloom J.S., Kulkarni S.R., and Djorgovski S.G., 2002. *AJ*, 123:1111–1148.
- Bloom J.S., Starr D., and Perley D.A., 2008. *GRB Coordinates Network*, 7434:1.



- Bloom J.S. et al., 1998. *ApJ*, 507(1):L25–L28.
- Bloom J.S. et al., 1999. *Nature*, 401(6752):453–456.
- Boella G. et al., 1997. *A&AS*, 122:299–307.
- Bolmer J. et al., 2019. *A&A*, 623:A43.
- Bolzonella M., Miralles J.M., and Pelló R., 2000. *A&A*, 363:476–492.
- Booth R.S. et al., 2009. *arXiv e-prints*, arXiv:0910.2935.
- Bouwens R.J. et al., 2012. *ApJ*, 752(1):L5.
- Bouwens R.J. et al., 2014. *ApJ*, 795(2):126.
- Bouwens R.J. et al., 2015. *ApJ*, 803:34.
- Briggs M.S., 1993. *ApJ*, 407:126.
- Brott I. et al., 2011. *A&A*, 530:A115.
- Brown G.C. et al., 2017. *MNRAS*, 472(4):4469–4479.
- Bruzual G. and Charlot S., 2003. *MNRAS*, 344(4):1000–1028.
- Burbidge E.M. et al., 1957. *Reviews of Modern Physics*, 29(4):547–650.
- Burrows D.N. et al., 2004. In K.A. Flanagan and O.H.W. Siegmund, editors, *X-Ray and Gamma-Ray Instrumentation for Astronomy XIII*, volume 5165 of *Proc. SPIE*, 201–216.
- Butler N. et al., 2014. *GRB Coordinates Network, Circular Service, No. 16076, #1 (2014)*, 16076.
- Butler N.R. et al., 2007. *ApJ*, 671:656–677.
- Caito L. et al., 2009. *A&A*, 498(2):501–507.
- Callingham J.R. et al., 2019. *Nature Astronomy*, 3:82–87.
- Campana S., Evans P.A., and Holland S.T., 2010. *GRB Coordinates Network, Circular Service, No. 10588, #1 (2010)*, 10588.
- Cano Z. et al., 2013. *GRB Coordinates Network, Circular Service, No. 14710, #1 (2013)*, 14710.

- Cano Z. et al., 2017. *Advances in Astronomy*, 2017:8929054.
- Cantiello M. et al., 2007. *A&A*, 465(2):L29–L33.
- Casertano S. et al., 2000. *AJ*, 120:2747–2824.
- Castro-Tirado A.J. et al., 2007. *A&A*, 475(1):101–107.
- Castro-Tirado A.J. et al., 2013. *GRB Coordinates Network, Circular Service, No. 14796*, 14796.
- Cavallo G. and Rees M.J., 1978. *MNRAS*, 183:359–365.
- Cenko S.B. et al., 2006. *GRB Coordinates Network, Circular Service, No. 5155*, 5155.
- Cenko S.B. et al., 2008. *ArXiv e-prints*, arXiv:0802.0874.
- Cenko S.B. et al., 2009. *ApJ*, 693:1484–1493.
- Cenko S.B. et al., 2012. *ApJ*, 753(1):77.
- Chabrier G., 2003. *PASP*, 115(809):763–795.
- Chambers K.C. et al., 2016. *ArXiv e-prints*, arXiv:1612.05560.
- Champion D.J. et al., 2016. *MNRAS*, 460(1):L30–L34.
- Chandrasekhar S., 1931. *ApJ*, 74:81.
- Charlot S. and Fall S.M., 2000. *ApJ*, 539:718–731.
- Chatterjee S. et al., 2017. *Nature*, 541(7635):58–61.
- Chen H.W., 2012. *MNRAS*, 419:3039–3047.
- Cherenkov Telescope Array Consortium et al., 2019. *Science with the Cherenkov Telescope Array*. World Scientific Publishing.
- Chester M.M. and Markwardt C.B., 2012. *GRB Coordinates Network, Circular Service, No. 13083, #1 (2012)*, 13083.
- Chevalier R.A. and Li Z.Y., 1999. *ApJ*, 520(1):L29–L32.
- Chevallard J. and Charlot S., 2016. *MNRAS*, 462(2):1415–1443.
- CHIME/FRB Collaboration et al., 2018. *ApJ*, 863:48.



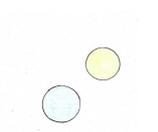
- CHIME/FRB Collaboration et al., 2019. *arXiv e-prints*, arXiv:1908.03507.
- Chincarini G. et al., 2007. *ApJ*, 671(2):1903–1920.
- Chornock R. and Fong W., 2015. *GRB Coordinates Network, Circular Service, No. 17358*, 17358.
- Chornock R., Fong W., and Fox D.B., 2014a. *GRB Coordinates Network, Circular Service, No. 17177*, 17177.
- Chornock R., Fox D.B., and Berger E., 2014b. *GRB Coordinates Network, Circular Service, No. 16269*, 16269.
- Chornock R. et al., 2014c. *arXiv e-prints*, arXiv:1405.7400.
- Chrimes A.A., Stanway E.R., and Eldridge J.J., 2020. *MNRAS*, 491(3):3479–3495.
- Chrimes A.A. et al., 2018. *MNRAS*, 478:2–27.
- Chrimes A.A. et al., 2019a. *MNRAS*, 486(3):3105–3117.
- Chrimes A.A. et al., 2019b. *MNRAS*, 488(1):902–909.
- Christensen L., Hjorth J., and Gorosabel J., 2004. *A&A*, 425:913–926.
- Christensen L. et al., 2008. *A&A*, 490(1):45–59.
- Cobb B.E., Cenko S.B., and Bloom J.S., 2010. *GRB Coordinates Network, Circular Service, No. 10365*, 10365.
- Condon J.J. et al., 1998. *AJ*, 115:1693–1716.
- Conroy C., 2013. *ARA&A*, 51(1):393–455.
- Conselice C.J., 2003. *ApJS*, 147:1–28.
- Conselice C.J., Bershadsky M.A., and Gallagher III J.S., 2000a. *A&A*, 354:L21–L24.
- Conselice C.J., Bershadsky M.A., and Jangren A., 2000b. *ApJ*, 529:886–910.
- Conselice C.J., Chapman S.C., and Windhorst R.A., 2003. *ApJ*, 596:L5–L8.
- Conselice C.J. et al., 2005. *ApJ*, 633:29–40.
- Cordes J.M. and Chatterjee S., 2019. *ARA&A*, 57:417–465.
- Corre D. et al., 2018. *A&A*, 617:A141.

- Costa E. et al., 1997. *Nature*, 387(6635):783–785.
- Croton D.J. et al., 2006. *MNRAS*, 365(1):11–28.
- Crowther P. and Smartt S., 2007. *Astronomy and Geophysics*, 48(1):1.35–1.38.
- Crowther P.A., 2007. *ARA&A*, 45(1):177–219.
- Crowther P.A. et al., 2016. *MNRAS*, 458(1):624–659.
- Csabai I. et al., 2007. *Astronomische Nachrichten*, 328(8):852.
- Cucchiara A. et al., 2007. *GRB Coordinates Network, Circular Service, No. 6083*, 6083.
- Cucchiara A. et al., 2010. *GRB Coordinates Network, Circular Service, No. 10374, #1 (2010)*, 10374.
- Cucchiara A. et al., 2011. *ApJ*, 736:7.
- Cucchiara A. et al., 2015. *ApJ*, 804(1):51.
- da Cunha E., Charlot S., and Elbaz D., 2008. *MNRAS*, 388:1595–1617.
- da Cunha E. et al., 2015. *ApJ*, 806:110.
- Darwin G.H., 1879. *Proceedings of the Royal Society of London Series I*, 29:168–181.
- D’Avanzo P. et al., 2018. *A&A*, 613:L1.
- Davies B. and Beasor E.R., 2020. *arXiv e-prints*, arXiv:2001.06020.
- Davies L.J.M. et al., 2017. *MNRAS*, 466:2312–2324.
- de Mink S.E. and Mandel I., 2016. *MNRAS*, 460(4):3545–3553.
- de Mink S.E. et al., 2009. *A&A*, 497(1):243–253.
- de Mink S.E. et al., 2013. *ApJ*, 764(2):166.
- de Mink S.E. et al., 2014. *ApJ*, 782(1):7.
- de Naurois M., 2019. *The Astronomer’s Telegram*, 13052:1.
- de Ugarte Postigo A. et al., 2010. In N. Kawai and S. Nagataki, editors, *American Institute of Physics Conference Series*, volume 1279 of *American Institute of Physics Conference Series*, 283–286.



- de Ugarte Postigo A. et al., 2013. *GRB Coordinates Network, Circular Service, No. 15187*, 15187.
- de Ugarte Postigo A. et al., 2014. *A&A*, 563:A62.
- de Ugarte Postigo A. et al., 2016. *GRB Coordinates Network, Circular Service, No. 20150*, 20150.
- Dereli H. et al., 2017. *ApJ*, 850(2):117.
- Dermer C.D., Chiang J., and Böttcher M., 1999. *ApJ*, 513(2):656–668.
- Dessart L., 2019. *A&A*, 621:A141.
- Dessart L., O’Connor E., and Ott C.D., 2012a. *ApJ*, 754(1):76.
- Dessart L. et al., 2011. *MNRAS*, 414(4):2985–3005.
- Dessart L. et al., 2012b. *MNRAS*, 424(3):2139–2159.
- Detmers R.G. et al., 2008. *A&A*, 484(3):831–839.
- Dirac P.A.M., 1996. *General Theory of Relativity*. John Wiley & Sons.
- Draine B.T., 2000. *ApJ*, 532:273–280.
- Draine B.T., 2003. *ARA&A*, 41:241–289.
- Dressler A., 1980. *ApJ*, 236:351–365.
- Dufton P.L. et al., 2019. *A&A*, 626:A50.
- Duncan R.C. and Thompson C., 1996. In R.E. Rothschild and R.E. Lingenfelter, editors, *High Velocity Neutron Stars*, volume 366 of *American Institute of Physics Conference Series*, 111–117.
- Dunne L. et al., 2003. *Nature*, 424(6946):285–287.
- Duric N., 2004. *Advanced astrophysics*. Cambridge University Press.
- Eckart M.E. et al., 2010. *ApJ*, 708:584–597.
- Eddington A.S., 1916. *MNRAS*, 77(1):16–35. ISSN 0035-8711.
- Eggleton P., 2006. *Evolutionary Processes in Binary and Multiple Stars*. Cambridge University Press.

- Eldridge J.J., Langer N., and Tout C.A., 2011. *MNRAS*, 414(4):3501–3520.
- Eldridge J.J. and Maund J.R., 2016. *MNRAS*, 461(1):L117–L121.
- Eldridge J.J. and Stanway E.R., 2012. *MNRAS*, 419(1):479–489.
- Eldridge J.J., Stanway E.R., and Tang P.N., 2019a. *MNRAS*, 482(1):870–880.
- Eldridge J.J. and Tout C.A., 2004. *MNRAS*, 353:87–97.
- Eldridge J.J. and Tout C.A., 2019. *The Structure and Evolution of Stars*, chapter 9. World Scientific.
- Eldridge J.J. and Xiao L., 2019. *MNRAS*, 485(1):L58–L61.
- Eldridge J.J. et al., 2013. *MNRAS*, 436:774–795.
- Eldridge J.J. et al., 2017. *Publ. Astron. Soc. Australia*, 34:e058.
- Eldridge J.J. et al., 2018. *Publ. Astron. Soc. Australia*, 35:49.
- Eldridge J.J. et al., 2019b. *Publ. Astron. Soc. Australia*, 36:e041.
- Elliott J. et al., 2013. *A&A*, 556:A23.
- Ertl T. et al., 2019. *arXiv e-prints*, arXiv:1910.01641.
- Evans P.A. et al., 2009. *MNRAS*, 397:1177–1201.
- Farrell E. et al., 2020. *arXiv e-prints*, arXiv:2001.08711.
- Farrow D.J. et al., 2014. *MNRAS*, 437:748–770.
- Ferrarese L. and Merritt D., 2000. *ApJ*, 539(1):L9–L12.
- Ferrarotti A.S. and Gail H.P., 2006. *A&A*, 447(2):553–576.
- Filgas R. et al., 2010. *GRB Coordinates Network, Circular Service, No. 10592, #1 (2010)*, 10592.
- Filippenko A.V., 1997. *ARA&A*, 35:309–355.
- Fishman G.J. et al., 1993. *A&AS*, 97:17–20.
- Fitzpatrick E.L., 1999. *PASP*, 111:63–75.
- Fong W. and Berger E., 2011. *GRB Coordinates Network, Circular Service, No. 12155, #1 (2011)*, 12155.



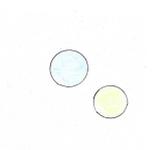
- Fong W. et al., 2016. *ApJ*, 833:151.
- Fonseca E. et al., 2020. *arXiv e-prints*, arXiv:2001.03595.
- Foreman-Mackey D., 2016. *The Journal of Open Source Software*, 1:24.
- Foreman-Mackey D. et al., 2013. *PASP*, 125(925):306.
- Fraija N. et al., 2019. *ApJ*, 885(1):29.
- Frail D.A. et al., 1997. *Nature*, 389(6648):261–263.
- Frail D.A. et al., 2001. *ApJ*, 562(1):L55–L58.
- Fraser-McKelvie A. et al., 2016. *MNRAS*, 462(1):L11–L15.
- Frederiks D., 2013. *GRB Coordinates Network, Circular Service, No. 14772*, 14772.
- Frederiks D. and Pal’Shin V., 2011. *GRB Coordinates Network, Circular Service, No. 12370*, 12370.
- Freedman W.L. et al., 2019. *ApJ*, 882(1):34.
- Fremling C. et al., 2018. *A&A*, 618:A37.
- Friis M. et al., 2015. *MNRAS*, 451:167–183.
- Fruchter A., Krolik J.H., and Rhoads J.E., 2001. *ApJ*, 563(2):597–610.
- Fruchter A.S., 1999. *ApJ*, 512:L1–L4.
- Fruchter A.S. and Hook R.N., 2002. *PASP*, 114:144–152.
- Fruchter A.S. et al., 1999a. *ApJ*, 519(1):L13–L16.
- Fruchter A.S. et al., 1999b. *ApJ*, 516(2):683–692.
- Fruchter A.S. et al., 2006. *Nature*, 441:463–468.
- Fryer C.L. and Heger A., 2005. *ApJ*, 623(1):302–313.
- Fryer C.L. and Woosley S.E., 1998. *ApJ*, 502(1):L9–L12.
- Fryer C.L. et al., 1999. *ApJ*, 520(2):650–660.
- Fryer C.L. et al., 2007. *PASP*, 119(861):1211–1232.
- Fryer C.L. et al., 2019. *European Physical Journal A*, 55(8):132.

- Fynbo J.P.U. et al., 2009. *ApJS*, 185:526–573.
- Fynbo J.U. et al., 2000. *ApJ*, 542(2):L89–L93.
- Fynbo J.U. et al., 2001. *A&A*, 369:373–379.
- Gaia Collaboration et al., 2018. *A&A*, 616:A1.
- Gal-Yam A., 2012. *Science*, 337(6097):927.
- Gal-Yam A. et al., 2006. *Nature*, 444(7122):1053–1055.
- Gal-Yam A. et al., 2009. *Nature*, 462(7273):624–627.
- Galama T.J. et al., 1998. *Nature*, 395(6703):670–672.
- Galama T.J. et al., 2000. *ApJ*, 536(1):185–194.
- Gardenier D.W. et al., 2019. *A&A*, 632:A125.
- Gatkine P., Vogel S., and Veilleux S., 2019. *arXiv e-prints*, arXiv:1910.13621.
- Gehrels N. et al., 2004. *ApJ*, 611:1005–1020.
- Gehrels N. et al., 2005. *Nature*, 437(7060):851–854.
- Gendre B. et al., 2013. *ApJ*, 766(1):30.
- Ghirlanda G., Ghisellini G., and Lazzati D., 2004. *ApJ*, 616(1):331–338.
- Gilmozzi R. and Spyromilio J., 2007. *The Messenger*, 127:11.
- Glover S.C.O. and Clark P.C., 2012. *MNRAS*, 426(1):377–388.
- Goad M.R. et al., 2007. *A&A*, 476:1401–1409.
- Goldreich P. and Nicholson P.D., 1989. *ApJ*, 342:1079.
- Goldstein A. et al., 2017. *ApJ*, 848:L14.
- Golenetskii S. et al., 2013. *GRB Coordinates Network, Circular Service, No. 15203*, 15203.
- Gomez S. et al., 2019. *ApJ*, 884(2):L55.
- Gompertz B. and Fruchter A., 2017. *ApJ*, 839(1):49.
- Gompertz B.P., Fruchter A.S., and Pe’er A., 2018. *ApJ*, 866(2):162.



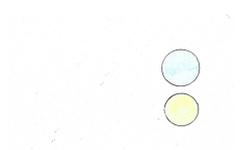
- Gompertz B.P., Fruchter A.S., and Peer A., 2018. *The Astrophysical Journal*, 866(2):162.
- Gompertz B.P. et al., 2013. *MNRAS*, 431(2):1745–1751.
- Gompertz B.P. et al., 2018. *ApJ*, 860(1):62.
- Goodman J. and Weare J., 2010. *Communications in Applied Mathematics and Computational Science*, 5(1):65–80.
- Gräfener G. et al., 2012. *A&A*, 547:A83.
- Graham J.F. and Fruchter A.S., 2013. *ApJ*, 774(2):119.
- Graham J.F. and Fruchter A.S., 2017. *ApJ*, 834:170.
- Graham J.F., Schady P., and Fruchter A.S., 2019. *arXiv e-prints*, arXiv:1904.02673.
- Graham J.F. et al., 2009. In C. Meegan, C. Kouveliotou, and N. Gehrels, editors, *American Institute of Physics Conference Series*, volume 1133 of *American Institute of Physics Conference Series*, 269–272.
- Graham J.F. et al., 2013. *GRB Coordinates Network, Circular Service, No. 15636, #1 (2013)*, 15636.
- Graham J.F. et al., 2015. *ArXiv e-prints*.
- Graur O. et al., 2017. *ApJ*, 837(2):120.
- Grazian A. et al., 2006a. *GRB Coordinates Network, Circular Service, No. 4545*, 4545.
- Grazian A. et al., 2006b. *A&A*, 449:951–968.
- Greiner J. et al., 2009. *ApJ*, 693:1610–1620.
- Greiner J. et al., 2011. *A&A*, 526:A30.
- Greiner J. et al., 2015a. *Nature*, 523(7559):189–192.
- Greiner J. et al., 2015b. *ApJ*, 809(1):76.
- Greis S.M.L. et al., 2016. *MNRAS*, 459(3):2591–2602.
- Greis S.M.L. et al., 2017. *MNRAS*, 470(1):489–499.
- Groh J.H., Oliveira A.S., and Steiner J.E., 2008. *A&A*, 485(1):245–256.

- Groh J.H. et al., 2014. *A&A*, 564:A30.
- Groot P.J. et al., 1998a. *ApJ*, 493(1):L27–L30.
- Groot P.J. et al., 1998b. *ApJ*, 502:L123–L127.
- Guépin C. and Kotera K., 2017. *A&A*, 603:A76.
- Gunn J.E. and Peterson B.A., 1965. *ApJ*, 142:1633–1636.
- Hainich R. et al., 2014. *A&A*, 565:A27.
- Hainich R. et al., 2015. *A&A*, 581:A21.
- Harding A.K., 1994. *ApJS*, 90:863.
- Hardy L.K. et al., 2017. *MNRAS*, 472(3):2800–2807.
- Hartmann D.H., 1999. *Proceedings of the National Academy of Sciences*, 96(9):4752–4755. ISSN 0027-8424.
- Hartoog O.E. et al., 2015. *A&A*, 580:A139.
- Hashimoto T. et al., 2015. *ApJ*, 806(2):250.
- Hashimoto T. et al., 2018. *ApJ*, 863(1):95.
- Hashimoto T. et al., 2019. *MNRAS*, 488(4):5029–5041.
- Hatsukade B. et al., 2019. *ApJ*, 876(2):91.
- Heckman T.M., Armus L., and Miley G.K., 1990. *ApJS*, 74:833.
- Heger A., Langer N., and Woosley S.E., 2000. *ApJ*, 528(1):368–396.
- Heger A. and Woosley S.E., 2002. *ApJ*, 567(1):532–543.
- Heintz K.E. et al., 2016. *GRB Coordinates Network, Circular Service, No. 20020, #1 (2016)*, 20020.
- Heintz K.E. et al., 2017. *A&A*, 601:A83.
- Heintz K.E. et al., 2019a. *A&A*, 621:A20.
- Heintz K.E. et al., 2019b. *A&A*, 629:A131.
- Heintz K.E. et al., 2019c. *MNRAS*, 486(2):2063–2074.



- Henden A. and Munari U., 2014. *Contributions of the Astronomical Observatory Skalnaté Pleso*, 43:518–522.
- Higgins A.B. et al., 2019. *MNRAS*, 484(4):5245–5255.
- Hirata K. et al., 1987. *Phys. Rev. Lett.*, 58(14):1490–1493.
- Hirschi R., Meynet G., and Maeder A., 2005. *A&A*, 443(2):581–591.
- Hjorth J., 2013. *Philosophical Transactions of the Royal Society of London Series A*, 371(1992):20120275–20120275.
- Hjorth J. and Bloom J.S., 2012. *The Gamma-Ray Burst - Supernova Connection*, 169–190. Cambridge University Press.
- Hjorth J. et al., 2003. *Nature*, 423(6942):847–850.
- Hjorth J. et al., 2012. *ApJ*, 756:187.
- Hodapp K.W. et al., 2003. *PASP*, 115:1388–1406.
- Holland S.T. et al., 2010. *ApJ*, 717:223–234.
- Hong Y., 2013. *Comput. Stat. Data Anal.*, 59:41–51. ISSN 0167-9473.
- Hook I.M. et al., 2004. *PASP*, 116:425–440.
- Hopkins A.M. and Beacom J.F., 2006. *ApJ*, 651(1):142–154.
- Horiuchi S. et al., 2011. *ApJ*, 738:154.
- Hoyle F., 1946. *MNRAS*, 106:343.
- Hoyle F., 1954. *ApJS*, 1:121.
- Hubble E., 1929. *Proceedings of the National Academy of Science*, 15(3):168–173.
- Hulse R.A. and Taylor J.H., 1975. *ApJ*, 195:L51–L53.
- Hunt L. et al., 2011. *ApJ*, 736(2):L36.
- Hurley J.R., Pols O.R., and Tout C.A., 2000. *MNRAS*, 315(3):543–569.
- Hurley J.R., Tout C.A., and Pols O.R., 2002. *MNRAS*, 329(4):897–928.
- Hut P., 1981. *A&A*, 99:126–140.
- IceCube Collaboration et al., 2018. *Science*, 361(6398):eaat1378.

- Ilbert O. et al., 2006. *A&A*, 457(3):841–856.
- Inserra C. et al., 2013. *ApJ*, 770(2):128.
- Ivezić Ž. et al., 2019. *ApJ*, 873(2):111.
- Iwamoto K. et al., 1998. *Nature*, 395(6703):672–674.
- Izzard R.G., Ramirez-Ruiz E., and Tout C.A., 2004. *MNRAS*, 348(4):1215–1228.
- Izzard R.G. et al., 2012. In *IAU Symposium*, volume 283, 95–102.
- Izzo L. et al., 2017. *MNRAS*, 472(4):4480–4496.
- Izzo L. et al., 2019. *Nature*, 565(7739):324–327.
- Jakobsson P. et al., 2004. *ApJ*, 617:L21–L24.
- Jakobsson P. et al., 2006. In S.S. Holt, N. Gehrels, and J.A. Nousek, editors, *Gamma-Ray Bursts in the Swift Era*, volume 836 of *American Institute of Physics Conference Series*, 552–557.
- Jakobsson P. et al., 2012. *ApJ*, 752(1):62.
- James C.W. et al., 2019. *arXiv e-prints*, arXiv:1912.07847.
- Janka H.T., 2012. *Annual Review of Nuclear and Particle Science*, 62(1):407–451.
- Janka H.T., 2017. *Neutrino Emission from Supernovae*, pp. 1575. Springer International Publishing.
- Japelj J. et al., 2016. *A&A*, 590:A129.
- Japelj J. et al., 2018. *A&A*, 617:A105.
- Jeong S. et al., 2014a. *GRB Coordinates Network, Circular Service, No. 15936*, 15936.
- Jeong S. et al., 2014b. *A&A*, 569:A93.
- Johns M. et al., 2012. *Giant Magellan Telescope: overview*, volume 8444 of *Society of Photo-Optical Instrumentation Engineers (SPIE) Conference Series*, 84441H. SPIE.
- Johnston S. et al., 2008. *Experimental Astronomy*, 22(3):151–273.
- Kann D.A. et al., 2018. *A&A*, 617:A122.



Kauffmann G., White S.D.M., and Guiderdoni B., 1993. *MNRAS*, 264:201–218.

Kawai N. et al., 2006. *Nature*, 440:184–186.

Kelly P.L., Kirshner R.P., and Pahre M., 2008. *ApJ*, 687(2):1201–1207.

Kennicutt Robert C. J., 1998. *ARA&A*, 36:189–232.

Kennicutt R.C. and Evans N.J., 2012. *ARA&A*, 50:531–608.

Kent S.M., 1985. *ApJS*, 59:115–159.

Kewley L.J. et al., 2001. *ApJ*, 556(1):121–140.

Kilpatrick C.D. et al., 2018. *MNRAS*, 480:2072–2084.

Kistler M.D. et al., 2009. *ApJ*, 705(2):L104–L108.

Klebesadel R.W., Strong I.B., and Olson R.A., 1973. *ApJ*, 182:L85.

Kobulnicky H.A. and Kewley L.J., 2004. *ApJ*, 617(1):240–261.

Kocevski D., West A.A., and Modjaz M., 2009. *ApJ*, 702(1):377–385.

Kocevski D. et al., 2010. *MNRAS*, 404:963–974.

Kouveliotou C. et al., 1993. *ApJ*, 413:L101.

Kovács A. and Szapudi I., 2015. *MNRAS*, 448:1305–1313.

Kriek M. et al., 2018. FAST: Fitting and Assessment of Synthetic Templates.

Kroupa P., 2001. *MNRAS*, 322(2):231–246.

Kruehler T. et al., 2013. *GRB Coordinates Network, Circular Service, No. 14264, #1 (2013)*, 14264.

Krühler T. et al., 2011. *A&A*, 534:A108.

Krühler T. et al., 2012a. *A&A*, 546:A8.

Krühler T. et al., 2012b. *ApJ*, 758(1):46.

Krühler T. et al., 2015. *A&A*, 581:A125.

Krühler T. et al., 2017. *A&A*, 602:A85.

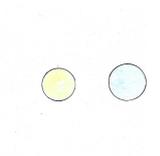
Kuiper G.P., 1938. *ApJ*, 88:472.

- Kumar P. and Zhang B., 2015. *Phys. Rep.*, 561:1–109.
- Kumar P. et al., 2019. *ApJ*, 887(2):L30.
- Kundu E. and Ferrario L., 2019. *MNRAS*, 3219.
- Kushnir D. et al., 2017. *MNRAS*, 467(2):2146–2149.
- Lamb D.Q. et al., 2004. *New Astron. Rev.*, 48(5-6):423–430.
- Langer N. and Norman C.A., 2006. *ApJ*, 638(2):L63–L66.
- Laskar T. et al., 2014. *ApJ*, 781:1.
- Law C.J. et al., 2019. *ApJ*, 886(1):24.
- Lawrence A. et al., 2007. *MNRAS*, 379:1599–1617.
- Le Floc’h E. et al., 2003. *A&A*, 400:499–510.
- Le Floc’h E. et al., 2006. *ApJ*, 642(2):636–652.
- Lee B. et al., 2013. *ApJ*, 774:47.
- Lee C.H., 2019. *ApJ*, 880(2):131.
- Lei W.H., Zhang B., and Liang E.W., 2013. *ApJ*, 765(2):125.
- Lei W.H. et al., 2017. *ApJ*, 849(1):47.
- Leloudas G. et al., 2015. *MNRAS*, 449(1):917–932.
- Leng M. and Giannios D., 2014. *MNRAS*, 445:L1–L5.
- Levan A. et al., 2005. *ApJ*, 624(2):880–888.
- Levan A. et al., 2006. *ApJ*, 647:471–482.
- Levan A. et al., 2016. *Space Sci. Rev.*, 202(1-4):33–78.
- Levan A.J. and Tanvir N.R., 2013. *GRB Coordinates Network, Circular Service, No. 14667, #1 (2013)*, 14667.
- Levan A.J. et al., 2007. *MNRAS*, 378:1439–1446.
- Levan A.J. et al., 2011. *Science*, 333(6039):199.
- Levan A.J. et al., 2014. *ApJ*, 781(1):13.



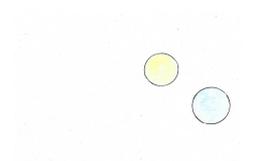
- Levan A.J. et al., 2017. *ApJ*, 848(2):L28.
- Levesque E.M. et al., 2010a. *ApJ*, 712(1):L26–L30.
- Levesque E.M. et al., 2010b. *AJ*, 139(2):694–711.
- Levesque E.M. et al., 2010c. *AJ*, 140(5):1557–1566.
- Li L.X. and Paczyński B., 1998. *ApJ*, 507(1):L59–L62.
- Liang E. et al., 2007. *ApJ*, 662:1111–1118.
- Lien A. et al., 2016. *ApJ*, 829(1):7.
- Littlejohns O. et al., 2013. *GRB Coordinates Network, Circular Service, No. 15067, #1 (2013)*, 15067.
- Littlejohns O. et al., 2014. *GRB Coordinates Network, Circular Service, No. 16050, #1 (2014)*, 16050.
- Lorimer D.R. et al., 2007. *Science*, 318(5851):777.
- Lotz J.M., Primack J., and Madau P., 2004. *AJ*, 128:163–182.
- Lunnan R. et al., 2014. *ApJ*, 787(2):138.
- Lunnan R. et al., 2015. *ApJ*, 804(2):90.
- Lyman J.D. et al., 2016. *MNRAS*, 457(1):328–350.
- Lyman J.D. et al., 2017. *MNRAS*, 467(2):1795–1817.
- Lyman J.D. et al., 2018. *Nature Astronomy*, 2:751–754.
- MacFadyen A.I. and Woosley S.E., 1999. *ApJ*, 524(1):262–289.
- MacFadyen A.I., Woosley S.E., and Heger A., 2001. *ApJ*, 550(1):410–425.
- Macquart J.P. et al., 2015. In *Advancing Astrophysics with the Square Kilometre Array (AASKA14)*, 55.
- Madau P., 1995. *ApJ*, 441:18–27.
- Madau P. and Dickinson M., 2014. *ARA&A*, 52:415–486.
- Madau P. and Haardt F., 2015. *ApJ*, 813:L8.
- Madison D.R. et al., 2019. *ApJ*, 887(2):252.

- Maeder A., 1987. *A&A*, 178:159–169.
- Maeder A. and Meynet G., 1987. *A&A*, 182:243–263.
- MAGIC Collaboration et al., 2019a. *Nature*, 575:459–463.
- MAGIC Collaboration et al., 2019b. *Nature*, 575:455–458.
- Mahony E.K. et al., 2018. *ApJ*, 867(1):L10.
- Maiolino R. et al., 2008. *A&A*, 488(2):463–479.
- Malesani D. et al., 2010. *GRB Coordinates Network, Circular Service, No. 10362*, 10362.
- Malesani D. et al., 2011. *GRB Coordinates Network, Circular Service, 12343, 1 (2011)*, 12343.
- Malesani D. et al., 2013. *GRB Coordinates Network, Circular Service, No. 14552, #1 (2013)*, 14552.
- Malesani D. et al., 2014. *GRB Coordinates Network, Circular Service, No. 17170*, 17170.
- Malesani D. et al., 2015. *GRB Coordinates Network, Circular Service, No. 17655, #1 (2015)*, 17655.
- Malesani D. et al., 2016. *GRB Coordinates Network, Circular Service, No. 20319, #1 (2016)*, 20319.
- Malmquist K.G., 1922. *Meddelanden fran Lunds Astronomiska Observatorium Serie I*, 100:1–52.
- Mandel I. and de Mink S.E., 2016. *MNRAS*, 458(3):2634–2647.
- Mapelli M. et al., 2019. *arXiv e-prints*, arXiv:1909.01371.
- Maraston C., 2005. *MNRAS*, 362(3):799–825.
- Marchant P. et al., 2016. *A&A*, 588:A50.
- Marchant P. et al., 2017. *A&A*, 604:A55.
- Marcote B. et al., 2020. *arXiv e-prints*, arXiv:2001.02222.
- Margalit B. and Metzger B.D., 2017. *ApJ*, 850(2):L19.



- Margalit B. and Metzger B.D., 2018. *ApJ*, 868(1):L4.
- Margalit B. et al., 2018a. *MNRAS*, 475(2):2659–2674.
- Margalit B. et al., 2018b. *MNRAS*, 481(2):2407–2426.
- Martin C. et al., 2003. In J.C. Blades and O.H.W. Siegmund, editors, *Future EUV/UV and Visible Space Astrophysics Missions and Instrumentation.*, volume 4854 of *Proc. SPIE*, 336–350.
- Martin D.C. and GALEX Science Team, 2005. In *American Astronomical Society Meeting Abstracts*, volume 37 of *Bulletin of the American Astronomical Society*, 1235.
- Martins F. et al., 2009. *A&A*, 495(1):257–270.
- Martins F. et al., 2013. *A&A*, 554:A23.
- Matz S.M. et al., 1988. *Nature*, 331(6155):416–418.
- Mazets E.P. et al., 1981. *Ap&SS*, 80(1):3–83.
- Mazets E.P. et al., 1982. *Ap&SS*, 84(1):173–189.
- Mazzali P.A. et al., 2008. *Science*, 321(5893):1185.
- Mazzali P.A. et al., 2014. *MNRAS*, 443(1):67–71.
- McCall M.L., 2004. *AJ*, 128:2144–2169.
- McGuire J.T.W. et al., 2016. *ApJ*, 825:135.
- Melandri A. and Immler S., 2013. *GRB Coordinates Network, Circular Service, No. 14540, #1 (2013)*, 14540.
- Men Y. et al., 2019. *MNRAS*, 489(3):3643–3647.
- Meszáros P. and Rees M.J., 1992. *MNRAS*, 257(2):29P–31P.
- Meszáros P., Rees M.J., and Papathanassiou H., 1994. *ApJ*, 432:181–193.
- Metcalfe N. et al., 2006. *MNRAS*, 370:1257–1273.
- Metzger B.D., Berger E., and Margalit B., 2017. *ApJ*, 841(1):14.
- Metzger B.D. et al., 2011. *MNRAS*, 413(3):2031–2056.

- Metzger B.D. et al., 2015. *MNRAS*, 454(3):3311–3316.
- Metzger M.R. et al., 1997. *Nature*, 387(6636):878–880.
- Michałowski M.J. et al., 2012. *ApJ*, 755(2):85.
- Michałowski M.J. et al., 2015. *A&A*, 582:A78.
- Michałowski M.J. et al., 2016. *A&A*, 595:A72.
- Michałowski M.J. et al., 2018a. *A&A*, 617:A143.
- Michałowski M.J. et al., 2018b. *A&A*, 616:A169.
- Milvang-Jensen B. et al., 2012. *ApJ*, 756(1):25.
- Mingarelli C.M.F., Levin J., and Lazio T.J.W., 2015. *ApJ*, 814(2):L20.
- Mirzoyan R., 2019. *The Astronomer’s Telegram*, 12390:1.
- Modjaz M. et al., 2008. *AJ*, 135(4):1136–1150.
- Modjaz M. et al., 2016. *ApJ*, 832:108.
- Modjaz M. et al., 2019. *arXiv e-prints*, arXiv:1901.00872.
- Moe M. and Di Stefano R., 2017. *ApJS*, 230(2):15.
- Mokiem M.R. et al., 2006. *A&A*, 456(3):1131–1151.
- Morgan H.L. and Edmunds M.G., 2003. *MNRAS*, 343(2):427–442.
- Moriya T.J. and Eldridge J.J., 2016. *MNRAS*, 461(2):2155–2161.
- Murphy D. et al., 2015. *GRB Coordinates Network, Circular Service, No. 17947, #1 (2015)*, 17947.
- Nakamura T. et al., 2001. *ApJ*, 550(2):991–999.
- Nandra K. et al., 2013. *arXiv e-prints*, arXiv:1306.2307.
- Nappo F. et al., 2017. *A&A*, 598:A23.
- Narayan R., Paczynski B., and Piran T., 1992. *ApJ*, 395:L83.
- Narayana Bhat P. et al., 2016. *ApJS*, 223(2):28.
- Navarro J.F., Frenk C.S., and White S.D.M., 1997. *ApJ*, 490(2):493–508.



- Nemiroff R.J., 1994. *Comments on Astrophysics*, 17:189.
- Neugent K. and Massey P., 2019. *Galaxies*, 7(3):74.
- Nicholl M., Guillochon J., and Berger E., 2017a. *ApJ*, 850(1):55.
- Nicholl M. et al., 2017b. *ApJ*, 843(2):84.
- Nicuesa A., Klose S., and Greiner J., 2010a. *GRB Coordinates Network, Circular Service, No. 10844, #1 (2010)*, 10844.
- Nicuesa A. et al., 2010b. *GRB Coordinates Network, Circular Service, No. 10383, 10383*.
- Nicuesa Guelbenzu A., Olivares E.F., and Greiner J., 2011. *GRB Coordinates Network, Circular Service, No. 11785, #1 (2011)*, 11785.
- Noeske K.G. et al., 2007. *ApJ*, 660:L43–L46.
- Noll S. et al., 2009. *A&A*, 507:1793–1813.
- Nomoto K. et al., 2004a. In C.L. Fryer, editor, *Astrophysics and Space Science Library*, volume 302 of *Astrophysics and Space Science Library*, 277–325.
- Nomoto K. et al., 2004b. *Progress of Theoretical Physics Supplement*, 155:299–302.
- Nomoto K. et al., 2005. *Ap&SS*, 298(1-2):81–86.
- Norris J.P. and Bonnell J.T., 2006. *ApJ*, 643(1):266–275.
- Nousek J.A. et al., 2006. *ApJ*, 642:389–400.
- Ofek E.O. et al., 2014. *ApJ*, 788(2):154.
- Oke J.B. and Gunn J.E., 1983. *ApJ*, 266:713–717.
- Oke J.B. et al., 1995. *PASP*, 107:375.
- Paczynski B., 1986. *ApJ*, 308:L43–L46.
- Paczynski B., 1991. *Acta Astron.*, 41:257–267.
- Paczynski B. and Rhoads J.E., 1993. *ApJ*, 418:L5.
- Page K.L. et al., 2009. *MNRAS*, 395:328–334.
- Palmerio J.T. et al., 2019. *A&A*, 623:A26.

- Panaitescu A. and Kumar P., 2001. *ApJ*, 560(1):L49–L53.
- Parsons S.G. et al., 2016. *MNRAS*, 463(2):2125–2136.
- Paul J. et al., 2011. *Comptes Rendus Physique*, 12:298–308.
- Peebles P.J.E., 1966. *ApJ*, 146:542.
- Peebles P.J.E., 1968. *ApJ*, 153:1.
- Peng Y.j. et al., 2010. *ApJ*, 721(1):193–221.
- Penrose R. and Floyd R.M., 1971. *Nature Physical Science*, 229(6):177–179.
- Pérez-Ramírez D. et al., 2013. In A.J. Castro-Tirado, J. Gorosabel, and I.H. Park, editors, *EAS Publications Series*, volume 61 of *EAS Publications Series*, 345–349.
- Perley D.A. et al., 2006. *GRB Coordinates Network, Circular Service, No. 5387*, 5387.
- Perley D.A. et al., 2007. In S. Immler, K. Weiler, and R. McCray, editors, *Supernova 1987A: 20 Years After: Supernovae and Gamma-Ray Bursters*, volume 937 of *American Institute of Physics Conference Series*, 526–529.
- Perley D.A. et al., 2009. *AJ*, 138(6):1690–1708.
- Perley D.A. et al., 2010. *GRB Coordinates Network, Circular Service, No. 10399*, 10399.
- Perley D.A. et al., 2012. *ApJ*, 758:122.
- Perley D.A. et al., 2013. *ApJ*, 778:128.
- Perley D.A. et al., 2015. *ApJ*, 801(2):102.
- Perley D.A. et al., 2016a. *ApJ*, 817(1):7.
- Perley D.A. et al., 2016b. *ApJ*, 817(1):8.
- Perley D.A. et al., 2017. *MNRAS*, 465(1):L89–L93.
- Perlmutter S. et al., 1999. *ApJ*, 517(2):565–586.
- Péroux C. et al., 2003. *MNRAS*, 345(2):480–496.
- Pescalli A. et al., 2016. *A&A*, 587:A40.



- Petroff E., Hessels J.W.T., and Lorimer D.R., 2019. *A&ARv*, 27(1):4.
- Petroff E. et al., 2016. *Publ. Astron. Soc. Australia*, 33:e045.
- Petrovic J. et al., 2005. *A&A*, 435(1):247–259.
- Pickles A.J., 1998. *PASP*, 110:863–878.
- Pinter S. et al., 2019. *Astronomische Nachrichten*, 340(7):618–621.
- Piran T., 2005. In E.M. de Gouveia dal Pino, G. Lugones, and A. Lazarian, editors, *Magnetic Fields in the Universe: From Laboratory and Stars to Primordial Structures.*, volume 784 of *American Institute of Physics Conference Series*, 164–174.
- Piran T. et al., 2013. *Philosophical Transactions of the Royal Society of London Series A*, 371(1992):20120273–20120273.
- Piran T. et al., 2019. *ApJ*, 871(2):L25.
- Planck Collaboration et al., 2018. *arXiv e-prints*, arXiv:1807.06209.
- Platts E. et al., 2019. *Phys. Rep.*, 821:1–27.
- Podsiadlowski P. et al., 2004. *ApJ*, 607(1):L17–L20.
- Podsiadlowski P. et al., 2010. *MNRAS*, 406(2):840–847.
- Prieto J.L., Stanek K.Z., and Beacom J.F., 2008. *ApJ*, 673(2):999–1008.
- Prochaska J.X., 1999. *ApJ*, 511(2):L71–L74.
- Prochaska J.X. et al., 2005. *GRB Coordinates Network, Circular Service, No. 3679*, 3679.
- Prochaska J.X. et al., 2006. *ApJ*, 642(2):989–994.
- Prochaska J.X. et al., 2008. *ApJ*, 685:344–353.
- Prochaska J.X. et al., 2009. *ApJ*, 691(1):L27–L32.
- Prochaska J.X. et al., 2019. *Science*, 365:aay0073.
- Qi Z. et al., 2015. *ApJ*, 150:137.
- Racusin J.L. et al., 2008. *Nature*, 455:183–188.
- Racusin J.L. et al., 2009. *ApJ*, 698(1):43–74.

- Racusin J.L. et al., 2010. *GRB Coordinates Network, Circular Service, No. 10361, #1 (2010)*, 10361.
- Ramírez-Agudelo O.H. et al., 2015. *A&A*, 580:A92.
- Ramírez-Agudelo O.H. et al., 2017. *A&A*, 600:A81.
- Ramirez-Ruiz E., Trentham N., and Blain A.W., 2002. *MNRAS*, 329:465–474.
- Ravi V. et al., 2019. *Nature*, 572(7769):352–354.
- Reddy N.A. and Steidel C.C., 2009. *ApJ*, 692(1):778–803.
- Rees M.J. and Meszaros P., 1992. *MNRAS*, 258:41.
- Rees M.J. and Meszaros P., 1994. *ApJ*, 430:L93.
- Rezzolla L., Most E.R., and Weih L.R., 2018. *ApJ*, 852(2):L25.
- Rhoads J.E., 1997. *ApJ*, 487(1):L1–L4.
- Rhoads J.E., 1999. *A&AS*, 138:539–540.
- Rhoads J.E., 2003. *ApJ*, 591(2):1097–1103.
- Riess A.G. et al., 1998. *AJ*, 116(3):1009–1038.
- Riess A.G. et al., 2016. *ApJ*, 826(1):56.
- Robertson B.E. and Ellis R.S., 2012. *ApJ*, 744(2):95.
- Robertson B.E. et al., 2010. *Nature*, 468(7320):49–55.
- Robertson B.E. et al., 2015. *ApJ*, 802(2):L19.
- Rodrigo C., Solano E., and Bayo A., 2012. SVO Filter Profile Service Version 1.0. IVOA Working Draft 15 October 2012.
- Rodrigo C., Solano E., and Bayo A., 2013. SVO Filter Profile Service Access Protocol Version 1.0. IVOA Working Draft 10 May 2013.
- Rol E. et al., 2005. *ApJ*, 624:868–879.
- Rol E. et al., 2007a. *ApJ*, 669(2):1098–1106.
- Rol E. et al., 2007b. *MNRAS*, 374:1078–1084.
- Roming P.W.A. et al., 2005. *Space Sci. Rev.*, 120:95–142.

- Rossi A. et al., 2014. *A&A*, 572:A47.
- Rueda J.A., Ruffini R., and Wang Y., 2019. *Universe*, 5:110.
- Ruiz-Velasco A.E. et al., 2007. *ApJ*, 669:1–9.
- Russell H.N., 1914. *Popular Astronomy*, 22:275–294.
- Ryan G. et al., 2015. *ApJ*, 799(1):3.
- Ryden B., 2003. *Introduction to cosmology*. Pearson Education.
- Salpeter E.E., 1955. *ApJ*, 121:161.
- Salvaterra R. et al., 2009. *Nature*, 461:1258–1260.
- Sana H. et al., 2012. *Science*, 337(6093):444.
- Santini P. et al., 2009. *VizieR Online Data Catalog*, 350.
- Sari R., Narayan R., and Piran T., 1996. *ApJ*, 473:204.
- Sari R. and Piran T., 1999. *ApJ*, 517(2):L109–L112.
- Sari R., Piran T., and Halpern J.P., 1999. *ApJ*, 519(1):L17–L20.
- Sari R., Piran T., and Narayan R., 1998. *ApJ*, 497:L17–L20.
- Savaglio S., Glazebrook K., and Le Borgne D., 2009. *ApJ*, 691(1):182–211.
- Savaglio S. et al., 2012. *MNRAS*, 420(1):627–636.
- Schady P., 2017. *Royal Society Open Science*, 4(7):170304.
- Schady P. et al., 2015. *A&A*, 579:A126.
- Schaerer D., 2002. *A&A*, 382:28–42.
- Schaerer D., 2003. *A&A*, 397:527–538.
- Schlafly E.F. and Finkbeiner D.P., 2011. *ApJ*, 737:103.
- Schlafly E.F., Meisner A.M., and Green G.M., 2019. *ApJS*, 240(2):30.
- Schlegel D.J., Finkbeiner D.P., and Davis M., 1998. *ApJ*, 500:525–553.
- Schmidt M., 1959. *ApJ*, 129:243.
- Schneider F.R.N. et al., 2018. *A&A*, 618:A73.

- Schulze S. et al., 2014. *A&A*, 566:A102.
- Schulze S. et al., 2015. *ApJ*, 808(1):73.
- Selsing J. et al., 2019a. *GRB Coordinates Network*, 23695:1.
- Selsing J. et al., 2019b. *A&A*, 623:A92.
- Serra P. et al., 2011. *ApJ*, 740:22.
- Shanks T. et al., 2015. *MNRAS*, 451:4238–4252.
- Sheffer Y. et al., 2009. *ApJ*, 701:L63–L67.
- Shivvers I. et al., 2017. *PASP*, 129(5):054201.
- Siegel D.M., Barnes J., and Metzger B.D., 2019. *Nature*, 569(7755):241–244.
- Siegel M.H. and Grupe D., 2013. *GRB Coordinates Network, Circular Service, No. 14180, #1 (2013)*, 14180.
- Skidmore W., TMT International Science Development Teams, and Science Advisory Committee T., 2015. *Research in Astronomy and Astrophysics*, 15(12):1945.
- Skrutskie M.F. et al., 2006. *AJ*, 131:1163–1183.
- Smartt S.J., 2009. *ARA&A*, 47(1):63–106.
- Smartt S.J., 2015. *Publ. Astron. Soc. Australia*, 32:e016.
- Sobacchi E. et al., 2017. *MNRAS*, 472(1):616–627.
- Sobral D. et al., 2016. *MNRAS*, 458(4):3443–3454.
- Sokolov V.V. et al., 2001. *A&A*, 372:438–455.
- Song H.F. et al., 2016. *A&A*, 585:A120.
- Songaila A., 2001. *ApJ*, 561(2):L153–L156.
- Sparre M. et al., 2014. *ApJ*, 785:150.
- Spitler L.G. et al., 2016. *Nature*, 531(7593):202–205.
- Stanek K.Z. et al., 2006. *Acta Astron.*, 56:333–345.
- Stanway E.R. and Eldridge J.J., 2018. *MNRAS*, 479(1):75–93.

- Stanway E.R. and Eldridge J.J., 2019. *A&A*, 621:A105.
- Stanway E.R., Eldridge J.J., and Becker G.D., 2016. *MNRAS*, 456(1):485–499.
- Stanway E.R. et al., 2015a. *MNRAS*, 446(4):3911–3925.
- Stanway E.R. et al., 2015b. *ApJ*, 798(1):L7.
- Starling R.L.C. et al., 2011. *MNRAS*, 411:2792–2803.
- Starling R.L.C. et al., 2012. *MNRAS*, 427(4):2950–2964.
- Stevance H.F. et al., 2017. *MNRAS*, 469(2):1897–1911.
- Stevance H.F. et al., 2018. *MNRAS*, 479(4):4535–4543.
- Sukhbold T. and Adams S., 2019. *arXiv e-prints*, arXiv:1905.00474.
- Sukhbold T. et al., 2016. *ApJ*, 821(1):38.
- Svensson K.M. et al., 2010. *MNRAS*, 405(1):57–76.
- Svensson K.M. et al., 2012. *MNRAS*, 421(1):25–35.
- Szécsi D. et al., 2015. *A&A*, 581:A15.
- Tanga M. et al., 2018. *A&A*, 615:A136.
- Tanvir N.R., Levan A.J., and Wold T., 2013a. *GRB Coordinates Network, Circular Service, No. 14175, #1 (2013)*, 14175.
- Tanvir N.R. et al., 2009. *Nature*, 461:1254–1257.
- Tanvir N.R. et al., 2010. *GRB Coordinates Network, Circular Service, No. 10366*, 10366.
- Tanvir N.R. et al., 2012. *ApJ*, 754:46.
- Tanvir N.R. et al., 2013b. *nat*, 500:547–549.
- Tanvir N.R. et al., 2017. *ApJ*, 848:L27.
- Tanvir N.R. et al., 2018. *ApJ*, 865:107.
- Tanvir N.R. et al., 2019. *MNRAS*, 483(4):5380–5408.
- Tarnopolski M., 2015. *A&A*, 581:A29.

- Tavani M., 1997. *ApJ*, 483(2):L87–L90.
- Taylor J.H., Fowler L.A., and McCulloch P.M., 1979. *Nature*, 277(5696):437–440.
- Taylor M.B., 2005. In P. Shopbell, M. Britton, and R. Ebert, editors, *Astronomical Data Analysis Software and Systems XIV*, volume 347 of *ASP Conference Series*, 29.
- Taylor P. and Kobayashi C., 2015. *MNRAS*, 448(2):1835–1846.
- Tendulkar S.P. et al., 2017. *ApJ*, 834(2):L7.
- The CHIME/FRB Collaboration et al., 2020. *arXiv e-prints*, arXiv:2001.10275.
- Thöne C.C. et al., 2008. *ApJ*, 676(2):1151–1161.
- Thornton D. et al., 2013. *Science*, 341(6141):53–56.
- Tremonti C.A. et al., 2004. *ApJ*, 613(2):898–913.
- Trentham N., Ramirez-Ruiz E., and Blain A.W., 2002. *MNRAS*, 334:983–989.
- Trenti M., Perna R., and Jimenez R., 2015. *ApJ*, 802(2):103.
- Trenti M. et al., 2012. *ApJ*, 749(2):L38.
- Troja E. et al., 2019. *MNRAS*, 489(2):1919–1926.
- Trotter A. et al., 2014. *GRB Coordinates Network, Circular Service, No. 17004, #1 (2014)*, 17004.
- Tunnicliffe R.L. and Levan A., 2012. In P. Roming, N. Kawai, and E. Pian, editors, *Death of Massive Stars: Supernovae and Gamma-Ray Bursts*, volume 279, 415–416.
- Tunnicliffe R.L. et al., 2014. *MNRAS*, 437(2):1495–1510.
- Urata Y., Huang K.Y., and Im M., 2010. *GRB Coordinates Network, Circular Service, No. 10375*, 10375.
- van der Horst A.J. et al., 2009. *ApJ*, 699:1087–1091.
- van der Horst A.J. et al., 2015. *MNRAS*, 446:4116–4125.
- Van Dyk S.D. et al., 2018. *ApJ*, 860(2):90.
- van Paradijs J. et al., 1997. *Nature*, 386(6626):686–689.

- Vanbeveren D., van Bever J., and De Donder E., 1997. *A&A*, 317:487–502.
- VanderPlas J., 2014. *arXiv e-prints*, arXiv:1411.5018.
- Vergani S.D. et al., 2015. *A&A*, 581:A102.
- Vernet J. et al., 2011. *A&A*, 536:A105.
- Vink J.S. and de Koter A., 2005. *A&A*, 442(2):587–596.
- Vink J.S., de Koter A., and Lamers H.J.G.L.M., 2001. *A&A*, 369:574–588.
- Vink J.S., Gräfener G., and Harries T.J., 2011a. *A&A*, 536:L10.
- Vink J.S. and Harries T.J., 2017. *A&A*, 603:A120.
- Vink J.S. et al., 2011b. *A&A*, 531:A132.
- Vogelsberger M. et al., 2019. *arXiv e-prints*, arXiv:1904.07238.
- Vreeswijk P.M. et al., 2001. *ApJ*, 546(2):672–680.
- Vreeswijk P.M. et al., 2018. *GRB Coordinates Network*, 22996:1.
- Walborn N.R. et al., 1987. *ApJ*, 321:L41.
- Wang J. et al., 2018. *ApJ*, 867(2):147.
- Wang L. et al., 2003. *ApJ*, 592(1):457–466.
- Wang S.Q. et al., 2017a. *ApJ*, 850(2):148.
- Wang Y.Z. et al., 2017b. *ApJ*, 851(1):L20.
- Waxman E., 1997a. *ApJ*, 489(1):L33–L36.
- Waxman E., 1997b. *ApJ*, 485(1):L5–L8.
- Waxman E. and Draine B.T., 2000. *ApJ*, 537:796–802.
- Wheeler J.C. et al., 2000. *ApJ*, 537(2):810–823.
- Whitaker K.E. et al., 2017. *ApJ*, 850:208.
- Whitmore B.C. et al., 2016. *AJ*, 151:134.
- Wiersema K. et al., 2012. *GRB Coordinates Network, Circular Service, No. 12991*, 12991.

- Wiersema K. et al., 2018. *MNRAS*, 481(1):1126–1132.
- Wijers R.A.M.J. and Galama T.J., 1999. *ApJ*, 523(1):177–186.
- Wijers R.A.M.J., Rees M.J., and Meszaros P., 1997. *MNRAS*, 288(4):L51–L56.
- Williams C.C. et al., 2018. *ApJS*, 236(2):33.
- Williams R.K., 1995. *Phys. Rev. D*, 51:5387–5427.
- Winkler C. et al., 2003. *A&A*, 411:L1–L6.
- Woosley S. and Janka T., 2005. *Nature Physics*, 1(3):147–154.
- Woosley S.E., 1993. *ApJ*, 405:273–277.
- Woosley S.E., 2010. *ApJ*, 719(2):L204–L207.
- Woosley S.E., 2019. *ApJ*, 878(1):49.
- Woosley S.E. and Bloom J.S., 2006. *ARA&A*, 44(1):507–556.
- Woosley S.E., Heger A., and Weaver T.A., 2002. *Reviews of Modern Physics*, 74(4):1015–1071.
- Woosley S.E. and MacFadyen A.I., 1999. *A&AS*, 138:499–502.
- Woźniak P.R. et al., 2009. *ApJ*, 691(1):495–502.
- Wright E.L., 2006. *PASP*, 118:1711–1715.
- Wright E.L. et al., 2010. *AJ*, 140:1868–1881.
- Xi Z.z., 1955. *Acta Astronomica Sinica*, 3:183–196.
- Xiao L., Stanway E.R., and Eldridge J.J., 2018. *MNRAS*, 477(1):904–934.
- Yoon S.C., Dierks A., and Langer N., 2012. *A&A*, 542:A113.
- Yoon S.C. and Langer N., 2005. *A&A*, 443(2):643–648.
- Yoon S.C., Langer N., and Norman C., 2006. *A&A*, 460(1):199–208.
- Yu Y.B. et al., 2015. *MNRAS*, 446(4):3642–3650.
- Zafar T. et al., 2011. *A&A*, 532:A143.
- Zafar T. et al., 2012. *ApJ*, 753(1):82.

- Zafar T. et al., 2018a. *ApJ*, 860(2):L21.
- Zafar T. et al., 2018b. *MNRAS*, 479:1542–1554.
- Zafar T. et al., 2018c. *MNRAS*, 480:108–118.
- Zahn J.P., 1975. *A&A*, 41:329–344.
- Zahn J.P., 1977. *A&A*, 500:121–132.
- Zahn J.P., 2008. In M.J. Goupil and J.P. Zahn, editors, *Tidal dissipation in binary systems*, volume 29 of *EAS Publications Series*, 67–90.
- Zalamea I. and Beloborodov A.M., 2011. *MNRAS*, 410(4):2302–2308.
- Zapartas E. et al., 2017a. *A&A*, 601:A29.
- Zapartas E. et al., 2017b. *ApJ*, 842(2):125.
- Zauderer B.A. et al., 2013. *ApJ*, 767:161.
- Zhang B. and Mészáros P., 2001. *ApJ*, 552(1):L35–L38.
- Zhang B. et al., 2006. *ApJ*, 642(1):354–370.
- Zhang B.B. et al., 2016. *ApJ*, 816(2):72.
- Zhang B.T. et al., 2018. *Phys. Rev. D*, 97(8):083010.
- Zhang Z.B. and Choi C.S., 2008. *A&A*, 484(2):293–297.
- Zheng W., Filippenko A.V., and Graham M., 2016. *GRB Coordinates Network, Circular Service, No. 19668, #1 (2016)*, 19668.

This thesis has been typeset from  $\text{\TeX}$ / $\text{\LaTeX}$  files prepared by the Author.